



# PACIFIC EARTHQUAKE ENGINEERING RESEARCH CENTER

## **Benchmarking of Nonlinear Geotechnical Ground Response Analysis Procedures**

**Jonathan P. Stewart**

**Annie On-Lei Kwok**

University of California, Los Angeles

**Youssef M.A. Hashash**

University of Illinois, Urbana-Champaign

**Neven Matasovic**

Geosyntec Consultants, Huntington Beach, California

**Robert Pyke**

Lafayette, California

**Zhiliang Wang**

Geomatrix Consultants, Inc., Oakland, California

**Zhaohui Yang**

URS Corporation, Oakland, California

# **Benchmarking of Nonlinear Geotechnical Ground Response Analysis Procedures**

**Jonathan P. Stewart**

**Annie On-Lei Kwok**

Department of Civil and Environmental Engineering  
University of California, Los Angeles

**Youssef M.A. Hashash**

Department of Civil and Environmental Engineering  
University of Illinois, Urbana-Champaign

**Neven Matasovic**

Geosyntec Consultants, Huntington Beach, California

**Robert Pyke**

Lafayette, California

**Zhiliang Wang**

Geomatrix Consultants, Inc., Oakland, California

**Zhaohui Yang**

URS Corporation, Oakland, California

PEER Report 2008/04

Pacific Earthquake Engineering Research Center

College of Engineering

University of California, Berkeley

August 2008

## ABSTRACT

One-dimensional seismic ground response analyses are often performed using equivalent-linear procedures, which require few, generally well-known parameters. Nonlinear analyses have the potential to more accurately simulate soil behavior, but implementation in practice has been limited because of poorly documented and unclear parameter selection and code usage protocols, as well as inadequate documentation of the benefits of nonlinear modeling relative to equivalent-linear modeling. Regarding code usage/parameter selection protocols, we note the following: (1) when input motions are from ground surface recordings, we show that the full outcropping motion should be used without converting to a “within” condition; (2) Rayleigh damping should be specified using at least two matching frequencies with a target level equal to the small-strain soil damping; (3) the “target” soil backbone curves used in analysis can be parameterized to capture either the soil’s dynamic shear strength when large-strain soil response is expected (strains approaching 1%), relatively small-strain response (i.e.,  $\gamma < 0.3\%$ ) as inferred from cyclic laboratory tests, or a hybrid of the two; (4) models used in nonlinear codes inevitably represent a compromise between the optimal fitting of the shapes of backbone and hysteretic damping curves, and we present two alternatives for model parameterization. The parameter selection and code usage protocols are tested by comparing predictions to data from vertical arrays. We find site amplification to be generally underpredicted at high frequencies and overpredicted at the elastic site period where a strong local resonance occurs that is not seen in the data. We speculate that this bias results from overdamping.

## **ACKNOWLEDGMENTS**

This study was sponsored by the Pacific Earthquake Engineering Research Center's (PEER's) Program of Applied Earthquake Engineering Research of Lifelines Systems supported by the California Department of Transportation and the Pacific Gas and Electric Company.

This work made use of the Earthquake Engineering Research Centers Shared Facilities supported by the National Science Foundation, under award number EEC-9701568 through PEER. Any opinions, findings, conclusions, or recommendations expressed in this publication are those of the authors and do not necessarily reflect those of the funding agencies.

This research has benefited from the helpful suggestions of an advisory panel consisting of Drs. Yousef Bozorgnia, Susan Chang, Brian Chiou, Ramin Golesorkhi, I.M. Idriss, Robert Kayen, Steven Kramer, Faiz Makdisi, Geoff Martin, Lelio Mejia, Tom Shantz, Walter Silva, and Joseph Sun. We would also like to thank T. Shakal, C. Real, Erol Kalkan, and K. Stokoe for their valuable suggestions and assistance in the blind prediction exercise.

# CONTENTS

<b>ABSTRACT</b> .....	<b>iii</b>
<b>ACKNOWLEDGMENTS</b> .....	<b>iv</b>
<b>TABLE OF CONTENTS</b> .....	<b>v</b>
<b>LIST OF FIGURES</b> .....	<b>ix</b>
<b>LIST OF TABLES</b> .....	<b>xvii</b>
<b>1 INTRODUCTION</b> .....	<b>1</b>
1.1 Statement of Problem.....	1
1.2 Organization of Report.....	3
<b>2 GROUND RESPONSE MODELING</b> .....	<b>5</b>
2.1 Equivalent-Linear Model .....	5
2.2 Nonlinear Models.....	8
2.2.1 Mathematical Representations of Soil Column and Solution Routines.....	8
2.2.2 Soil Material Models.....	9
2.2.3 Viscous Damping Formulations.....	14
2.3 Examples of Specific Nonlinear Codes .....	15
2.3.1 D-MOD_2 .....	16
2.3.2 DEEPSOIL.....	25
2.3.3 TESS .....	29
2.3.4 OpenSees.....	31
2.3.5 SUMDES .....	35
2.4 Verification Studies of Ground Response Analysis Codes.....	38
2.5 Comparisons of Results of Equivalent-Linear and Nonlinear Analyses.....	44
<b>3 ELEMENT TESTING</b> .....	<b>47</b>
3.1 Symmetrical Loading.....	47
3.2 Asymmetrical Sinusoidal Loading.....	49
3.3 Monotonic Loading with Small Reversals.....	49
<b>4 KEY ISSUES IN NONLINEAR GROUND RESPONSE ANALYSIS</b> .....	<b>55</b>
4.1 Parameterization of Backbone Curve.....	55
4.1.1 Backbone Curve.....	55
4.1.2 Material Damping .....	58

4.1.3	Parameter Selection for Backbone Curve and Damping.....	58
4.2	Limitation in Layer Thickness .....	70
4.3	Specification of Input Motion .....	70
4.4	Specification of Viscous Damping.....	71
<b>5</b>	<b>VERIFICATION OF NONLINEAR CODES AGAINST EXACT SOLUTIONS.....</b>	<b>73</b>
5.1	Introduction .....	73
5.2	One-Dimensional Ground Response Analysis Procedures .....	73
5.2.1	Frequency-Domain Analysis.....	74
5.2.2	Time-Domain Analysis .....	77
5.3	Specification of Input Motion .....	77
5.4	Modeling of Damping in Nonlinear Time-Domain Analyses.....	80
5.4.1	Viscous Damping.....	81
5.4.2	Hysteretic Damping .....	83
5.5	Validation against Known Theoretical Elastic Solutions .....	85
5.5.1	Shallow Stiff Site: Simi Valley Knolls School .....	86
5.5.2	Soft Clay Medium Depth Site: Treasure Island .....	89
5.5.3	Deep Stiff Site: La Cienega .....	91
5.5.4	Recommendations .....	93
5.6	Conclusions.....	94
<b>6</b>	<b>TURKEY FLAT BLIND PREDICTION .....</b>	<b>97</b>
6.1	Introduction.....	97
6.2	Turkey Flat Array.....	99
6.3	Site Properties and Baseline Geotechnical Model .....	101
6.4	Nonlinear Seismic Ground Response Analysis Codes .....	104
6.5	Code Usage Protocols .....	104
6.6	Results of Simulations and Comparisons to Data .....	106
6.6.1	Blind Prediction Results Using Baseline Model.....	106
6.6.2	Uncertainty in Prediction Results from Variability in Material Properties.....	110
6.6.3	Investigation of Possible Sources of Bias .....	112
6.7	Event-to-Event Variability of Turkey Flat Site Response .....	115
6.8	Code Performance at Higher Shaking Levels .....	116

6.9	Conclusions .....	118
<b>7</b>	<b>VERIFICATION OF NONLINEAR CODES AGAINST VERTICAL ARRAY DATA .....</b>	<b>119</b>
7.1	Introduction .....	119
7.2	Site Conditions .....	119
7.3	Geotechnical Model .....	120
7.3.1	Shear Wave Velocity Model .....	120
7.3.2	Nonlinear Soil Properties .....	121
7.4	Recorded Motions .....	122
7.5	Results .....	143
7.5.1	Prediction Results with Unscaled Input Motions .....	143
7.5.2	Prediction Results with Input Motions Scaled to Different Levels for La Cienega .....	161
7.6	Trends in Prediction Results across Various Vertical Array Sites .....	161
7.7	Comparison of Results from Equivalent-Linear and Nonlinear Analyses .....	167
<b>8</b>	<b>SUMMARY AND CONCLUSIONS .....</b>	<b>169</b>
8.1	Scope of Research .....	169
8.2	Research Finding and Recommendations .....	170
8.3	Recommendations for Future Research .....	173
	<b>REFERENCES .....</b>	<b>175</b>

## LIST OF FIGURES

Figure 2.1	Hysteresis loop of soil loaded in shear illustrating measurement of secant shear modulus ( $G$ ) and hysteretic damping ratio ( $\beta$ ) .....	6
Figure 2.2	Variation of normalized modulus ( $G/G_{max}$ ) and $\beta$ with shear strain. ....	7
Figure 2.3	(a) Lumped-mass system; (b) distributed mass system.....	8
Figure 2.4	Backbone curve .....	10
Figure 2.5	Extended Masing rules from Vucetic (1990) .....	11
Figure 2.6	Schematic of yield surface (after Potts and Zdravković 1999) .....	12
Figure 2.7	Schematic of plastic potential surface (after Potts and Zdravković 1999).....	13
Figure 2.8	Schematic of two hardening types (after Potts and Zdravković 1999) .....	14
Figure 2.9	Schematic illustration of MKZ constitutive model showing stress-strain behavior in first cycle (at time $t=0$ ) and subsequent cycle (at time $t$ ) .....	17
Figure 2.10	Comparison of positive portion of initial backbone curves obtained from KZ and MKZ models (Matasovic and Vucetic 1993a) .....	18
Figure 2.11	Measured and calculated initial modulus reduction curves (Matasovic and Vucetic 1993b) .....	19
Figure 2.12	Measured and calculated initial damping curves (Matasovic and Vucetic 1993a) .....	20
Figure 2.13	Families of degraded backbone curves (Matasovic and Vucetic 1993a) .....	22
Figure 2.14	Influence of soil plasticity on degradation parameter $t$ (Tan and Vucetic 1989; Vucetic 1994) .....	23
Figure 2.15	Influence of overconsolidation on degradation parameter $t$ (Vucetic and Dobry 1988).....	23
Figure 2.16	Comparisons of modulus reduction curves (top frame) and damping curves (bottom frame) obtained from Hashash and Park (2001) modified MKZ model with Laird and Stokoe (1993) experimental data .....	27
Figure 2.17	Cylindrical Von Mises yield surfaces for clay (after Prevost 1985, Lacy 1986, Parra 1996, and Yang 2000).....	33
Figure 2.18	Conical Drucker-Prager yield surfaces for sand (after Prevost 1985, Lacy 1986, Parra 1996, and Yang 2000).....	33

Figure 2.19	Hyperbolic backbone curve for soil nonlinear shear stress-strain response and piecewise-linear representation in multi-surface plasticity (after Prevost 1985 and Parra 1996) .....	33
Figure 2.20	Schematic of constitutive model response showing octahedral stress-effective confinement response and octahedral stress-octahedral strain response.....	34
Figure 2.21	Schematic of bounding surface plasticity framework (after Wang et al. 1990).....	36
Figure 2.22	Schematic showing stress-confinement response (after Li <i>et. al.</i> 1992).....	37
Figure 2.23	Comparison between recorded and calculated response spectra at representative soft clay sites, from Dickenson (1994).....	39
Figure 2.24	Comparison between recorded and calculated response spectra at (a) selected deep stiff clay sites in San Francisco Bay Area, from Chang (1996) and at (b) selected deep alluvial sites in Los Angeles area, from Chang (1996).....	40
Figure 2.25	Comparison of acceleration response spectrum of recorded motion at Treasure Island strong motion site (1989 Loma Prieta earthquake) with calculated spectra from ground response analyses. Calculations in upper frame utilized nearby rock recording (Yerba Buena Island) as control motion; lower frame presents statistical variation in calculated spectra for suite of control motions from rock sites in region surrounding Treasure Island. From Idriss 1993.....	42
Figure 2.26	Comparison of recorded ground surface accelerations and predictions by SHAKE (top two frames) and SPECTRA (third frame from top). Bottom frame shows recording at base of array (47-m depth). After Borja et al. 1999.....	43
Figure 2.27	Amplification factors predicted by equivalent-linear and nonlinear models for NEHRP category C (Silva et al. 2000).....	45
Figure 2.28	Amplification factors predicted by equivalent-linear and nonlinear models for NEHRP category E (Silva et al. 2000).....	46
Figure 3.1	Results of symmetrical loading with strain at constant amplitude from DEEPSOIL, D-MOD_2, OpenSees, and SUMDES (left frames), and TESS (right frames).....	48
Figure 3.2	Results of symmetrical loading with varying strain amplitude from all codes.....	49
Figure 3.3	Results of asymmetrical loading predicted by DEEPSOIL and OpenSees.....	51

Figure 3.4	Results of asymmetrical loading predicted by SUMDES (left frames) and TESS (right frames).....	51
Figure 3.5	Results of monotonic loading predicted by all codes.....	52
Figure 3.6	Results of monotonic loading with small reversal predicted by DEEPSOIL, D-MOD_2, OpenSees, and SUMDES (left frames), and TESS (right frames). .....	52
Figure 3.7	Results of reverse loading without unloading to failure predicted by DEEPSOIL, D-MOD_2, OpenSees, and SUMDES (left frames), and TESS (right frames). .....	53
Figure 3.8	Results of reverse loading with unloading to failure predicted by DEEPSOIL, D-MOD_2, OpenSees, and SUMDES (left frames), and TESS (right frames). .....	53
Figure 4.1	Schematic illustration of backbone curve used for nonlinear ground response analyses .....	57
Figure 4.2	Comparison of $G_{max} / S_u$ ratio from Weiler (1988) to inverse of pseudo-reference strain ( $1/\gamma_r$ ) from Darendeli (2001). Quantity $1/\gamma_r$ is approximately ratio of $G_{max}$ to shear strength implied by use of pseudo-reference strain for fitting nonlinear backbone curves .....	57
Figure 4.3	Modulus-reduction-strain values in database used by Darendeli (2001) .....	59
Figure 4.4	Modulus reduction and stress-strain curves implied by pseudo-reference strain from Darendeli (2001), reference strain model, and proposed procedure ( $PI=20$ , $OCR=1$ , $\sigma_v'=100$ kPa, $V_s=135$ m/s).....	60
Figure 4.5	Different approaches in fitting modulus reduction and damping curves in nonlinear analysis.....	62
Figure 4.6	Comparison of Bay Mud curves as determined from laboratory testing and hyperbolic stress-strain models .....	65
Figure 4.7	Stress-strain curve as implied by different reference and pseudo-reference strain values.....	66
Figure 4.8	Maximum strain and PGA profiles for $PHA^r=0.05$ g from nonlinear analyses .....	66
Figure 4.9	Maximum strain and PGA profiles for $PHA^r=0.17$ g from nonlinear analyses .....	67
Figure 4.10	Maximum strain and PGA profiles for $PHA^r=0.68$ g from nonlinear analyses .....	67
Figure 4.11	Maximum strain and PGA profiles for $PHA^r=1$ g from nonlinear analyses .....	68
Figure 4.12	Comparison of response spectra calculated from engineering models with different reference strain estimates of Bay Mud, shown for different $PHA^r$ .....	68

Figure 4.13	Prediction results for soft clay site (Apeel 2) and stiff soil site (Sepulveda) with model curves obtained from different approaches to fitting modulus reduction and damping curves in nonlinear analysis.....	69
Figure 4.14	Predicted response spectra computed using different numbers of layer .....	70
Figure 5.1	Incident and reflected waves in base rock layer for case of soil overlying rock and outcropping rock (amplitudes shown are relative to unit amplitude in Case 1 surface layer).....	75
Figure 5.2	Ratio of within to outcropping amplitudes for (a) various equivalent viscous damping ratios, (b) various base layer velocities ( $V_{s-H}$ ), and (c) mode shapes for various conditions .....	76
Figure 5.3	Acceleration histories for one-layer problem.....	79
Figure 5.4	Schematic illustration of viscous damping models and model parameters (after Park and Hashash 2004).....	82
Figure 5.5	Comparison of stress-strain loops generated from (a) Masing rules and Cundall-Pyke hypothesis; (b) Cundall-Pyke hypothesis with and without low-strain damping scheme (LSDS); and (c) comparison of damping curves generated from different schemes.....	85
Figure 5.6	Comparison of response spectra for shallow stiff site (Simi Valley Knolls School) for D-MOD_2, DEEPSOIL, and OPENSEES.....	88
Figure 5.7	Comparison of response spectra for shallow stiff site (Simi Valley Knolls School) for SUMDES and TESS .....	89
Figure 5.8	Comparison of response spectra for mid-period site with large impedance contrast (Treasure Island) for D-MOD_2, DEEPSOIL, and OPENSEES.....	90
Figure 5.9	Comparison of response spectra for mid-period site with large impedance contrast (Treasure Island) for SUMDES and TESS.....	91
Figure 5.10	Comparison of response spectra for long-period site (La Cienega) for D-MOD_2, DEEPSOIL, and OPENSEES .....	92
Figure 5.11	Comparison of response spectra for long-period site (La Cienega) for SUMDES and TESS.....	93
Figure 6.1	Plan and section views of Turkey Flat strong-motion array (adapted from Real 1988).....	100

Figure 6.2	Shear wave velocity profiles at mid-valley site (V1- D3 array). Data from Real (1988).....	103
Figure 6.3	Modulus reduction and damping curves based on material-specific testing (left side) and Darendeli (2001) model predictions (right side), mid-valley location. Data from Real (1988).....	104
Figure 6.4	Target and modeled damping curves for 0.91–1.82 m (depth range at which largest strains occur in soil profile).....	106
Figure 6.5	Acceleration histories for data and simulation results from DEEPSOIL. Results shown for two horizontal directions and two elevations (V1, ground surface; D2, 10-m depth. Recorded input motions at elevation D3 also shown.....	108
Figure 6.6	Acceleration response spectra for data and simulation results compared through direct spectral ordinates and prediction residuals. Results shown for two horizontal directions and two elevations (V1 = ground surface; D2 = 10 m depth). Results shown to maximum period of $1/(1.25 \times f_{HP})$ , where $f_{HP}$ = high-pass corner frequency.....	109
Figure 6.7	Standard deviation terms associated with geometric mean acceleration response spectral ordinates for location V1. $T_s$ denotes elastic site period.....	111
Figure 6.8	Median $\pm$ one standard deviation residuals using total standard deviation estimate from Fig. 6.7.....	112
Figure 6.9	Geometric mean acceleration response spectra and prediction residuals for DEEPSOIL simulation results obtained with alternative material curves and viscous damping formulation.....	113
Figure 6.10	Geometric mean acceleration response spectra and prediction residuals for DEEPSOIL simulation results obtained with alternative velocity profiles.....	114
Figure 6.11	Theoretical and observed V1/D3 amplification factors at Turkey Flat site for events listed in Table 6.2.....	116
Figure 6.12	Comparison of spectral shapes of predictions at different shaking levels for EW component.....	117
Figure 6.13	Comparison of spectral shapes of predictions at different shaking levels for NS component.....	117
Figure 7.1	Velocity data and model used for analysis of La Cienega site.....	123

Figure 7.2	Velocity data and model used for analysis of KWHH02 site .....	124
Figure 7.3	Velocity data and model used for analysis of Lotung site .....	125
Figure 7.4	Variation of standard deviation and correlation coefficient with depth for generic and site-specific site profiles (Toro 1997).....	126
Figure 7.5	Material curves for rock developed by Silva et al. (1996).....	128
Figure 7.6	Target upper and lower bounds ( $\pm\sqrt{3}\sigma$ ) of modulus reduction curve for La Cienega.....	129
Figure 7.7	Target upper and lower bounds ( $\pm\sqrt{3}\sigma$ ) of damping curves for La Cienega .....	130
Figure 7.8	Target, upper and lower bounds ( $\pm\sqrt{3}\sigma$ ) of modulus reduction curve for KGWH02 .....	131
Figure 7.9	Target upper and lower bounds ( $\pm\sqrt{3}\sigma$ ) of damping curves for KGWH02 .....	132
Figure 7.10	Target, upper and lower bounds ( $\pm\sqrt{3}\sigma$ ) of modulus reduction curve for Lotung .....	133
Figure 7.11	Target upper and lower bounds ( $\pm\sqrt{3}\sigma$ ) of damping curves for Lotung .....	133
Figure 7.12	Reference strains used in different nonlinear codes for La Cienega.....	134
Figure 7.13	Reference strains used in different nonlinear codes for KGWH02.....	135
Figure 7.14	Reference strains used in different nonlinear codes for Lotung.....	136
Figure 7.15	Acceleration histories recorded at La Cienega array .....	139
Figure 7.16	Acceleration histories recorded at Kiknet KGWH02 array .....	140
Figure 7.17	Acceleration histories for (a) EW direction recorded at Lotung array and (b) NS direction recorded at Lotung array .....	141
Figure 7.18	Acceleration response spectra for data and simulation results compared through direct spectral ordinates and prediction residuals for ground surface. Results shown for two horizontal directions.....	145
Figure 7.19	Acceleration response spectra for data and simulation results compared through direct spectral ordinates and prediction residuals for 18.3 m.....	146
Figure 7.20	Acceleration response spectra for data and simulation results compared through direct spectral ordinates and prediction residuals for 100.6 m.....	146
Figure 7.21	Acceleration histories for data and simulation results from DEEPSOIL for ground surface .....	147

Figure 7.22	Acceleration histories for data and simulation results with different viscous damping formulations from DEEPSOIL for ground surface .....	148
Figure 7.23	Acceleration response spectra for data and simulation results (with model curves obtained from both “MRD” and “MR” fitting approaches) compared through direct spectral ordinates and prediction residuals for ground surface.....	149
Figure 7.24	Acceleration response spectra for data and simulation results (using 1D and 2D simulation options in OpenSees) compared through direct spectral ordinates and prediction residuals for ground surface .....	149
Figure 7.25	Standard deviation terms associated with geometric mean acceleration response spectral ordinates for ground surface. $T_s$ denotes elastic site period .....	150
Figure 7.26	Acceleration response spectra for data and simulation results compared through direct spectral ordinates and prediction residuals for ground surface.....	152
Figure 7.27	Acceleration histories for data and simulation results from DEEPSOIL for ground surface .....	152
Figure 7.28	Acceleration response spectra for data and simulation results (with model curves obtained from both “MRD” and “MR” fitting approaches) compared through direct spectral ordinates and prediction residuals for ground surface.....	153
Figure 7.29	Acceleration response spectra for data and simulation results (using 1D and 2D simulation options in OpenSees) compared through direct spectral ordinates and prediction residuals for ground surface .....	153
Figure 7.30	Standard deviation terms associated with geometric mean acceleration response spectral ordinates for ground surface. $T_s$ denotes elastic site period (calculated excluding rock layers below 68 m) .....	154
Figure 7.31	Acceleration response spectra for data and simulation results (using DEEPSOIL with different velocity profiles) compared through direct spectral ordinates and prediction residuals for ground surface.....	154
Figure 7.32	Acceleration response spectra for data and simulation results compared through direct spectral ordinates and prediction residuals for ground surface. Results shown for two horizontal directions.....	156
Figure 7.33	Acceleration response spectra for data and simulation results compared through direct spectral ordinates and prediction residuals for 6 m.....	156

Figure 7.34	Acceleration response spectra for data and simulation results compared through direct spectral ordinates and prediction residuals for 11 m.....	157
Figure 7.35	Acceleration response spectra for data and simulation results compared through direct spectral ordinates and prediction residuals for 17 m.....	157
Figure 7.36	Acceleration histories for data and simulation results from DEEPSOIL for ground surface .....	158
Figure 7.37	Standard deviation terms associated with geometric mean acceleration response spectral ordinates for ground surface. $T_s$ denotes elastic site period .....	160
Figure 7.38	Acceleration response spectra for data and simulation results (using DEEPSOIL with different target material curves) compared through direct spectral ordinates and prediction residuals for ground surface .....	160
Figure 7.39	Theoretical and observed amplification factors at La Cienega site.....	161
Figure 7.40	Comparison of variabilities across three vertical array sites.....	164
Figure 7.41	Comparison of empirical and theoretical amplification factors across periods for Turkey Flat site using Parkfield event.....	165
Figure 7.42	Comparison of empirical and theoretical amplification factors across periods for La Cienega site using 09/09/2001 event .....	165
Figure 7.43	Comparison of empirical and theoretical amplification factors across periods for KGWH02 site using 03/24/2001 event .....	166
Figure 7.44	Comparison of empirical and theoretical amplification factors across periods for Lotung site using the 5/20/1986 event (“Event 7”).....	166
Figure 7.45	Comparison of spectral shapes of predictions at different shaking levels for La Cienega site .....	168

## LIST OF TABLES

Table 2.1	Computer codes for one-dimensional nonlinear ground response analyses .....	10
Table 2.2	Degradation index functions and corresponding coefficients (Matasovic and Vucetic 1993b) .....	21
Table 2.3	Verification studies of ground response codes.....	39
Table 4.1	Weight criterion for different fitting approaches .....	61
Table 5.1	Mass representation and constitutive models used in nonlinear codes .....	77
Table 5.2	Available viscous damping formulation for nonlinear codes and summary of analyses discussed in text.....	81
Table 6.1	Estimated values of material density at valley center site.....	101
Table 6.2	Earthquake events used to compile site amplification factors .....	115
Table 7.1	Target material curves for La Cienega .....	126
Table 7.2	Target material curves for KGWH02.....	127
Table 7.3	Target material curves for Lotung.....	127
Table 7.4	Summary of engineering model for La Cienega .....	137
Table 7.5	Summary of engineering model for Kiknet KGWH02 .....	138
Table 7.6	Summary of engineering model for Lotung.....	138

# 1 Introduction

## 1.1 STATEMENT OF PROBLEM

Ground motion prediction equations (GMPEs) are used in seismic hazard analyses to provide a probabilistic distribution of a particular ground motion intensity measure ( $IM$ ), such as 5% damped response spectral acceleration, conditional on magnitude, site-source distance, and parameters representing site condition and style of faulting. Ground motion data are often log-normally distributed, in which case the distribution can be represented by a median and standard deviation,  $\sigma$  (in natural logarithmic units). Site condition is often characterized in modern GMPEs by the average shear wave velocity in the upper 30 m ( $V_{s30}$ ). Actual conditions at strong motion recording sites are variable with respect to local site conditions, underlying basin structure, and surface topography, and hence estimates from GMPEs are necessarily averaged across the range of possible site conditions for a given  $V_{s30}$ .

The physical processes that contribute to “site effects” are referred to as local ground response, basin effects, and surface topographic effects. Local ground response consists of the influence of relatively shallow geologic materials ( $\pm 100$  m depth) on nearly vertically propagating body waves. Basin effects represent the influence of two-dimensional (2D) or three-dimensional (3D) sedimentary basin structures on ground motions, including critical body-wave reflections and surface-wave generation at basin edges. Finally, ground motions for areas with irregular surface topography such as ridges, canyons or slopes, can differ significantly from the motions for level sites.

In earthquake engineering practice, site effects are quantified either by *theoretical* or *empirical* models. Such models can in general be implemented for *site-specific* analyses or for more general analyses of *site factors*. The distinctions between these various terms are described in the following paragraphs.

*Theoretical* modeling of site response consists of performing wave propagation analyses, which are widely used to simulate ground response effects (e.g., Idriss and Sun 1992; Hudson et al. 1994) and basin effects (e.g., Olsen 2000; Graves 1996). The models for ground response generally consider nonlinear soil behavior and encompass a soil domain of limited dimension (on the order of tens to hundreds of meters), whereas models for basin effects are based on linear sediment properties and cover much broader regions (on the order of kilometers to tens of kilometers). Ground response effects are most commonly evaluated using one-dimensional (1D) models, which assume that seismic waves propagate vertically through horizontal sediment layers. A key factor that distinguishes 1D ground response models from each other is the choice of soil material model. Three categories of material models are equivalent-linear and nonlinear models for one horizontal direction of shaking, and nonlinear models for multiple directions of shaking.

*Empirical models* are derived from statistical analysis of strong motion data, and quantify the variations of ground motion across various site conditions. One component of empirical models are amplification factors, which are defined as the ratio of the median  $IM$  for a specified site condition to the median that would have been expected for a reference site condition (usually rock). The other principal component of empirical models is standard deviation, which can be a function of site condition. The modified median and standard deviation define the moments of a log-normal probability density function of the  $IM$  that would be expected at a site, conditioned on the occurrence of an earthquake with magnitude  $M$  at distance  $r$  from the site.

A *site-specific* evaluation of site effects generally requires the use of theoretical models because only these models allow the unique geometry and stratigraphy of a site to be taken into consideration. Conceptually, empirical models are possible if there are many ground motion recordings at the site of interest, but as a practical matter, such data are seldom (if ever) available.

Theoretical modeling of 1D site response can generally be accomplished using equivalent-linear (EL) or nonlinear (NL) analysis. EL ground response modeling is by far the most commonly utilized procedure in practice (Kramer and Paulsen 2004) as it requires the specification of well-understood and physically meaningful input parameters (shear-wave velocity, unit weight, modulus reduction, and damping). NL ground response analyses provide a more accurate characterization of the true nonlinear soil behavior, but implementation in practice

has been limited principally as a result of poorly documented and unclear parameter selection and code usage protocols. Moreover, previous studies have thoroughly investigated the sensitivity of site response results to the equivalent-linear parameters (e.g., Roblee et al. 1996), but this level of understanding is not available for the nonlinear parameters.

The objectives of the project described in this report are related to the use of 1D theoretical models for the evaluation of site effects. There are several issues related to the application of such models, namely:

- *How do non-expert users properly perform ground response analyses using nonlinear theoretical models?* Parameter selection and usage protocols are developed / improved in this study.
- *What is the uncertainty in predictions from nonlinear theoretical models?* This is addressed by considering different sources of variability in material properties and modeling schemes.
- *What is the difference between the predictions from site-specific nonlinear and equivalent-linear analyses?* The predictions from both types of analyses are compared at different strain levels.

## **1.2 ORGANIZATION OF REPORT**

Following the introduction in Chapter 1, Chapter 2 discusses existing procedures for ground response modeling, with an emphasis on solution algorithms used in several leading computer codes and the model parameters required by the codes. Chapter 3 documents the results of element testing performed to verify that the constitutive models implemented in the nonlinear codes do not have numerical bugs related to several common load paths. In Chapter 4, critical issues that are common to the implementation of nonlinear ground response analysis codes are presented. Chapter 5 is a discussion of the use of exact solutions of wave propagation problems to tackle some of the implementation issues of nonlinear codes described in Chapter 4. Chapter 6 documents the blind prediction of ground shaking at the Turkey Flat vertical array site during the 2004 Parkfield earthquake using nonlinear ground response analyses. Chapter 7 summarizes the (non-blind) nonlinear ground response analyses performed for three additional vertical array sites and discusses the trends and bias observed in the analysis results. Finally in Chapter 8, principal findings of the study are synthesized, along with recommendations for future work.

## 2 Ground Response Modeling

In this chapter, ground response analysis routines utilizing different soil material models are reviewed and several issues related to their application are discussed. Sections 2.1 and 2.2 describe general aspects of equivalent-linear and nonlinear modeling, respectively. To illustrate the issues involved with nonlinear modeling more thoroughly, five leading nonlinear seismic ground response analysis codes: D-MOD\_2 (Matasovic 2006) and DEEPSOIL (Hashash and Park 2001, 2002; Park and Hashash 2004; [www.uiuc.edu/~deepsoil](http://www.uiuc.edu/~deepsoil)), TESS (Pyke 2000), a ground response module in the OpenSees simulation platform (Ragheb 1994; Parra 1996; Yang 2000; McKenna and Fenves 2001; [opensees.berkeley.edu](http://opensees.berkeley.edu)) and SUMDES (Li *et al.* 1992) are described in some detail in Section 2.3.

Equivalent-linear ground response modeling is by far the most commonly utilized procedure in practice (Kramer and Paulsen 2004). In an effort to increase the use of nonlinear models, several past studies have investigated the benefits of nonlinear modeling and have attempted to verify that they can be applied with confidence. The results of several such studies are discussed. In Section 2.4, verification studies comparing the results of ground response models to array data are presented. In Section 2.5, the results of numerical sensitivity studies comparing the results of equivalent-linear and nonlinear models are presented. These sensitivity studies are of interest because they can be used to establish the conditions for which the results of the two procedures are significantly different, which in turn can be used to help evaluate when nonlinear modeling is needed in lieu of equivalent linear.

### 2.1 EQUIVALENT-LINEAR MODEL

Equivalent-linear soil material modeling is widely used in practice to simulate true nonlinear soil behavior for applications such as ground response analyses. The advantages of equivalent-linear modeling include small computational effort and few input parameters. The most commonly

used equivalent-linear computer code is SHAKE (Schnabel *et al.* 1972). Modified versions of this program include SHAKE91 (Idriss and Sun 1992) and SHAKE04 (Youngs 2004).

Equivalent-linear modeling is based on a total stress representation of soil behavior. As shown in Figure 2.1, the hysteretic stress-strain behavior of soils under symmetrical cyclic loading is represented by (1) an equivalent shear modulus ( $G$ ), corresponding to the secant modulus through the endpoints of a hysteresis loop and (2) equivalent viscous damping ratio ( $\beta$ ), which is proportional to the energy loss from a single cycle of shear deformation. Both  $G$  and  $\beta$  are functions of shear strain as shown in Figure 2.2. Strictly speaking, the only required properties for ground response analyses are  $G$  and  $\beta$ . However,  $G$  is evaluated as the product of small-strain shear modulus  $G_{max}$  and  $G/G_{max}$ , where  $G_{max} = \rho V_s^2$  ( $\rho$  = mass density,  $V_s$  = shear wave velocity) and  $G/G_{max}$  is the modulus reduction, which is a function of shear strain as shown in Figure 2.2. Hence, the soil properties actually needed for analysis are shear wave velocity  $V_s$ , mass density  $\rho$ , curves for the modulus reduction ( $G/G_{max}$ ), and damping ( $\beta$ ) as a function of shear strain.

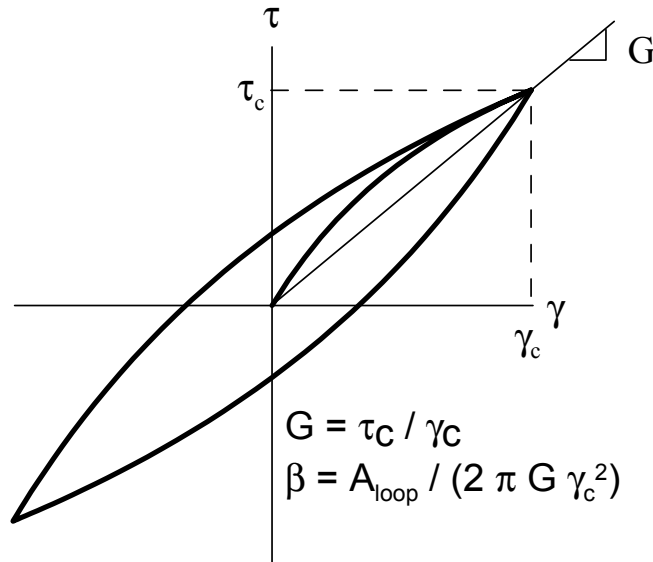


**Fig. 2.1 Hysteresis loop of soil loaded in shear illustrating measurement of secant shear modulus ( $G$ ) and hysteretic damping ratio ( $\beta$ ).**

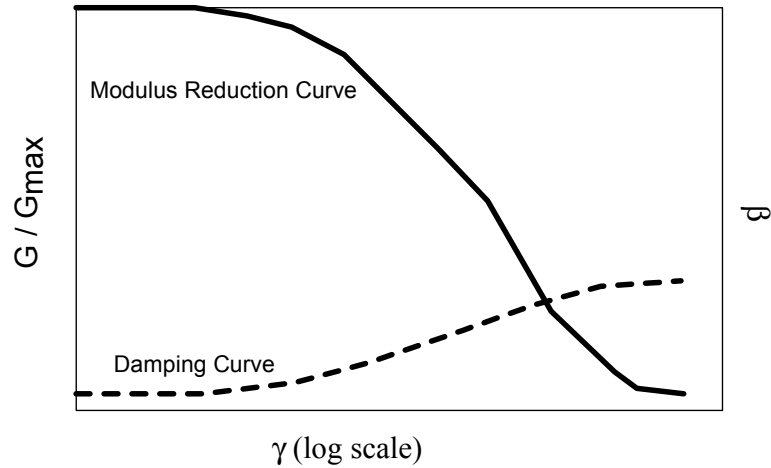


**Fig. 2.2 Variation of normalized modulus ( $G/G_{max}$ ) and  $\beta$  with shear strain.**

The analysis of site response with equivalent-linear modeling is an iterative procedure in which initial estimates of shear modulus and damping are provided for each soil layer. Using these linear, time-invariant properties, linear dynamic analyses are performed and the response of the soil deposit is evaluated. Shear strain histories are obtained from the results, and peak shear strains are evaluated for each layer. The effective shear strains are taken as a fraction of the peak strains. The effective shear strain is then used to evaluate an appropriate  $G$  and  $\beta$ . The process is repeated until the strain-compatible properties are consistent with the properties used to perform the dynamic response analyses. At that point, the analysis is said to have “converged,” and the analysis is concluded.

Modified frequency-domain methods have also been developed (Kausel and Assimaki 2002; Assimaki and Kausel 2002) in which soil properties in individual layers are adjusted on a frequency-to-frequency basis to account for the strong variation of shear strain amplitude with frequency. Since the frequencies present in a ground motion record vary with time, this can provide a reasonable approximation of the results that would be obtained from a truly nonlinear time-stepping procedure.

## 2.2 NONLINEAR MODELS

### 2.2.1 Mathematical Representations of Soil Column and Solution Routines

The method of analysis employed in time-stepping procedures can in some respects be compared to the analysis of a structural response to input ground motion (Clough and Penzien 1993; Chopra 2000). Like a structure, the layered soil column is idealized either as a multiple-degree-of-freedom lumped-mass system (Fig. 2.3a) or a continuum discretized into finite elements with distributed mass (Fig. 2.3b). Whereas frequency-domain methods are derived from the solution of the wave equation with specified boundary conditions, time-domain methods solve a system of coupled equations that are assembled from the equation of motion. The system is represented by a series of lumped masses or discretized into elements with appropriate boundary conditions.

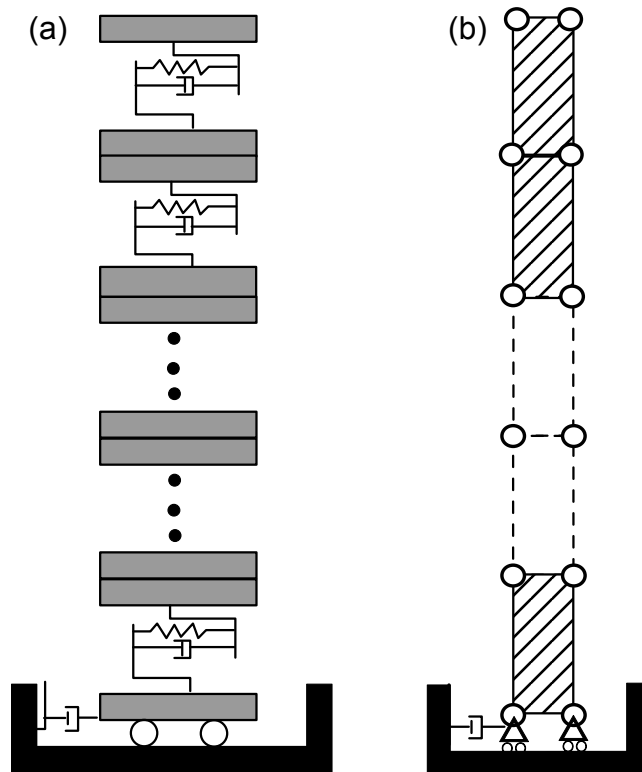


**Fig. 2.3 (a) Lumped-mass system; (b) distributed mass system.**

The system of coupled equations is discretized temporally and a time-stepping scheme such as the Newmark  $\beta$  method (Newmark 1959) is employed to solve the system of equations and to obtain the response at each time step. Some nonlinear programs such as TESS utilize an explicit finite-difference solution of the wave propagation problem that is the same as the

solution scheme used in FLAC developed by HClitasca. Unlike in frequency-domain analysis where the control motion could be specified anywhere within the soil column, in time-domain analysis, the control motion must be specified at the bottom of the system of lumped masses or finite elements. Most nonlinear codes are formulated to analyze one horizontal direction of shaking, although SUMDES and OpenSees allow analysis of multi-directional shaking.

### **2.2.2 Soil Material Models**

Soil material models employed range from relatively simple cyclic stress-strain relationships (e.g., Ramberg and Osgood 1943; Kondner and Zelasko 1963; Finn et al. 1977; Pyke 1979; Vucetic 1990) to advanced constitutive models incorporating yield surfaces, hardening laws, and flow rules (e.g., Roscoe and Schofield 1963; Roscoe and Burland 1968; Mroz 1967; Prevost 1977; Dafalias and Popov 1979). Nonlinear models can be formulated so as to describe soil behavior with respect to total or effective stresses. Effective stress analyses allow the modeling of the generation, redistribution, and eventual dissipation of excess pore pressure during and after earthquake shaking. Table 2.1 is a list of some computer codes for 1D nonlinear ground response analysis.

**Table 2.1 Computer codes for 1D nonlinear ground response analyses.**

Program	Nonlinear Model	Reference for computer code	TSA/ESA
DEEPSOIL	Hashash and Park (2001, 2002)	Hashash and Park (2001, 2002); www.uiuc.edu/~deepsoil	TSA (ESA option available in Fall 2007)
DESRA-2	Konder and Zelasko (1963); Masing (1926)	Lee and Finn (1978)	TSA or ESA
DESRAMOD	same as DESRA-2; with pore-water pressure generation model by Dobry <i>et al.</i> (1985)	Vucetic and Dobry (1986)	TSA or ESA
DESRAMUSC	Same as DESRA-2 + Qiu (1997)	Qiu (1997)	TSA or ESA
D-MOD_2	Matasovic and Vucetic (1993, 1995)	Matasovic (2006)	TSA or ESA
MARDESRA	Martin (1975)	Mok (pers. comm., 1990)	TSA or ESA
OpenSees	Ragheb (1994); Parra (1996); Yang (2000)	McKenna and Fenves (2001); opensees.berkeley.edu	TSA or ESA
SUMDES	Wang (1990)	Li <i>et al.</i> (1992)	TSA or ESA
TESS	Pyke (1979)	Pyke (2000)	TSA or ESA

Cyclic stress-strain relationships are generally characterized by a backbone curve and a series of rules that describe unloading-reloading behavior, pore-water generation, and cyclic modulus degradation. The backbone curve (Fig. 2.4) is the shear stress–shear strain relationship for monotonic loading.

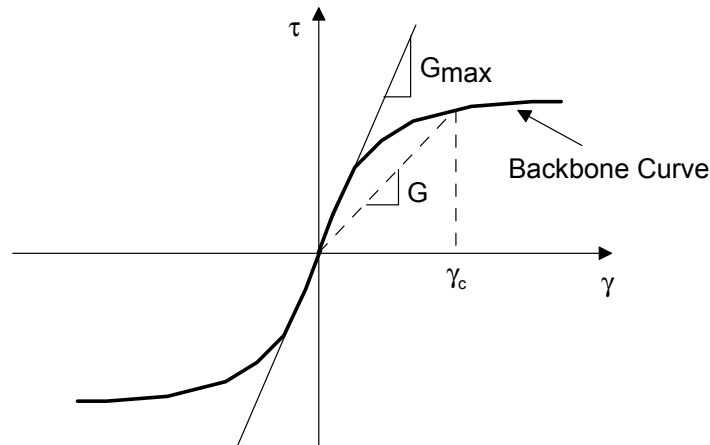


**Fig. 2.4 Backbone curve.**

Masing rules (Masing 1926) and extended Masing rules (Pyke 1979; Wang et al 1980; Vucetic 1990) are often used in conjunction with the backbone curve to describe the unloading-reloading and cyclic degradation behavior of soil. The Masing (rules 1–2) and extended Masing rules (1–4) are as follows (illustrated graphically in Fig. 2.5):

1. The stress-strain curve follows the backbone curve for initial loading.
2. The reloading curve of any cycle starts with a shape that is identical to the shape of the positive initial loading backbone curve enlarged by a factor of two. The same applies to the unloading curve in connection with the negative part of the initial loading backbone curve.
3. If the unloading or loading curve exceeds the maximum past strain and intersects the backbone curve, it follows the backbone curve until the next stress reversal.
4. If an unloading or loading curve crosses an unloading or loading curve from a previous cycle, the stress-strain curve follows that of the previous cycle.

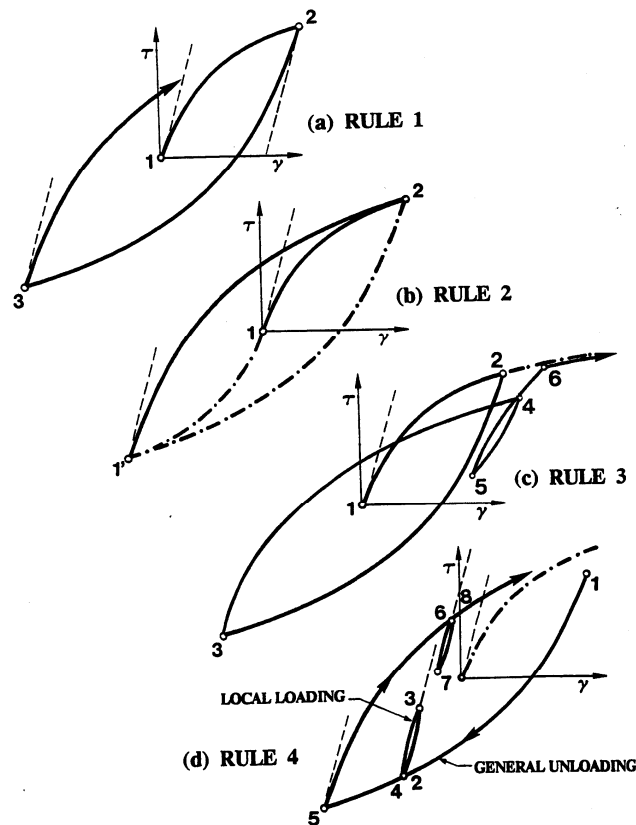


**Fig. 2.5** Extended Masing rules from Vucetic (1990).

Advanced constitutive models are based on the framework of plasticity, which are capable of simulating complex soil behavior under a variety of loading conditions. The key components of such models include a yield surface, flow rules, and hardening (or softening) laws. To facilitate the discussion (in Sections 2.3.4 and 2.3.5) of two specific ground response analysis codes that employ the advanced constitutive models, basic concepts of plasticity (after Potts and Zdravković 1999) are reviewed here.

**(a) Yield Function**

A yield function describes the limiting stress conditions for which elastic behavior is observed. It depends on the stress state  $\{\sigma\}$  and state parameters  $\{k\}$ , which are related to yield stresses and hardening/softening parameters. A yield function is defined as:

$$F(\{\sigma\}, \{k\}) = 0 \tag{2.1}$$

For perfect plasticity,  $\{k\}$  is constant and equal to the magnitude of yield stresses. If hardening/softening is allowed,  $\{k\}$  would vary with plastic straining to represent how the magnitude of the stress state at yield changes. A yield function is an indicator of the type of material behavior. If  $F(\{\sigma\}, \{k\})$  is negative, the material would experience elastic behavior; whereas if  $F(\{\sigma\}, \{k\})$  is equal to zero, the material would experience elasto-plastic behavior. A positive value of  $F(\{\sigma\}, \{k\})$  would be an impossible stress state. Figure 2.6 is a schematic of a yield surface (curve) plotted in principal stress space.

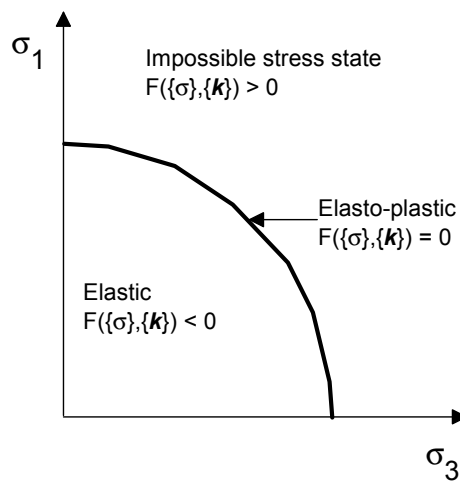


**Fig. 2.6 Schematic of yield surface (after Potts and Zdravković 1999).**

**(b) Flow Rules**

Flow rules relate increments of plastic strain to increments of stress. It can be expressed as:

$$\Delta \epsilon_i^p = \Lambda \frac{\partial P(\{\boldsymbol{\sigma}\}, \{\mathbf{m}\})}{\partial \sigma_i} \quad (2.2)$$

where  $\Delta \epsilon_i^p$  is the incremental plastic strain and  $\Lambda$  is a scalar multiplier depending on hardening/softening rules.  $P(\{\boldsymbol{\sigma}\}, \{\mathbf{m}\})$  is called the plastic potential function which depends on the stress state  $\{\boldsymbol{\sigma}\}$  and a vector of state parameters  $\{\mathbf{m}\}$ . The outward vector normal to the plastic potential surface at current stress states can be decomposed into different components of plastic strain increment. Figure 2.7 is a schematic of plastic potential surface (curve) plotted in principal stress space. If the plastic potential function is chosen to be the same as the yield function, the flow rule is said to be associated and the incremental plastic strain vector would then be normal to the yield surface.

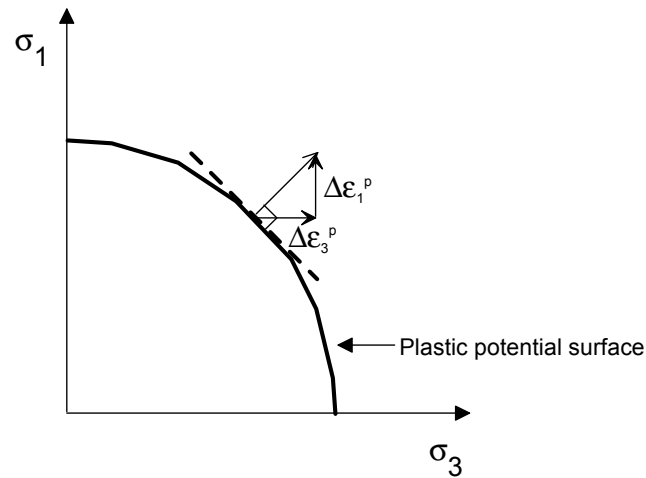


**Fig. 2.7 Schematic of plastic potential surface (after Potts and Zdravković 1999).**

**(c) Hardening (or Softening) Laws**

Hardening (or softening) laws describe changes in the size and shape of the yield surface as plastic deformation occurs. There are two types of hardening. The first type is called isotropic hardening, which occurs when the yield surface changes size but maintains the same center. The second type is called kinematic hardening, which occurs when the yield surface moves around the stress space without any change in size. Figure 2.8 shows schematics for the two types of hardening.

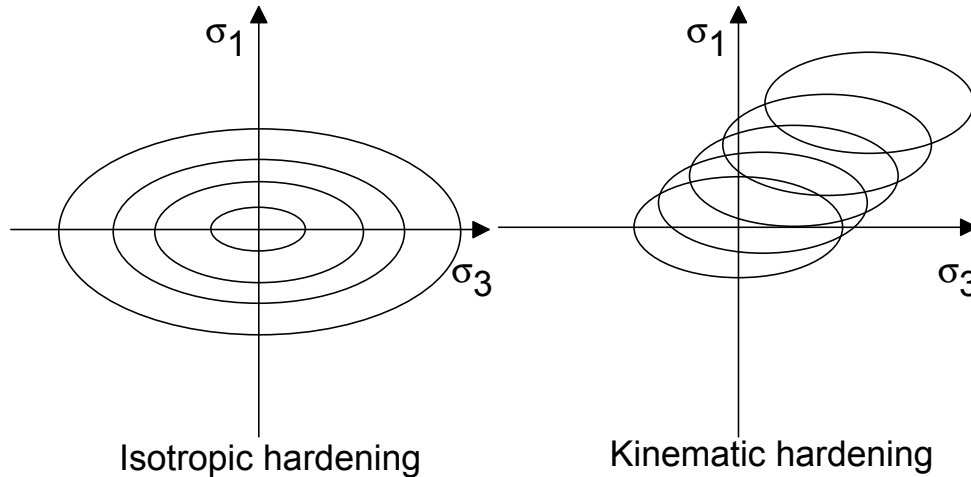


**Fig. 2.8 Schematic of two hardening types (after Potts and Zdravković 1999).**

Examples of ground response programs utilizing advanced constitutive models are DYNAID (Prevost 1989), SUMDES (Li et al. 1992), SPECTRA (Borja and Wu 1994), AMPLE (Pestana and Nadim 2000), and the ground response module in the OpenSees simulation platform (Ragheb 1994; Parra 1996; Yang 2000; McKenna and Fenves 2001; [opensees.berkeley.edu](http://opensees.berkeley.edu)).

### 2.2.3 Viscous Damping Formulations

Viscous damping is incorporated into most nonlinear response analysis procedures because damping at very small strains (less than  $10^{-4}$ – $10^{-2}\%$ ) is not adequately captured by nonlinear models. This occurs because the backbone curve is nearly linear at these strains, which produces nearly zero hysteretic damping when the backbone curve is used in conjunction with the (extended) Masing rules. The addition of a viscous damping term in the analysis avoids unrealistic responses for problems involving small strains (Vucetic and Dobry 1986). Viscous damping is often assumed to be proportional to both the mass and stiffness of the system. This damping formulation, originally proposed by Rayleigh and Lindsay (1945), takes the viscous damping matrix  $[C]$  as follows:

$$[C] = a_0[M] + a_1[K] \quad (2.3)$$

where  $a_0$  and  $a_1$  are called Rayleigh damping coefficients.

Past practice has been that the viscous damping matrix is simplified by assuming that it is proportional only to the stiffness of the soil layers, which is referred as the “simplified Rayleigh damping formulation.” In that formulation, the calculation of the damping matrix reduces to:

$$[C] = a_1 [K] \quad (2.4)$$

and the value of viscous damping ratio,  $\zeta$ , becomes

$$\zeta = \frac{a_1 \pi}{T_1} \quad (2.5)$$

where  $T_1$  is the period of oscillation of a target mode (usually the first mode).

If no simplification of viscous damping matrix is used,  $a_0$  and  $a_1$  take the following form:

$$a_0 = \frac{4\pi\zeta}{(T_1 + T_2)} \quad (2.6)$$

$$a_1 = \frac{T_1 T_2 \zeta}{\pi(T_1 + T_2)} \quad (2.7)$$

where  $T_2$  is the period of oscillation of another target mode. It should be noted that Equations 2.6 and 2.7 are based on the assumption that the damping ratio for the two target modes of oscillation is the same. This “full Rayleigh damping formulation” is available in most nonlinear ground response analysis codes.

### 2.3 EXAMPLES OF SPECIFIC NONLINEAR CODES

The following subsections present detailed discussions of five nonlinear codes: D-MOD\_2 (Matasovic 2006) and DEEPSOIL (Hashash and Park 2001, 2002; Park and Hashash 2004; [www.uiuc.edu/~deepsoil](http://www.uiuc.edu/~deepsoil)), a ground response module in the OpenSees simulation platform (Ragheb 1994; Parra 1996; Yang 2000; McKenna and Fenves 2001; [opensees.berkeley.edu](http://opensees.berkeley.edu)), and SUMDES (Li *et al.* 1992) and TESS (Pyke 2000). All of them analyze 1D shaking, although OpenSees and SUMDES are capable of simulating multi-dimensional shaking. The purpose of this discussion is to illustrate the key components of nonlinear codes, and to show the types of model parameters that are needed to use the codes. These five codes are used in subsequent analyses presented in Chapters 4–7. Several of the codes have been revised during the course of this project, and these revisions are presented in the respective sections below. It should be noted that only the total stress analysis option is utilized in Chapters 4–7.

### 2.3.1 D-MOD\_2

D-MOD\_2 (Matasovic 2006) is an enhanced version of D-MOD (Matasovic and Vucetic 1993a). It solves the wave propagation problem by assuming that shear waves vertically propagate through horizontally layered soil deposits. The unbounded medium is idealized as a discrete lumped-mass system as illustrated in Figure 2.3a. The stiffness and hysteretic damping of soil are represented with nonlinear hysteretic springs. Additional viscous damping is included through the use of viscous dashpots. D-MOD\_2 uses the full Rayleigh viscous damping formulation discussed in Section 2.2. An energy-transmitting boundary follows the model by Joyner and Chen (1975) although a rigid boundary option is also available. The dynamic response scheme used by Lee and Finn (1978) is also employed in D-MOD\_2 to solve the dynamic equation of motion in the time domain. In 2003, the Newmark  $\beta$  integration scheme (Newmark 1959) replaced the Wilson  $\theta$  method (Wilson 1968) to achieve a more stable numerical solution. In addition, D-MOD\_2 has a variable width shear slice option that enables a more accurate site response calculation of levees and dams founded on bedrock. This option allows a more realistic mass distribution (i.e., mass is made proportional to the width of the model as the width increases with depth) and stiffness (i.e., section modulus in the horizontal plane is calculated based upon the actual width of the slice but not based upon unit width as in conventional 1D analysis). Moreover, D-MOD\_2 is enhanced from DMOD to simulate the seismically induced slip that may occur along the weak interfaces.

#### (a) Backbone Curve

D-MOD\_2 incorporates the MKZ constitutive model (Matasovic and Vucetic 1993a) to define the initial backbone curve. The MKZ constitutive model is presented in Figure 2.9. The MKZ model is a modification of the hyperbolic model by Kondner and Zelasko (1963) (KZ model). Two curve-fitting constants  $\alpha$  and  $s$  are added to the KZ model, and the normalized form of the MKZ model is given by:

$$\tau^* = \frac{G_{mo}^* \gamma}{1 + \alpha \left( \frac{G_{mo}^*}{\tau_{mo}^*} \gamma \right)^s} \quad (2.8)$$

where  $G^*_{mo} = G_{mo} / \sigma'_{vc}$ ,  $\tau^*_{mo} = \tau_{mo} / \sigma'_{vc}$ ,  $\sigma'_{vc}$  = initial vertical effective stress,  $G_{mo}$  = initial shear modulus, and  $\tau_{mo}$  = shear strength of the soil.

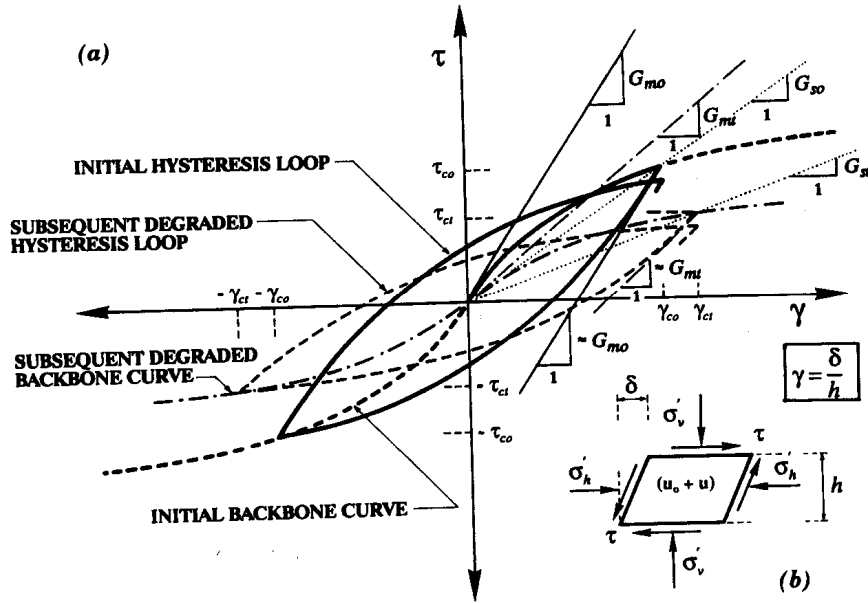


**Fig. 2.9 Schematic illustration of MKZ constitutive model showing stress-strain behavior in first cycle (at time  $t=0$ ) and subsequent cycle (at time  $t$ ).**

The original KZ model was intended to cover a large range of strains all the way up to failure. However, the dominant strains in the seismic response of soil deposits are relatively small, usually less than 1–3%, which are much lower than typical static failure strains in soil. In order to model accurately the initial loading curve, Matasovic and Vucetic (1993a) suggested that  $\tau_{mo}$  can be arbitrarily chosen as the  $\tau$  ordinate corresponding approximately to the upper boundary of the dominant shear strain range. Figure 2.10 shows how different values of  $\tau^*_{mo}$  affect the KZ model prediction on the positive portion of the initial backbone curve. Note that the prediction by the MKZ model shown in Figure 2.10 used  $\tau^*_{mo}$  corresponding to a shear strain of 1%.

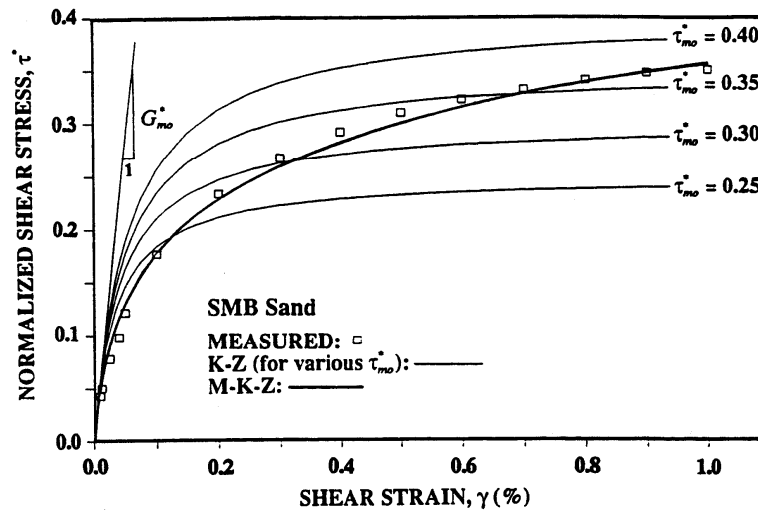


**Fig. 2.10 Comparison of positive portion of initial backbone curves obtained from KZ and MKZ models (Matasovic and Vucetic 1993a).**

The ratio  $\tau_{mo}^* / G_{mo}^*$  is often termed the reference shear strain (Hardin and Drnevich 1972) and is considered to be a material constant (see Section 4.1). Parameters  $\alpha$  and  $s$  were introduced in the MKZ model and, as shown in Figure 2.10, the approximation of the initial backbone curve from experimental data is improved when MKZ model is used in lieu of the KZ model. Matasovic and Vucetic (1993a) found that the range of  $\alpha$  for sand is  $\approx 1.0$ – $1.9$ , while the range of  $s$  is  $\approx 0.67$ – $0.98$ . As shown in Figure 2.11, the modulus reduction curves obtained from the MKZ models were found to be in agreement with experimental data.

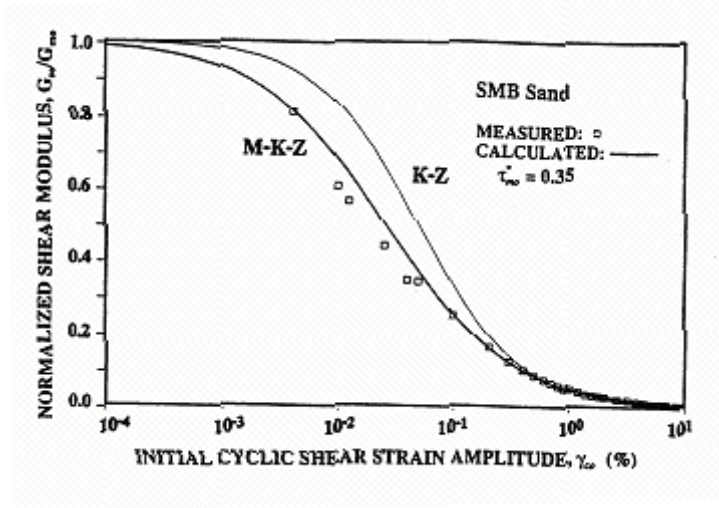


**Fig. 2.11 Measured and calculated initial modulus reduction curves (Matasovic and Vucetic 1993b).**

**(b) Hysteretic Soil Damping**

Using the Masing rules, the hysteretic damping,  $\beta$ , is calculated by the MKZ model as follows (Jacobson 1930; Ishihara 1986; Vucetic and Dobry 1986):

$$\beta = \frac{4}{\pi} \frac{\int_0^{\gamma_{co}} f(\gamma) d\gamma}{f(\gamma_{co}) \gamma_{co}} - \frac{2}{\pi} \quad (2.9)$$

where  $f(\gamma) = \tau$ , which is the initial backbone curve, and  $\gamma_{co}$  is the strain amplitude for which  $\beta$  is evaluated. Equation 2.9 indicates a relative measure of damping that works only when elliptical loops are closed. Comparisons of damping ratios calculated using Equation 2.7 (with the MKZ backbone curve) to damping from experimental data are shown in Figure 2.12. Damping is underestimated at small strains and overestimated at large strains.

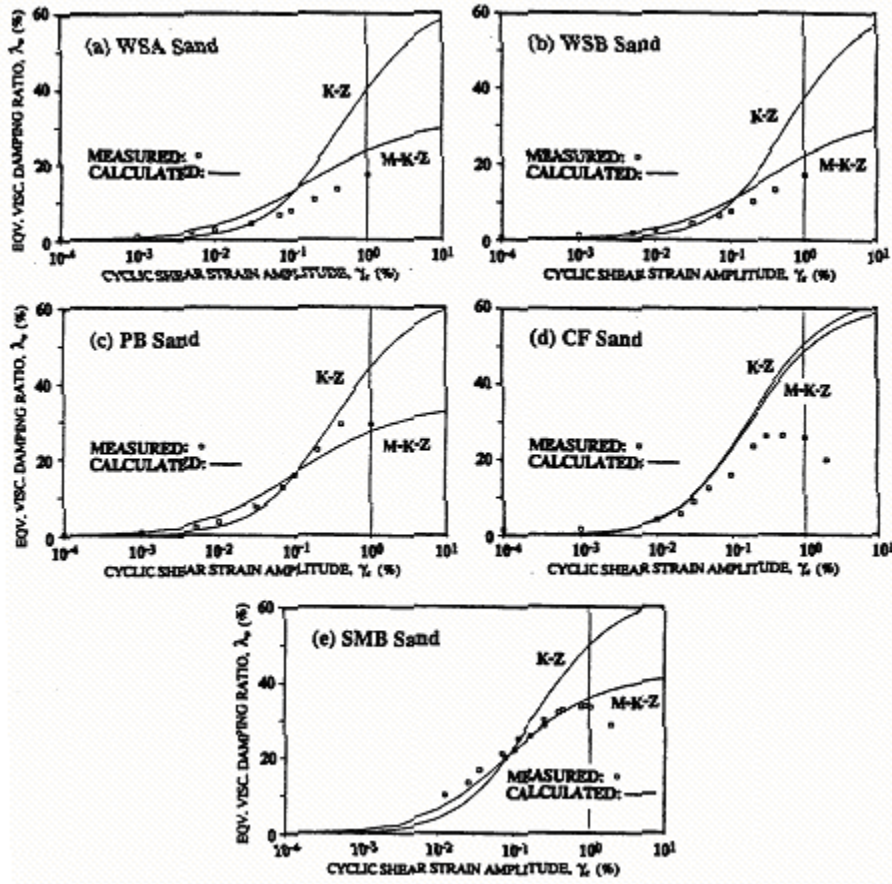


Fig. 2.12 Measured and calculated initial damping curves (Matasovic and Vucetic 1993a).

(c) *Material Degradation*

The degradation of material strength and stiffness with repeated cycling is taken into account with the use of degradation index functions for modulus ( $\delta_G$ ) and strength ( $\delta_\tau$ ). Degradation functions used for sand and clay are shown in Table 2.2. Incorporating these degradation functions into the equation for the MKZ backbone curve (originally given in Eq. 2.6) leads to the following equation:

$$\tau^* = \frac{\delta_G G_{mo}^* \gamma}{1 + \alpha \left( \frac{\delta_G G_{mo}^*}{\delta_\tau \tau_{mo}^*} \gamma \right)^s} \quad (2.10)$$

**Table 2.2 Degradation index functions and corresponding coefficients (Matasovic and Vucetic 1993b).**

Material	Degradation Index Function	Coefficients	
		v	t
Sand	$\delta_G = [1 - u^*]^{0.5}$	-	-
	$\delta_\tau = [1 - (u^*)^v]$	1.0-5.0	-
Clay	$\delta_G = \delta_\tau = \delta = N^{-t}$	-	$t = f(\text{PI}, \text{OCR}, \gamma_c, \gamma_{\text{tup}})$

As shown in Table 2.2, different forms of degradation index functions are used for sand and clay. For sand, cyclic degradation is mainly a function of the normalized residual cyclic pore pressure,  $u^* \equiv u / \sigma'_{vc}$ . Parameter  $v$  is a fitting parameter for strength degradation and increases as the degradation becomes more pronounced. Figure 2.13 shows degraded backbone curves obtained with different values of  $u^*$ . The pore-water pressure model for saturated sand layers implemented in D-MOD\_2 was originally developed by Dobry *et al.* (1985) and modified by Vucetic and Dobry (1986). This model allows the evaluation of the normalized residual cyclic pore pressure after cycle  $N_c$  as follows:

$$u_N^* = \frac{p \cdot f \cdot N_c \cdot F \cdot (\gamma_{ct} - \gamma_{tup})^b}{1 + f \cdot N_c \cdot F \cdot (\gamma_{ct} - \gamma_{tup})^b} \quad (2.11)$$

where  $\gamma_{ct}$  is the cyclic shear strain amplitude and  $\gamma_{tup}$  is the volumetric threshold shear strain below which no significant pore-water pressure is generated, and is usually between 0.01 and 0.02% for most sands (Dobry *et al.* 1982; Vucetic 1994). Parameter  $f$  can be taken as 1 or 2, depending on whether pore pressures are generated by shaking in one or two directions. Parameters  $F$ ,  $p$ , and  $b$  are obtained by fitting laboratory data from cyclic strain-controlled tests. The above formulation is for symmetrical cyclic loading and can be modified to account for irregular cyclic loading. This procedure was originally introduced by Finn *et al.* (1977) and modified by Vucetic and Dobry (1986). A detailed description of the procedure can be found in Vucetic and Dobry (1986).

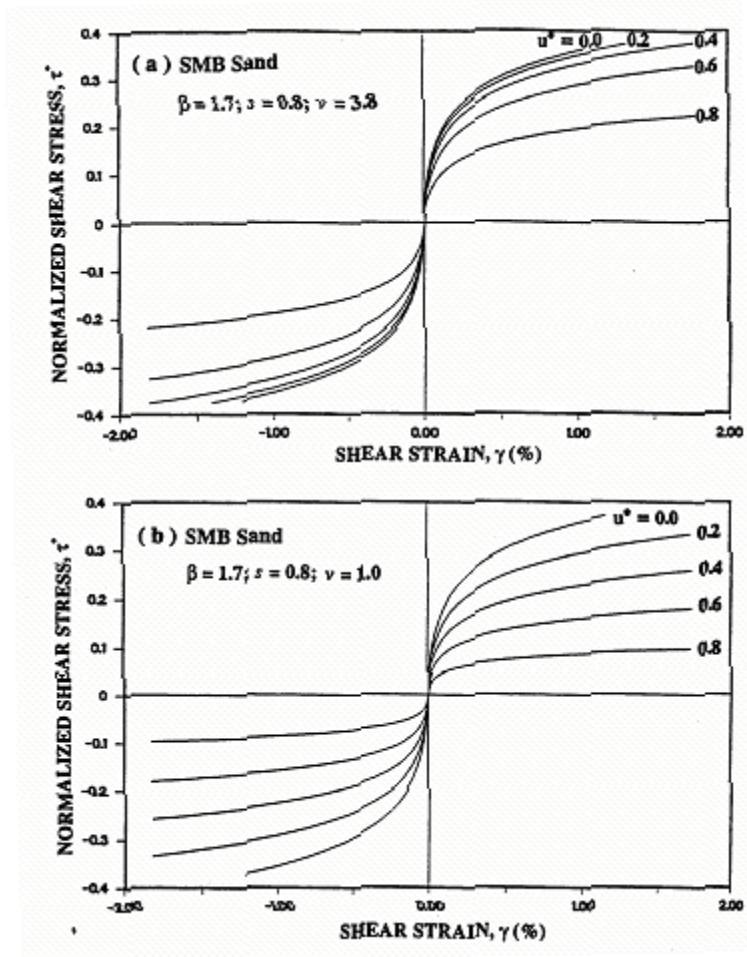


**Fig. 2.13 Families of degraded backbone curves (Matasovic and Vucetic 1993a).**

For clay, cyclic degradation can result from both pore-water pressure generation and deterioration of clay microstructure. As indicated in Table 2.2, the degradation function for clay takes the form of  $N^{-t}$  (Idriss et al. 1978) where  $t = g(\gamma_{ct} - \gamma_{up})^r$ . Parameters  $g$  and  $r$  are curve-fitting parameters introduced by Pyke (2000). In general,  $t$  is a function of the overconsolidation ratio (OCR) and plasticity index (PI) as shown in Figures 2.14–2.15. In D-MOD\_2, residual pore-water pressure after cycle  $N$  is expressed as (Matasovic and Vucetic 1995):

$$u_N^* = AN^{-3t} + BN^{-2} + CN^{-t} + D \quad (2.12)$$

where  $A$ ,  $B$ ,  $C$ , and  $D$  are fitting constants that are determined experimentally.

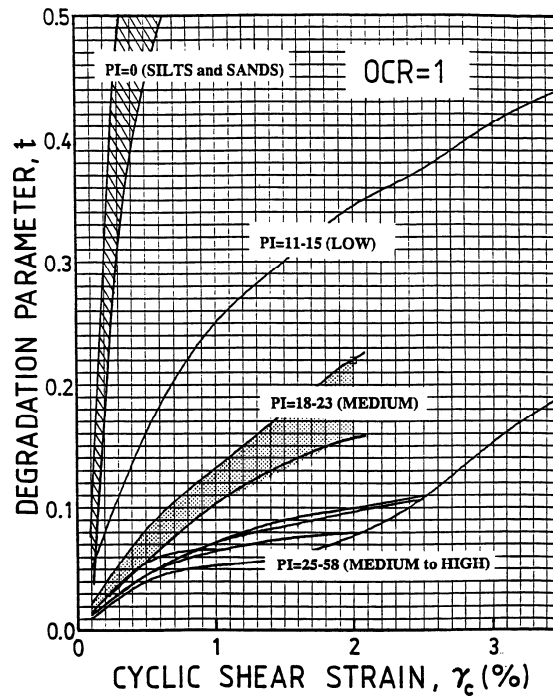


Fig. 2.14 Influence of soil plasticity on degradation parameter  $t$  (Tan and Vucetic 1989; Vucetic 1994).

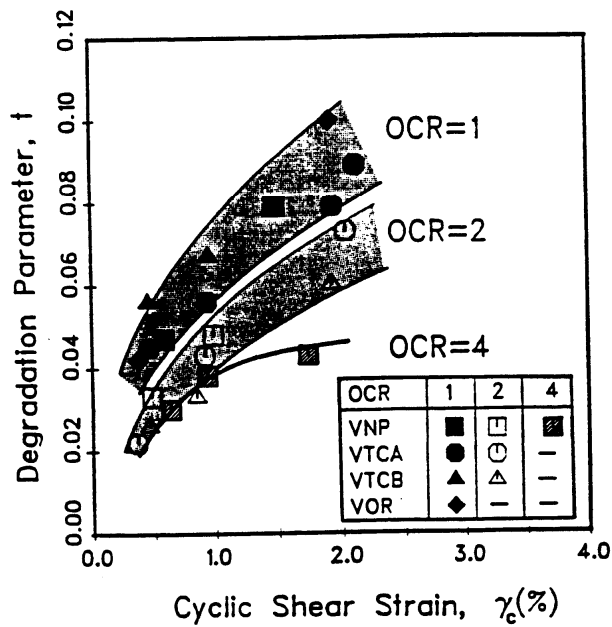


Fig. 2.15 Influence of overconsolidation on degradation parameter  $t$  (Vucetic and Dobry 1988).

D-MOD\_2 includes a pore-water pressure dissipation and redistribution model, which was originally used in DESRA-2 (Lee and Finn 1978). This is to account for the fact that if a saturated layer can drain, simultaneous generation, dissipation, and redistribution of pore-water pressure during and after shaking are possible. This may in turn have a significant impact on the magnitudes of residual pore-water pressures. The model employed in D-MOD\_2 was taken from Lee and Finn (1975, 1978) and Martin and Seed (1978) and can be written as:

$$\frac{\partial u}{\partial t} = \bar{E}_r \frac{k}{\gamma_w} \left( \frac{\partial^2 u}{\partial z^2} \right)_{st} + \left( \frac{\partial u}{\partial t} \right)_{cy} \quad (2.13)$$

where  $u$ ,  $\bar{E}_r$ ,  $k$ , and  $\gamma_w$  represent pore pressure, constrained rebound modulus, hydraulic conductivity, and unit weight of water, respectively. The first term of the right-hand side of Equation 2.13. represents the effects of dissipation via Terzaghi's 1D consolidation equation, while the second term represents the rate of cyclic pore-water pressure development. This differential equation is solved using a slightly modified finite difference solution from DESRA-2.

**(d) Viscous Damping**

Full Rayleigh damping formulation is used in D-MOD\_2.

**(e) Summary of Input Parameters**

The following seven types of input parameters are needed to implement D-MOD\_2 for dynamic nonlinear response analysis:

1. Parameters to define the MKZ backbone curve: initial tangent shear modulus of soil,  $G_{mo}$ , shear stress at reference strain,  $\tau_{mo}$ , and curve-fitting constants,  $\alpha$  and  $s$ ;
2. Parameters for cyclic degradation:  $\nu$  (for sand),  $g$  and  $r$  (for clay), and volumetric threshold shear strain,  $\gamma_{up}$ ;
3. Parameters for pore-water pressure generation model of sand:  $f$  (either 1 or 2), curve-fitting constants  $p$ ,  $F$ , and  $b$ ;
4. Parameters for pore-water pressure generation model of clay: fitting constants  $A$ ,  $B$ ,  $C$ ,  $D$ ;

5. Parameters for the pore-water pressure dissipation and redistribution model: constrained rebound modulus,  $\bar{E}_r$  or hydraulic conductivity,  $k$ , and other constants to define the Martin *et al.* (1975) model;
6. Properties of each layer and visco-elastic halfspace: width, thickness, saturated unit weight, and wet unit weight for each layer, unit weight and shear wave velocity of visco-elastic halfspace;
7. Rayleigh damping coefficients.

Parameters (1)–(6) correspond to parameters that are related to soil profile conditions and soil properties. Some of these parameters can be readily evaluated from the data generated in a typical geotechnical investigation, while others cannot. In addition to soil properties, the parameters in (7) require a relatively high degree of judgment and are not uniquely related to ordinary soil properties. For total stress analyses, only the parameters in (1) and (7) are needed.

### 2.3.2 DEEPSOIL

The DEEPSOIL code includes equivalent-linear and nonlinear analysis modes. The equivalent-linear analysis mode is similar to other available codes (e.g., SHAKE). It has no limitations on the number of layers, material properties, or length of input motion. The implementation includes a robust convergence algorithm and several choices for complex shear modulus formulation. The nonlinear mode is described next.

#### (a) *Backbone Curve*

DEEPSOIL (Hashash and Park 2001, 2002; Park and Hashash 2004) is a nonlinear site response analysis model for vertical propagation of horizontal shear waves in deep soil deposits. The code utilizes the same MDOF lumped-mass system as DESRA-2. The dynamical equilibrium equation of motion is solved numerically using the Newmark  $\beta$  method (1959). The DEEPSOIL version used in this document (V2.6) uses a total stress analysis approach. At the writing of this document, an effective stress analysis component has been implemented in the computational engine of DEEPSOIL and is being integrated with the user interface. The nonlinear constitutive model used in DEEPSOIL is based on the MKZ model, but Hashash and Park (2001) modified the reference strain definition as follows:

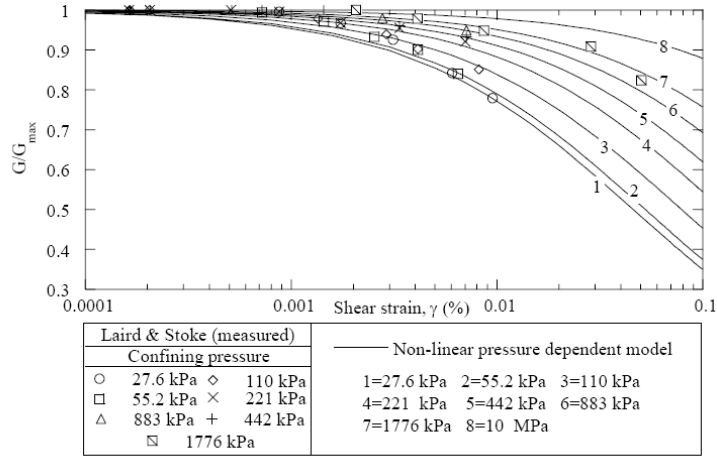
$$\gamma_r = a \left( \frac{\sigma_{vo}'}{\sigma_{ref}} \right)^b \quad (2.14)$$

where  $\sigma_{vo}'$  and  $\sigma_{ref}$  represent effective vertical stress and reference confining pressure, respectively, and parameters  $a$  and  $b$  are curve-fitting parameters for the initial backbone curve and can be determined from experimental data for a particular type of soil. This modification is to allow the reference strain to be pressure dependent.

The hysteretic model utilized in DEEPSOIL is given by:

$$\tau = \frac{G_{mo} \gamma}{1 + \alpha \left( \frac{\gamma}{\gamma_r} \right)^s} \quad (2.15)$$

Figure 2.16 (top frame) shows the match of the modified MKZ model to experimental modulus reduction curves by Laird and Stokoe (1993).



(a) Modulus degradation curves

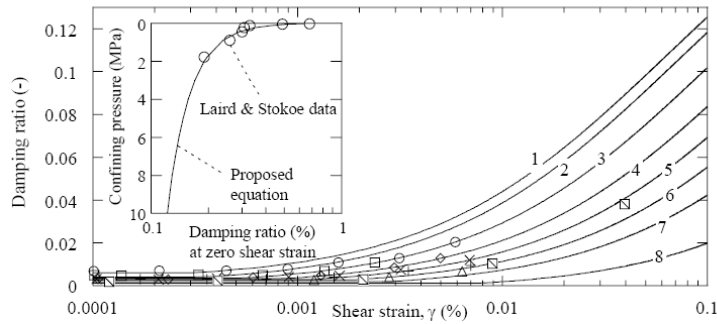


**Fig. 2.16 Comparisons of modulus reduction curves (top frame) and damping curves (bottom frame) obtained from Hashash and Park (2001) modified MKZ model with Laird and Stokoe (1993) experimental data.**

**(b) Hysteretic Soil Damping**

Hysteretic soil damping in DEEPSOIL is evaluated using the backbone curve in conjunction with the Masing criteria. The procedure is essentially the same as that presented in Section 2.3.1b.

Experimental data show a dependence of soil damping at very small strains on confining pressure. Hashash and Park (2001) therefore proposed the small-strain hysteretic damping ratio, denoted “zero strain equivalent” damping ratio  $\zeta_s$ . Parameter  $\zeta_s$  is taken as follows:

$$\zeta_s = \frac{c}{(\sigma')^d} \tag{2.16}$$

where  $c$  and  $d$  are fitting constants determined experimentally. Figure 2.16 (bottom frame) shows that the proposed pressure-dependent damping ratio equation matches the experimental data well at small strains.

(c) **Viscous Damping Term**

DEEPSOIL allows viscous damping to be specified using simplified or full Rayleigh damping schemes as described in Section 2.2.3. In addition, DEEPSOIL incorporates an extended Rayleigh viscous damping formulation. In this formulation, the damping matrix can consist of any combination of mass and stiffness matrices (Clough and Penzien 1993) and is given by:

$$[C] = [M] \sum_{b_e}^{N-1} a_b \left[ [M]^{-1} \quad [K] \right]^{b_e} \quad (2.17)$$

where  $N$  is the number of modes incorporated. The damping ratio  $\zeta_n$  can be expressed as:

$$\zeta_n = \frac{1}{4\pi f_n} \sum_{b=0}^{N-1} a_b (2\pi f_n)^{2b} \quad (2.18)$$

Park and Hashash (2004) included four modes in their study and thus  $a_b$  is found by:

$$\begin{bmatrix} \zeta_m \\ \zeta_n \\ \zeta_o \\ \zeta_p \end{bmatrix} = \frac{1}{4\pi} \begin{bmatrix} \frac{1}{f_m} & f_m & f_m^2 & f_m^5 \\ \frac{1}{f_n} & f_n & f_n^2 & f_n^5 \\ \frac{1}{f_o} & f_o & f_o^2 & f_o^5 \\ \frac{1}{f_p} & f_p & f_p^2 & f_p^5 \end{bmatrix} \begin{Bmatrix} a_0 \\ a_1 \\ a_2 \\ a_3 \end{Bmatrix} \quad (2.19)$$

where  $f_m, f_n, f_o,$  and  $f_p$  are selected frequencies and  $\zeta_m, \zeta_n, \zeta_o,$  and  $\zeta_p$  are the damping ratios at these frequencies that may take the value of the zero strain equivalent damping ratio in Equation (2.16). Park and Hashash (2004) performed linear wave propagation analysis, and found that time-domain solutions using the extended Rayleigh damping formulation are closer to the frequency-domain solution than time-domain solutions developed using simplified or full Rayleigh damping. Park and Hashash suggested that the first two frequencies can be chosen in part to cover the range of frequencies where there is significant energy in the input motion. The third and fourth frequencies should be approximately 10 Hz. In general, they recommended that an iterative procedure should be performed and the selected frequencies should give the best agreement between the results of a linear time-domain analysis and a linear frequency-domain solution.

**(d) Summary of Input Parameters**

For DEEPSOIL, four types of soil profile properties are needed:

1. Parameters to define the modified MKZ backbone curve: initial tangent shear modulus of soil,  $G_{mo}$ , shear stress at reference strain,  $\tau_{mo}$ , and curve-fitting constants,  $\alpha, s$ ; a and b;
2. Properties of each layer and visco-elastic halfspace: width, thickness, saturated unit weight, and wet unit weight for each layer, and unit weight and shear wave velocity of visco-elastic halfspace;
3. Viscous damping ratios and frequencies for the Rayleigh damping formulation.

The parameters in (1)–(2) correspond to parameters that are related to soil profile conditions and soil properties. In addition to soil properties, the parameters in (3) require a relatively high degree of judgment and are not uniquely related to ordinary soil properties.

**2.3.3 TESS**

**(a) Backbone Curve**

TESS is a 1D site response analysis code that utilizes the explicit finite difference scheme to solve the equation of motion. The backbone curve used in TESS is a hyperbolic function similar to that used in D-MOD\_2 and DEEPSOIL. The form of the equation used in TESS is:

$$\tau = \frac{G_{mo}\gamma}{1 + \left(\frac{G_{mo}}{\tau_{mo}}\gamma\right)^a} \quad (2.20)$$

where  $G_{mo}$  is the initial small-strain shear modulus, ratio  $\tau_{mo}/G_{mo}$  is the reference strain, and  $a$  is a fitting parameter.

**(b) Hysteretic Damping**

Hysteretic soil damping in TESS is evaluated using the backbone curve in conjunction with the Cundall-Pyke hypothesis (Pyke 1979). This hypothesis represents a modification of Masing rules and is discussed in detail in Section 5.4. Similar to the Masing rules, the Cundall-Pyke hypothesis underestimates damping at small strains and overestimates damping at large strains.

(c) **Material Degradation**

Similar to DMOD\_2, material degradation due to repeated cycling in TESS is handled by using the concept of a degradation index. At the degradation index (either for material strength or stiffness) is defined as the ratio of material strength (or stiffness) on the  $N^{\text{th}}$  cycle to the same quantity on the first cycle. For irregular cyclic loading, the degradation index after each half cycle of loading is given by:

$$\delta_N = \delta_{N-1} (1 + 0.5(\delta_{N-1})^{1/t})^{-t} \quad (2.21)$$

where  $t$  is a parameter determined experimentally which depends on the number of cycles, cyclic shear strain, and plasticity index. In addition, a modified degradation index (multiplicative to  $\delta_N$ ) is included:

$$\delta_N^* = 1 - (1 - \delta_N) \left( 1 - \left| \frac{\gamma - \gamma_0}{g\gamma_r} \right| \right)^e \quad (2.22)$$

where  $\gamma_0$  is the average of the shear strains at the last two zero-crossings of shear stress, and  $r$  and  $e$  are fitting parameters.

Alternatively, TESS can also model degradation and degeneration of stress-strain loops by directly calculating the excess pore pressures based on the Seed et al. (1976) model. Under this option, a pore-water pressure generation curve is specified. This curve describes the relationship between the normalized residual pore pressure ratio ( $r_u = u / \sigma'_{vc}$ ) and  $N/N_L$  ( $N_L$  is the number of cycles to initial liquefaction or failure). Note that  $N_L$  varies with the amplitude of the applied cyclic shear stress,  $\tau_{av}$ . Using the  $r_u$ - $N/N_L$  curve, the pore pressure generated by a particular shear stress history is evaluated as a two-step process: (1) the irregular shear stress history is converted to an equivalent series of uniform shear stress cycles (e.g., Seed et al. 1975; Liu et al. 2001) with a specified cyclic amplitude ( $\tau_{av}$ ) and number of cycles ( $N$ ); (2)  $N_L$  is determined based on  $\tau_{av}$  and soil characteristics using material-specific curves or tests from the literature (e.g., Seed 1979); and (3)  $r_u$  is determined by entering the  $r_u$ - $N/N_L$  curve using the value of  $N$  from Step 1 and  $N_L$  from Step 2.

TESS also includes a pore-water pressure dissipation and redistribution model that is based on the following equation (Terzaghi 1925):

$$\frac{\partial}{\partial z} \left( k \frac{\partial u}{\partial z} \right) = \gamma_w m_v \frac{\partial u}{\partial t} \quad (2.23)$$

where  $k$ ,  $\gamma_w$ , and  $m_v$  are the permeability of soil, coefficient of volume, change of soil, and unit weight of water, respectively.

**(d) *Low-Strain Damping Scheme***

Unlike the other nonlinear codes presented in this section, TESS does not have a viscous damping scheme. Instead, it has a low-strain (hysteretic) damping scheme that produces non-zero hysteretic damping at small strains. The most recent version of this scheme is discussed in detail in Section 5.4.

**(e) *Summary of Parameters***

For TESS, three types of soil profile properties are needed:

1. Parameters describing the initial backbone curve: initial tangent shear modulus of soil,  $G_{mo}$ , shear stress at reference strain,  $\tau_{mo}$ , and curve-fitting constants,  $a$
2. Parameters controlling the degradation of shear modulus and shear strength (either through the degradation parameters or specification of pore pressure generation curve and  $N_L$ )
3. Parameters controlling pore pressure generation and dissipation
4. Properties of each layer and visco-elastic halfspace: width, thickness, saturated unit weight and wet unit weight for each layer, and unit weight and shear wave velocity of visco-elastic halfspace;
5. Parameters controlling the low strain damping scheme

### **2.3.4 OpenSees**

The ground response module in the OpenSees simulation platform (Ragheb 1994; Parra 1996; Yang 2000; McKenna and Fenves 2001; [opensees.berkeley.edu](http://opensees.berkeley.edu)) utilized a two-phase (solid-fluid) fully coupled finite element (FE) formulation which is capable of simulating permanent shear-strain accumulation in clean medium-dense cohesionless soils during liquefaction and dilation due to increased cyclic shear stiffness and strength. The constitutive model is based on the framework of multi-surface (nested-surface) plasticity (Iwan 1967; Prevost 1985; Mroz 1967), with modifications by Yang (2000). The major components of the plasticity model (in

terms of yield function, hardening rule, and flow rule) are briefly described below (more detailed descriptions can be found from Kramer and Elgamal. 2001; Parra 1996; Yang 2000), which is then followed by a summary of input parameters needed for analysis.

**(a) Yield Function**

For clay, which undergoes fast undrained loading during earthquakes, the yield function is assumed to follow the Von Mises shape, which is illustrated in Figure 2.17. The Von Mises yield surface is a function solely of undrained shear strength. For sand, which may exhibit within-cycle pore pressure induced softening followed by relatively large strain dilatancy during earthquake shaking, the yield function is assumed to follow the Drucker-Prager shape, as illustrated in Figure 2.18. The Drucker-Prager yield surface is described in effective stress space as a function of friction angle and cohesion (as defined in the Mohr-Coulomb failure criteria). Both yield surface types are incorporated into the multi-surface framework.

**(b) Hardening Rule**

A purely deviatoric kinematic hardening rule (Prevost 1985) is employed in order to generate soil hysteretic response under cyclic loading. This kinematic rule dictates that all yield surfaces may translate in stress space within the failure envelope (Parra 1996; Yang 2000) and is consistent with the Masing unloading/reloading criteria.

Under drained monotonic shear loading, the hardening zone is represented by a number of similar yield surfaces for which the (tangent) elastoplastic modulus can be defined by using a piecewise linear approximation of a hyperbolic backbone curve. As shown in Figure 2.19, each linear segment represents the domain of a yield surface  $f_m$  with a shear modulus  $H_m$  and size  $M_m$ , for  $m = 1, 2, \dots, NYS$  (= total number of yield surfaces).  $H_m$  is defined by

$$H_m = \frac{2(\tau_{m+1} - \tau_m)}{\gamma_{m+1} - \gamma_m} \quad (2.24)$$

where  $H_{NYS} = 0$ . It should be noted that the outermost surface is the envelope of peak shear strength (failure size), the size of which can be calculated as:

$$M_f = M_{NYS} = \frac{6 \sin \phi}{3 - \sin \phi} \quad (2.25)$$

where  $\phi$  is the friction angle.

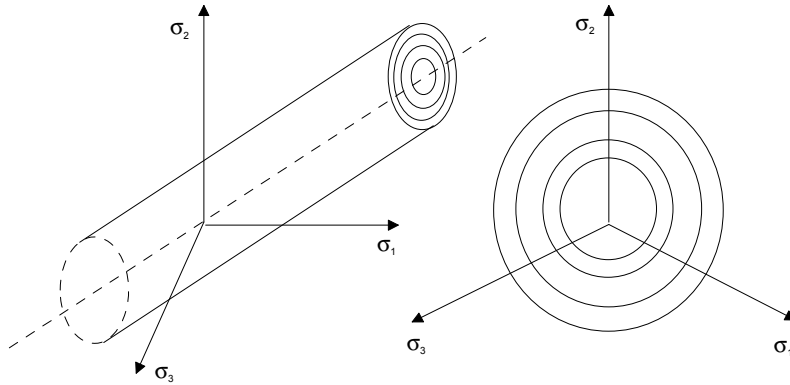


Fig. 2.17 Cylindrical Von Mises yield surfaces for clay (after Prevost 1985, Lacy 1986, Parra 1996, and Yang 2000).

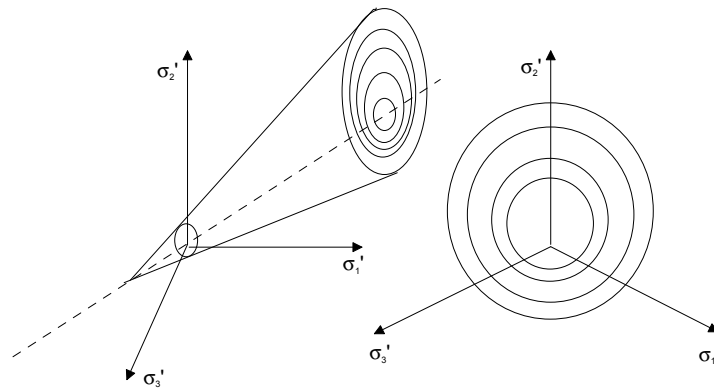


Fig. 2.18 Conical Drucker-Prager yield surfaces for sand (after Prevost 1985, Lacy 1986, Parra 1996, and Yang 2000).

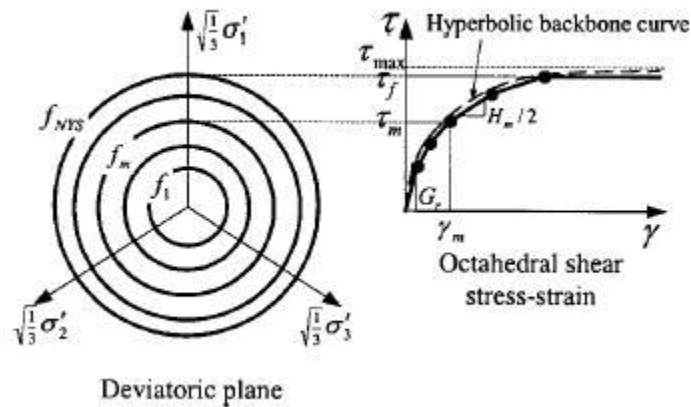
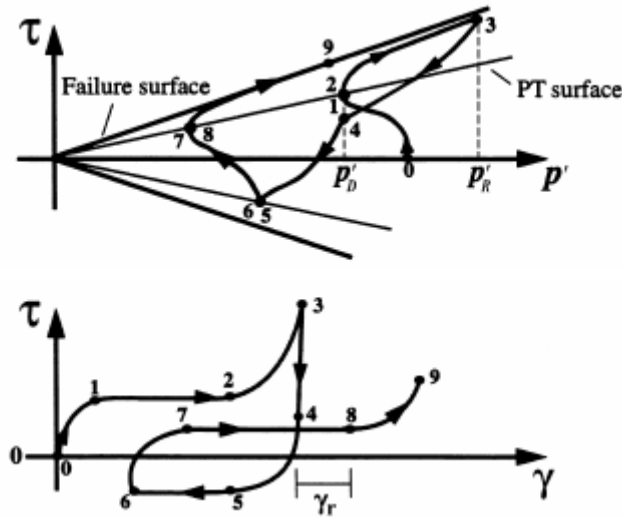


Fig. 2.19 Hyperbolic backbone curve for soil nonlinear shear stress-strain response and piecewise-linear representation in multi-surface plasticity (after Prevost 1985 and Parra 1996).

(c) *Flow Rule*

The associated flow rule is used for clay, in which the incremental plastic strain vector is normal to the yield surface (Section 2.2.2b). For the sand model, a non-associated flow rule (Parra 1996) handles the soil contractive/dilative behavior during shear loading to achieve appropriate interaction between shear and volumetric responses. In particular, non-associativity is restricted to the volumetric component ( $P''$ ) of the plastic flow tensor (outer normal to the plastic potential surface in stress space). Therefore, depending on the relative location of the stress state (as shown in Fig. 2.20) with respect to the phase transformation (PT) surface, different expressions for  $P''$  were specified for (Parra 1996):

1. The contractive phase, with the stress state inside the PT surface (Fig. 2.20, Phase 0-1),
2. The dilative phase during loading, if the stress state lies outside the PT surface (Fig. 2.20, Phase 2-3), and
3. The contractive phase during unloading, with the stress state outside the PT surface (Fig. 2.20, Phase 3-4).



**Fig. 2.20 Schematic of constitutive model response showing octahedral stress-effective confinement response and octahedral stress-octahedral strain response.**

(d) *Viscous Damping*

Full Rayleigh damping formulation is used in OpenSees.

### **(e) Summary of Input Parameters**

For OpenSees, four types of soil profile properties are needed:

1. Parameters describing the yield surfaces (for both sand and clay): either defining the modulus reduction at different strain values or a hyperbolic backbone curve (in terms of small-strain shear modulus and reference strain)
2. Parameters controlling contraction and dilatency response.
3. Properties of each layer and visco-elastic halfspace: thickness, saturated (or wet) unit weight, low-strain shear modulus and bulk modulus; unit weight and shear wave velocity of visco-elastic halfspace;
4. Frequencies/modes for the Rayleigh damping formulation.

### **2.3.5 SUMDES**

SUMDES (Li *et al.* 1992) is a nonlinear finite element program which can model the dynamic response of sites under multi-directional earthquake shaking. It utilizes an effective stress approach, and wave propagation and diffusion effects are fully coupled. It can predict three-directional motions as well as pore pressure build-up and dissipation within soil deposits. The soil constitutive model is based on the bounding surface hypoplasticity model (Wang 1990; Wang *et al.* 1990) in which the incremental plastic strain vector direction depends on the incremental stress direction (in addition to the stress state). The major components of this plasticity model (in terms of yield function, hardening rule, and flow rule) are described briefly below, which is then followed by a summary of input parameters needed for analysis.

#### **(a) Yield Function**

The plasticity framework consists of a bounding surface (or a failure surface) which is similar to a conventional yield surface. However, elasto-plastic behavior occurs when the stress state is inside the bounding surface. A maximum prestress memory surface is also defined. This serves as the first bounding surface, the shape of which is similar to the yield surface. A new loading surface forms as loading occurs inside the maximum prestress memory surface. The relative position of the current loading surface with respect to the maximum prestress memory surface and bounding surface would determine the elasto-plastic behavior for the current stress state.

Similar to the outermost yield surface in OpenSees, the bounding (failure) surface is related to the friction angle, as given by Equation 2.25. Figure 2.21 is a schematic of the yield surfaces, the maximum prestress memory surface (the middle one), and the loading surface (in dash line), used in the bounding surface hypoplasticity framework. The flow rule can be related to the normal at the maximum prestress memory surface as well as the normal on the failure surface (when the “rotational shear” effect is simulated as needed).

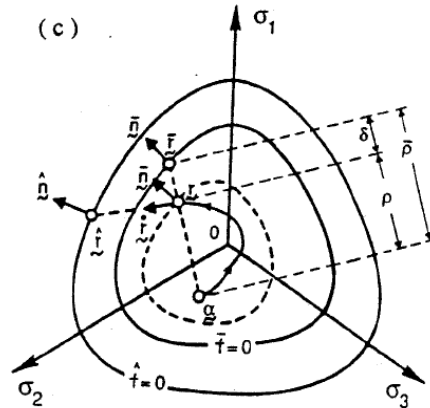


**Fig 2.21 Schematic of the bounding surface plasticity framework (after Wang et al. 1990).**

**(b) Hardening Rule**

A kinematic hardening rule is employed to simulate soil hysteretic response under cyclic loading. This rule is consistent with the Masing unloading/reloading scheme. Similar to OpenSees, the plastic shear modulus in the hardening zone can be determined from a modulus reduction curve (hence the backbone curve). However, only one parameter, called  $h_r$ , is used in the calibration process.

**(c) Flow Rule**

Non-associated flow rule is used to handle the soil contractive/dilative behavior. Similar to OpenSees, different flow rules are used depending on the relative location of the stress state (as shown in Fig. 2.22) with respect to the phase transformation surface (the slope of which is defined as  $R_p$  in SUMDES).

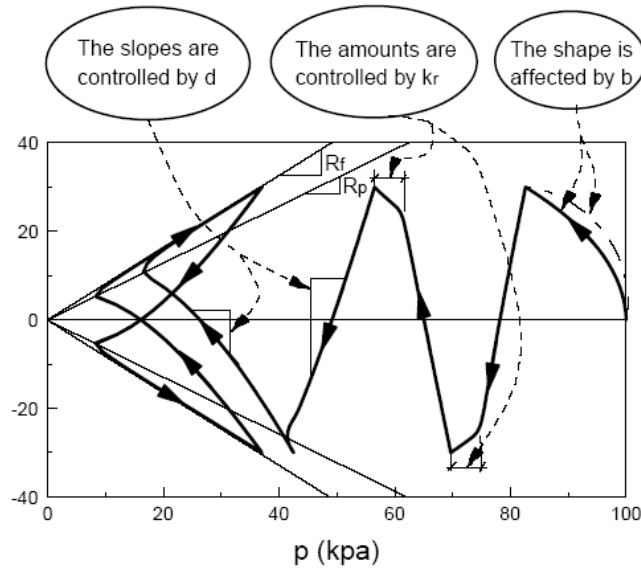


**Fig. 2.22 Schematic showing stress-confinement response (after Li et. al. 1992).**

**(d) Viscous Damping Formulation**

Only the simplified Rayleigh damping formulation is available in SUMDES. It is assumed by the program that the damping ratio is given at 1 Hz. Any desired damping ratio at a desired frequency (e.g.,  $f_s$ ) can be converted to a damping ratio at 1 Hz using simple proportionality, e.g.,  $\zeta_{fi} = \zeta_{fs} / f_s$ . This is because in the simplified Rayleigh damping formulation, the damping ratio is proportional to the frequency.

**(e) Summary of Input Parameters**

For SUMDES, four types of soil profile properties are needed:

1. Parameter controlling the plastic shear modulus (which can be determined from the modulus reduction curve and some basic soil profile properties including void ratio, initial tangent shear modulus, shear strength, and mean normal stress);
2. Parameters controlling contraction and dilation response;
3. Properties of each layer and visco-elastic halfspace: width, thickness, saturated unit weight, and wet unit weight for each layer, unit weight, and shear wave velocity of visco-elastic halfspace; and
4. Viscous damping ratio for the simplified Rayleigh damping formulation.

## 2.4 VERIFICATION STUDIES OF GROUND RESPONSE ANALYSIS CODES

The effectiveness of 1D ground response analysis schemes can be studied when a rock recording is available near a soil recording, or when vertical array data are available. In this section, several studies that have utilized either rock/soil recording pairs or vertical array data to investigate the ability of 1D ground response analyses to simulate observed site effects are discussed.

Verification studies utilizing rock/soil recording pairs take the rock motion as input to ground response analysis, and the computed and recorded soil motions are compared. Several examples of studies of this type are summarized in Table 2.3. For example, Dickenson (1994) used SHAKE and MARDESRA to study the ground response of 11 Bay Mud soft soil sites in the San Francisco Bay Area and found that both models were able to predict reasonably well variations between soil/rock spectra across a broad period range (Fig. 2.23). Chang (1996) and Chang *et al.* (1996) used SHAKE and DMOD to study ground response effects for deep clay sites in both northern California and Los Angeles area alluvial sites. They found that predictions were relatively good for the northern California sites for  $T < 1$  s (e.g., Fig. 2.24a) and relatively poor for the Los Angeles sites (e.g., Fig. 2.24b). They concluded that the difference in model accuracy at Bay Area and Los Angeles area sites may be associated with basin effects (particularly at long periods) because the geometry at the Bay Area sites is relatively wide and flat as compared to the Los Angeles area sedimentary basins. It should be noted that no formal parameter selection protocols were followed when conducting the nonlinear ground response analyses for these sites—hence, some adjustments of key parameters to match observed responses were possible.

**Table 2.3 Verification studies of ground response codes.**

Earthquake	Soil Condition - Recording Locations	Reference	Codes Investigated
<i>(a) Nearby Rock-Soil Pairs</i>			
1985 Michoacan-Guerrero	Soft clay - Mexico City (2)	Seed et al. (1987)	SHAKE
1989 Loma Prieta	Bay mud - San Francisco Bay Area (11 sites)	Idriss (1990); Dickenson (1994)	SHAKE; SHAKE, MARDESRA
1989 Loma Prieta	Deep stiff clay - Oakland, Emeryville; Gilroy (4 sites)	Chang (1996); Darragh and Idriss (1997)	SHAKE, D-MOD_2; SHAKE
1994 Northridge	Deep alluvium - Sylmar, Hollywood, Santa Monica (3 sites)	Chang et al. (1996)	SHAKE, D-MOD_2
1994 Northridge	Oil Landfill - Monterey Park	Matasovic et al. (1995)	SHAKE, D-MOD_2
<i>(b) Vertical Arrays</i>			
unnamed $m=6.2, 7.0$ events	Soft silt - Lotung	Chang et al. (1990) and Li et al. (1998); Beresnev et al. (1995); Borja et al. (1999); Elgamal et al. (1995)	SUMDES; DESRA2; SPECTRA; unnamed code
1995 Kobe	Liquefiable sand - Kobe Port Island	Wang et al.(2001); Elgamal et al. (1996)	SUMDES; unnamed code
1987 Superstition Hills	Liquefiable sand - Wildlife site, CA	Matasovic and Vucetic (1996)	D-MOD_2

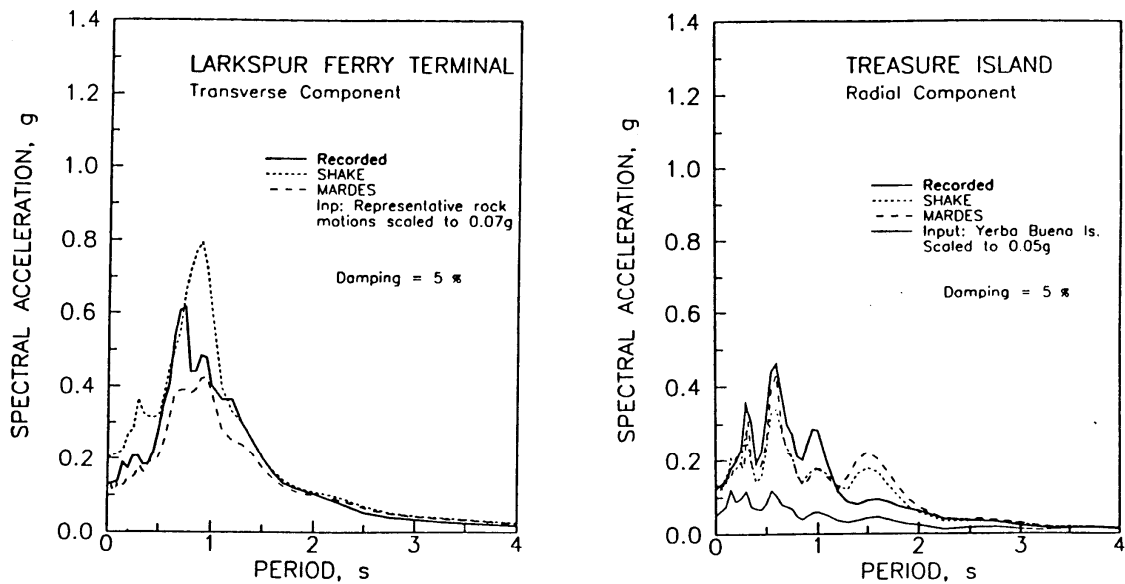


**Fig. 2.23 Comparison between recorded and calculated response spectra at representative soft clay sites, from Dickenson (1994).**

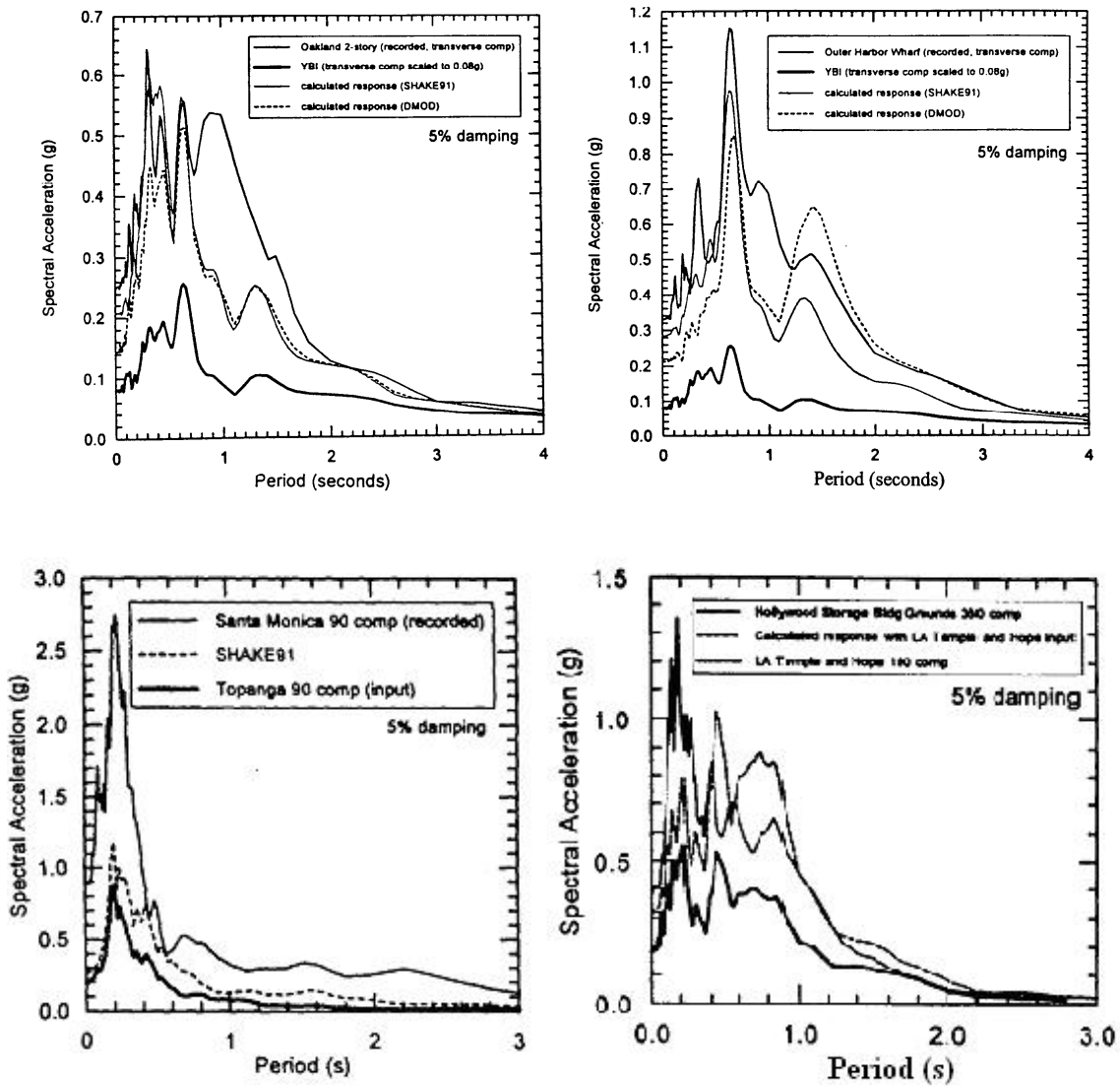
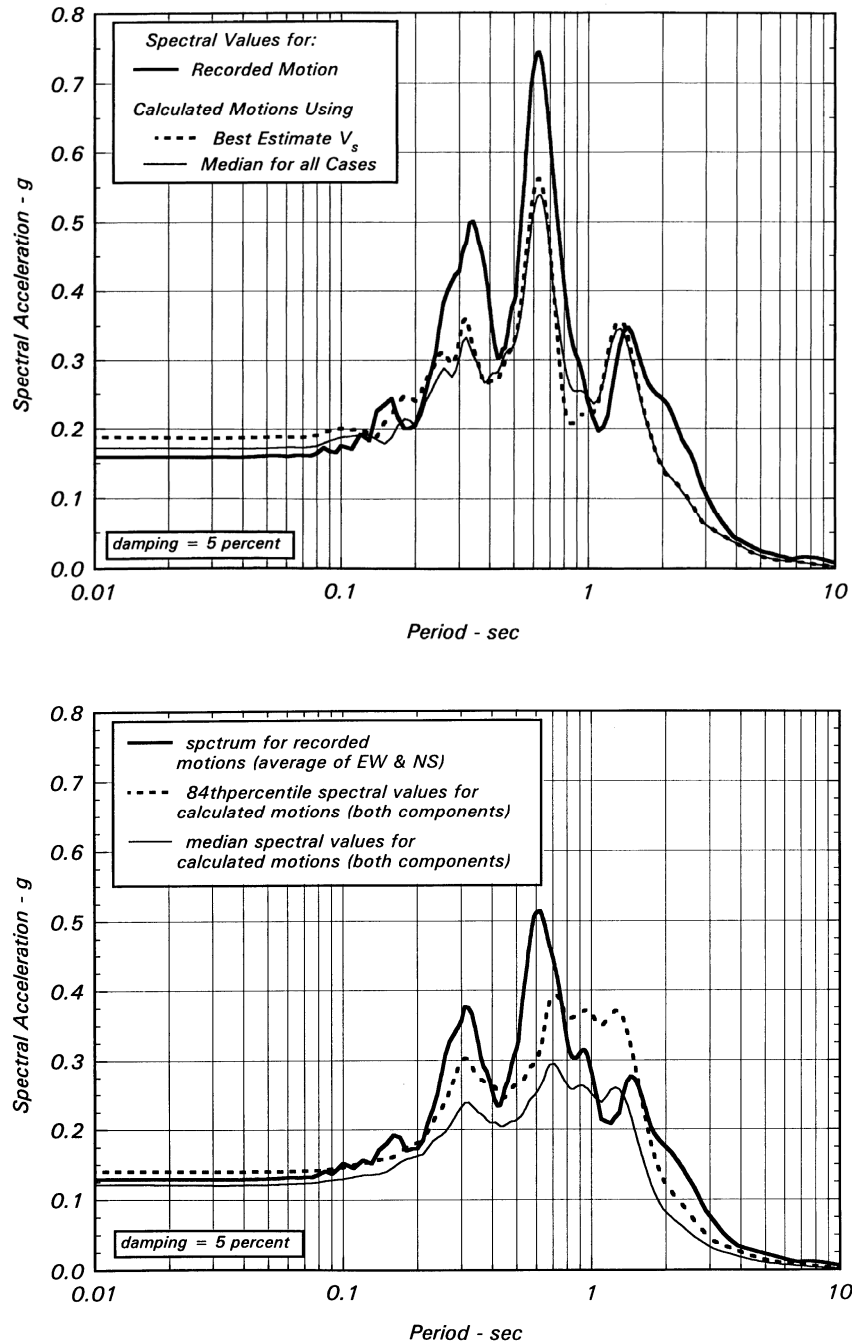


Fig. 2.24 Comparison between recorded and calculated response spectra at (a) selected deep stiff clay sites in San Francisco Bay Area, from Chang (1996) and at (b) selected deep alluvial sites in Los Angeles area, from Chang (1996).

One important outcome of the above studies is that the accuracy of predicted spectra on soil depends significantly on the rock (control) motion characteristics. This was well illustrated by Idriss (1993), who found that predicted spectra at the Treasure Island soil site is matched well when the control rock motion is taken from nearby Yerba Buena Island (Fig. 2.25, top frame), but is matched relatively poorly when control motions are taken from other San-Francisco-Oakland–Berkeley area rock stations (Fig. 2.25, bottom frame). Since in a design setting the detailed characteristics of rock motions cannot be known precisely, it is clear that significant uncertainty is introduced to predicted soil spectra from uncertainty in input motion characteristics.

A more direct verification of 1D ground response analyses can be performed using recordings from vertical arrays. Examples of a few prior studies that have utilized vertical array data to validate ground response analysis codes are listed in Table 2.3. Lotung, a non-liquefiable large-scale seismic test site in Taiwan, is one of the vertical arrays that is used to validate various ground response analysis codes. Figure 2.26 shows the results of such analyses obtained from both a nonlinear analysis code (SPECTRA) as well as SHAKE. Borja *et al.* (1999) found that both analysis procedures provided good predictions in the time domain to the recorded motions.



**Fig. 2.25 Comparison of acceleration response spectrum of recorded motion at Treasure Island strong motion site (1989 Loma Prieta earthquake) with calculated spectra from ground response analyses. Calculations in upper frame utilized nearby rock recording (Yerba Buena Island) as control motion; lower frame presents statistical variation in calculated spectra for suite of control motions from rock sites in region surrounding Treasure Island. From Idriss 1993.**

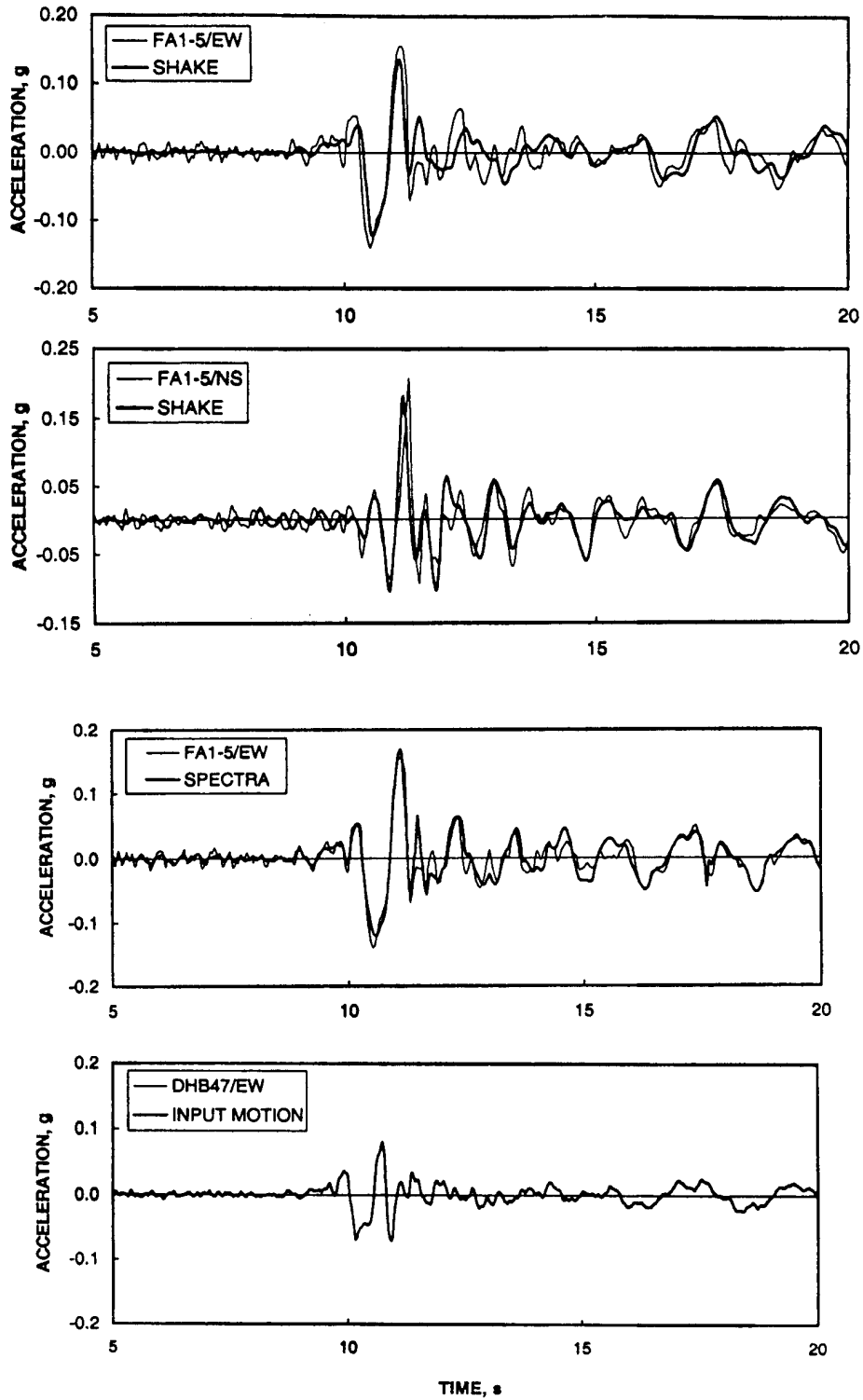


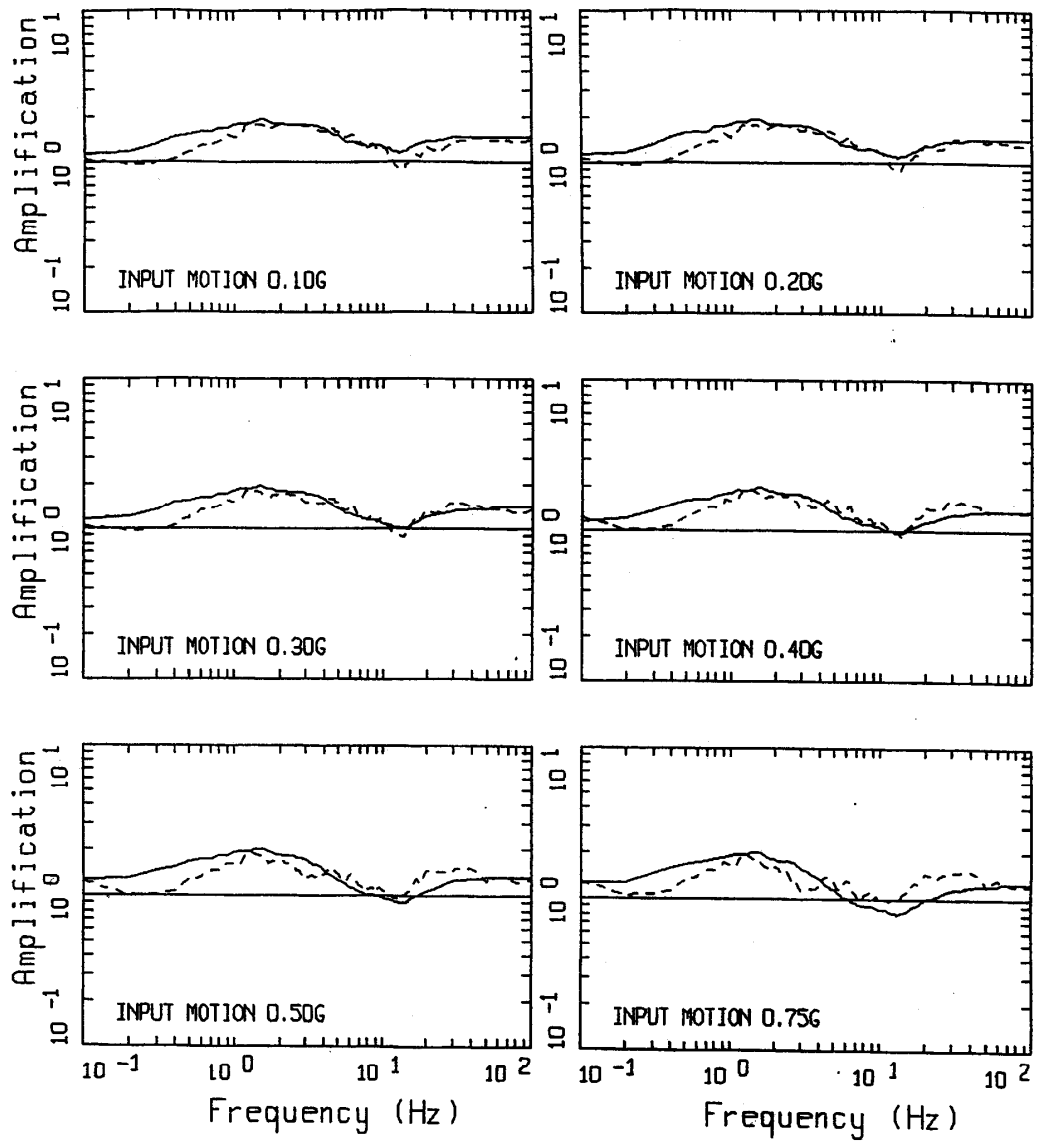
**Fig. 2.26 Comparison of recorded ground surface accelerations and predictions by SHAKE (top two frames) and SPECTRA (third frame from top). Bottom frame shows recording at base of array (47-m depth). After Borja et al. 1999.**

## 2.5 COMPARISONS OF RESULTS OF EQUIVALENT-LINEAR AND NONLINEAR ANALYSES

An important finding from past verification studies mentioned above is that prediction residuals from nonlinear methods were not significantly smaller than those from equivalent-linear methods. However, the amplitude of shaking at those sites was relatively small in comparison to typical design basis ground motion in seismically active regions like California.

For stronger shaking, comparisons have been performed by Silva *et al.* (2000), although a “calibration motion” in the form of recordings is not available. Silva *et al.* (2000) used simulated motions with a wide range of amplitudes as input into equivalent-linear (RASCAL, Silva and Lee, 1987) and nonlinear (DESRA-MUSC, Qiu 1997) ground response analyses for the calculation of amplification factors. In general, there was good agreement between the two approaches over most of the frequency range 0.1–100 Hz. This is illustrated in Figure 2.27 which compares amplification factors predicted for NEHRP class site C by equivalent-linear and nonlinear models. The two sets of amplification factors are reasonably consistent across the frequency range of 1–10 Hz at all input levels. At higher loading levels ( $\geq 0.4 g$ ), high-frequency amplification ( $>10$  Hz) is larger by nonlinear than by equivalent linear. This discrepancy may be due to differences in the damping curves utilized in the equivalent-linear and nonlinear analyses (see further discussion below), but no explanation is offered by Silva *et al.* (2000).

As shown in Figure 2.28, for soft soils (represented by NEHRP class site E), nonlinear codes give smaller amplification factors than equivalent-linear for high levels of shaking. Silva *et al.* (2000) attribute this to the larger high-strain damping predicted by DESRA-MUSC model relative to what is given in standard damping-strain curves that are utilized in the equivalent-linear model (similar to Fig. 2.12). Using nonlinear backbone curve models, it is relatively easy to match the modulus reduction curves, but the use of Masing or extended Masing rules with the backbone curves often provides poor fits to damping curves. Another reason for smaller amplification is that the nonlinear model is able to accommodate yielding or soil failure at very high strain levels. Near-surface yield will attenuate high-frequency surface motions, which cannot be simulated by equivalent-linear analysis.



NEHRP AMPLIFICATION, CATEGORY C, WUS, PENINSULAR RANGE CURVES

LEGEND  
 ——— MEDIAN, EQUIVALENT-LINEAR  
 - - - - MEDIAN, NONLINEAR

Fig. 2.27 Amplification factors predicted by equivalent-linear and nonlinear models for NEHRP category C (Silva et al. 2000).

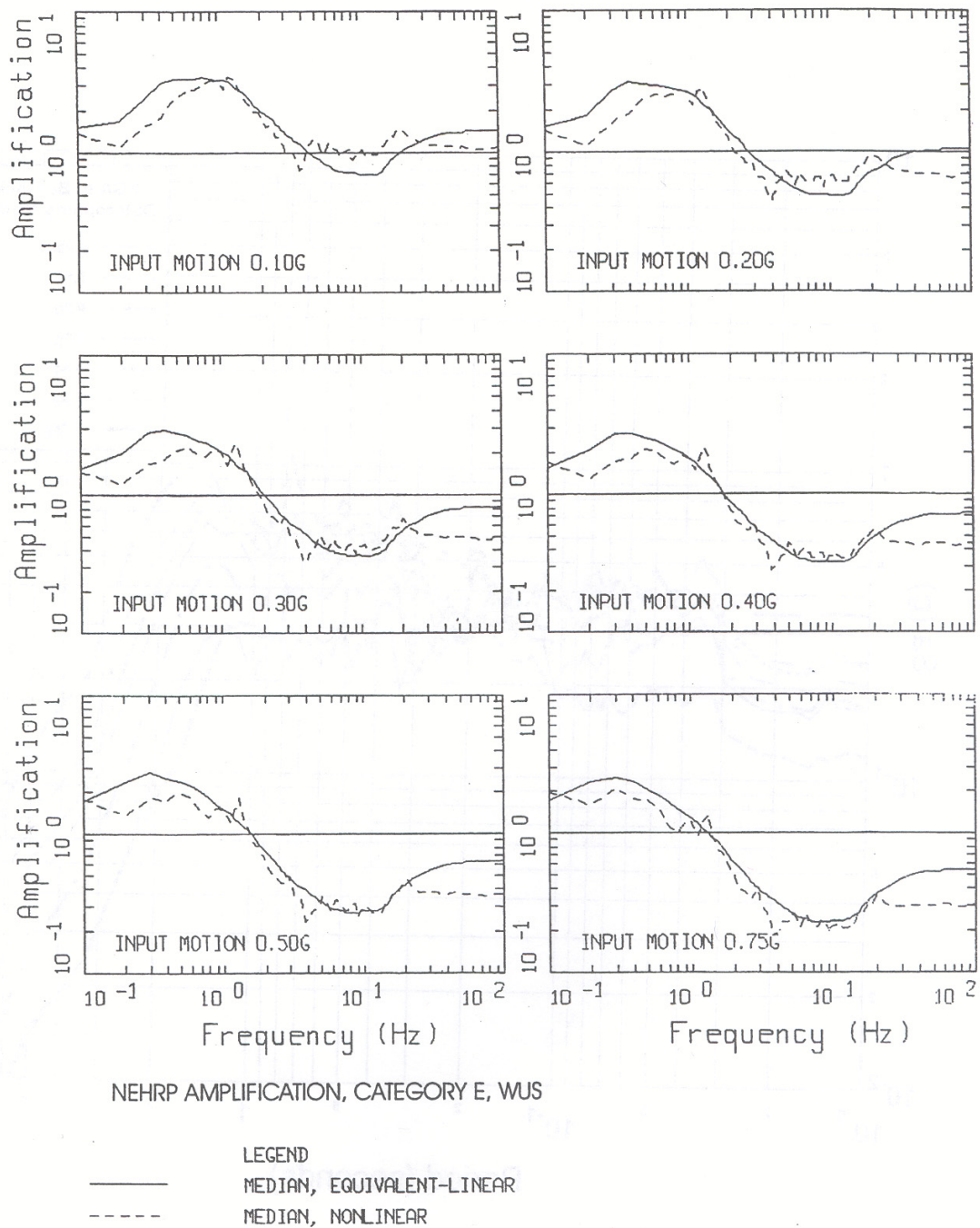


**Fig. 2.28 Amplification factors predicted by equivalent-linear and nonlinear models for NEHRP category E (Silva et al. 2000).**

## 3 Element Testing

Prior to the development of parameter selection and usage protocols for nonlinear codes, it is important to verify the constitutive model implementation to ensure that soil behavior is modeled properly. Element testing is performed on the five nonlinear codes (D-MOD\_2, DEEPSOIL, TESS, OpenSees, TESS, and SUMDES) discussed in Section 2.3. Three groups of analyses are performed corresponding to different loading patterns (symmetric, asymmetric, and reversal loadings). For most codes, these analyses are performed by specifying a shear strain history and then calculating a shear stress history from the constitutive model. For DMOD\_2, an acceleration history is assigned instead of strain history and the response is calculated using a nonlinear single-degree-of-freedom system analysis.

### 3.1 SYMMETRICAL LOADING

Two types of symmetrical loading histories are tested. The first type is a sinusoidal strain history with constant amplitude. The analysis is repeated with different strain amplitudes. The purpose of using such loading is to check if stress accumulates in one direction under symmetric loading, which may occur with some Masing-type unload/reload models. All nonlinear codes tested, except TESS, predicted a stress history that is sinusoidal, constant-amplitude and in-phase with the imposed strain history. Figure 3.1 (left frames) shows the typical result obtained from DEEPSOIL. For TESS, material softening after the first cycle is observed. This is due to the Cundall-Pyke hypothesis, which is a mathematical formulation (implemented in TESS) such that the unloading and reloading curves have the same shape of the initial backbone curve but are enlarged by a factor ranging from zero to two (for Masing behavior implemented in all other codes, the factor is a constant of 2). Figure 3.1 (right frames) shows the results obtained using TESS.

The second type of sinusoidal loading history gradually ramps the amplitude up to 1% and then gradually decreases back to zero. This is to test constitutive behavior for successive cycles of different amplitude. As shown in Figure 3.2, the predicted stress histories from the five nonlinear codes are all in-phase with the imposed strain history. The change in the stress amplitude follows the trend of strain amplitude.

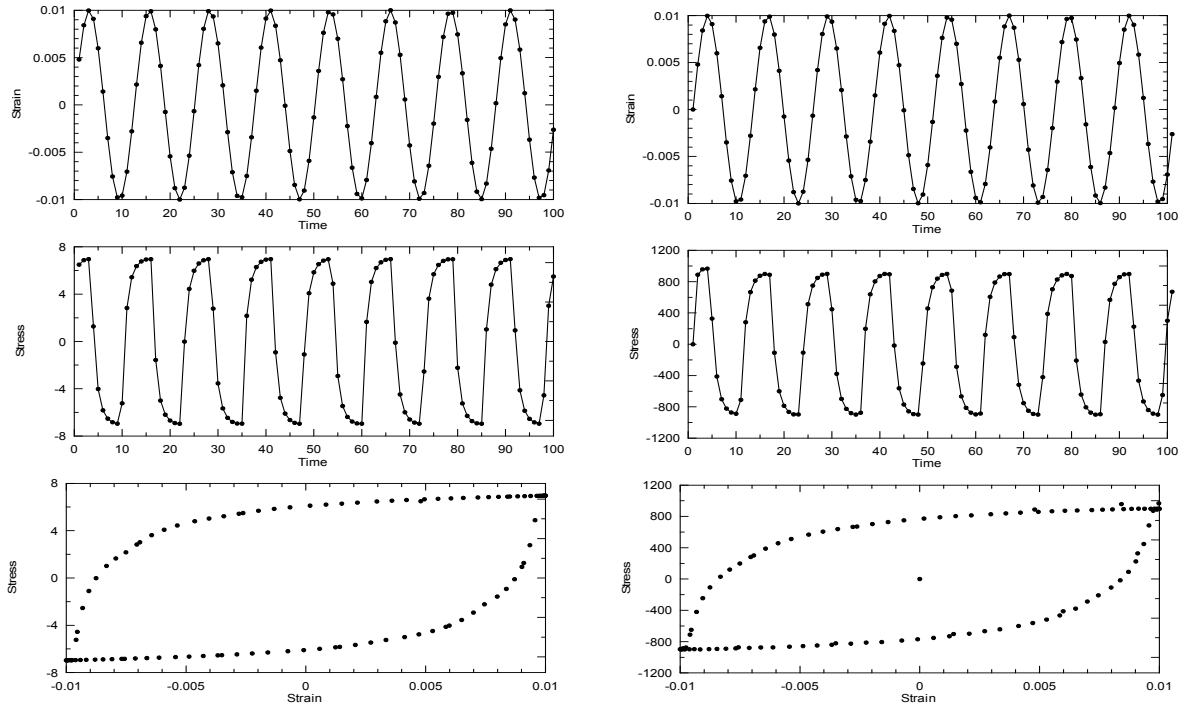


**Fig. 3.1 Results of symmetrical loading with strain at constant amplitude from DEEPSOIL, D-MOD\_2, OpenSees, and SUMDES (left frames), and TESS (right frames).**

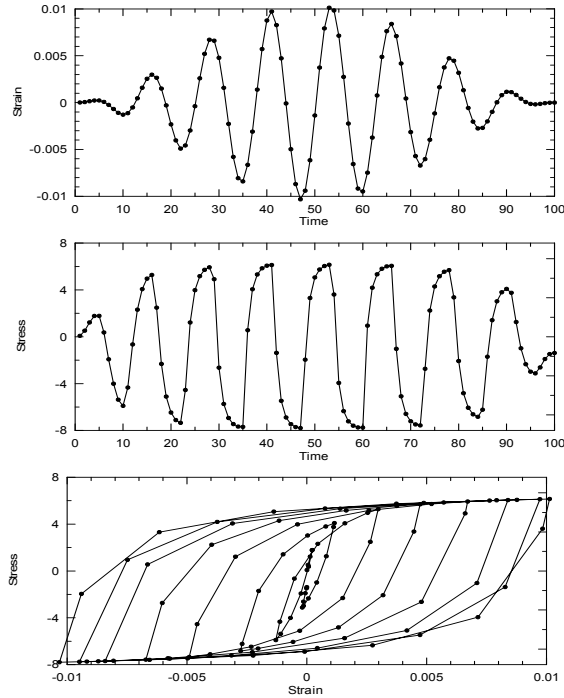


**Fig. 3.2 Results of symmetrical loading with varying strain amplitude from all codes.**

### 3.2 ASYMMETRICAL SINUISODAL LOADING

A constant-amplitude sinusoidal loading with initial static shear strain is imposed. This test is not performed on D-MOD\_2 as it does not allow the specification of initial static shear strain. As shown in Figure 3.3, DEEPSOIL and OpenSees predict similarly predict constant-amplitude shear stress cycles. As shown in Figure 3.4, the results from SUMDES show material softening after the first cycle that produces non-overlapping stress-strain loops. This occurs because the SUMDES constitutive model includes a rate-of-loading dependency, which allows deformation accumulation. Similar behavior is observed with TESS, which is associated with material softening that results from the use of the Cundall-Pyke hypothesis.

### 3.3 MONOTONIC LOADING WITH SMALL REVERSALS

Four types of monotonic loading are tested. The first type consists of straight-forward monotonic loading of the element to failure and holding this strain level. All codes predict a similar stress history as shown in Figure 3.5.

The second type of monotonic loading is similar to the first type except that there is a small reversal in the monotonic loading history. The purpose of including the small reversal is to test for potential numerical instabilities brought on by a small reversal. The concern was that some models might revert to the small-strain modulus ( $G_{max}$ ) upon reloading and not return to the backbone curve. All codes except TESS predict a stress history as shown in Figure 3.6 (left frames) in which the shear modulus remains the same after the small reversal. For TESS, material hardening is observed after the small reversal. This is due to the Cundall-Pyke hypothesis for which two hyperbolic models are used to describe the unloading and reloading. Hardening is a by-product of this formulation.

The third type of test involves monotonically loading the element to nearly fail, then unloading to strains that are just slightly negative, followed by a reversal of the loading until failure is reached. All codes except TESS give predictions similar to those shown in Figure 3.7 (left frame) in which the stress-strain loop is closed. As shown in Figure 3.7 (right side), for TESS the stress-strain loop is not closed and the material is degraded so that the original ultimate shear stress cannot be reached.

The fourth type of test is to load the element nearly to failure, unload to failure with a small reversal in the unloading path, and then reload to failure. As shown in Figure 3.8, all codes except TESS predict that the shear modulus remains unchanged after the small reversal and also that the ultimate shear strain is reached. For TESS, the shear modulus is hardened after the small reversal and the material is also degraded (thus the stress-strain loop is not closed).

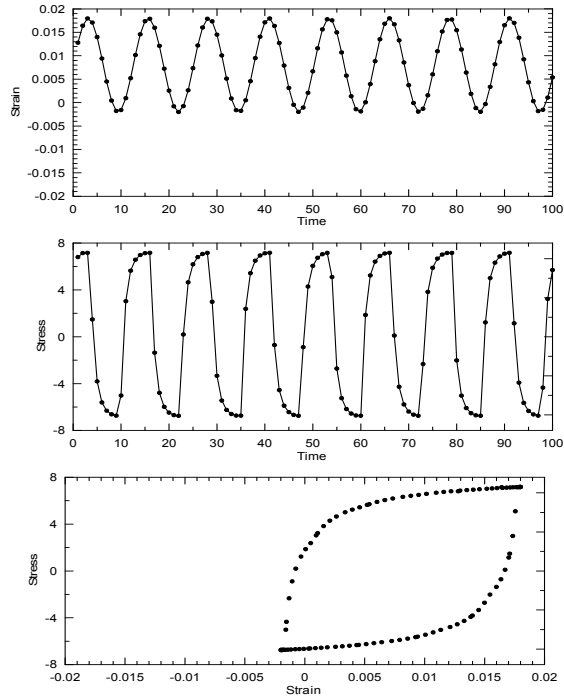


**Fig. 3.3 Results of asymmetrical loading predicted by DEEPSOIL and OpenSees.**

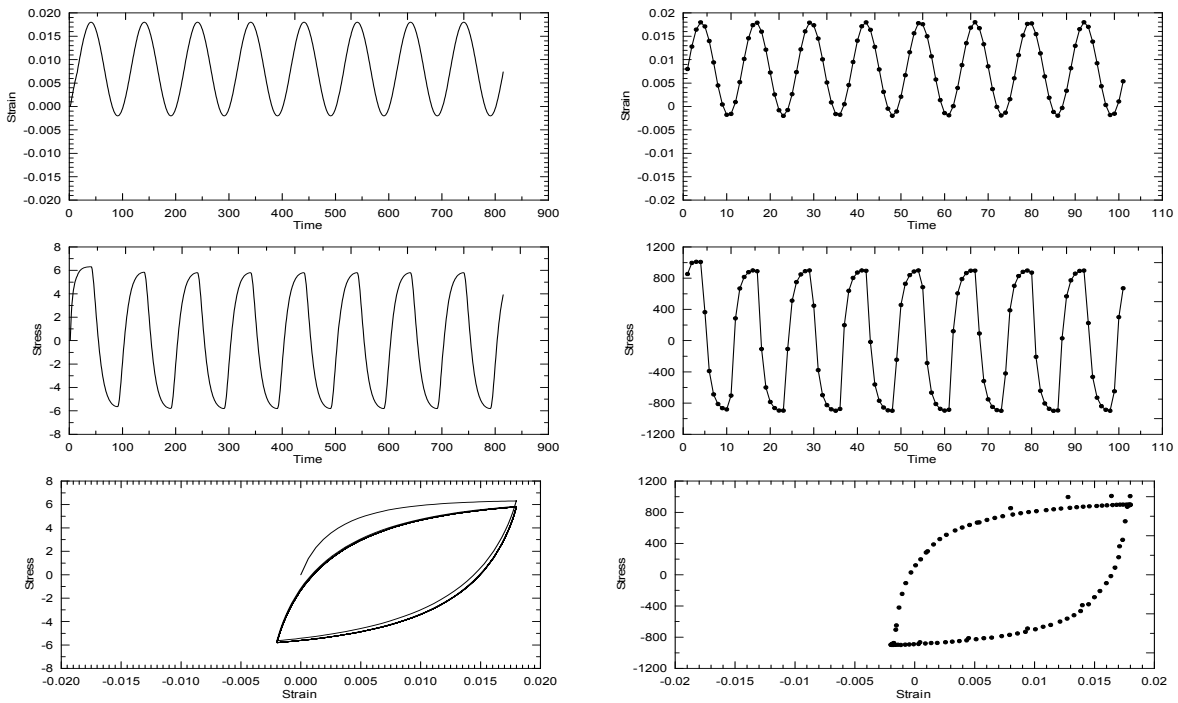


**Fig. 3.4 Results of asymmetrical loading predicted by SUMDES (left frames) and TESS (right frames).**

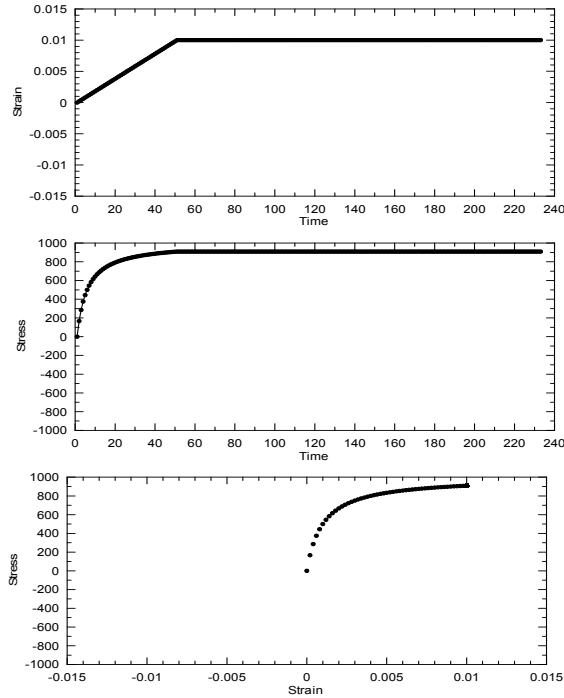


**Fig. 3.5 Results of monotonic loading predicted by all codes.**

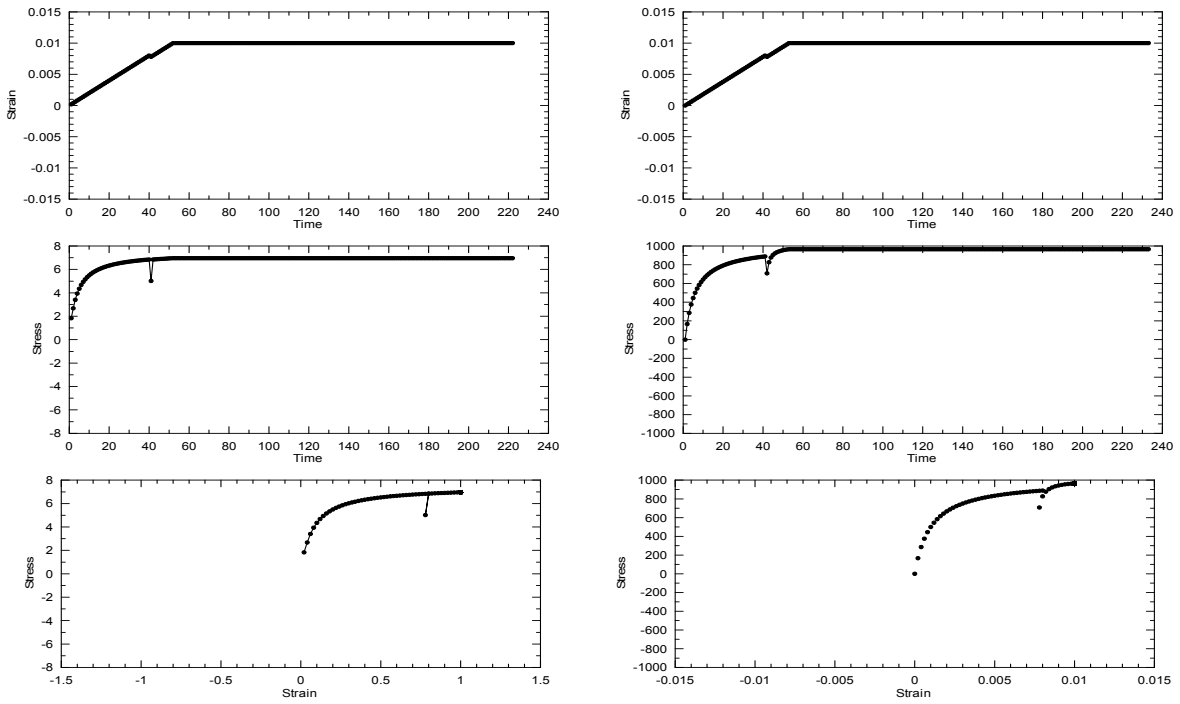


**Fig. 3.6 Results of monotonic loading with a small reversal predicted by DEEPSOIL, D-MOD\_2, OpenSees, and SUMDES (left frames), and TESS (right frames).**

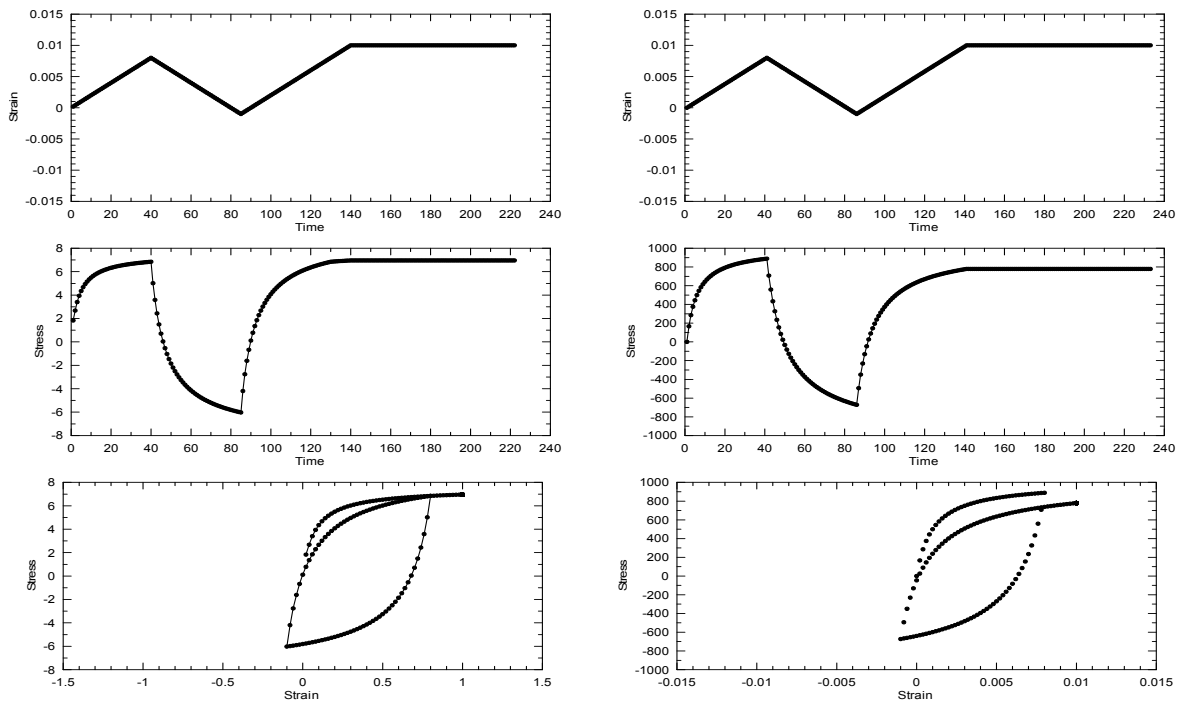


**Fig. 3.7 Results of reverse loading without unloading to failure predicted by DEEPSOIL, D-MOD\_2, OpenSees, and SUMDES (left frames), and TESS (right frames).**

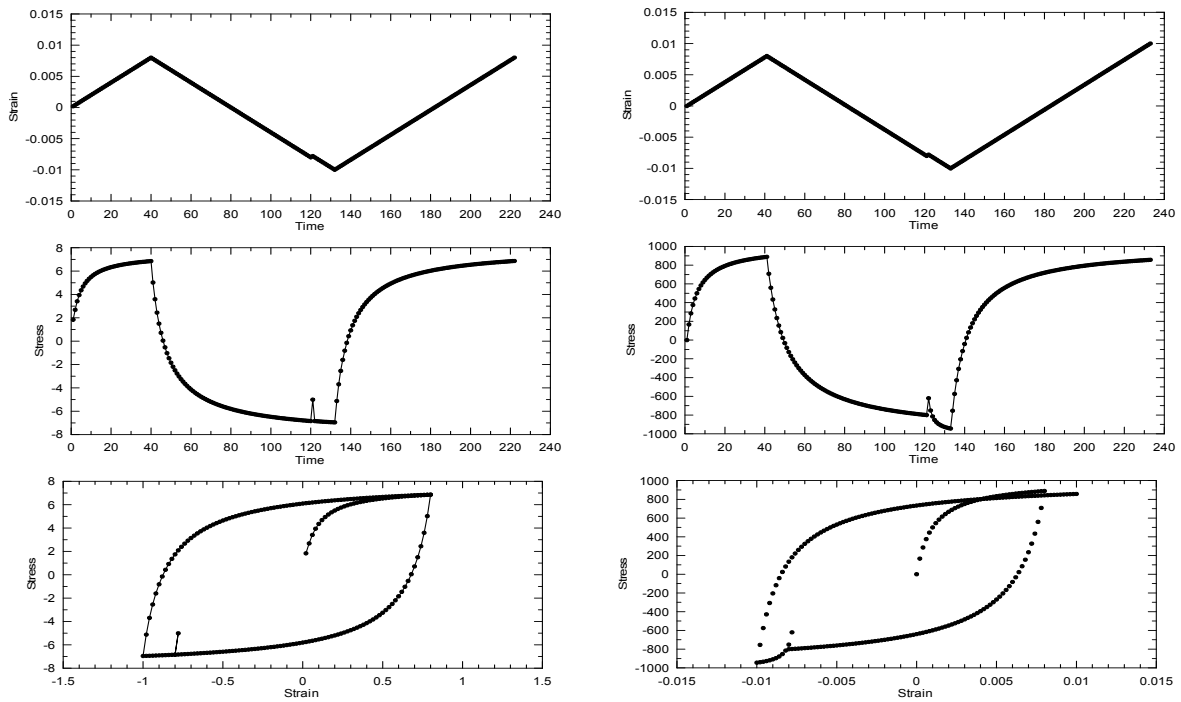


**Fig. 3.8 Results of reverse loading with unloading to failure predicted by DEEPSOIL, D-MOD\_2, OpenSees, and SUMDES (left frames), and TESS (right frames).**

## 4 Key Issues in Nonlinear Ground Response Analysis

As discussed in Chapter 2, equivalent-linear analyses require the specification of well-understood and physically meaningful input parameters (shear-wave velocity, unit weight, modulus reduction, and damping), while nonlinear ground response analyses often require the specification of poorly understood parameters (such as viscous damping) that may or may not be clearly associated with measurable soil properties. Previous studies have thoroughly investigated the sensitivity of site response results to the equivalent-linear parameters (e.g., Roblee et al. 1996), but this level of understanding is not available for the nonlinear parameters. Moreover, prior to this research, parameter selection criteria for many of those nonlinear parameters were often poorly documented and were unavailable to users other than the code developers. This situation has limited the application of nonlinear ground response analyses in engineering practice (Kramer and Paulsen 2004). The objective of this chapter is to identify five key issues that need to be understood to properly perform nonlinear ground response analyses. Several of these issues are addressed directly in the chapter, while others are addressed in subsequent chapters following detailed investigations to justify the recommendations that are provided. Most of the material presented in this chapter was previously presented in Stewart et al. (2006) and Stewart and Kwok (2008).

### 4.1 PARAMETERIZATION OF BACKBONE CURVE

#### 4.1.1 Backbone Curve

Figure 4.1 shows a typical nonlinear backbone curve for a soil element, which has a hyperbolic shape defined by the initial small-strain secant shear modulus ( $G_{max}$ ) and the shear strength ( $\tau_{ff}$ ). The classical definition of reference strain is the ratio  $\gamma_{ref} = \tau_{ff} / G_{max}$  (Hardin and Drnevich 1972). The parametric description of the nonlinear backbone curve in the past has generally required the

specification of this reference strain along with a number of curve-fitting parameters. A practical problem with this approach is that the shear strength at rapid strain rate, needed to define the reference strain, is often not available. Another problem is that the shape of the backbone curve at small strains, as established by hyperbolic models based on  $\gamma_{ref}$ , may be inconsistent with laboratory test data.

At least for problems involving low to moderate strain levels, a “pseudo-reference strain” ( $\gamma_r$ ) can be used in lieu of the strength-based reference strain. The term pseudo-reference strain is used to avoid confusion with the reference strain as defined by Hardin and Drnevich (1972). The pseudo-reference strain is defined from a laboratory modulus reduction curve as the shear strain at which  $G/G_{max} = 0.5$ . This definition arises from hyperbolic fits of  $G/G_{max}$  curves according to

$$G / G_{max} = \frac{1}{1 + \beta(\gamma/\gamma_r)^a} \quad (4.1)$$

where  $\beta$  and  $a$  are fitting parameters generally taken as 1 and 0.92, respectively (Darendeli 2001). The advantages of using the pseudo-reference strain are that (1)  $\gamma_r$  can be readily evaluated from the material-specific modulus reduction curves evaluated from laboratory testing and (2) lacking material-specific testing, empirical relationships exist to predict  $\gamma_r$  as a function of basic parameters such as PI, overburden stress, and overconsolidation ratio (Darendeli 2001; Zhang et al. 2005).

Because pseudo-reference strains are determined from modulus reduction curves that are typically defined for strains less than 1%, a backbone curve described by a hyperbolic curve fit using  $\gamma_r$  would not necessarily be expected to accurately represent soil behavior at large strain, including the shear strength. This problem is investigated by examining the degree to which the shear strength implied by the use of Equation 4.1 (approximately  $G_{max} \times \gamma_r$ ) is realistic. This is done using ratios of  $G_{max}$  to shear strength, for which empirical relationships are available from Weiler (1988). The ratios from Weiler are for soils with OCR of 1–5, confining pressures  $\sigma = 100$ –500, kPa (1–5 tsf), and PI=15–45. Weiler’s undrained shear strengths ( $S_u$ ) are based on direct simple shear testing. Weiler’s  $G_{max} / S_u$  ratio is compared to the inverse of Darendeli’s (2001) estimate of  $\gamma_r$  (which is approximately the ratio of  $G_{max}$  to the large-strain asymptote of the hyperbolic curve, taken as shear strength).

As observed from Figure 4.2, the  $G_{max}$ /effective-strength ratios implied by pseudo-reference strain  $\gamma_r$  are significantly higher than those from Weiler for an overburden stress of  $\sigma$

=100 kPa. This bias implies that the shear strength implied by  $\gamma_r$  is underestimated by Darendeli's relationships at  $\sigma = 100$  kPa. This bias disappears at larger overburden pressures ( $\sigma=500$  kPa). Accordingly, at relatively shallow depths, the use of backbone curves derived from the pseudo-reference strain parameter may overestimate the soil nonlinearity at large strains.

Recommendations for the evaluation of backbone curve parameters are given in a subsequent section following a discussion of material damping.

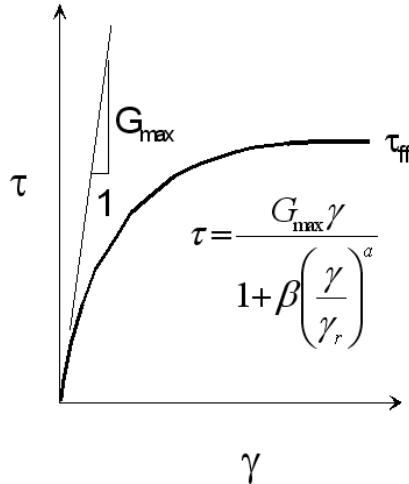


**Fig. 4.1 Schematic illustration of backbone curve used for nonlinear ground response analyses.**

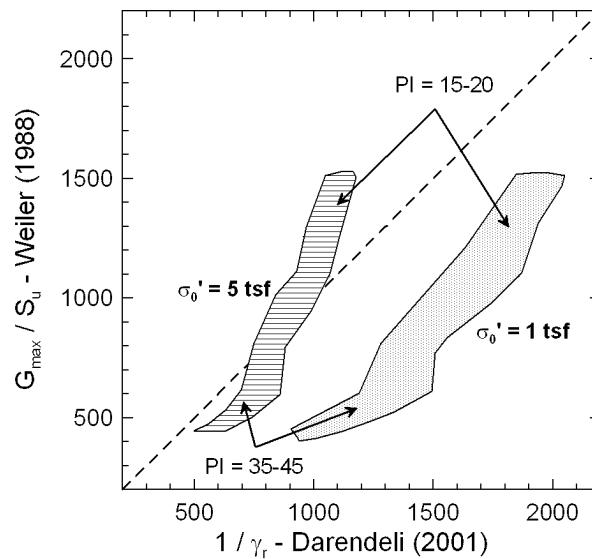


**Fig. 4.2 Comparison of  $G_{max} / S_u$  ratio from Weiler (1988) to inverse of pseudo-reference strain ( $1/\gamma_r$ ) from Darendeli (2001). Quantity  $1/\gamma_r$  is approximately ratio of  $G_{max}$  to shear strength implied by use of pseudo-reference strain for fitting nonlinear backbone curves.**

### **4.1.2 Material Damping**

Masing's rules (Masing 1926) and extended Masing rules (Vucetic 1990; Pyke 1979) are employed in nonlinear analysis in conjunction with the backbone curve to describe unloading, reloading, and cyclic degradation behavior of soil. Material damping is directly proportional to the area contained within a cyclic stress-strain loop, and hence is sensitive to the shape of the backbone curve and unload/reload rules. The damping at large strain that results from the use of Masing or extended Masing rules tends to be overestimated relative to laboratory measurements.

There are three schools of thought on managing the overestimation of damping. One approach is to select model parameters for the backbone curve (and hence modulus reduction curves) that optimally fit the target data and to accept the resulting overestimation of damping using Masing's rules. A second approach is to select model parameters that optimize the fitting of modulus reduction and damping curves simultaneously (across the strain range of interest).

The third approach is to introduce an additional parameter that changes the shape of the unload/reload curves so that both modulus reduction and damping curves can be fit simultaneously. Lo Presti et al. (2006) allows unloading and reloading curves to have a shape scaled from that of the backbone curve by a factor of  $n$  (for the original Masing criteria,  $n = 2$ ). Lo Presti et al. provides recommendations for estimating  $n$  as a function of soil type, strain level, and number of cycles for the motion. Wang et al. (1980) suggest an approach in which a damping correction factor is applied to the Masing rule damping. These unload/reload rules are not yet implemented in the nonlinear codes considered in this study, which are the codes most often used in engineering practice, and hence this approach is not discussed further. The relative merits of the first two approaches were investigated using vertical array data, and the results of that investigation are discussed in Chapter 7.

### **4.1.3 Parameter Selection for Backbone Curve and Damping**

There are two basic elements to the specification of parameters describing the nonlinear backbone curve and damping. The first element is to select the target shape of the backbone curve (equivalently, the modulus reduction curve) and the damping curve. The second element is to select model parameters that describe the target relationships within a reasonable degree of approximation for the problem at hand. Following the discussion of each element below, we

present results of sensitivity studies illustrating the implications for the computed site response of alternative parameter selection procedures.

**Element (1)—Target Curves:** The ideal characterization would involve material-specific cyclic testing across the strain range of interest. This testing would include characterization of the material’s dynamic shear strength for large-strain problems. However, material-specific testing is usually not available, requiring the nonlinear behavior to be described using published correlations relating soil index properties, stress state, and stress history to parameters describing modulus reduction and damping curves (e.g., Darendeli 2001; Zhang et al. 2005). Those relationships are usually well defined to shear strains of approximately 0.3–0.7%. This is illustrated in Figure 4.3, which shows the modulus reduction-strain values in the database used by Darendeli (2001). As described previously, these relationships do not typically provide an adequate representation of the shear strength. Guidelines for undrained shear strength evaluation and estimation are given in Ladd (1991); these estimates should be adjusted in consideration of rate effects, as described for example by Sheahan et al. (1996).

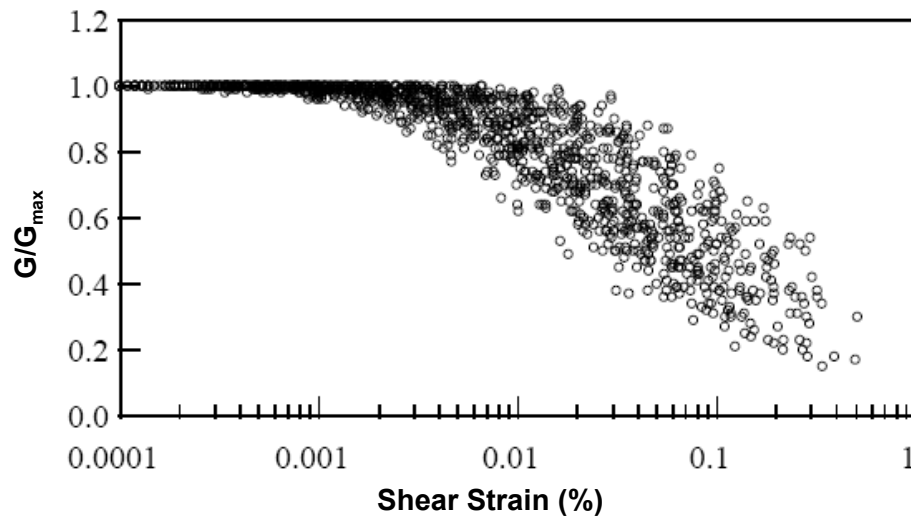


**Fig. 4.3 Modulus-reduction-strain values in database used by Darendeli (2001).**

For problems involving large-strain soil response, traditional practice has been to use a hyperbolic stress-strain curve (Eq. 4.1) with the strength-based reference strain. However, as shown in Figure 4.4, because of the misfit of the reference and pseudo-reference strains, this approach provides a poor match to small-strain modulus reduction behavior from laboratory tests. Accordingly, we recommend an alternative approach illustrated in Figure 4.4 and explained

in the following: (1) use cyclic test results or correlation relationships to define the shape of the backbone curve to strain level  $\gamma_l$  (typically taken as 0.1–0.3%); (2) estimate the material shear strength ( $\tau_{ff}$ ) for simple shear conditions with appropriate adjustment for rate effects; (3) estimate the modulus reduction ordinates between strain  $\gamma_l$  and the shear strength with the following hyperbolic relationship:

$$G/G_{\gamma_l} = \frac{1}{1 + G_{\gamma_l}(\gamma - \gamma_l)/\tau_{ff}} \quad (\text{applies for } \gamma > \gamma_l \text{ only}) \quad (4.2)$$

where  $G_{\gamma_l}$ =secant shear modulus from Step (1) at  $\gamma = \gamma_l$ . An example application of this procedure is given by Chiu et al. (2008). In some cases this procedure can produce a noticeable kink in the modulus reduction curve, and additional smoothing is necessary to achieve a satisfactory result. At present, only OpenSees allows the input of the  $G/G_{max}$  curve ordinates so that this formulation could be directly applied.

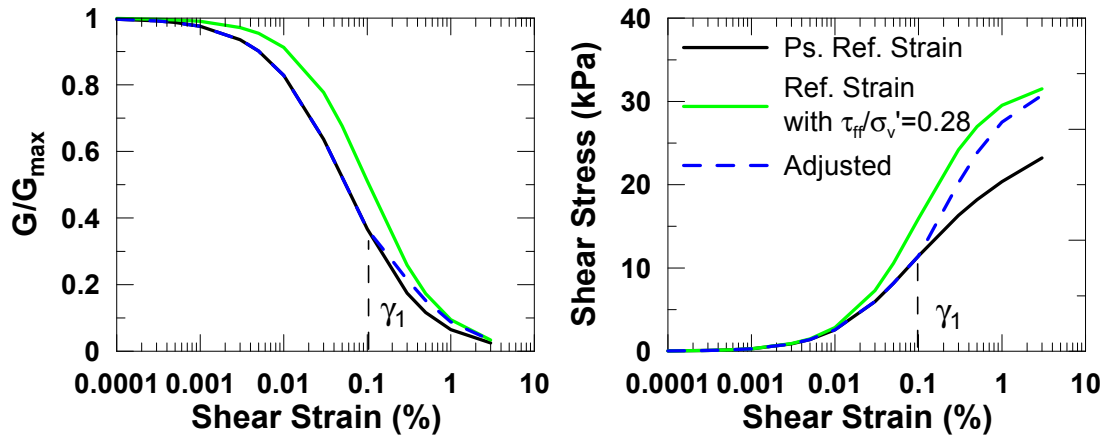


**Fig. 4.4 Modulus reduction and stress-strain curves implied by pseudo-reference strain from Darendeli (2001), reference strain model, and proposed procedure ( $PF=20$ ,  $OCR=1$ ,  $\sigma_v \approx 100$  kPa,  $V_s=135$  m/s).**

**Element (2)—Approximation of Target Curves:** As noted above, an exact match of target curves is not possible when Masing rules or extended Masing rules are used to describe the unload-reload relationship. Until nonlinear codes implement the capability to simultaneously match both modulus reduction and damping curves, mismatch of one or both of these curves is unavoidable. As mentioned previously, one approach is to match the target modulus reduction curve as accurately as possible and accept the misfit of damping. Another is to optimize the fit of both simultaneously.

We have worked with Hashash and Phillips (pers. comm. 2006) to devise a scheme to search for model parameters to achieve the aforementioned fitting approaches (in addition, the scheme allows optimization of the fitting of the damping curve only, although this approach is usually not considered). The scheme requires the specification of target material curves at (user-) predetermined strain levels. The fitting error is considered up to a maximum strain level (usually between 0.1 and 1%). The best combination of model parameters would be the one that gives the least error between the target curves and model curves. This error is quantified as:

$$\varepsilon = \sqrt{(w_{G/G_{\max}} \times \bar{\varepsilon}_{G/G_{\max}})^2 + (w_{\beta} \times \bar{\varepsilon}_{\beta})^2} \quad (4.3)$$

where  $\bar{\varepsilon}_{G/G_{\max}}$  and  $\bar{\varepsilon}_{\beta}$  represent the mean error for the fitting of modulus reduction and damping curves, respectively. Error term  $\bar{\varepsilon}_{G/G_{\max}}$  is calculated as:

$$\bar{\varepsilon}_{G/G_{\max}} = \frac{\sqrt{\sum (\varepsilon_{G/G_{\max}}(\gamma_i))^2}}{N} \quad (4.4)$$

The numerator in Equation 4.4 is the summation of fitting error from the lowest specified strain level to the maximum strain level.  $N$  is the number of strain levels included in the summation. Error term  $\bar{\varepsilon}_{\beta}$  is calculated in a similar way as for  $\bar{\varepsilon}_{G/G_{\max}}$ . Terms  $w_{G/G_{\max}}$  and  $w_{\beta}$  in Equation 4.3 are weight factors whose values depend on the choice of fitting approach. Table 4.1 summarizes the values of weight factors under different fitting approaches. Figure 4.5 shows differences in the fitted modulus reduction and damping curves (relative to target data) when different fitting approaches are employed.

**Table 4.1 Weight criterion for different fitting approaches.**

Fitting Approach	Weight Criterion
MR	$w_{G/G_{\max}} = 1; w_{\beta} = 0$
MRD	$(w_{G/G_{\max}})^2 + (w_{\beta})^2 = 1$ $\frac{w_{G/G_{\max}}}{w_{\beta}} = \begin{cases} 1, & \beta_{\max} > 25\% \\ 1 + \frac{0.25 - \beta_{\max}}{0.15}, & 10\% < \beta_{\max} < 25\% \\ 2, & \beta_{\max} < 10\% \end{cases}$
D	$w_{G/G_{\max}} = 0; w_{\beta} = 1$

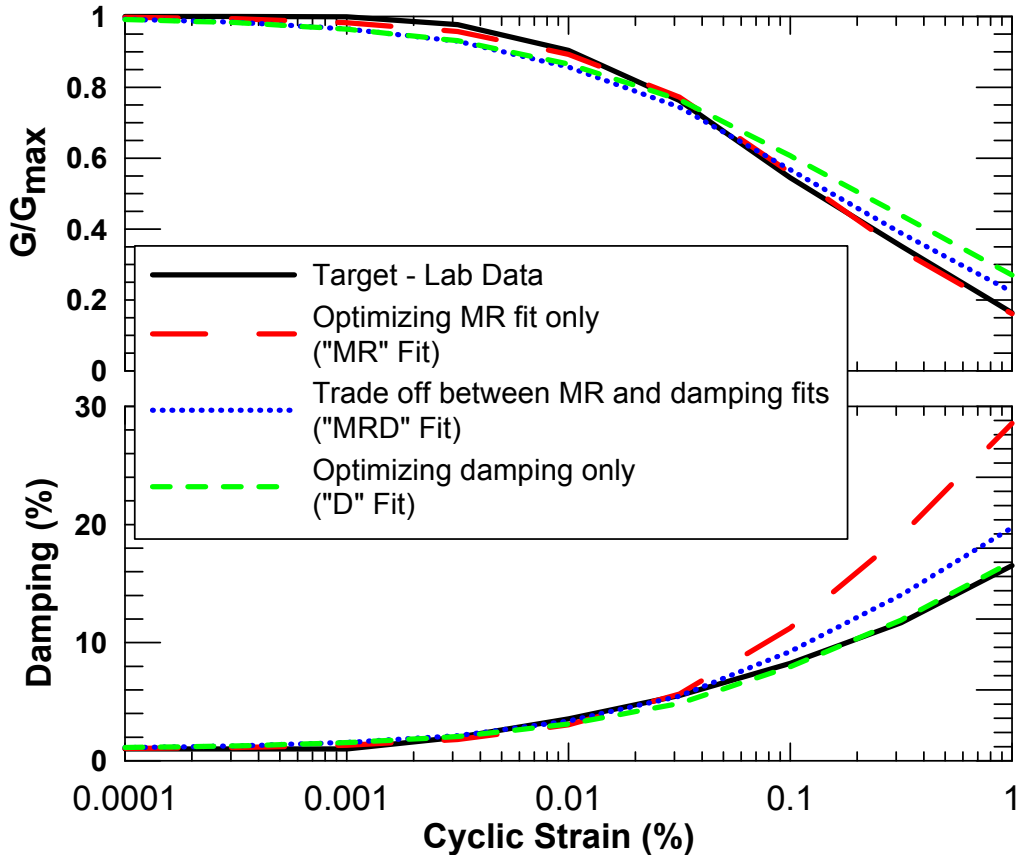


**Fig. 4.5 Different approaches in fitting modulus reduction and damping curves in nonlinear analysis.**

**Effect of Parameter Selection Procedures on Computed Response (Overview):** To illustrate the sensitivity of the computed site response to details of the parameter selection protocols, we describe below the results of two suites of analysis. The first suite concerns the implications of selecting alternative target nonlinear curves — the principle issue being the use of curves constrained by shear strength (i.e., true reference strain) or not. The second suite concerns the implications of alternative fitting procedures for a given set of target nonlinear curves.

**Effect of Parameter Selection Procedures on Computed Response—(1) Alternative Target Nonlinear Curves:** As described above, it is possible to select parameters describing the backbone curve so that misfit is minimized between the modulus reduction and damping behavior represented by the soil model and target curves from laboratory testing. However, as shown in Figure 4.2, there is a potential for significant underestimation of shear strength with such approaches. Accordingly, utilization of the shear strength in the parameterization of the backbone curves (e.g., by using the true reference strain) is often preferred for depth intervals

where very large strains are expected. In this section, we investigate the effect of backbone curve characteristics at large strain on-site response. We specifically seek to answer two questions: (1) What is the effect of underestimating shear strength through the use of pseudo-reference strain? and (2) What is the effect on-site response of using the true reference strain, which accurately captures large-strain behavior but produces a misfit in modulus reduction and damping curves at small strains?

We seek to answer the above questions using nonlinear ground response analyses for the Apeel 2 site, located in Redwood City, California, and has a soft clay layer near the ground surface (Bay Mud). Large-strain response during strong shaking is expected in the Bay Mud layer (3.4–8.8 m depth). Shear strengths for this layer are estimated using the SHANSEP method (Ladd 1991). Bay Mud is assumed to be normally consolidated with a dynamic shear strength ratio of  $s_u/\sigma'_c = 0.32$ . As shown in Figures 4.6–4.7 (black curves), modulus reduction/damping, and backbone curves for different depths within the Bay Mud are obtained using reference strains calculated from  $s_u$  and  $\beta=a=1.0$  (to enforce a limiting shear stress =  $s_u$ ).

The results obtained using the above curves are compared to additional results obtained by matching small-strain behavior. Pseudo-reference strain is estimated using two methods: (1) based on recommendations by Darendeli's (2001) for  $PI = 50$ ,  $OCR=1.0$ ,  $\sigma' = 52\text{--}85$  kPa for modulus reduction, and allowing overestimation of damping (MR fitting) and (2) based on MRD fitting (described in Section 4.2) in which  $\gamma_r$  and the fitting parameters are optimized to simultaneously fit Darendeli's modulus reduction and damping curves. Additional analyses are performed using the hybrid approach illustrated in Figure 4.4 in which small-strain behavior is matched to Darendeli (2001) and large-strain behavior is controlled by the shear strength. The modulus reduction/damping and backbone curves obtained using these approaches are shown in Figures 4.6 and 4.7, respectively. Figure 4.6 shows that the modulus reduction and damping curves calculated from  $\gamma_r$  based on Darendeli's method demonstrate more nonlinearity than those based on  $\gamma_{ref}$ . In addition, Figure 4.7 shows that the shear strength is underestimated by the use of pseudo-reference strain, which is consistent with the results in Figure 4.2. With respect to MRD fitting (using Darendeli's curves as the target), the nonlinearity is reduced (Fig. 4.6) but the peak shear stress is increased to a level that happens to roughly match the shear strength (Fig. 4.7). This is accidental and will not generally be the case. In general, misfit of shear strength will

occur at large strains and therefore the MRD-fitting procedures, as currently formulated, should be used only for relatively small strains (less than 1%).

Nonlinear ground response analyses are performed with the above four sets of backbone curves (shear-strength based; Darendeli with MR fitting; Darendeli with MRD fitting; hybrid). The input motion is the same broadband synthetic considered previously with scaling to  $PHA' = 0.05, 0.17 \text{ g}, 0.68 \text{ g},$  and  $1.0 \text{ g}$ . Maximum strain and PGA profiles are plotted in Figures 4.8–4.11 and response spectra are compared in Figure 4.12.

We draw two principal conclusions from these results. The first has to do with underestimating shear strength by using pseudo-reference strain with MR fitting. To investigate this effect, we focus on results involving large-strain response which, as indicated in Figures 4.8–4.11, occurs for input  $PHA'$  levels of  $0.17 \text{ g}$  and above. For these high levels of shaking the results using the hybrid approach are considered to be mostly nearly “correct” because they accurately capture both small and large-strain behavior. As shown in Figure 4.12, the underestimation of shear strength can significantly limit the ground surface accelerations, as reflected by low spectral acceleration for periods less than about 2–5 sec (depending on the level of shaking). We note that the MRD method also provides good results in this case because of the (accidental) match of large-strain behavior. As noted previously, this will generally not be the case.

The second conclusion that can be drawn from these results concerns the effect of misfit of modulus reduction and damping curves at small and mid-level strains (< about 0.5%) by using the true reference strain in defining the backbone curve. As before, results from the hybrid approach (and to a lesser extent, the MRD approach) are taken as most nearly “correct” because they provide the best fit to the modulus reduction and damping curves over a wide range of strains. We note that the reference-strain-based approach overestimates the response, which we interpret to result from the underestimation of damping. This is one potential drawback to the use of true reference strain —relatively small-strain response could be biased, and this bias will tend to be toward overprediction of response because damping will be lower than target levels (this occurs because the  $G/G_{max}$  curve is more linear).

The general recommendation is to use shear strength data in the development of backbone curves when large-strain response is anticipated. This can be done in two ways. The first is to use Equation 4.1 with the true reference strain ( $s_u/G_{max}$  using measured shear strengths)

and with  $\beta$  and  $a$  set to 1. The second approach for capturing large-strain response, which is generally preferred, is the hybrid procedure represented in Equation 4.2 and illustrated in Figure 4.4. If the response involves small strains only, the pseudo-reference strain can be used to develop the target modulus reduction curve (using Eq. 4.1) per empirical recommendations such as those presented by Darendeli (2001). When developing the curves used for analysis, efforts should be made to simultaneously fit modulus reduction and damping curves (MRD fitting). When strength data are not available, MRD-fitting can be performed on empirical target nonlinear curves, but the results should be trusted only when shear failure is not expected (small strains).

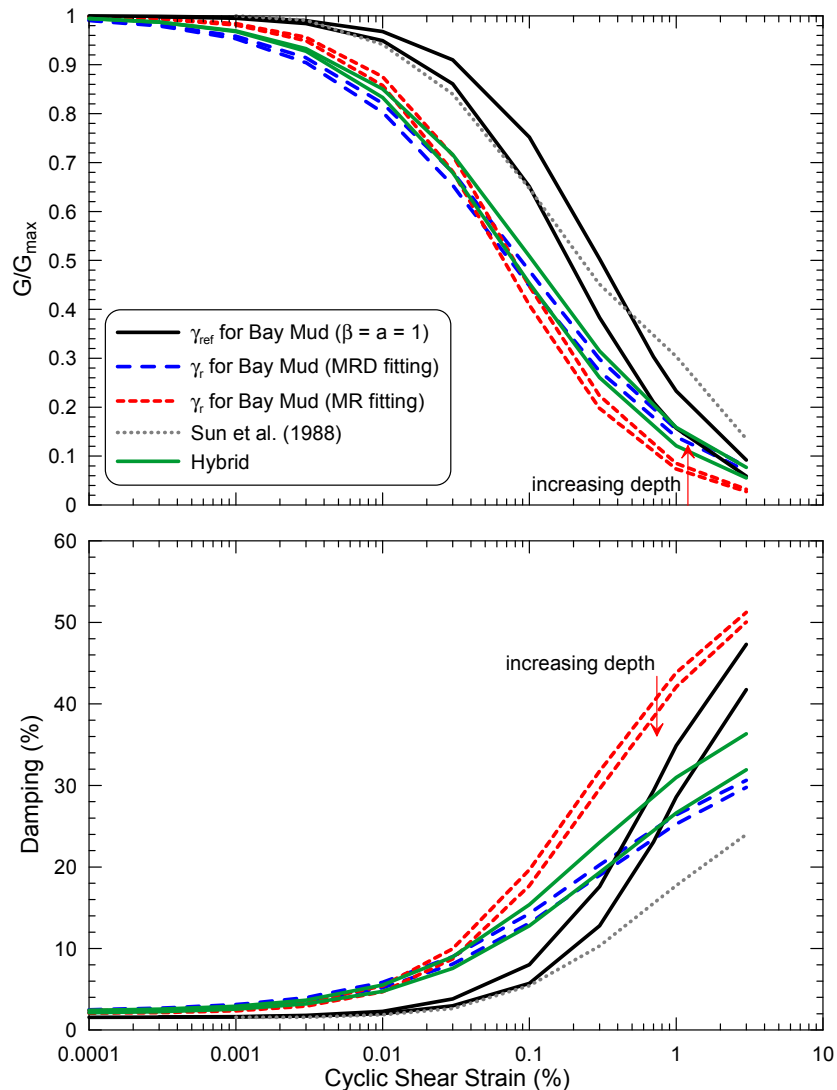


**Fig. 4.6 Comparison of Bay Mud curves as determined from laboratory testing and hyperbolic stress-strain models.**

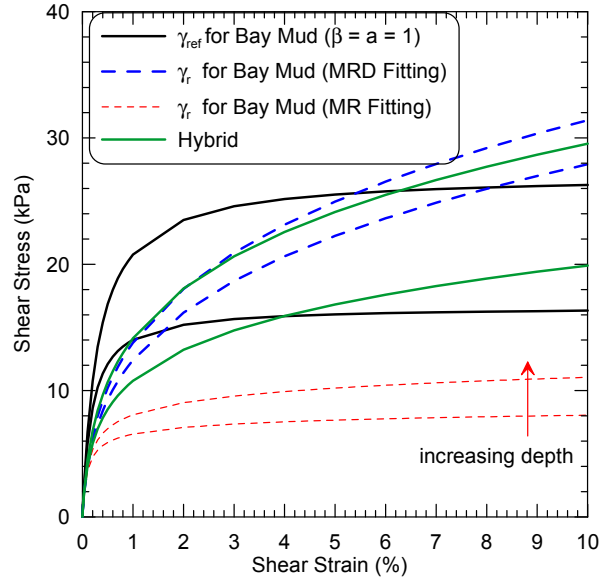


**Fig. 4.7 Stress-strain curve as implied by different reference and pseudo-reference strain values.**

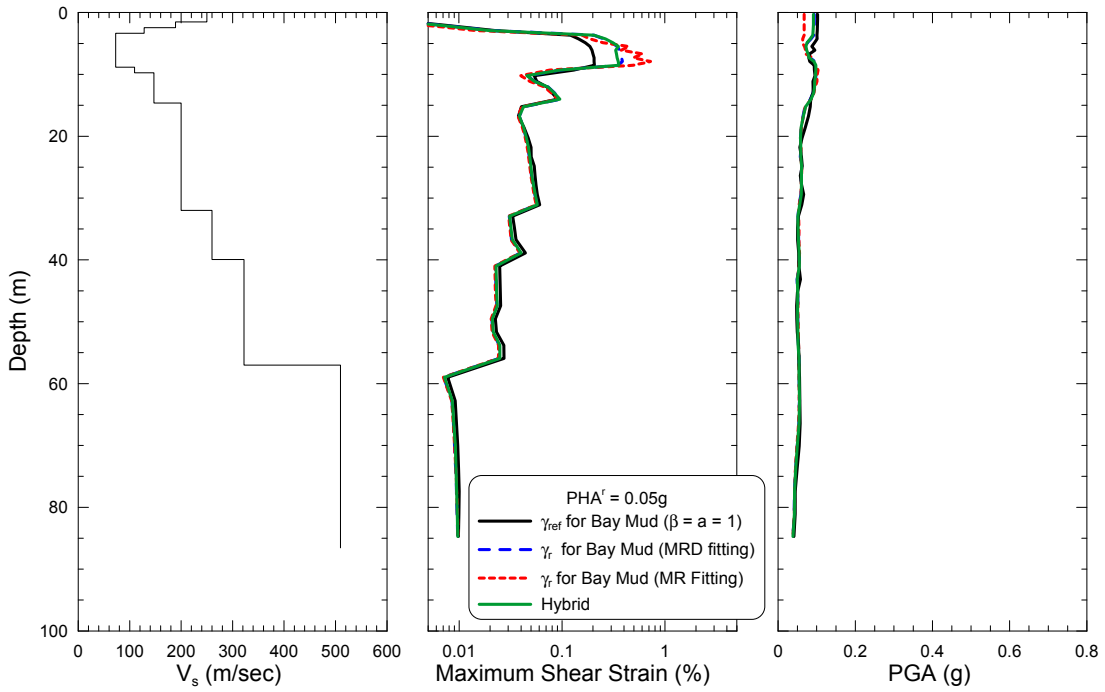


**Fig. 4.8 Maximum strain and PGA profiles for  $PHA^r=0.05$  g from nonlinear analyses.**

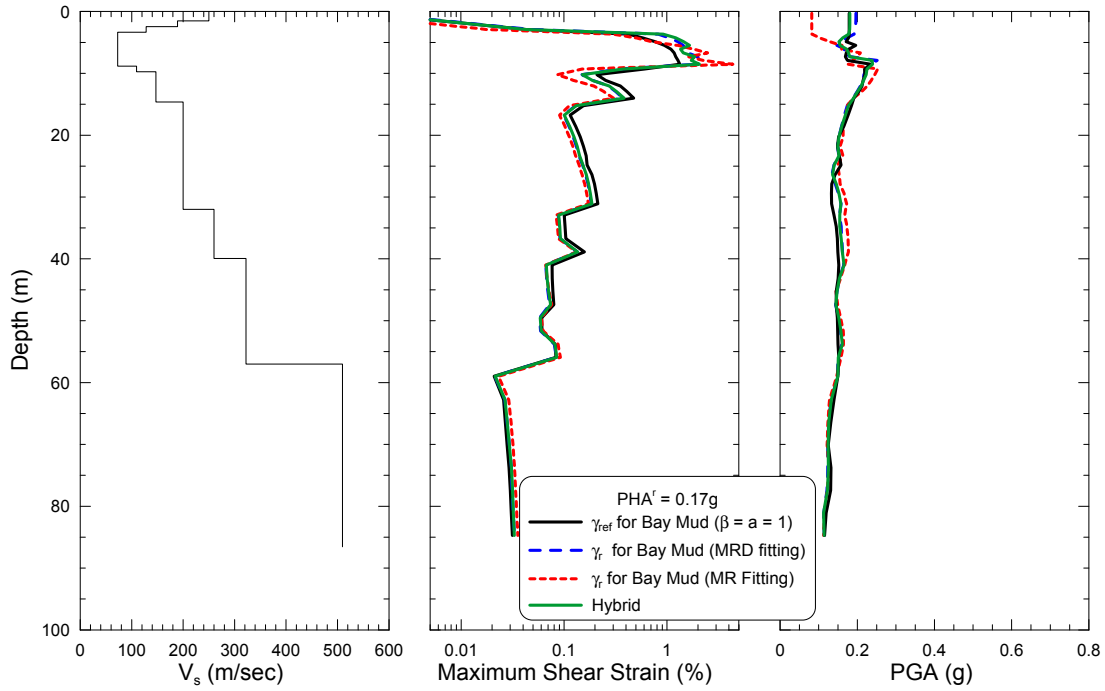


**Fig. 4.9** Maximum strain and PGA profiles for  $PHA^r=0.17\text{ g}$  from nonlinear analyses.

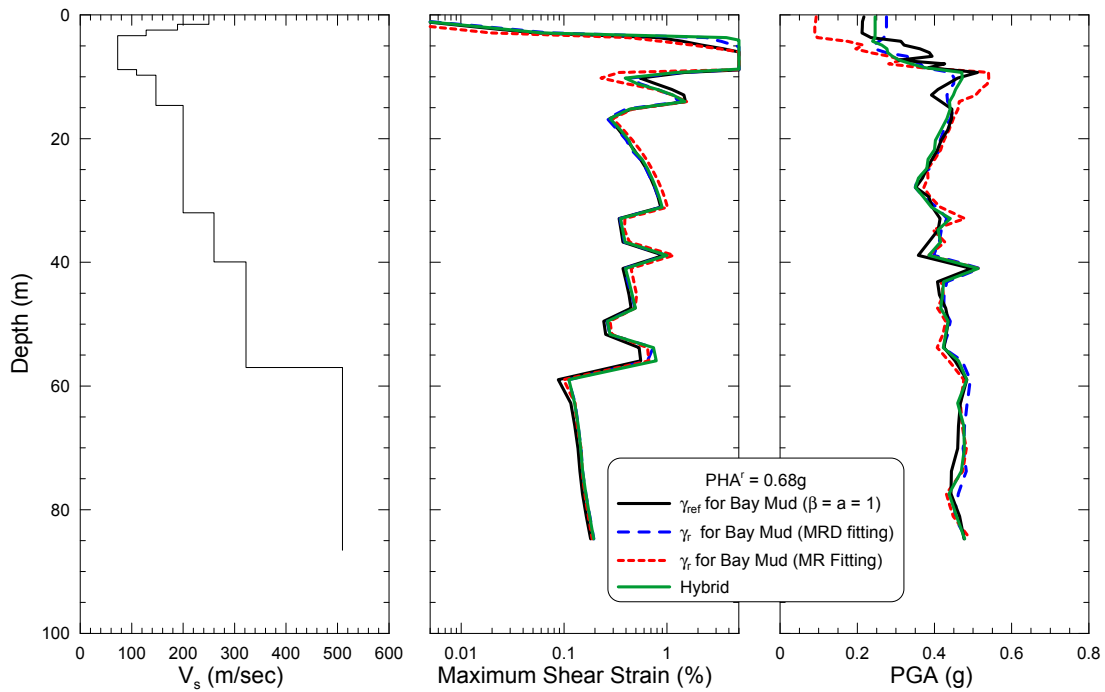


**Fig. 4.10** Maximum strain and PGA profiles for  $PHA^r=0.68\text{ g}$  from nonlinear analyses.

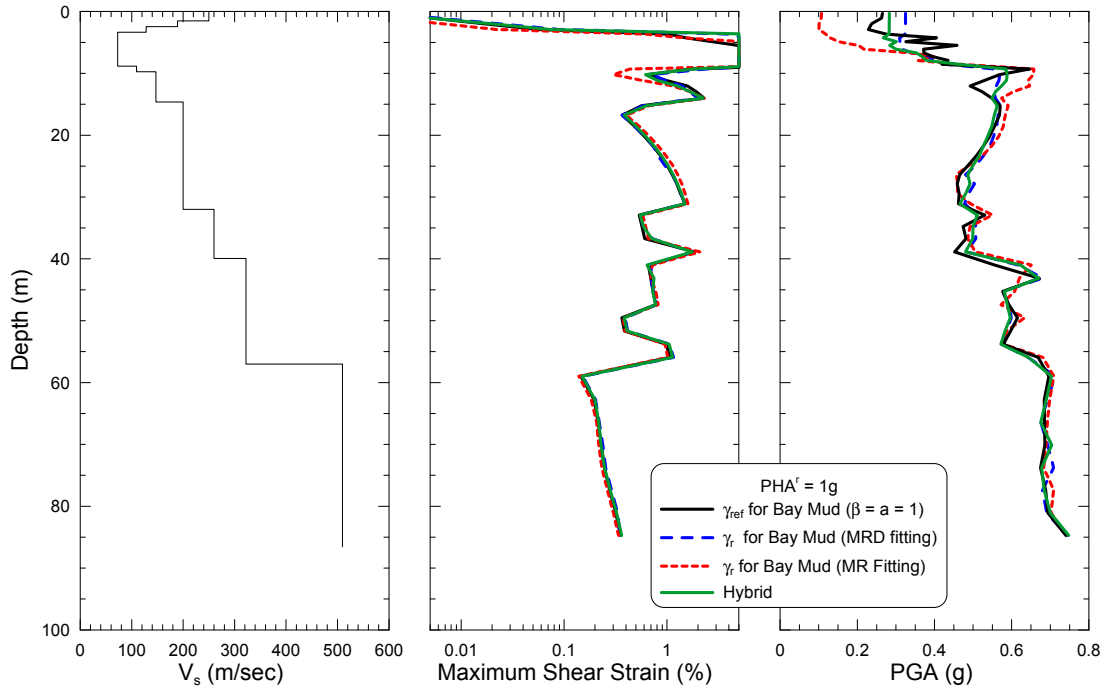


**Fig. 4.11** Maximum strain and PGA profiles for  $PHA^r=1$  g from nonlinear analyses.

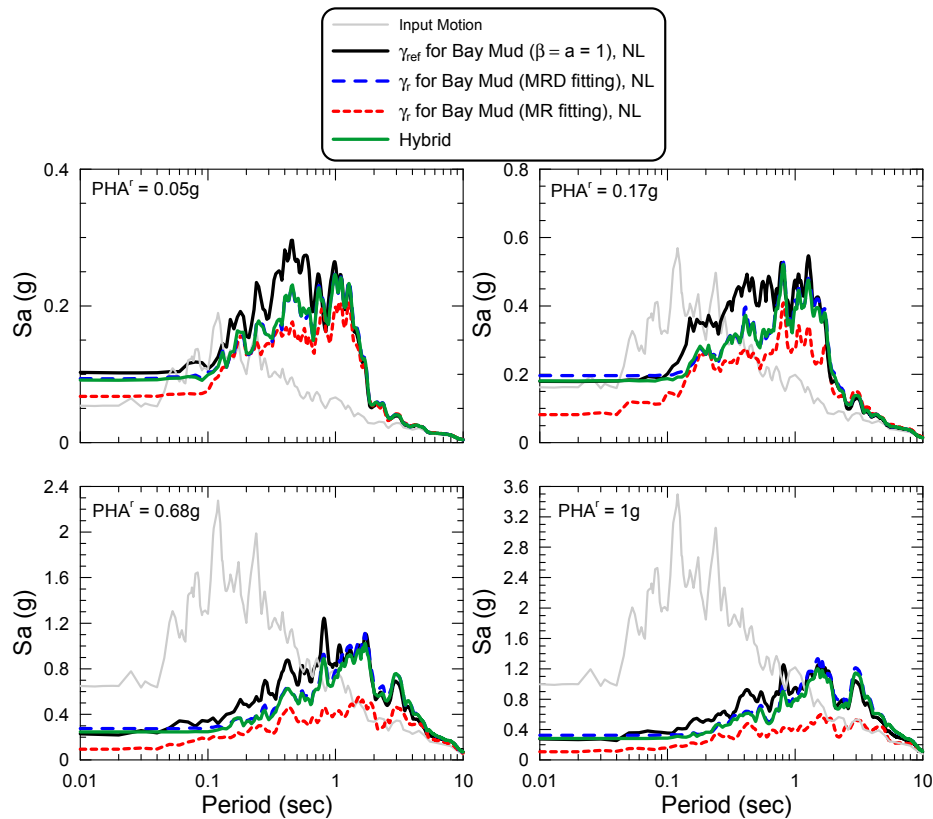


**Fig. 4.12** Comparison of response spectra calculated from engineering models with different reference strain estimates of Bay Mud, shown for different  $PHA^r$ .

**Effect of Parameter Selection Procedures on Computed Response—(2) Alternative Fitting of Target Curves:** To illustrate how different fitting approaches may influence ground motion predictions, nonlinear ground response analyses are performed for two strong motion accelerograph sites with different fitting of target curves. The two sites are the soft clay Apeel 2 site described above and Sepulveda VA hospital in Los Angeles, which is a relatively stiff soil site. The calculations were performed using the DEEPSOIL code. The target nonlinear modulus reduction and damping curves were taken as the Seed and Idriss (1970) upper bound for modulus reduction and lower bound for damping in shallow sand layers, the EPRI (1993) deep curves (251–500 ft) for deep sand (> 60 m), the Sun et al. (1988) for Bay Mud at Apeel 2, and the Vucetic and Dobry (1991) for other clayey soils. Scaled versions of an outcropping broadband synthetic motion (Silva, pers. comm. 2004) are used as input. Figures 4.13 shows predicted ground surface motions for Apeel 2 and Sepulveda, respectively. It is observed that when the input motion is relatively low-amplitude (about 0.2 g), predictions for all three fitting approaches are very similar. When the shaking level is relatively strong (about 0.7 g), the predictions for the “MR” fitting approach are smaller than those from the other approaches, which is due to the larger high-strain damping ratio associated with the “MR” fitting approach. Another observation is that the soft site is more sensitive to the different fitting approaches than the stiff site. This occurs because the softer site has larger strains for a given input motion amplitude.

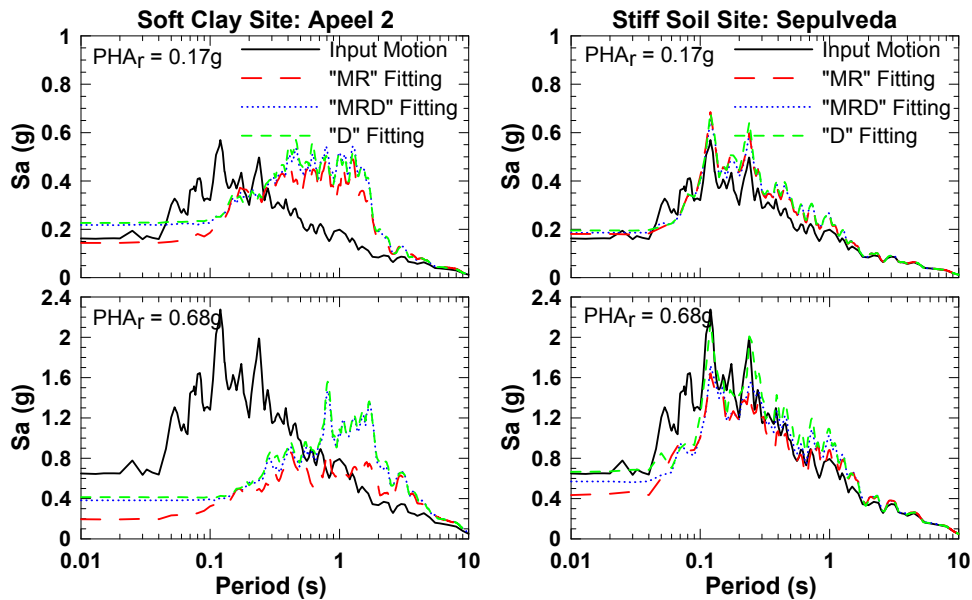


**Fig. 4.13 Prediction results for soft clay site (Apeel 2) and stiff soil site (Sepulveda) with model curves obtained from different approaches to fitting modulus reduction and damping curves in nonlinear analysis.**

## 4.2 LIMITATION IN LAYER THICKNESS

The maximum frequency of a layer is the highest frequency that the layer can propagate and is calculated as  $V_s/4H$  ( $V_s$  and  $H$  are the shear wave velocity and thickness of the layer, respectively) which corresponds to the fundamental frequency of the soil layer. If a layer is too thick the maximum frequency that a layer can propagate would be small. Figure 4.14 compares the predicted response spectra using different numbers of layers in modeling the Gilroy 2 with a broadband synthetic motion provided by Silva (pers. comm. 2004). It can be seen that using fewer layers (hence thicker layers) would result in lower pseudo spectral accelerations especially at small periods as the high-frequency waves are filtered out. This issue is often not addressed in the user's manuals of nonlinear ground response analysis codes. Therefore, it is necessary to improve the manuals by reminding users of the importance of checking the maximum frequency of each layer. The most commonly used maximum frequency is 25 Hz.

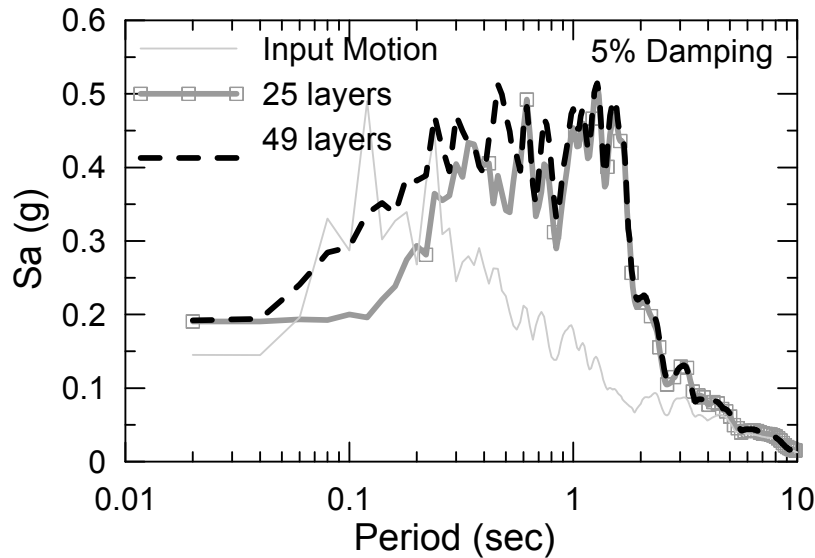


**Fig. 4.14 Predicted response spectra computed using different numbers of layer.**

## 4.3 SPECIFICATION OF INPUT MOTION

Input motions are specified at the bottom of the 1D site profile in nonlinear analyses. There has been confusion regarding whether the motions specified at the base of the profile should represent an outcropping condition (i.e., equivalent free-surface motions that are twice the amplitude of the incident wave due to full reflection) or a within condition (i.e., the sum of the

incident waves and downward propagating waves reflected from overlying layer interfaces). A closely related question is whether the base condition (representing the material below the site column) should be elastic or rigid. This issue is addressed by using exact solutions of wave propagation problems for elastic conditions in Chapter 5.

#### **4.4 SPECIFICATION OF VISCOUS DAMPING**

As discussed in Chapter 3, most nonlinear codes use some form of viscous damping to provide for damping in the analysis at very small strains where the hysteretic damping from the nonlinear soil models is nearly zero (an exception is TESS, which does not require viscous damping and has a low strain damping scheme). Few protocols are available for guiding the selection of an appropriate viscous damping scheme. In Chapter 5, guidelines on this issue are developed by using exact solutions of wave propagation problems for elastic conditions.

# 5 Verification of Nonlinear Codes against Exact Solutions

## 5.1 INTRODUCTION

In this chapter, two key issues related to the practical application of nonlinear ground response analysis codes are resolved by comparing the results of such analyses (under linear condition) to known theoretical solutions. These two issues are the specification of input motions as “outcropping” (i.e., equivalent free-surface motions) versus “within” (i.e., motion occurring at a depth within a site profile), and the specification of the damping that occurs within a soil element at small strains, which is either accomplished using viscous damping or unload-reload rules that produce non-zero small-strain hysteretic damping. The five nonlinear seismic ground response analysis codes discussed in Chapter 2 (D-MOD\_2, DEEPSOIL, TESS, OpenSees, and SUMDES) are considered in the analyses.

The chapter begins with a brief review of the solution characteristics in the frequency-domain and time-domain ground response analysis procedures. This is followed by sections describing verification studies addressing the issues of input motion specification and modeling of small-strain damping. The content of this chapter also appears in a journal paper by Kwok *et al.* (2007).

## 5.2 ONE-DIMENSIONAL GROUND RESPONSE ANALYSIS PROCEDURES

In 1D seismic ground response analyses, soil deposits are assumed to be horizontally layered over a uniform halfspace. The incident wave is assumed to consist of vertically propagating shear waves. The response of a soil deposit to the incident motion can be modeled in the frequency or time domains, as described below.

### 5.2.1 Frequency-Domain Analysis

Frequency-domain analyses are based on a closed-form solution of the wave equation for shear wave propagation through a layered continuous medium, with each layer  $i$  having a specified density  $\rho_i$ , shear modulus  $G_i$ , and hysteretic damping  $\beta_i$ . The solution was presented by Roesset and Whitman (1969), Lysmer *et al.* (1971), Schnabel *et al.* (1972), and is also described in detail by Kramer (1996). In these frequency-domain methods, a control motion of frequency  $\omega$  is specified at any layer  $j$  in the system. An exact solution of the system response can be expressed as a transfer function relating the sinusoidal displacement amplitude in any arbitrary layer  $i$  to the amplitude in layer  $j$ ,

$$F_{ij} = \frac{a_i(\omega) + b_i(\omega)}{a_j(\omega) + b_j(\omega)} \quad (5.1)$$

where  $F_{ij}$  = amplitude of transfer function between layers  $i$  and  $j$ ,  $a_i$  and  $a_j$  = normalized amplitudes of upward propagating waves in layers  $i$  and  $j$ , and  $b_i$  and  $b_j$  = normalized amplitudes of downward propagating waves in layers  $i$  and  $j$ . The normalization of the wave amplitudes is generally taken relative to the amplitude in layer 1, for which  $a_1 = b_1$  due to perfect wave reflection at the free surface. The normalized amplitudes  $a_i$ ,  $a_j$ ,  $b_i$ , and  $b_j$  can be computed from a closed-form solution of the wave equation, and depend only on profile characteristics (i.e., material properties  $\rho$ ,  $G$ , and  $\beta$  for each layer and individual layer thicknesses).

The frequency-domain solution operates by modifying, relative to the control motion, the wave amplitudes in any layer  $i$  for which results are required. These analyses are repeated across all the discrete frequencies for which a broadband control motion is sampled, using the fast Fourier transform. Once amplitudes  $a_i$  and  $b_i$  have been computed for a given layer at all these frequencies, time-domain displacement histories of layer  $i$  can be calculated by an inverse Fourier transformation.

Control motions for use in frequency-domain analyses are most often recorded at the ground surface and are referred to as “outcropping.” As perfect wave reflection occurs at the ground surface, incident and reflected wave amplitudes are identical, and hence outcropping motions have double the amplitude of incident waves alone. Consider the example in Figure 5.1. Rock layer  $n$  occurs at the base of a soil column in Case 1 and as outcropping rock in Case 2. In the outcropping rock case, incident and reflected waves are equivalent ( $a_n^* = b_n^*$ ). The incident waves are identical in both cases ( $a_n^* = a_n$ ), assuming equal rock moduli, but the reflected waves

differ ( $b_n^* \neq b_n$ ) because some of the incident wave transmits into the soil (nonperfect reflection) for Case 1, whereas perfect reflection occurs in Case 2. The motion at the base of the soil column in Case 1 (referred to as a “within” motion) can be evaluated from the outcropping motion using the transfer function:

$$F_{mn^*} = \frac{u_n}{u_n^*} = \frac{a_n(\omega) + b_n(\omega)}{2a_n(\omega)} \quad (5.2)$$

As with any other transfer function,  $F_{mn^*}$  can be readily computed for any frequency  $\omega$  and depends only on profile characteristics. Accordingly, through the use of Equation 5.2, the within motion can be calculated for a given outcropping motion. The base-of-profile (within) motion can in turn be used to calculate motions at any other layer per Equation 5.1.

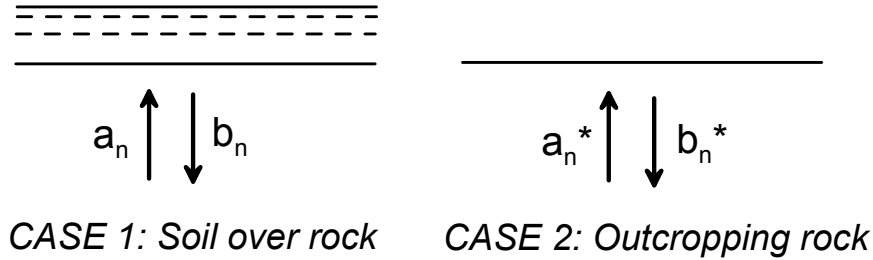


**Fig. 5.1 Incident and reflected waves in base rock layer for case of soil overlying rock and outcropping rock (amplitudes shown are relative to unit amplitude in Case 1 surface layer).**

The application of Equation 5.2 results in a within motion that is reduced from an outcropping motion at the site (modal) frequencies. Consider, for example, a single soil layer with thickness = 30 m,  $V_s = 300$  m/s [giving a fundamental mode site frequency of  $f_s = (300 \text{ m/s}) / (4 \times 30 \text{ m}) = 2.5$  Hz] overlying a halfspace with shear wave velocity  $V_{s-H}$ . The results of the within/outcropping calculation (i.e., Eq. 5.2) are shown in Figure 5.2a for various values of equivalent viscous damping ratio (equal damping values are applied in both the soil layer and halfspace) with  $V_{s-H} = 2V_s$  and in Figure 5.2b for zero damping and various levels of velocity contrast ( $V_s/V_{s-H}$ ). As shown in Figure 5.2 (a and b), the transfer function amplitude (within/outcropping) drops below unity near the site frequencies, with the amplitudes at site frequencies decreasing only with decreasing amounts of equivalent viscous damping. At frequencies between the site frequencies, amplitudes decrease both with increasing damping and with decreasing velocity contrast.

At zero damping the transfer function amplitude goes to zero at site frequencies. To understand this phenomenon, consider that (1) control motion and response are in phase in this case because of the lack of damping and (2) the site frequencies correspond to  $2n+1$  quarter wave lengths, where  $n = 0, 1, 2$ , etc. (zero and positive integers). As shown in Figure 5.2c, at a depth below the surface of  $2n+1$  quarter-wave lengths, the wave amplitude is zero (i.e., there is a “node” in the response at that depth), which in turn must produce a zero transfer function amplitude (Fig. 5.2c shows mode shapes for the 1<sup>st</sup> and 3<sup>rd</sup> modes, i.e.,  $n=0$  and 1). Additionally, as shown in Figure 5.2c (lower right frame), as damping increases, the input and response are increasingly out of phase, and there are no true nodes in the site response.

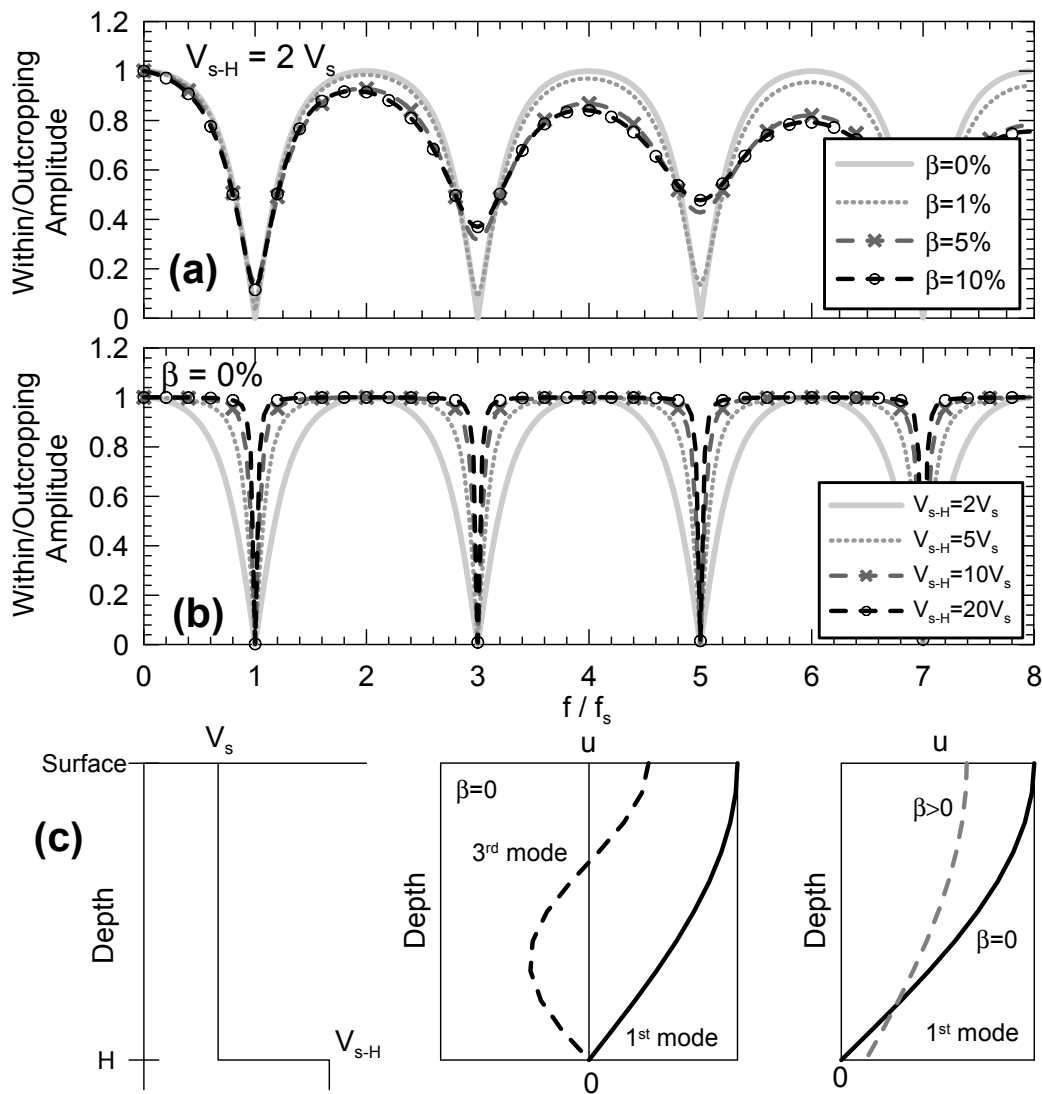


**Fig. 5.2** Ratio of within to outcropping amplitudes for (a) various equivalent viscous damping ratios; (b) various base layer velocities ( $V_{s-H}$ ); and (c) mode shapes for various conditions.

The trends shown in Figures 5.2 (a and b) at frequencies between the site frequencies can be explained as follows: (1) the decrease of within motion amplitude with increasing damping results from a reduction of reflected energy from the ground surface as damping increases, thus reducing the amplitude of within motions (that are the sum of incident and reflected waves); (2) the decrease of within motion amplitude with decreasing  $V_{s-H}$  results from increased transmission of reflected (downward propagating) waves from the surface into the halfspace (i.e., less reflection), which causes energy loss from the system.

### 5.2.2 Time-Domain Analysis

As mentioned in Section 2.2, the layered soil column in the time-domain analysis is idealized either as a multiple-degree-of-freedom lumped-mass system (Fig. 2.3a) or a continuum discretized into finite elements with distributed mass (Fig. 2.3b). Table 5.1 summarizes the manner in which mass is distributed and nonlinear behavior is simulated for the five nonlinear codes considered here. The system of coupled equations is discretized temporally and solved by a time-stepping scheme to obtain the response at each time step. Unlike in frequency-domain analysis where the control motion could be specified anywhere within the soil column, in time-domain analysis the control motion must be specified at the bottom of the system of lumped masses or finite elements.

**Table 5.1 Mass representation and constitutive models used in nonlinear codes.**

<b>Nonlinear Code</b>	<b>Mass Representation</b>	<b>Constitutive Model</b>
D-MOD_2	Lumped Mass	MKZ (Matasovic and Vucetic 1993)
DEEPSOIL	Lumped Mass	Extended MKZ (Hashash and Park 2001)
OpenSees	Distributed Mass	Multi-yield surface plasticity (Ragheb 1994; Parra 1996; Yang 2000)
SUMDES	Distributed Mass	Bounding surface plasticity (Wang 1990) and other models
TESS	Distributed Mass	HDCP (EPRI 1993)

### 5.3 SPECIFICATION OF INPUT MOTION

There has been confusion regarding the nature of the input motion that should be specified for time-domain analyses at the base of the profile. Consider the common case where the motion that

is to be applied was recorded at the surface of a rock site (outcrop motion). One school of thought that has been applied in practice for many years is that the outcropping motion should be converted to a within motion using frequency-domain analysis (e.g., Eq. 5.2), and that this within motion should then be specified for use at the base of the site profile for application in time-domain analysis. Most users of this approach were aware that the layer properties used in the outcropping-to-within conversion were a potentially crude approximation to the actual nonlinear soil properties. The approximation was accepted, however, due to the lack of a practical alternative for obtaining within motions. The second school of thought is that the outcropping rock motion should be applied directly at the base of the site profile without modification. Normally, this direct use of the outcropping motion is accompanied by the use of a compliant base in the site profile (the base stiffness being compatible with the character of the underlying rock), which allows some of the energy in the vibrating soil deposit to radiate down into the halfspace (Joyner and Chen 1975). Rigid base options are also available in all time-domain codes but are seldom used because the conditions under which the rigid base should be applied are poorly understood.

To evaluate which of the two above approaches is correct, time-domain analyses with elastic material properties are exercised, for which frequency-domain analyses provide an exact solution. This can be investigated using linear analyses because the underlying issue involves the differences in linear wave propagation modeling with frequency-domain and time-domain analyses. Consider for example a single soil layer with thickness = 30 m and a shear wave velocity  $V_s = 300$  m/s (site frequency = 2.5 Hz) that overlies an elastic halfspace with  $V_{s-H} = 2 V_s = 600$  m/s. Equivalent viscous damping is assumed constant at 5%. A control motion is selected to represent an extreme scenario with respect to the variability between outcropping and within, which is a sine wave at the site frequency. As shown in Figure 5.3c, the particular motion selected has a frequency of 2.5 Hz, 12 cycles of shaking, and cosine tapers at the beginning and end of the signal with a four-cycle taper duration (the tapers have the shape of half a cosine wavelength). The control motion is specified for an outcropping condition. A large suppression of the within motion relative to the outcropping motion would be expected for this signal (e.g., as suggested by Fig. 5.2).

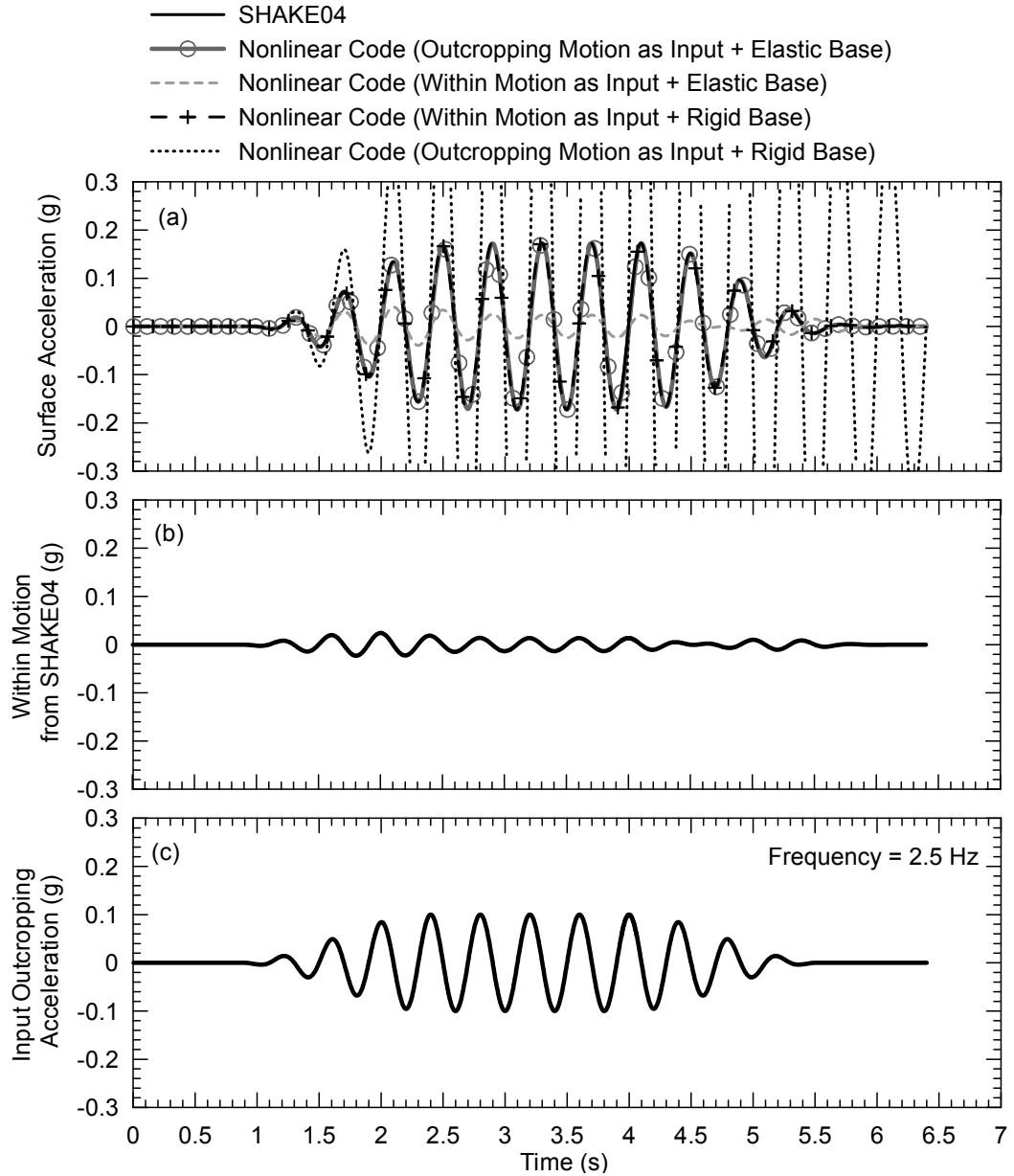


**Fig. 5.3 Acceleration histories for one-layer problem.**

A frequency-domain solution is exact because the material properties are elastic (i.e., strain-invariant). The frequency-domain calculations are performed with the computer program SHAKE04 (Youngs 2004), which is a modified version of the original SHAKE program (Schnabel *et al.* 1972). Both the within motion and the motion at the surface of the soil layer are calculated, with the results shown in Figure 5.3 (a and b) with the solid black lines.

Linear time-domain analyses are performed for this site using the “nonlinear” codes listed

in Table 5.1 (the codes are implemented with linear backbone curves). Four combinations of control motion and base condition are considered:

1. Outcropping motion (Fig. 5.3c) with elastic base ( $V_{s-H} = 600$  m/s).
2. Within motion (which is extracted from frequency-domain analysis, see Fig. 5.3b) with elastic base.
3. Outcropping motion with rigid base ( $V_{s-H} = 30000$  m/s or select the “rigid base” option in nonlinear code, if available).
4. Within motion with rigid base.

The results in Figure 5.3a show that the surface acceleration histories for cases (1) and (4) match the known solution from frequency-domain analysis. Using the within motion with an elastic base (Case 2) underestimates the surface motions, while using the outcropping motion with a rigid base (Case 3) overestimates the surface motions.

Based on the above, our recommendations are as follows: (1) for the common case in which the control motion is recorded as outcropping, the motion should be applied without modification for time-domain analyses with an elastic base and (2) if time-domain analyses are to be used to simulate the response of a vertical array using a control motion recorded at depth within the site, the “within” motion should be used without modification in conjunction with a rigid base.

#### **5.4 MODELING OF DAMPING IN NONLINEAR TIME-DOMAIN ANALYSES**

In nonlinear time-domain response models, there are generally two sources of damping. One source is hysteretic damping (frequency independent) associated with the area bounded by hysteretic stress-strain loops. When Masing (Masing 1926) and extended Masing rules (Pyke 1979; Wang *et al.* 1980; Vucetic 1990) are used to represent the unload-reload behavior of soil, zero damping is encountered at small strains, where the backbone curve is linear. The zero damping condition is incompatible with soil behavior measured in the laboratory at small strains (e.g., Vucetic *et al.* 1998; Darendeli 2001) and can result in overestimation of propagated ground motion. One solution to this problem is to add velocity-proportional viscous damping in the form of dashpots embedded within the material elements depicted in Figure 2.3 (this approach is used by DMOD\_2, DEEPSOIL, OpenSees, and SUMDES). An alternative approach is to introduce a

scheme that produces non-zero hysteretic damping at small strains (e.g., TESS). It should be noted that the nature of soil damping at small strains is neither perfectly hysteretic nor perfectly viscous (Vucetic and Dobry 1986; Lanzo and Vucetic 1999). The incorporation of hysteretic or viscous damping schemes into nonlinear codes is merely a convenient approximation for simulation purposes and is required to ensure numerical stability of lumped-mass solutions.

### 5.4.1 Viscous Damping

There are a number of options for modeling viscous damping, which vary by code (Table 5.2). As illustrated in Figure 5.4, there are three principal issues: (1) the form of the damping formulation (simplified versus full or extended Rayleigh damping; Hashash and Park 2002); (2) the target viscous damping ratio (labeled  $\zeta_{tar}$  in Fig. 5.4) that is matched at specified target frequencies; and (3) the matching frequencies (one, two, and four for the cases of simplified, full, and extended Rayleigh damping, respectively).

**Table 5.2 Available viscous damping formulation for nonlinear codes and summary of analyses discussed in text.**

Nonlinear Code	Rayleigh Damping Option	Rayleigh Damping Option Considered in Current Analyses	Best Match to Frequency-Domain Solution for all Three Sites
D-MOD_2	Simplified & Full	Simplified ( $f_s^a$ ; $f_m^a$ ; $f_p^a$ ) $\zeta_{tar}=0.5\% \text{ \& } 5\%$ Full ( $f_s + 3 \times f_s$ ; $f_s + 5 \times f_s$ ) $\zeta_{tar}=0.5\% \text{ \& } 5\%$	Full ( $5 \times f_s$ ) at $\zeta_{tar}=5\%$
DEEPSOIL	Simplified, Full & Extended	Simplified ( $f_s$ ; $f_m$ ; $f_p$ ) $\zeta_{tar}=0.5\% \text{ \& } 5\%$ Full ( $f_s + 3 \times f_s$ ; $f_s + 5 \times f_s$ ) $\zeta_{tar}=0.5\% \text{ \& } 5\%$	Full ( $5 \times f_s$ ) at $\zeta_{tar}=5\%$
OpenSees	Simplified & Full	Simplified ( $f_s$ ; $f_m$ ; $f_p$ ) $\zeta_{tar}=0.5\% \text{ \& } 5\%$ Full ( $f_s + 3 \times f_s$ ; $f_s + 5 \times f_s$ ) $\zeta_{tar}=0.5\% \text{ \& } 5\%$	Full ( $5 \times f_s$ ) at $\zeta_{tar}=5\%$
SUMDES	Simplified (Assuming damping ratio given at 1 Hz) <sup>b</sup>	Simplified ( $\zeta_{fi} = 5\%/f_s$ ; $5\%/f_p$ ; $1\%/f_p$ ; $1\%$ )	$\zeta_{fi} = 1\%$
TESS	No viscous damping		
<sup>a</sup> $f_s$ , $f_m$ , and $f_p$ represent site frequency, mean frequency, and predominant frequency of motion, respectively. <sup>b</sup> Any damping ratio at a desired frequency (e.g., $f_s$ ) can be converted to damping ratio at 1 Hz using simple proportionality (e.g., $\zeta_{fi} = \zeta_{fs} / f_s$ )			

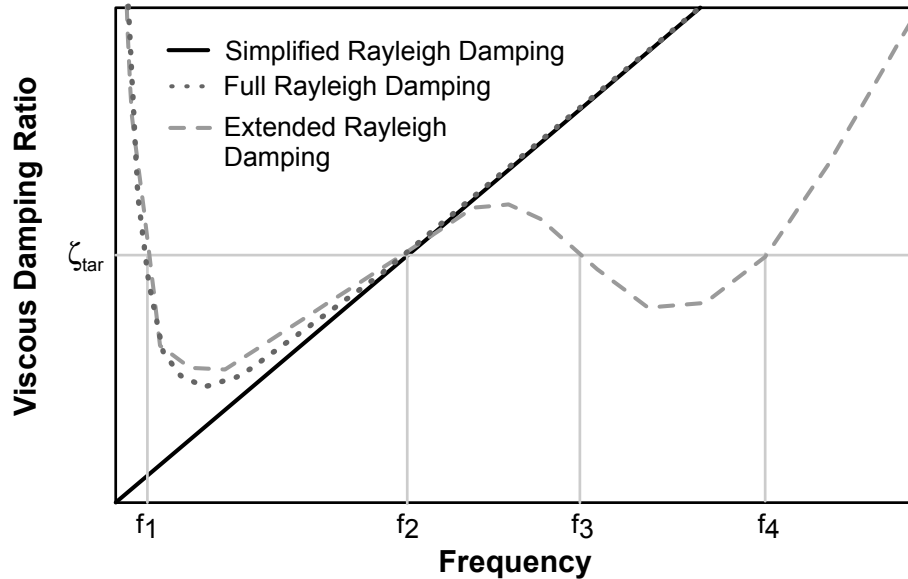


**Fig. 5.4 Schematic illustration of viscous damping models and model parameters (after Park and Hashash 2004).**

Few formal protocols are available to guide users in the selection of the Rayleigh damping model type and parameters described above. With regard to the form of the damping formulation, most practitioners use simplified or full Rayleigh damping. Extended Rayleigh damping is seldom applied in practice. There are two schools of thought on the target damping level ( $\zeta_{tar}$ ), which in practice is either taken as the small-strain damping or as the smallest numerical value that appears to provide a stable solution in the judgment of the analyst (e.g., the SUMDES manual suggests 0.02%–1%). With regard to matching frequencies, the lower target frequency is generally taken as the site fundamental frequency. The larger target frequency is generally taken as an odd-integer multiplier of the fundamental frequency (e.g., 3, 5, 7) (Hudson *et al.* 1994).

An alternative set of guidelines was presented by Park and Hashash (2004), in which the model parameters are selected through an iterative process in which frequency and time-domain elastic solutions are matched within a reasonable degree of tolerance over a frequency range of interest. The procedure is implemented through a user interface in the code DEEPSOIL but is unavailable for other codes.

In the following, we develop recommended procedures for the specification of Rayleigh damping that are intended to resolve some of the ambiguities in current practice with respect to the three aforementioned issues (formulation, target damping, target frequencies). Such

recommendations are intended to meet two practical needs: (1) to form the basis for the specification of Rayleigh damping parameters for most time-domain codes, which lack a user interface to implement an iterative matching procedure such as Park and Hashash (2004) and (2) for codes such as DEEPSOIL with a user interface to provide a reasonable starting point for iterative analyses, which might be needed when dealing with deep soil profiles and very soft soils.

#### 5.4.2 Hysteretic Damping

An alternative to viscous damping is the use of schemes that generate low-strain hysteretic damping (e.g., TESS). Such schemes produce damping that is additive to the hysteretic damping generated by nonlinear behavior at higher strains. Because TESS also employs an alternative hypothesis for controlling unloading and reloading behavior, the large-strain damping that results from this alternate hypothesis is first compared to that generated by the more conventional Masing hypothesis. When Masing rules are utilized, the unload and reload stress-strain curves have the same shape as the backbone curve but are enlarged by a factor of two. This can be represented mathematically as:

$$\frac{\tau - \tau_c}{n} = F_{bb} \left( \frac{\gamma - \gamma_c}{n} \right) \quad (5.3)$$

where  $F_{bb}(\gamma) =$  the backbone function and  $(\gamma_c, \tau_c) =$  the strain/stress coordinates of the last reversal point. Masing rules fix  $n$  at two. A by-product of using Masing rules is that the tangent shear modulus upon load reversal matches the small-strain modulus of the backbone curve ( $G_{max}$ ). Pyke (1979) and Lo Presti *et al.* (2006) have suggested alternative unload-reload rules in which  $n$  in Equation 5.3 can deviate from two. Alternatively, Wang *et al.* (1980) introduced a damping correction factor to Equation 5.3 that allows the damping to be corrected based on the desired damping curve. All of these modifications to Masing rules produce a tangent shear modulus upon unloading (or reloading) that is not equal to  $G_{max}$ .

Among the five nonlinear codes considered in this study, only TESS has implemented non-Masing unload-reload rules. The scheme by Pyke (1979), also known as the Cundall-Pyke hypothesis, is used in which  $n$  is evaluated as follows:

$$n = \left| \pm 1 - \frac{\tau_c}{\tau_y} \right| \quad (5.4)$$

where  $\tau_y$  = the shear strength (always taken as positive). The first term in Equation 5.4 is negative for unloading and positive for reloading. Figures 5.5(a) and 5.5(c) compare the stress-strain loops and damping curves, respectively, generated by the original Masing rules and the Cundall-Pyke hypothesis. Note from Figure 5.5(c) that the small-strain damping produced by the Cundall-Pyke hypothesis is still zero; hence, by itself this formulation does not solve the small-strain damping problem.

TESS also uses a low-strain damping scheme (LSDS) to produce non-zero hysteretic damping at small strains (originally described in EPRI 1993 and recently updated). As shown in Figure 5.5(b), the LSDS increases (in an absolute sense) the shear stress relative to that produced by standard unload-reload rules (e.g., Cundall-Pyke). The stress increase is proportional to the normalized strain rate (i.e., current strain rate divided by the strain rate for the first time step following the last reversal). The constant of proportionality is termed VT. The parameter VT was initially based on the measured rate of strain effects on the shear modulus of young Bay Mud reported by Isenhower and Stokoe (1981), but as a practical matter is now set so that the model produces the desired low strain damping. Note that in Figure 5.5(b)–(c) LSDS produces non-zero low strain damping (due to the fattening of the hysteresis curves).

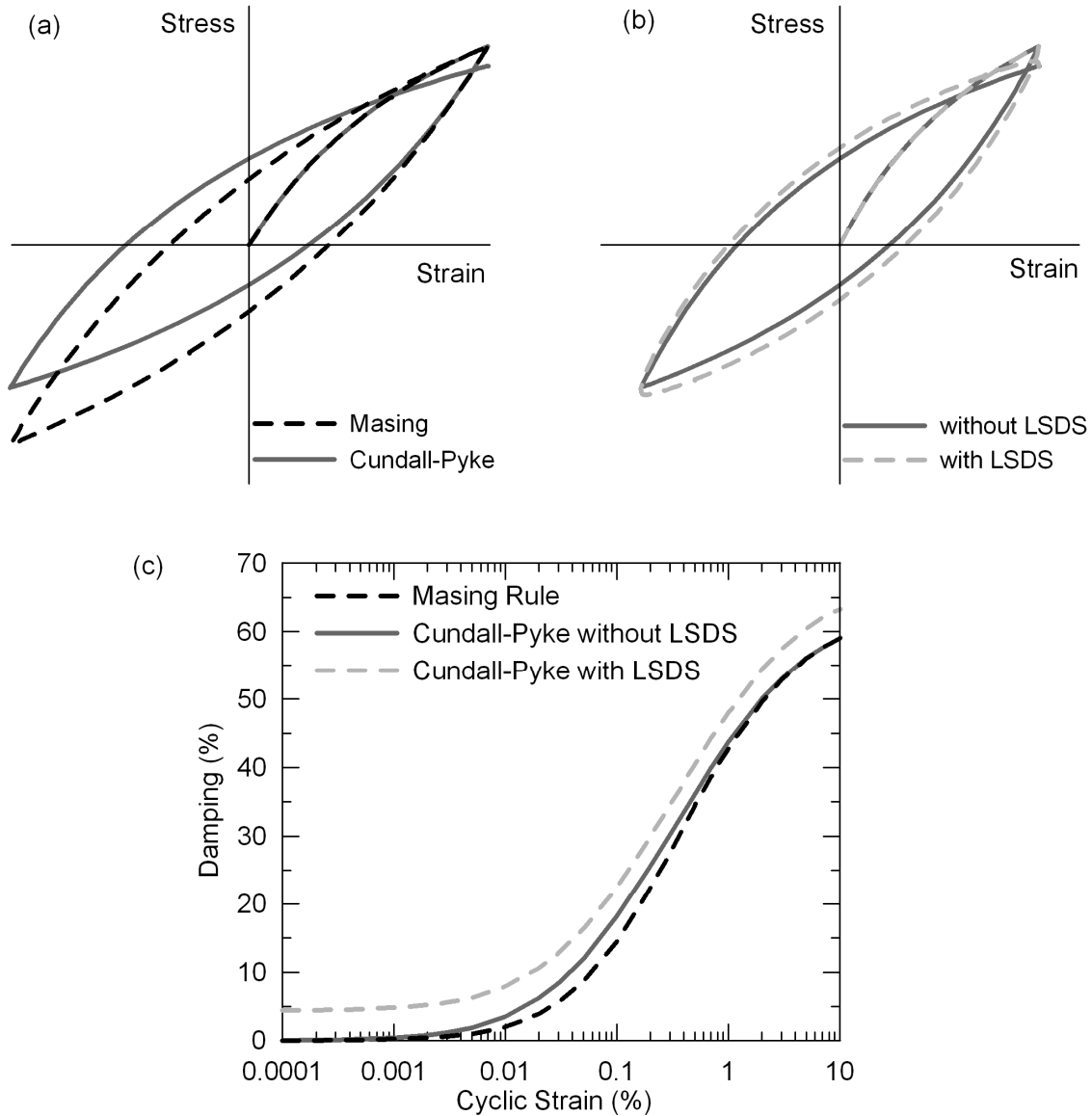


**Fig. 5.5 Comparison of stress-strain loops generated from (a) Masing rules and Cundall-Pyke hypothesis; (b) Cundall-Pyke hypothesis with and without the low-strain damping scheme (LSDS); and (c) comparison of damping curves generated from different schemes.**

## 5.5 VALIDATION AGAINST KNOWN THEORETICAL ELASTIC SOLUTIONS

Validation is performed by comparing results of linear time-domain analyses performed with alternative specifications of damping (viscous or LSDS) to an exact solution from linear frequency-domain analyses. The frequency-domain analyses are exact because of the use of linear soil properties and frequency-independent damping. This issue can be investigated using

linear analyses because the problem is associated with small-strain conditions at which soil behavior is practically linear. The analyses are conducted for three selected sites that represent a broad range of site conditions: shallow stiff soil over rock, soft clay overlying stiffer sediments and rock, and very deep stiff soils typical of the Los Angeles basin (site frequencies range from 0.45–6.4 Hz). The control motion is a broadband synthetic acceleration history calculated for an outcropping rock site condition (motion provided by Dr. Walter Silva, pers. comm. 2004). Similar results were obtained when other control motions were utilized. The equivalent viscous damping ratio used in the frequency-domain analysis is 5% for all layers. For the time-domain codes D-MOD\_2, DEEPSOIL, and OpenSees, target damping ratios of 0.5% and 5% are used to evaluate whether the target viscous damping ratio should match the small-strain material damping or a much smaller value. Both simplified and full Rayleigh damping formulations are used for these three codes (see Table 5.2 for details).

For SUMDES, only simplified Rayleigh damping was available at the time this report was written (implementation of full Rayleigh damping is in progress), and the SUMDES manual calls for the target damping ratio to be specified at 1 Hz (Li *et al.* 1992). Past practice has been that the 1 Hz damping ( $\zeta_{f1}$ ) is scaled from the target damping level ( $\zeta_{tar}$ , e.g., 5%) at some specified frequencies (often the predominant frequency of the input motion,  $f_p$ ) as

$$\zeta_{f1} = \zeta_{tar} / f_p \quad (5.5)$$

For SUMDES analyses, we use a 5% target damping level with matching frequencies at  $f_p$  (predominant frequency  $\equiv$  frequency having maximum spectral acceleration) and  $f_s$  (elastic site frequency). We also use a 1% target damping level with a matching frequency of  $f_p$ . Finally, we use a fixed damping ratio of  $\zeta_{f1} = 1\%$ . These options are summarized in Table 5.2.

For TESS it is recommended that the numerical value of the parameter VT be set to equal the desired low strain damping ratio, 0.05 in this case. As indicated in Table 5.2, we also utilize values of 0.01 and 0.10 to test the sensitivity of the computed results to VT and hence to the amount of hysteretic damping that is introduced.

### 5.5.1 Shallow Stiff Site: Simi Valley Knolls School

The upper 14 m of Simi Valley Knolls School is composed of silty sand, which has shear wave velocities of about 300 m/s and is underlain by sandstone (site frequency  $f_s = 6.4$  Hz). Figures 5.6

and 5.7 compare 5% damped acceleration response spectra of surface motions from the frequency-domain solution (developed using SHAKE04; Youngs 2004) with time-domain results from the five codes listed in Table 5.2.

The trends in the D-MOD\_2, DEEPSOIL, and OPENSEES results are similar. Comparing the left and right frames, the results are somewhat better for the 5% target damping ratio, but are relatively insensitive to the damping for this shallow site. Both simplified and full Rayleigh damping formulations are reasonably effective, although simplified Rayleigh damping with the target frequency set to the mean frequency of the input motion overdamps the computed response at short periods (the site frequency is a preferred target).

For SUMDES, the results in Figure 5.7 show that a target damping ratio of 5% produces overdamping at high frequencies regardless of the matching frequency ( $f_p$  or  $f_s$ ), whereas  $\zeta_{tar}=1\%$  provides a slightly improved fit. However, the results for all the different damping formulations fall within a narrow range for this shallow stiff site. For TESS, results are shown for three values of VT. The best fit is obtained by using values of VT that are one or two times the viscous damping ratio from frequency-domain analysis.

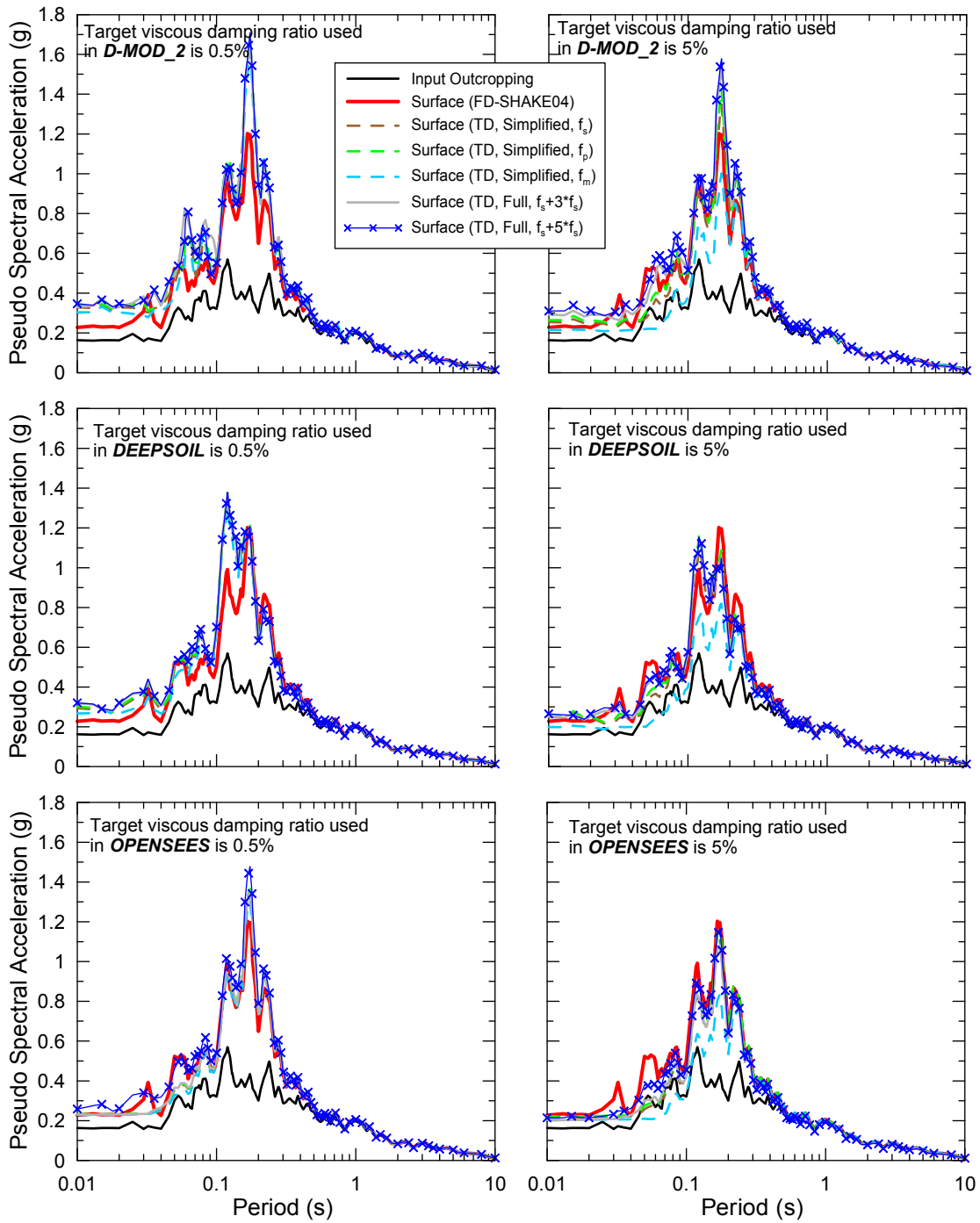


**Fig. 5.6 Comparison of response spectra for shallow stiff site (Simi Valley Knolls School) for D-MOD\_2, DEEPSOIL, and OPENSEES.**

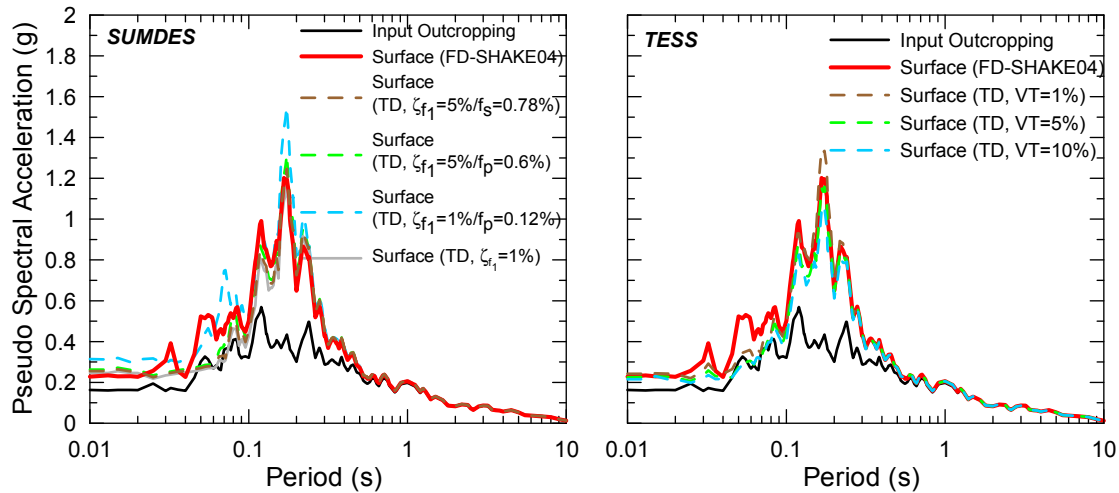


**Fig. 5.7 Comparison of response spectra for shallow stiff site (Simi Valley Knolls School) for SUMDES and TESS.**

### 5.5.2 Soft Clay Medium Depth Site: Treasure Island

The Treasure Island site has a 16-m-layer of San Francisco Bay Mud that overlies stiffer sands and clays. The site frequency is dominated by the soft clay layer, and is 1.06 Hz. The frequency-domain solution is developed using SHAKE04 (Youngs 2004). As shown in Figure 5.8, the analysis results for D-MOD\_2, DEEPSOIL, and OpenSees indicate a much better match for  $\zeta_{tar} = 5\%$  than for 0.5%. The greater sensitivity to  $\zeta_{tar}$  (relative to the Simi Valley site) results from the thicker site profile relative to the predominant wavelength. Simplified Rayleigh damping generally overdamps at low periods, although the results are reasonable when the target frequency is set at the mean frequency of the input motion. Full Rayleigh damping is preferred, with the results being fairly insensitive to the second target frequency ( $3f_s$  or  $5f_s$ ).

For SUMDES, the results in Figure 5.9 show that the use of  $f_p$  as the matching frequency produces underdamping for  $\zeta_{tar}=1\%$  and  $5\%$ . Conversely, the use of  $f_s$  as the matching frequency produces overdamping. The best fit is obtained for a viscous damping of 1% (i.e.,  $\zeta_{fl}=1\%$ ). For TESS, the best fit is again obtained when VT is set to either one or two times the viscous damping from frequency-domain analysis.

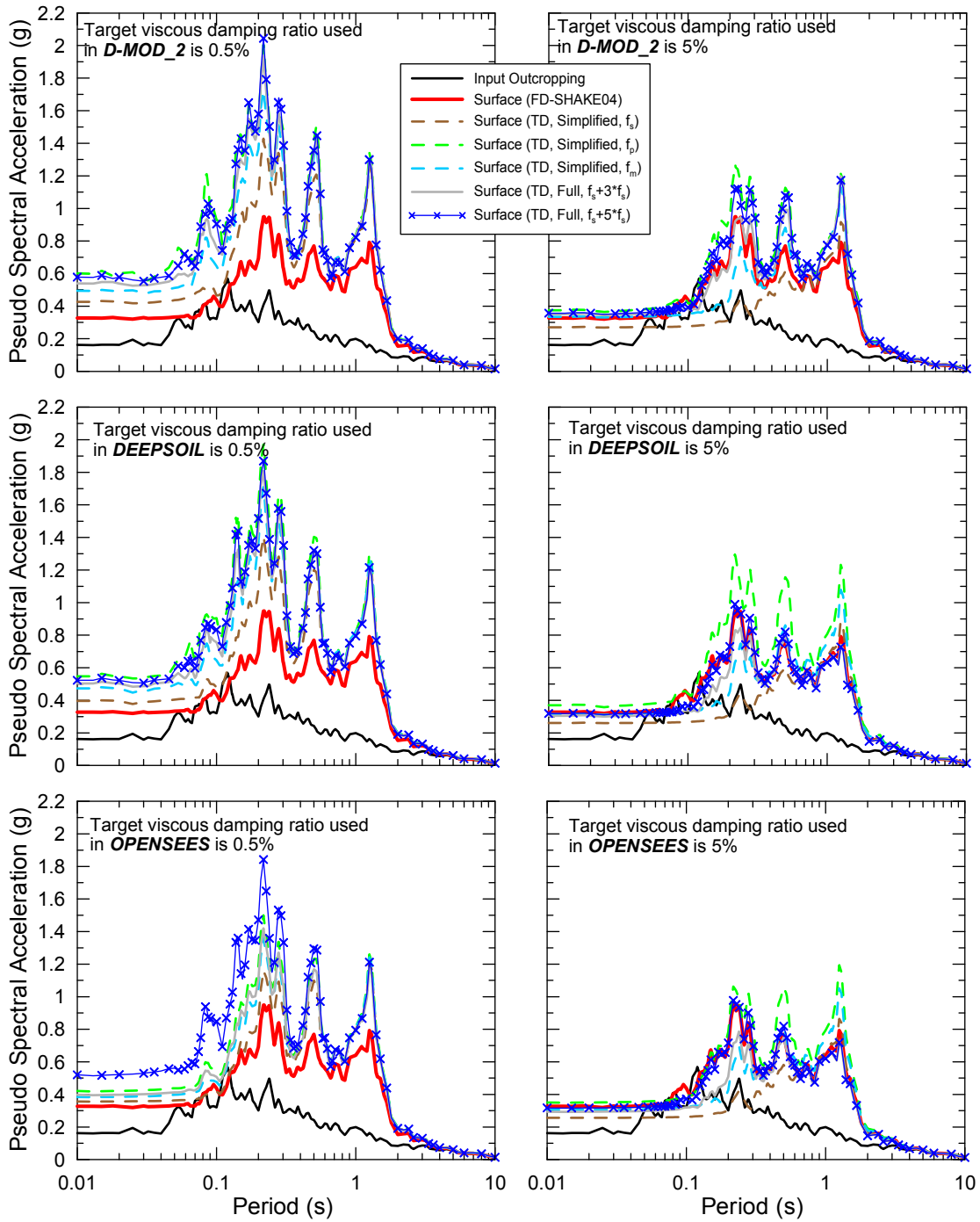


**Fig. 5.8 Comparison of response spectra for mid-period site with large impedance contrast (Treasure Island) for *D-MOD\_2*, *DEEPSOIL*, and *OPENSEES*.**

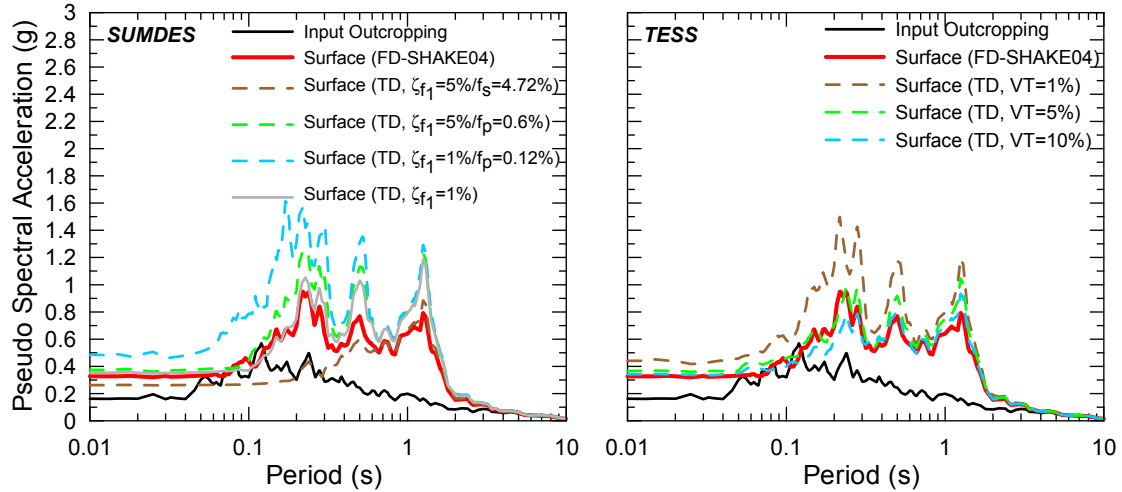


**Fig. 5.9 Comparison of response spectra for mid-period site with large impedance contrast (Treasure Island) for SUMDES and TESS.**

### 5.5.3 Deep Stiff Site: La Cienega

The La Cienega site consists of bedded sands, silts, and clays that gradually increase in stiffness with depth. Only the upper 305 m of the profile is modeled, which has a site frequency of 0.45 Hz, although the true first-mode site frequency is much lower because crystalline bedrock occurs at great depth.

The frequency-domain solution is developed using SHAKE04 (Youngs 2004). As shown in Figure 5.10, analysis results for D-MOD\_2, DEEPSOIL, and OpenSees show high sensitivity to  $\zeta_{tar}$  (with 5% providing the better match). Simplified Rayleigh damping is most effective when the target frequency is set to the mean frequency of the input motion ( $f_m$ ), and overdamps the computed response otherwise. Full Rayleigh damping generally provides an improved fit, with a slight preference towards the second frequency being  $5f_s$ .

For SUMDES, the results in Figure 5.11 show similar trends to those for Treasure Island: the use of  $f_p$  at the matching frequency produces underdamping whereas the use of  $f_s$  produces overdamping. The best fit is again obtained for a viscous damping of  $\zeta_{f1}=1\%$ . For TESS the best fit is again obtained when VT is set to either one or two times the viscous damping from the frequency-domain analysis.

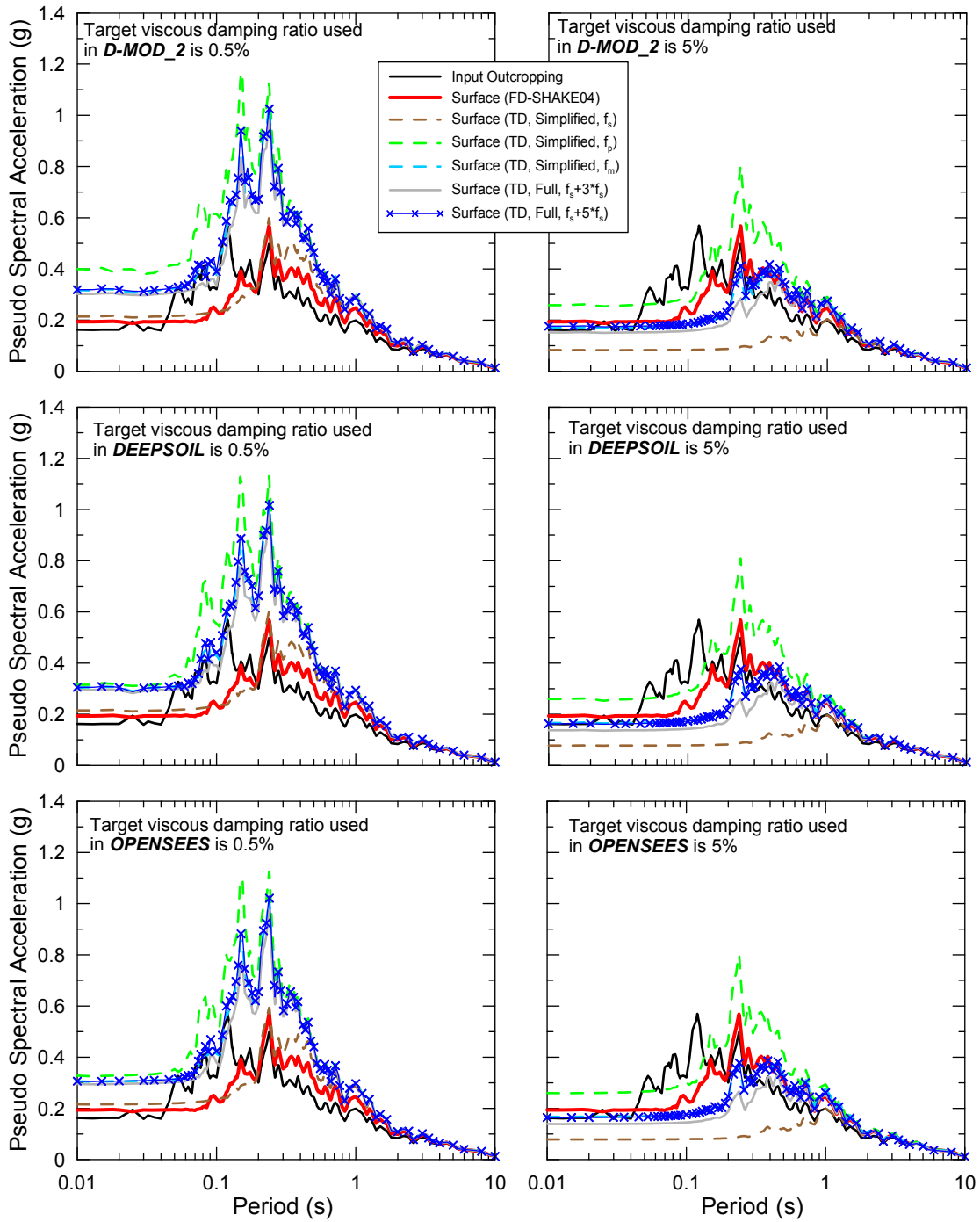


**Fig. 5.10 Comparison of response spectra for long-period site (La Cienega) for D-MOD\_2, DEEPSOIL, and OPENSEES.**

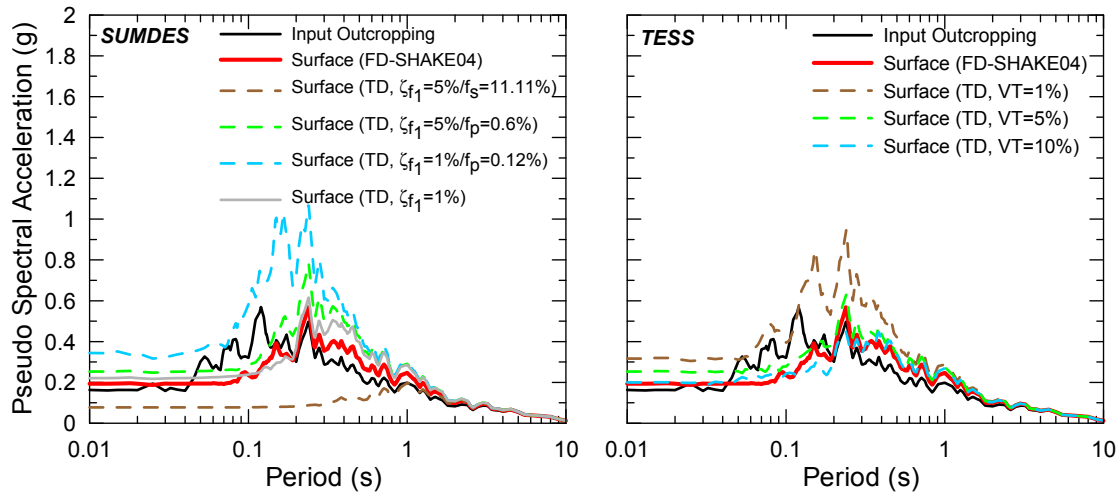


**Fig. 5.11 Comparison of response spectra for long-period site (La Cienega) for SUMDES and TESS.**

#### 5.5.4 Recommendations

Where available, viscous damping should be estimated using the full Rayleigh damping formulation (available in DEEPSOIL, D-MOD\_2, and OPENSEES). The target damping ratio should be set to the small-strain material damping, and the two target frequencies should be set to the site frequency and five times the site frequency. For DEEPSOIL these frequencies would be a suitable starting point, and can be further refined using the matching procedure between the linear frequency and time-domain solutions available via a user interface. While simplified Rayleigh damping can produce reasonable results in limited circumstances (e.g., shallow site), in general, its use is discouraged. When simplified Rayleigh damping is applied, our current recommendation is to set the target damping value as described above and the target frequency as the site frequency when there is a strong impedance contrast in the profile (e.g., Simi Valley, Treasure Island), and the mean frequency of the input motion when a strong impedance contrast is not present (e.g., La Cienega).

The code SUMDES has only a simplified Rayleigh damping option at the time this report was written (a new version with full Rayleigh damping is available but has not yet been tested). The past practice of scaling the 1 Hz damping based on a target damping at the predominant period does not appear to generally produce satisfactory results. The use of 1% damping at 1 Hz

appears to provide improved performance, and is simpler to apply. For TESS, a good match to the SHAKE04 results is obtained when the parameter VT is set equal to the desired damping ratio but the results obtained are not particularly sensitive to VT across the range of the desired damping ratio to two times that figure.

## 5.6 CONCLUSIONS

Frequency-domain equivalent-linear methods of performing site response analysis remain significantly more popular in practice than time-domain nonlinear methods (Kramer and Paulsen 2004). One reason this practice persists is that parameter selection for frequency-domain analysis is relatively straightforward, requiring only mass density, shear wave velocity, and nonlinear modulus reduction and damping versus shear strain curves. As a profession, we are well equipped to provide estimates of these quantities on a site-specific basis at reasonable cost.

In contrast, time-domain nonlinear methods of analysis require the use of parameters that are less familiar to most engineers and/or relatively difficult to obtain (details below). Three major hurdles must be overcome before nonlinear analysis methods can be more widely adopted in practice. The first is clarification of the manner in which input motions should be specified. The second is the development of simple, practical guidelines for the specification of parameters that provide element damping at small strains. In this chapter, these first two issues are addressed by comparing the results of linear time-domain analyses to exact solutions from the frequency-domain analyses for elastic conditions. The third issue, which would be investigated in subsequent chapters, is the development of practical and well-validated guidelines for estimating parameters that describe the backbone curve of soil and the unload/reload behavior given conventionally available data from a site investigation program (shear wave velocity and soil index properties).

The major finding on the input motion issue is that outcropping control motions should be used as-recorded with an elastic base. Motions recorded at depth should also be used as-recorded but with a rigid base. In both cases, the motions are specified at the base of the site profile. For within motions, the depth at which the recording was made should match the depth of the profile base.

With respect to the viscous damping issue, when the option of using more than one target frequency is available (such as the full Rayleigh damping formulation), it should be applied in

lieu of simplified Rayleigh damping because significant bias at high frequencies can occur with the latter. Target damping ratios should be set to the small-strain material damping, and the two target frequencies in a full Rayleigh damping formulation should be set to the site frequency and five times the site frequency. For DEEPSOIL these frequencies would be a suitable starting point, and can be further refined using the matching procedure between linear frequency and time-domain solutions available via a user interface. Specialized recommendations were developed for SUMDES and its simplified Rayleigh damping formulation. Recommendations are also developed for relating parameter VT to small-strain damping in the LSDS utilized in TESS. Whenever possible, it is recommended that a check be made that linear time-domain and linear frequency-domain solution provide similar results.

## **6 Turkey Flat Blind Prediction**

In this chapter, ground response analysis codes (equivalent-linear and nonlinear codes described in Chapter 2) are exercised for the blind prediction of motions recorded at the Turkey Flat vertical array. The chapter begins with a review of previous studies performed at the Turkey Flat site. The site conditions and the geotechnical model used for analysis are then described. Nonlinear code usage protocols that are based on material originally presented in Chapters 4 and 5 are then summarized. The sensitivity of the predictions to model variability and to variability in the site velocity profile and nonlinear soil properties is documented. The blind predictions are compared to data and reasons for the misfit are investigated. Data from multiple earthquakes recorded between 2003 and 2004 at the Turkey Flat site are used to compile site amplification factors at specific frequencies, which are compared with model predictions to investigate event-to-event variability in the misfit. Lastly, code performance at higher input shaking levels is studied, from which the variability between equivalent-linear and nonlinear results are evaluated.

### **6.1 INTRODUCTION**

In 1987, the California Geological Survey (CGS) and its strong-motion instrumentation program established a seismic site effects test area at Turkey Flat, which is a shallow valley site. The Turkey Flat site is located near Parkfield in the central California Coastal Range about 5 km east of the Parkfield segment of the San Andreas fault. The objective of the Turkey Flat experiment was to systematically test and compare the reliability of contemporary methods of estimating the influence of site conditions on ground motions during earthquakes (Tucker and Real 1986). An extensive site characterization program, including field and laboratory geotechnical measurements, was conducted by numerous industrial, academic, and government organizations to develop a standard geotechnical model of the test area, which would provide the input parameters necessary for the site response estimation (Real 1988). Strong- and weak-motion

instruments were installed and have recorded numerous earthquakes with weak and strong ground motions since 1987.

Weak motions recorded in the early years of operation of the Turkey Flat array were used to develop empirical transfer functions for the site (Cramer 1995) and to conduct a weak-motion blind prediction exercise (Real and Cramer 1989; Cramer and Real 1992). The chosen weak motion for the prediction exercise was an  $M_w$  2 event located about 32 km north of the test site that was recorded on 27 April 1988. The blind prediction had a first stage in which participants were given the outcrop motion at a nearby bedrock site in the first phase and a downhole motion below the middle of the valley in the second phase. Participants were required to predict the site response of the valley and uncertainties of their results using the standard geotechnical model. They were also encouraged to submit predictions based on their own preferred geotechnical model. The major results of the weak-motion blind prediction exercise were that (1) most predictions tended to cluster together regardless of the geotechnical and site response model used (preferred and standard velocity profiles were generally fairly similar) and (2) the shape and frequency of resonant peaks predicted by models were similar to observation, but the amplitude of site amplification was significantly overestimated for frequencies higher than the site frequency.

Cramer and Real (1992) concluded that variability in the geotechnical model associated with uncertainty in stiffness and damping characteristics more significantly impacted the predicted motions than variability between different methods of analysis utilizing relatively consistent velocity profiles (i.e., from preferred versus standard geotechnical models). To further investigate the prediction bias noted in the weak-motion blind prediction exercise, Field and Jacob (1993) performed Monte-Carlo simulations to investigate the sensitivity of site response predictions to variability in the seismic velocity profile (including variability in layer velocities and layer thickness) and variability in damping, using the standard geotechnical model as a baseline. Factors that significantly contributed to the scatter of the predicted site amplification included the first-layer shear wave velocity and thickness, as well as the profile damping (one value was used for the entire soil layer). The variability in the properties of deeper layers did not significantly impact the results. Cramer (1995) performed sensitivity studies similar to those of Field and Jacob (1993), and found that the fit of the predicted response to observation was optimized by increasing (relative to the standard geotechnical model) shear wave velocities

throughout the site profile by 5% and increasing the damping from the average laboratory-reported value of 1.5%–7%.

The strongest motions recorded at the Turkey Flat site are from the  $M_w$  6.0 Parkfield earthquake on 28 September 2004, which occurred on the Parkfield segment of the San Andreas fault (Rymer *et al.* 2006). The strong motions from this event were used in a second blind prediction exercise for the Turkey Flat site (Real and Shakal 2005). The strong-motion blind test procedure was similar to that for the weak-motion blind test, with the additional consideration that nonlinear geotechnical properties (such as modulus reduction and damping curves) were a significant component of these analyses. The emphasis of this chapter is on Phase II of the blind prediction exercise, which focuses on ground response at the valley center conditioned on the within (rock) motion.

## 6.2 TURKEY FLAT ARRAY

Turkey Flat is a shallow stiff-soil alluvial valley near Parkfield, California. The valley is instrumented with surface and downhole sensors as indicated in the vertical schematic section shown in Figure 6.1. One of the vertical arrays is outside the valley (location is referred to as rock south) in upper Cretaceous and Tertiary sedimentary sandstone bedrock materials and consists of two instruments referred to as R1 (surface) and D1 (downhole). The second vertical array is at the valley center and consists of three instruments: V1 (surface) and D2–D3 (downhole). As shown in Figure 6.1, additional surface instruments are at the north end of the valley (valley north, V2) and on rock north of the valley (rock north, R2).

At the time of the original array installation in 1987, each sensor location consisted of digital three-component forced-balance accelerometers and three-component velocity sensors (Real *et al.* 2006). In 2001, the data acquisition system was upgraded with 12-bit solid-state digital recorders, which recorded all of the data utilized in this chapter.

The blind predictions reported in this chapter were part of a larger blind prediction exercise organized by the California Strong Motion Instrumentation Program in 2005 (Real and Shakal 2005) with multiple U.S. and international participants. The prediction exercise consisted of two phases, both using data from the 2004 Parkfield earthquake. In the first phase, rock-surface motion R1 was released, and the motions were predicted at D1 and D3 (rock downhole) and D2 and V1 (soil motions). In the second phase, rock downhole motion D3 was provided, and

soil motions D2 and V1 were predicted. In this chapter, focus is put on the results associated with the second prediction phase as the site response analysis codes used are 1-D in nature and cannot account for ground motion incoherency between D1 and D3.

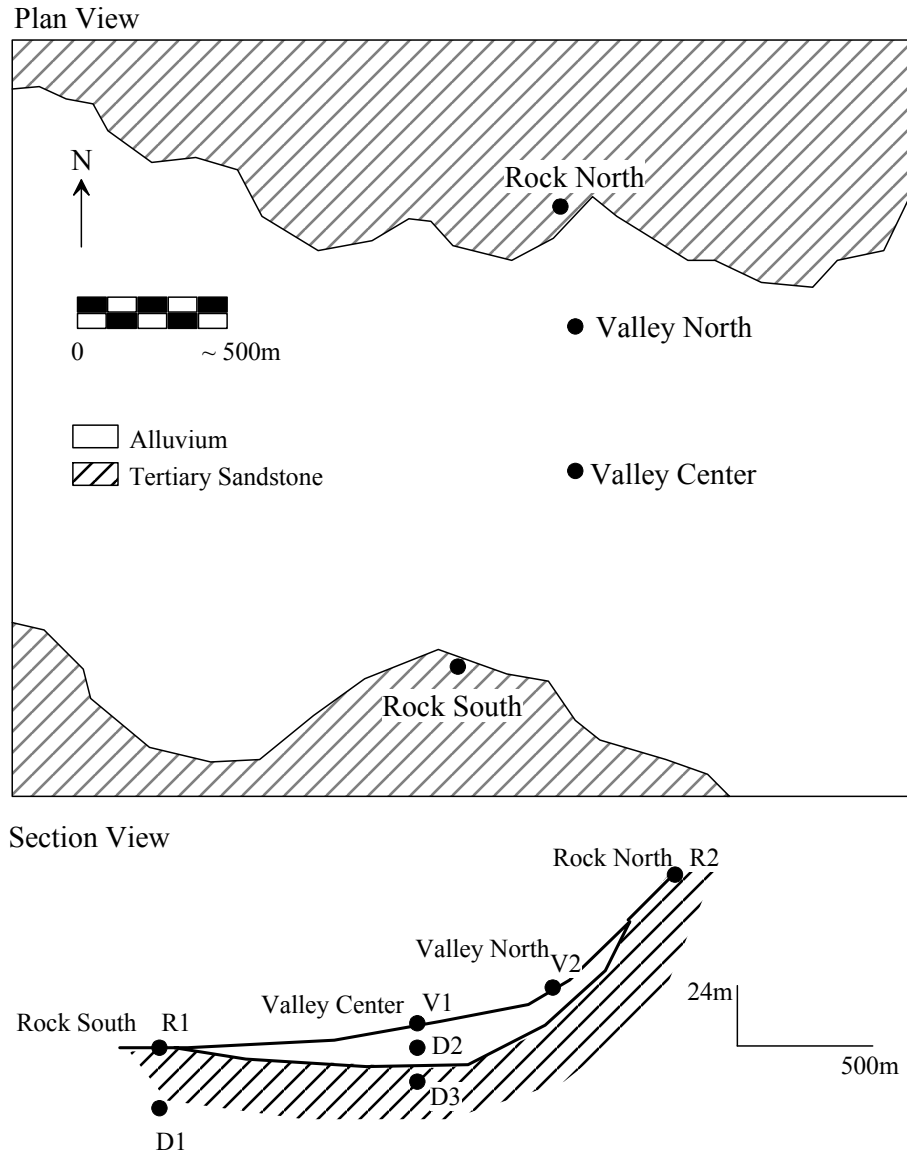


**Fig. 6.1 Plan and section views of Turkey Flat strong-motion array (adapted from Real 1988).**

### 6.3 SITE PROPERTIES AND BASELINE GEOTECHNICAL MODEL

According to Real (1988), boreholes were drilled at Turkey Flat in 1986–1987 at the locations of the two vertical arrays to investigate geotechnical conditions and to enable installation of downhole sensors. The maximum depths of exploration were 25 m and 40 m for rock south and valley center, respectively. At the rock south array, surficial materials consist of weathered grayish-brown sandstone that transition to a lower degree of weathering at approximately 14 m (as indicated, e.g., by color change to bluish gray). At the valley center array, the soil profile consists of dark-brown silty clay near the surface (about 1.8–4.6 m), which is underlain by clayey sand to a depth of about 20 m. Underlying the soil materials is a sandstone bedrock profile similar to that at rock south. Estimated values of material density at the valley center site are shown in Table 6.1.

**Table 6.1 Estimated values of material density at valley center site.**

	<b>Depth (m)</b>	<b>Unit Weight (kN/m<sup>3</sup>)</b>
Soft surface soil	0 - 1.8	15.7
Deep stiff soil and weathered rock	1.8 - 22.9	17.6
Bedrock below weathering zone	> 22.9	21.5

Shear wave velocity ( $V_s$ ) measurements were made in boreholes at the two vertical arrays using downhole, crosshole, and suspension logging methods performed by numerous groups including LeRoy Crandall and Associates, Hardin Lawson Associates, QEST Consultants, OYO Corporation, Kajima Corporation, the California Division of Mines and Geology, and Woodward-Clyde Consultants. Figure 6.2 shows data for the valley center site (V1-D3) along with a weighted mean and mean  $\pm$  one standard deviation profiles. Equal weights were given to all velocity profiles except for the OYO suspension-logger profile, which was given double weight below 4.5 m depth (because of relatively high signal/noise ratios at depth with OYO data due to a constant spacing between source and receiver; Nigbor and Imai 1994). It is noteworthy that the mean  $V_s$  profile in Figure 6.2 implies an upward wave travel time of 0.045 sec, which compares favorably to travel times derived from analysis of V1-D3 seismographs (using cross-correlations functions) of  $0.05 \pm 0.01$  sec.

Also shown in Figure 6.2 is a smoothed velocity profile developed by K. Stokoe (2006, pers. comm.) that includes a transition zone from 1–3.6 m depth between a soft surface layer and relatively stiff soils at depth and a second transition zone reflecting apparent bedrock weathering from 20–26 m depth. This smoothed profile implies a median travel time of 0.042 sec, and hence is also consistent with seismograph data. A similar bedrock transition zone thickness was observed at the rock site south vertical array (R1-D3) near the ground surface.

Finally, we show in Figure 6.2 a profile developed following the blind prediction exercise from a spectral analysis of surface waves (SASW) tested by R. Kayen (personal comm. 2007). The line of sensors used for SASW testing was positioned adjacent to the valley center recording station. This velocity profile has a similar shape to the earlier profiles but has lower shear-wave velocities from 2–33 m. The shear-wave travel time implied by this model is 0.056 sec, which is in the plausible range of observed values from seismograms ( $0.05 \pm 0.01$  sec).

During the 1986–1987 field work, soil samples were retrieved from boreholes at the mid valley location using Pitcher barrel (pushed/carved) and Crandall (driven-tube) samplers. Cyclic laboratory testing was performed on specimens carved from those samples to measure nonlinear relationships between shear stress and shear strain and between hysteretic damping ratio and shear strain. The former are expressed in normalized form as modulus-reduction curves ( $G/G_{max}$  curves), the latter as damping ratio versus strain curves ( $\beta$  curves). The results obtained using resonant column and cyclic triaxial testing are plotted on the left-hand side of Figure 6.3. Regression model-based predictions of  $G/G_{max}$  and  $\beta$  curves from Darendeli (2001) (which account for soil plasticity, overconsolidation ratio, and overburden pressure) computed for different depths are shown on the right-hand side of Figure 6.3. Values for all of the input parameters needed to exercise the Darendeli model are given in Figure 6.3. The material-specific  $G/G_{max}$  curves and Darendeli model predictions generally compare favorably. There are differences in the damping, with the Darendeli damping predictions generally being lower than the measured values. It is possible that the laboratory data, which date from 1986–1987, have an overprediction bias (this is commonly the case with data from that time period). Accordingly, the Darendeli curves are taken as the preferred model for the analyses described below.

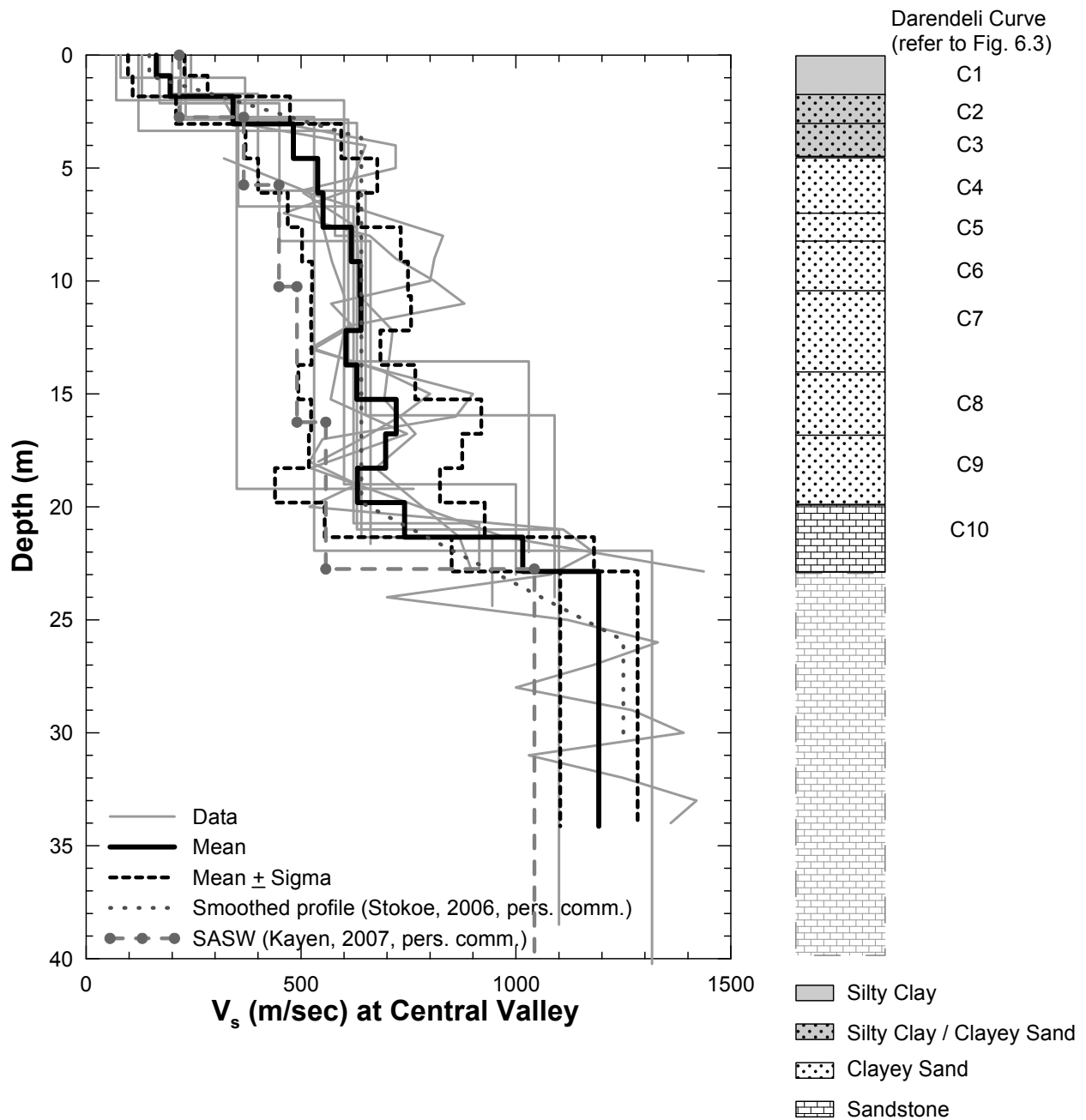
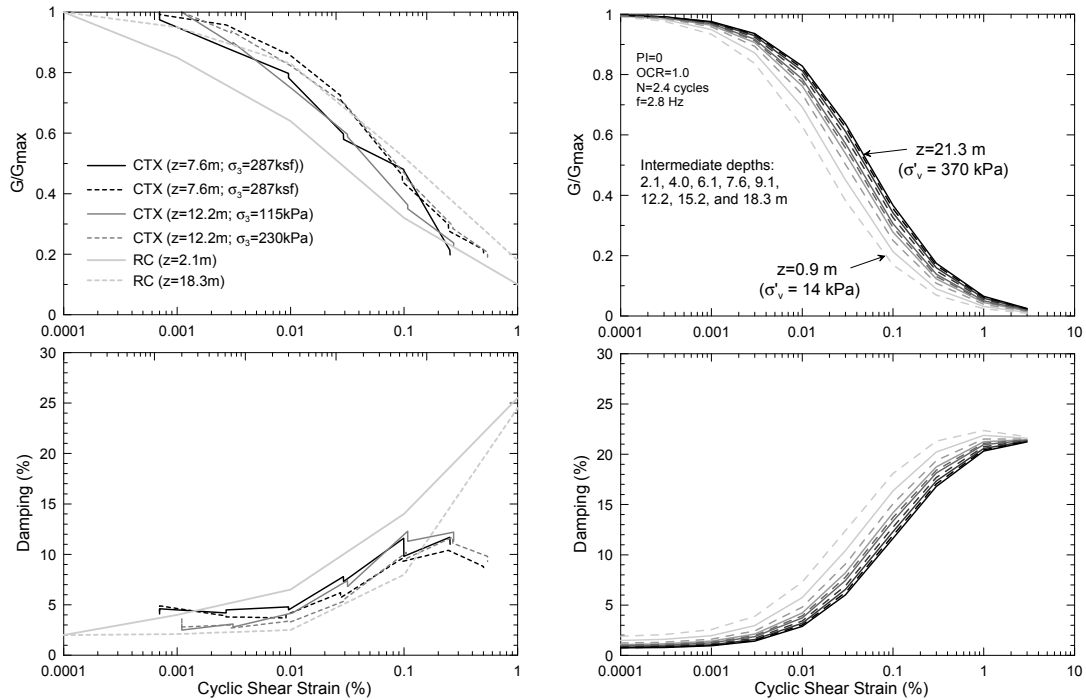


Fig. 6.2 Shear wave velocity profiles at mid-valley site (V1- D3 array). Data from Real, (1988).



**Fig. 6.3 Modulus reduction and damping curves based on material-specific testing (left side) and Darendeli (2001) model predictions (right side), mid-valley location. Data from Real (1988).**

## 6.4 NONLINEAR SEISMIC GROUND RESPONSE ANALYSIS CODES

Six different ground response analysis codes were utilized: SHAKE04 (Youngs 2004), which is a modified version of SHAKE91 (Idriss and Sun 1992); D-MOD\_2 (Matasovic 2006); DEEPSOIL (Hashash and Park 2001, 2002; Park and Hashash 2004); TESS (Pyke 2000); OpenSees (Ragheb 1994; Parra 1996; Yang 2000; McKenna and Fenves 2001); and SUMDES (Li *et al.* 1992). The total stress analysis option is used for all nonlinear codes considered.

## 6.5 CODE USAGE PROTOCOLS

The code usage protocols relate principally to three issues: (1) specification of input motion; (2) specification of viscous damping model and parameters; and (3) specification of parameters describing the nonlinear backbone curve and hysteretic damping behavior given a target set of  $G/G_{max}$  curves and  $\beta$  curves. It is possible to address the first two issues purely through the comparison of simulation results from the nonlinear (time-stepping) codes to known theoretical

solutions for linear conditions. As presented in Chapter 5, the results of this work support the following protocols, which were applied for the Turkey Flat analyses:

1. The recorded “within“ motions (D3) are taken as the input motion without modification, and are used with a rigid base. Although not applied for Turkey Flat, we note for completeness that an outcropping motion to be used as input would also be applied without modification but would be specified in the nonlinear codes with a compliant base.
2. For codes DEEPSOIL, D-MOD\_2, and OpenSees, viscous damping is specified using full Rayleigh damping, with the target frequencies set to the first-mode site frequency ( $f_s$ ) and  $3 \times f_s$ . The general protocol that is followed here is to use full Rayleigh damping (two matching frequencies) in lieu of simplified Rayleigh damping (one matching frequency) when available. The level of damping that is specified is the small-strain hysteretic damping, referred to as  $D_{min}$ . The frequencies at which matching of the target damping value are enforced are the site frequency above the elevation at which the input motion is specified ( $f_s$ ) and a higher frequency selected to optimize the match of linear frequency and time-domain analyses (Hashash and Park 2002). In the case of the Turkey Flat site, this optimal match occurred for a second matching frequency of  $3 \times f_s$ . For TESS, parameter VT is taken as equal to  $D_{min}$ . For SUMDES, the target damping ratio is set to be 1% as demonstrated in Chapter 5.

The remaining parameters required to apply the nonlinear codes describe the nonlinear backbone curve and hysteretic damping behavior. There are two principal issues here. The first is the selection of target soil properties to be replicated as accurately as possible in the codes’ nonlinear models. The second issue is the manner in which input parameters describing the codes’ nonlinear models are selected given a set of target material properties. Regarding the former issue, the required soil properties are the small-strain shear wave velocity ( $V_s$ ) profile, density, and modulus reduction and damping curves ( $G/G_{max}$  and  $\beta$ ). We define our baseline geotechnical model as the mean  $V_s$  profile in Figure 6.2, the unit weight values in Table 6.1, and Darendeli model-based  $G/G_{max}$  and  $\beta$  curves in Figure 6.3. the variability in the most important of these parameters (i.e., the  $V_s$  profile and  $G/G_{max}$  and  $\beta$  curves) is also considered, as described further in the next paragraph.

The input parameters in nonlinear codes that describe nonlinear backbone curves and hysteretic damping behavior generally consist of  $G_{max}$ , a pseudo-reference strain parameter ( $\gamma_r$ ) defined as the value of shear strain at which  $G/G_{max}=0.5$ , and additional curve-fitting parameters. The specification of  $G_{max}$  is trivial. The specification of  $\gamma_r$  and additional fitting parameters are relatively subjective because it is not possible to simultaneously match (1) the target  $G/G_{max}$  curves to the  $G/G_{max}$  behavior of the backbone curve and (2) the target  $\beta$  curves to the hysteretic damping that results from the application of extended Masing rules (or similar Cundall-Pyke rules) for unload-reload behavior to the backbone curve. For the present analysis, we selected  $\gamma_r$  and additional curve-fitting parameters to match the target  $G/G_{max}$  curves. Although this generally would produce misfit of the target  $\beta$  curves as shown in Figure 6.4, the misfit is negligibly small over the strain range of interest from the recorded ground motions (as noted in the figure).

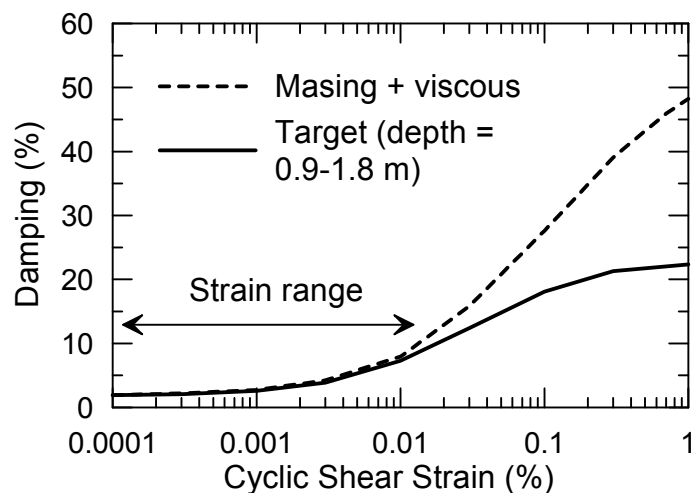


**Fig. 6.4 Target and modeled damping curves for 0.91–1.82 m (depth range at which largest strains occur in soil profile).**

## 6.6 RESULTS OF SIMULATION AND COMPARISONS TO DATA

### 6.6.1 Blind Prediction Results Using Baseline Model

We performed ground response analyses to estimate soil motions V1 and D2 using recording D3 as the input motion. Analyses were performed using the six different codes described above. Each code was exercised for the same baseline site condition.

Figures 6.5 and 6.6 present the results of the simulations and how they compare to the recorded data. The simulation results in Figures 6.5 and 6.6 are truly “blind,” meaning they were established before the strong motion data were released [the simulation results were published in the proceedings of a conference from August 30–September 1, 2006 (Kwok *et al.* 2006), which was prior to a Turkey Flat workshop at which all the data were released on September 21, 2006]. Figure 6.5 compares the recorded acceleration histories to the simulations from DEEPSOIL. It can be seen that shear waves dominate the signal and that the predicted waveforms are similar to observation except for amplitudes that are slightly too low. The results in Figure 6.6 are presented in terms of 5% damped pseudo-acceleration response spectra ( $S_a$ ) and  $S_a$  residuals ( $R$ ) defined as:

$$R(T) = \ln(S_a(T))_{data} - \ln(S_a(T))_{pre} \quad (6.1)$$

where  $(S_a(T))_{data}$  indicates the spectra of recordings and  $(S_a(T))_{pre}$  indicates the spectra of model predictions. The results are shown for two horizontal directions at the surface (V1) and at 10 m depth (D2).

The elastic fundamental period ( $T_s = 1/f_s$ ) of the Turkey Flat site is 0.18 sec. Given the modulus reduction relationships for the site soils, the elongated site period is approximately 0.19–0.20 sec. As shown in Figure 6.6a–d, at periods well beyond the elongated site period, the simulation results match the surface recordings well and are very similar to each other, which is expected because the computed site effect at such periods is negligible (nearly rigid body motion). At shorter periods, the simulations generally underpredict the surface recorded motions (especially in the EW direction) and the simulation results demonstrate significant code-to-code variability. An exception to this underprediction trend occurs in the NS direction near the site period, where the motions are overpredicted. As shown in Figure 6.5e–h, the positive residuals that are present in the surface recordings are significantly reduced for the downhole soil recording, which suggests that the upper part of the profile contributes significantly to the underprediction misfit. However, the overprediction in the NS direction near the site period is not reduced, indicating that the source of this misfit is not only related to surficial soil conditions.

Because the codes are being run for the same geotechnical model, the aforementioned code-to-code variability arises from issues such as the manner in which the backbone curve is parameterized and the viscous damping is specified. For example, the DEEPSOIL and D-MOD\_2 results are similar to each other because of the similarity of these models. The

SHAKE04 residuals are lower. The relatively high residuals from SUMDES result from overdamping at high frequencies due to the use of the simplified Rayleigh damping formulation. The TESS residuals are slightly higher because the damping generated by the Cundall-Pyke hypothesis coupled with Pyke’s low-strain damping scheme is higher than what is generated by Masing rules (see Chapter 5). The modulus reduction/damping curves and viscous damping scheme used in OpenSees is similar to those used in DEEPSOIL and D-MOD\_2; hence, the differences in residuals (which are smaller in this case for OpenSees) is likely related both to small differences in the constitutive models and to the soil being modeled as a finite element continuum in OpenSees versus as lumped masses in DEEPSOIL and D-MOD\_2. The code-to-code variability shown in Figure 6.6 is found to be approximately log-normally distributed with a standard deviation  $\sigma_m$  (subscript ‘m’ for model) ranging from zero beyond the site period to approximately 0.15–0.20 (in natural log units) at shorter periods.

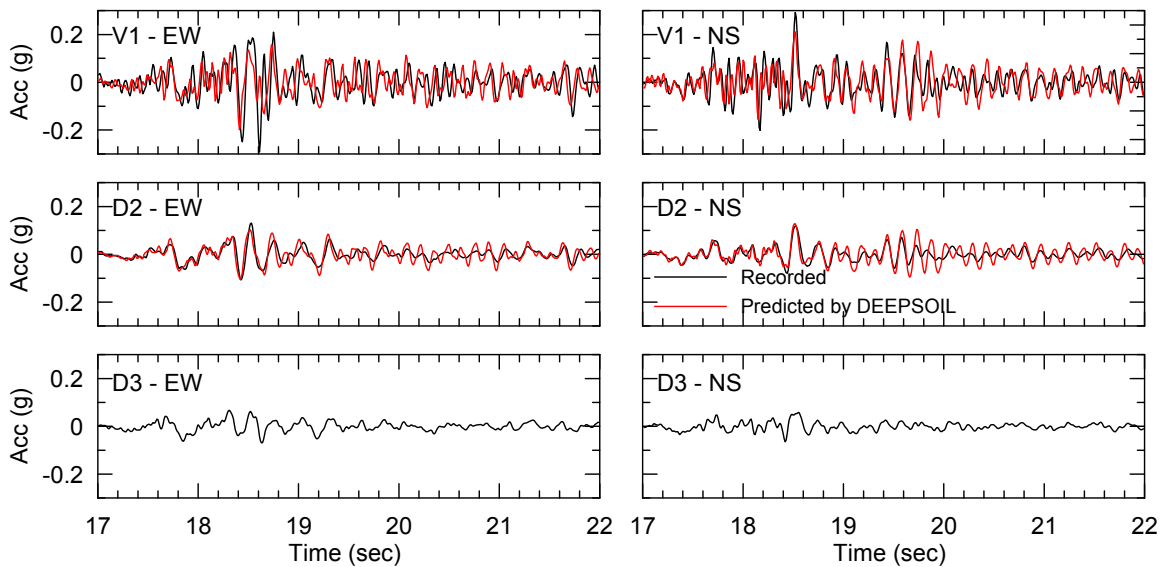


**Fig. 6.5 Acceleration histories for data and simulation results from DEEPSOIL. Results shown for two horizontal directions and two elevations (V1, ground surface; D2, 10-m depth. Recorded input motions at elevation D3 also shown.**

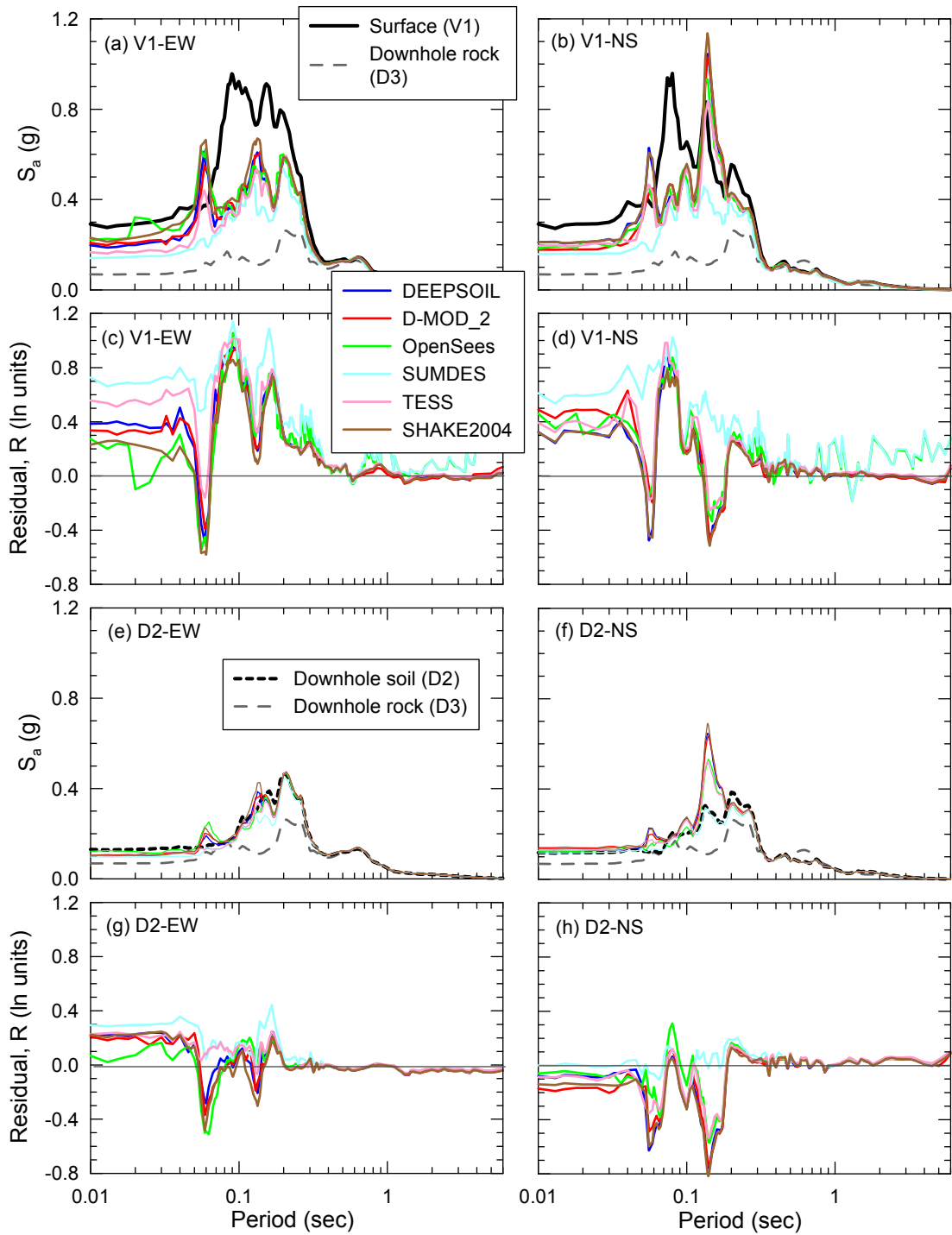


**Fig. 6.6** Acceleration response spectra for data and simulation results compared through direct spectral ordinates and prediction residuals. Results shown for two horizontal directions and two elevations (V1 = ground surface; D2 = 10 m depth). Results shown to a maximum period of  $1/(1.25 \times f_{HP})$ , where  $f_{HP}$  = high-pass corner frequency.

## 6.7 UNCERTAINTY IN PREDICTION RESULTS FROM VARIABILITY IN MATERIAL PROPERTIES

As shown in Figures 6.2 and 6.3, there is significant uncertainty in soil properties at the Turkey Flat site. The impact of that uncertainty on the simulation results is of interest both from the standpoint of understanding whether “observations” lie within an expected band of prediction results and understanding the most important sources of variability in the predictions. Two sources of material property variability are considered—variability in  $V_s$  as represented by the scatter of the field measurements and variability in modulus reduction and damping relationships as established in the literature.

The impact of variability in the velocity profile was investigated by performing analyses with the baseline geotechnical model, but with velocities varied to reflect mean  $\pm \sqrt{3}$  standard deviation profiles. The corresponding response variability was assessed using three runs (for the three different velocity profiles) with the DEEPSOIL code. A weighted variance is calculated from the three results, giving a weight of 2/3 to the mean velocity profile and 1/6 to the mean  $\pm \sqrt{3}$  standard deviation profiles. The standard deviation of the ground motions due to the variability in velocity (denoted  $\sigma_v$ ) is then taken as the square root of the weighted variance. This is consistent with a *first-order second-moment* method for estimating response variability given input parameter variability (Melchers 1999; Baker and Cornell 2003).

The target modulus reduction and damping curves used in the predictions are from an empirical model (Darendeli 2001). The Darendeli model includes estimates of standard deviation on the modulus reduction and damping curves. These standard deviation estimates are based on the scatter of the laboratory data used to develop the regression model. We utilize these standard deviation estimates to evaluate the uncertainty on modulus reduction behavior. At  $G/G_{max} = 0.5$ , the uncertainty on the modulus reduction curves corresponds to a coefficient of variation of approximately 0.2. Since in the nonlinear codes the shape of the backbone curve also affects the damping, uncertainty in damping curves is not considered separately (i.e., variability in damping was assumed to be perfectly correlated to variability in modulus reduction). So the impact of material curve variability was evaluated by performing analyses with the baseline geotechnical model and modulus reduction curves varied to reflect mean  $\pm \sqrt{3}$  standard deviation. The

standard deviation of the ground motions associated with material curve variability is termed  $\sigma_G$  and is evaluated in a manner similar to what was described previously for  $\sigma_v$ .

The values of the standard deviation terms  $\sigma_m$ ,  $\sigma_v$ , and  $\sigma_G$  are summarized in Figure 6.7 for the geometric mean of the spectral accelerations at location V1 in the two horizontal directions. Also shown in Figure 6.7 is the total standard deviation ( $\sigma$ ) calculated assuming that the three sources of variability are uncorrelated:

$$\sigma = \sqrt{\sigma_m^2 + \sigma_v^2 + \sigma_G^2} \quad (6.2)$$

The most significant source of dispersion below the site period ( $T_s = 0.18$  sec) is velocity variability. The dominant effect of velocity variability across a relatively broad range of periods, including the elastic and elongated site period, is consistent with the previous simulation results of Field and Jacob (1993).

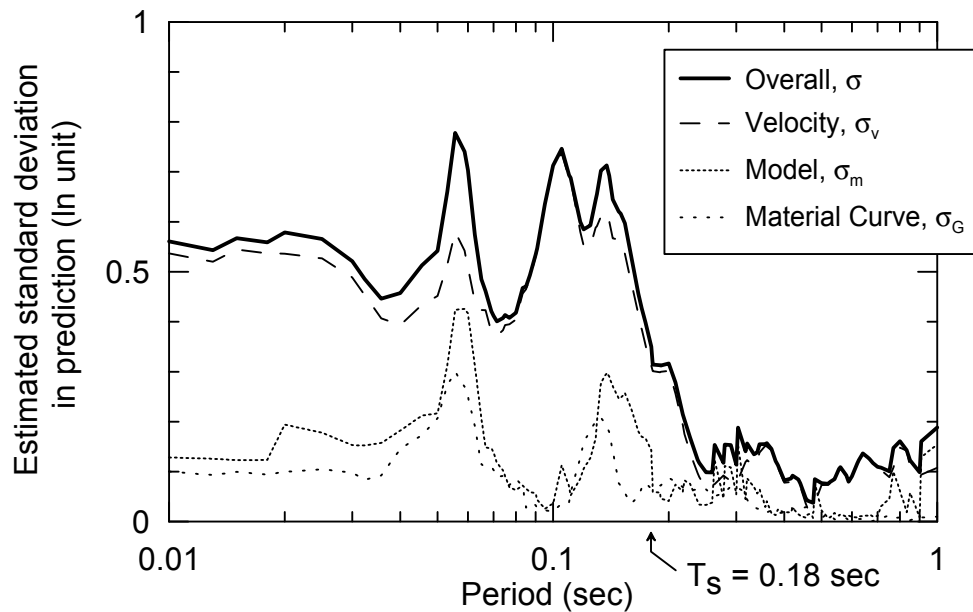


**Fig. 6.7 Standard deviation terms associated with geometric mean acceleration response spectral ordinates for location V1.  $T_s$  denotes elastic site period.**

To evaluate whether model and material property variability could explain the underprediction bias reported in Figure 6.6 for surface recordings (V1), we add and subtract the total standard deviation (black line in Fig. 6.7) to the median of the residuals for the baseline geotechnical model (i.e., the median of the residuals shown in Fig. 6.6). As shown in Figure 6.8, the results indicate that at a mean  $\pm$  one standard deviation level, the prediction residuals include an unbiased condition (zero residual) for most periods smaller than the site period. This result

indicates that 1D ground response analysis with the material data available at the time of the blind prediction exercise may be capable of explaining the observed site amplification. Nonetheless, the best-estimate properties produce a clear bias for which we postulate two explanations. One is that the analytical models contain inherent flaws in model formulation (e.g., the assumption of 1D wave propagation). The other possibility is that the measured or assumed material properties are incorrect. This issue is explored further in the next section.

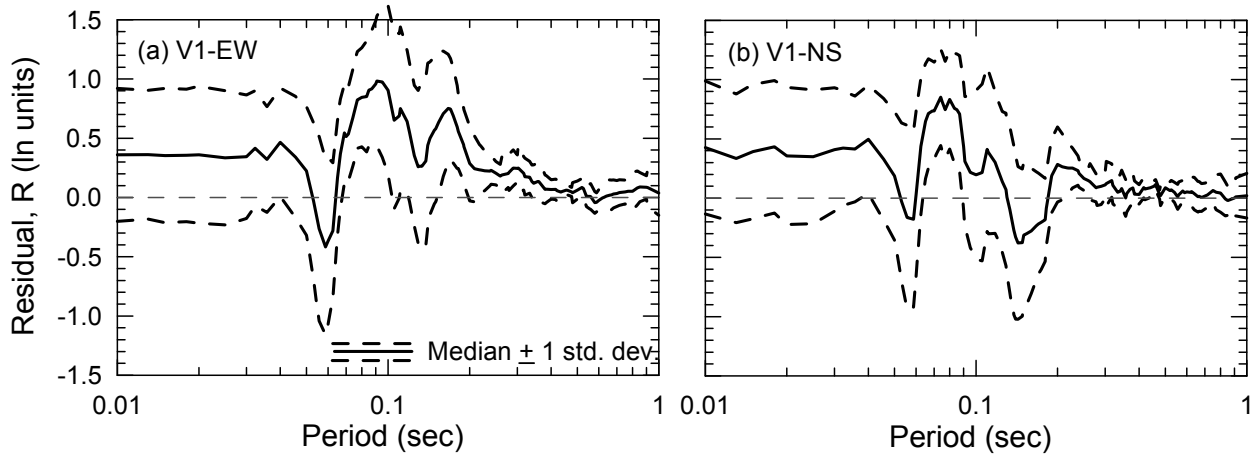


**Fig. 6.8 Median  $\pm$  one standard deviation residuals using total standard deviation estimate from Fig. 6.7.**

## 6.8 INVESTIGATION OF POSSIBLE SOURCES OF BIAS

As noted in the previous section, the prediction bias reported in Figures 6.6 and 6.8 could result from errors in the model formulation or errors in material properties. We consulted with a number of collaborating experts in nonlinear ground response analysis (N. Matasovic, R. Pyke, Y. Wang, Z. Yang 2006, pers. comm. 2006) asking them to independently investigate possible reasons for the bias. Most investigated the potential for the bias to have resulted from overestimation of damping in the models (hysteretic and viscous) and overestimation of shear wave velocity ( $V_s$ ) in the near-surface soils. In this section, we report representative results of such sensitivity studies using the code DEEPSOIL are reported. Similar results were obtained by the aforementioned code developers using each of their respective nonlinear codes.

Modifications of damping were found to significantly affect the prediction bias only at very low periods ( $T < 0.07$  sec). A typical result is shown in Figure 6.9, which shows DEEPSOIL residuals with the baseline geotechnical model, the baseline model with lower

hysteretic damping (one standard deviation lower than the baseline damping), and lower viscous damping (decreased from 0.7–1.9% to 0.5 % for all layers).

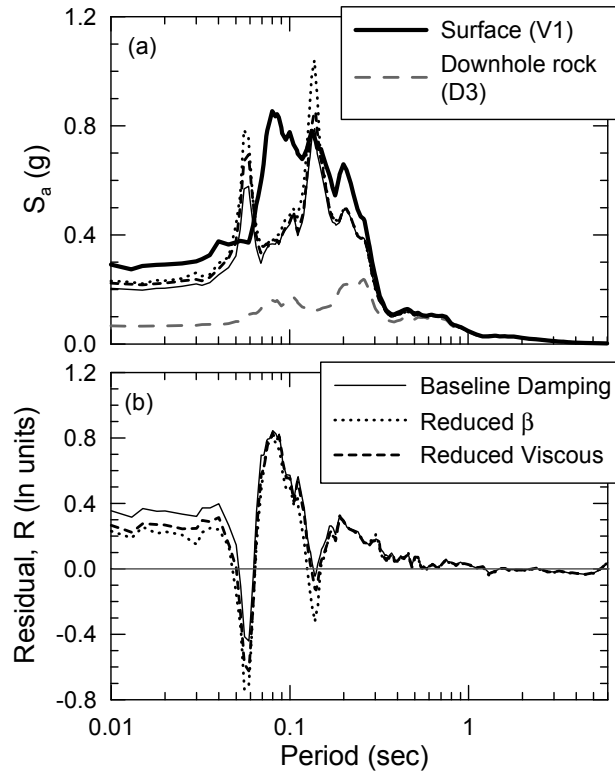


**Fig. 6.9 Geometric mean acceleration response spectra and prediction residuals for DEEPSOIL simulation results obtained with alternative material curves and viscous damping formulation.**

Two types of modifications to the  $V_s$  profile were considered by the code developers in their attempts to reduce high-frequency residuals. The first involved smoothing the relatively jagged baseline profile. This tended to further increase residuals because the smoothing process would typically involve decreasing the thickness of the low velocity surface layer. For example, the modification of residuals obtained using the smoothed profile from Figure 6.2 are shown in Figure 6.10. Additional attempts to smooth the  $V_s$  profile without changing the thickness of the surface layer resulted in effectively no change in residuals relative to the baseline result.

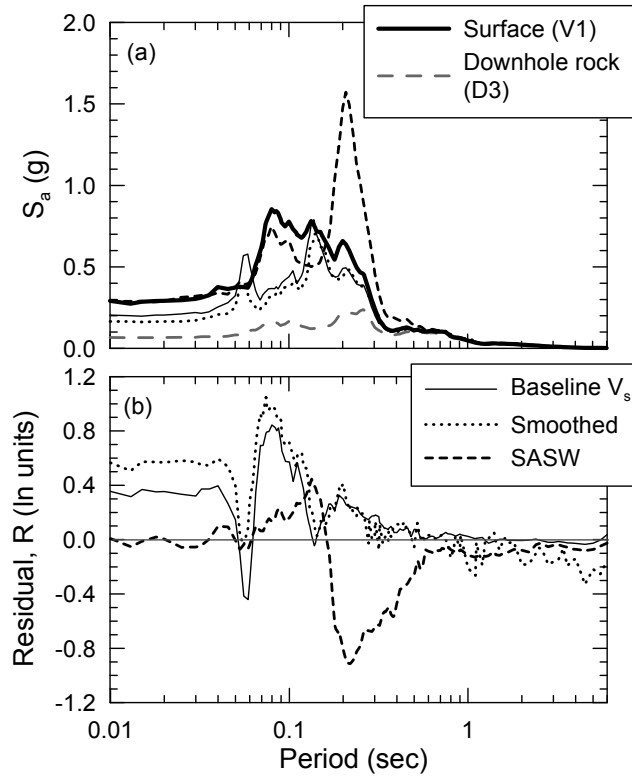


**Fig. 6.10 Geometric mean acceleration response spectra and prediction residuals for DEEPSOIL simulation results obtained with alternative velocity profiles.**

As noted previously and shown in Figure 6.2, a velocity profile was obtained for the Turkey Flat mid-valley site based on SASW testing after the blind prediction exercise was completed (R. Kayen, pers. comm. 2007). The velocities in the soil portions of this profile are generally slower than those that had been previously available. The use of this alternative profile profiles a second way to test the sensitivity of result to the  $V_s$  profile. As shown in Figure 6.10, the results obtained with the SASW profile indicate much lower residuals for high frequencies ( $T \geq 0.15$  sec), which removes the aforementioned underprediction bias. However, a large overprediction bias at the site period of approximately 0.2 sec is introduced. This overprediction at the site period is a common feature of 1D codes (Kwok and Stewart 2006; Kwok 2007) and may be due to artificially high resonances associated with the use of 1D modeling of a relatively complex 3D basin structure (Day et al. 2004). These results suggest the bias in ground response predictions made with the baseline geotechnical model were likely caused primarily from bias in the velocity profile.

## 6.9 EVENT-TO-EVENT VARIABILITY OF TURKEY FLAT SITE RESPONSE

As noted in the introduction, the first blind prediction exercise found the measured site response at Turkey Flat from weak motions to be overpredicted using elastic wave propagation codes (Cramer and Real 1992). Conversely, the strong motion site response from the 2004 Parkfield earthquake is underpredicted. Although the codes used for the two prediction exercises are different, it is nonetheless clear that there is some event-to-event variability in the ground response analysis residuals. To investigate this more formally, we compile site amplification factors from ground motions recorded at Turkey Flat from 2003–2004. The earthquake events considered are summarized in Table 6.2.

**Table 6.2 Earthquake events used to compile site amplification factors.**

Event	Year	Month	Day	hhmm	Magnitude	Latitude (N)	Longitude (W)	Hypocentral Depth (km)	Site-source Distance (km)	PGA at D3 (Geo Mean, g)	PGA at V1 (Geo Mean, g)
San Simeon	2003	12	22	1115	6.5	35.71	121.10	4.7	70.4	0.019	0.034
Parkfield Mainshock	2004	9	28	1015	6.0	35.81	120.37	7.9	8.2	0.067	0.292
Parkfield Aftershock 1	2004	9	28	1019	4.2	35.86	120.41	9.2	5.9	0.030	0.127
Parkfield Aftershock 2	2004	9	28	1022	4.0	35.84	120.39	5.6	5.9	0.011	0.071
Parkfield Aftershock 3	2004	9	28	1033	3.7	35.82	120.36	6.9	7.0	0.006	0.025
Parkfield Aftershock 4	2004	9	28	1035	3.6	35.95	120.49	10.2	14.7	0.002	0.007
Parkfield Aftershock 5	2004	9	28	1223	3.1	35.83	120.38	6.5	6.4	0.003	0.016
Parkfield Aftershock 6	2004	9	28	1231	4.0	35.84	120.39	9.3	5.9	0.007	0.037
Parkfield Aftershock 7	2004	9	29	1010	5.0	35.95	120.50	11.5	15.5	0.016	0.036
Parkfield Aftershock 8	2004	9	29	1012	3.8	35.95	120.49	10.2	14.7	0.002	0.006

Amplification factors (V1/D3) of geometric mean response spectral accelerations are derived at specified periods using the baseline geotechnical model for all codes. To estimate amplification factors for different amplitudes of input motions, the D3 Parkfield recording is scaled down to various degrees. Sensitivity analyses performed using different D3 waveforms indicate that the amplification factors are not particularly sensitive to the details of the waveform, and hence the amplification factors derived using the Parkfield mainshock recording are sufficiently representative for the present application.

In Figure 6.11, we plot the theoretical amplification factors as a function of base motion peak acceleration ( $PGA'$ ) for comparison to the observed site amplification factors from recordings. As shown in Figure 6.11, the trend with  $PGA'$  is similar for the theoretical and empirical results, but for most events the site amplification is underpredicted by the models. The model-to-model variation is generally small relative to this misfit. Accordingly, the conclusions

reached above about bias are unlikely to be event-specific phenomena, but something more germane to the modeling.

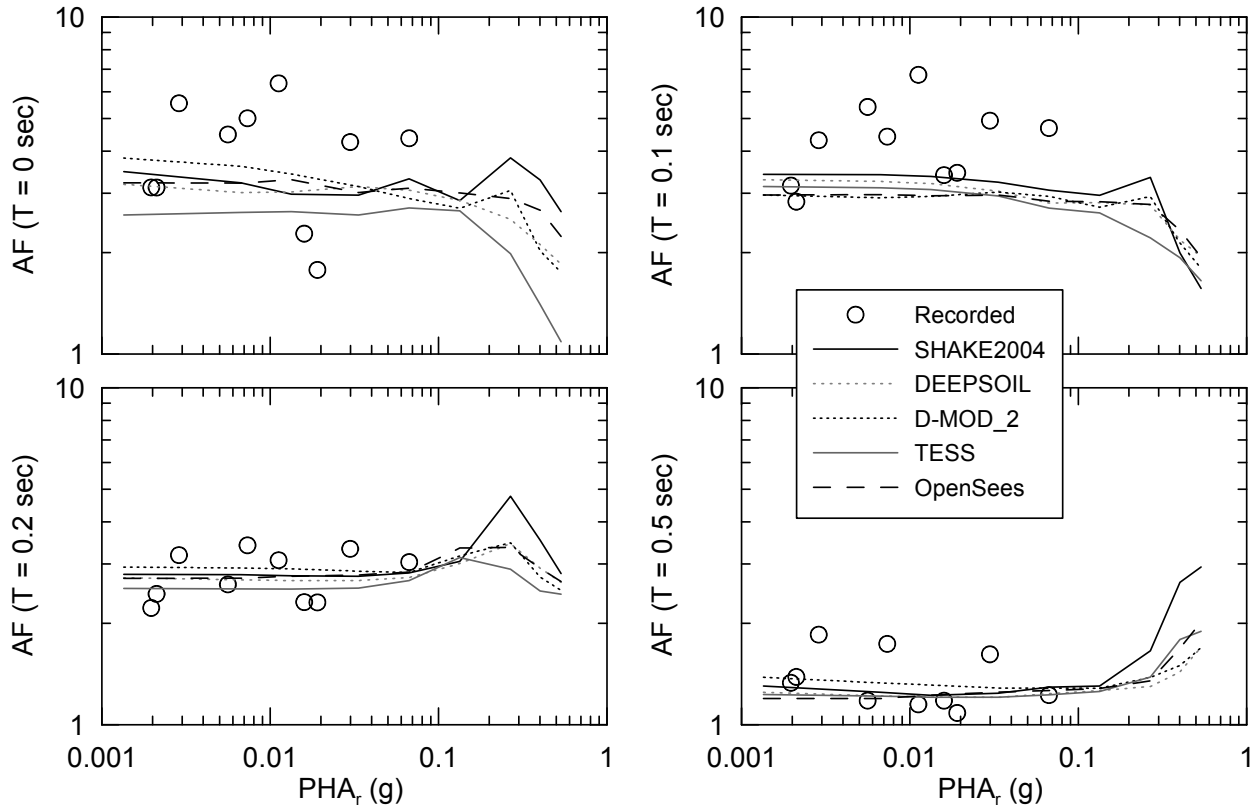


**Fig. 6.11 Theoretical and observed V1/D3 amplification factors at Turkey Flat site for events listed in Table 6.2.**

## 6.10 CODE PERFORMANCE AT HIGHER SHAKING LEVELS

In this section, the code-to-code variability of spectral shape for different levels of site nonlinearity is investigated. Ground response analyses with the baseline geotechnical model are performed with input motions (Parkfield mainshock recording at D3) scaled to higher shaking levels. Spectral shapes of the calculated motions at the ground surface for both horizontal directions are studied.

It can be observed from Figures 6.12 and 6.13 that the spectral shapes from equivalent-linear and nonlinear models are similar when the input motion level is low. However, at high shaking levels (above  $PHA'$  of 0.2 g which corresponds to scale factor above 4), the spectral shapes from equivalent-linear and nonlinear analyses start to deviate from each other. At periods below the site frequency, the spectral shapes from equivalent-linear analyses are flatter and have

less period-to-period fluctuations than those from nonlinear analyses. The spectral shapes ordinates at the site period also tend to be larger for nonlinear models. Note also that at strong shaking levels, the results of the various nonlinear codes differ significantly from each other.

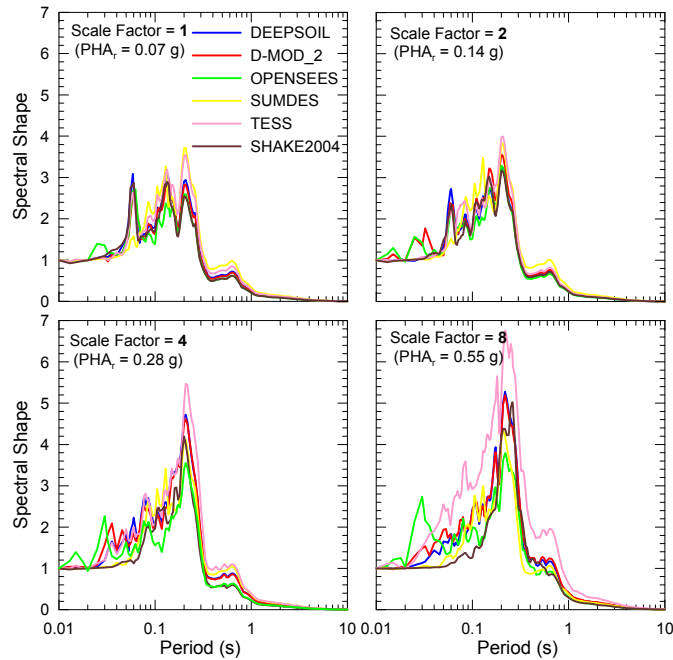


**Fig. 6.12 Comparison of spectral shapes of predictions at different shaking levels for EW component.**

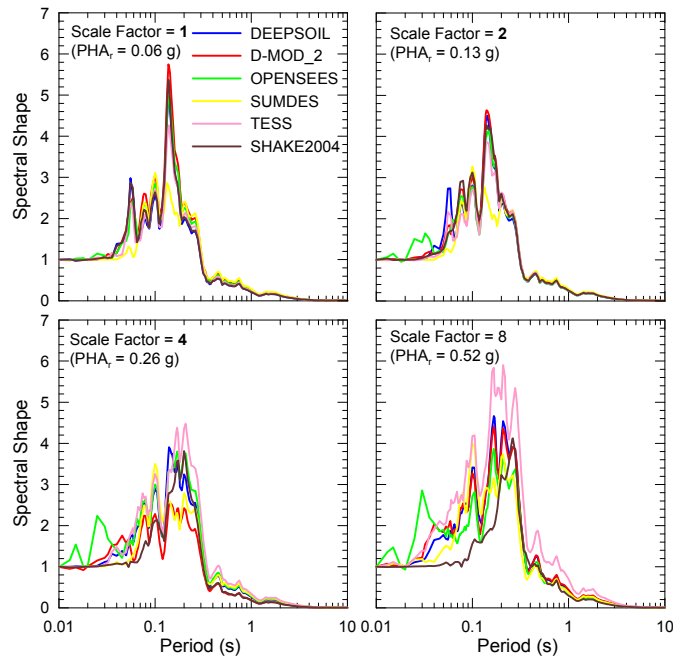


**Fig. 6.13 Comparison of spectral shapes of predictions at different shaking levels for NS component.**

## 6.11 CONCLUSIONS

The two blind prediction exercises performed using the Turkey Flat vertical array have provided a valuable opportunity to investigate our ability to estimate seismic site response. This chapter has focused on the second phase of the most recent blind prediction exercise and subsequent analysis, involving relatively strong motion data from the 2004 Parkfield earthquake.

Using the original material properties provided as part of the prediction exercise, we find that a series of equivalent-linear and nonlinear 1D ground response analysis codes generally underestimate the observed site response over the period range where site response effects are significant (i.e., below the elongated site period). It does not appear that the underestimation can be explained by errors in the representation of damping in the models. We believe the observed bias is a result of errors in the velocity profile. A recently obtained SASW profile (R. Kayen, pers. comm. 2007) has slower velocities through much of the soil column, and results in a significant reduction of residuals for periods lower than the site period. However, analyses with this profile significantly overestimate the site response near the fundamental-mode site period. The cause of this overestimation is the subject of ongoing research, but we suspect that it may be a by-product of 1D modeling of relatively complex 3D site effects, as suggested by previous simulation-based work (Day et al. 2004).

# 7 Verification of Nonlinear Codes against Vertical Array Data

## 7.1 INTRODUCTION

Having developed the parameter selection protocols as described in Chapters 4 and 5, it is necessary to test the effectiveness of these protocols by studying the trends and biases (if any) in the predictions from nonlinear ground response analysis codes. It is also important to study the uncertainties in predictions due to various sources of variability (material properties and modeling schemes). These two issues can be addressed by using vertical array sites by which the predictions can be compared to the “correct” answer from empirical data. Furthermore, it is of interest to compare the performance of equivalent-linear and nonlinear analyses for different levels of shaking (different strain conditions). Four vertical array sites are considered: Turkey Flat, La Cienega, KGWH02 (from the Japanese Kiknet network of strong motion stations), and Lotung. The Turkey Flat study was conducted as part of a blind prediction exercise, and these results are presented separately in Chapter 6. This chapter focuses on the latter two sites (non-blind predictions) and the ground response analyses are performed by using both equivalent-linear (SHAKE04) and nonlinear codes (DEEPSOIL, D-MOD\_2, OpenSees, SUMDES, and TESS). The chapter begins with a description of site conditions for the selected sites, which is followed by a discussion of the geotechnical models employed in the analyses. The results are then presented, followed by a discussion of the trends in the results and the significance of these trends.

## 7.2 SITE CONDITIONS

The available site data include velocity logs and boring logs. Figures 7.1–7.3 show the available shear wave velocity logs from geophysical measurements and the boring logs for the La Cienega, KGWH02, and Lotung sites, respectively (see Fig. 6.2 for the profile of the Turkey Flat site). For

La Cienega, the profile is from SASW testing over a depth range of 0–27.4 m (Roblee, pers. comm. 2002) and suspension logging from 26–278.3 m depth (<http://geoinfo.usc.edu/rosrine/>, last accessed on May 31, 2005). For KGWH02, the shear wave velocity profiles are from SASW testing (Kayen, pers. comm. 2006) and downhole logging (<http://www.kik.bosai.go.jp/>, last accessed on February 12, 2007). For Lotung, the profile over a depth range of 0–47 m was presented by EPRI (1993), which in turn was developed based on crosshole and uphole tests by Anderson and Tang (1989).

## 7.3 GEOTECHNICAL MODEL

### 7.3.1 Shear Wave Velocity Model

The best estimates of the median  $V_s$  profiles for La Cienega, KGWH02, and Lotung, which are used as the baseline geotechnical model for analysis, are shown as solid black lines in Figures 7.1–7.3, respectively. The variability in the  $V_s$  profiles is also considered. Whereas for the Turkey Flat site profile uncertainty was estimated from data (due to multiple measurements at the same site), for the La Cienega, KGWH02, and Lotung sites, profile variability was estimated based on the empirical model of Toro (1997).

The Toro model is based on 176 velocity profiles from the Savannah River site and is a statistical model that can be used to generate randomized velocity profiles. This model consists of a submodel describing the random stratigraphy at a site, a median velocity profile, and a submodel that describes the deviations of the velocity in each layer from the median and its correlation with the velocity in the layer above. It should be mentioned that Toro developed the standard deviation / correlation submodel for both generic (broad geographic region) and site-specific conditions. The variations of standard deviation and correlation coefficient with depth in the Toro model are shown in Figure 7.4. In current analyses, the random stratigraphy feature of the model and the correlation of velocity between layers are not considered.

The alternative velocity profiles for soil are obtained by adding and subtracting to the baseline profile  $\sqrt{3}$  times the depth-dependent site-specific standard deviation from Toro (1997). The  $\sqrt{3}$  factor is used because the theoretical optimal three-point representation of a normal distribution involves sampling the distribution at the mean ( $\mu$ ) and  $\mu \pm \sqrt{3}\sigma$ , and then providing the samples with weights of 2/3 and 1/6 (twice). These sample points and weights preserve the

first (mean), second (variance), and fourth central moments of the underlying distribution (Rosenblueth 1975; Ching et al. 2006). For KGWH02 where the array extends into rock, the standard deviation of velocity in rock region is taken as 0.2 (ln units) (Silva, pers. comm. 2006). The alternative profiles for rock are calculated in a similar way as for the soil. These profiles are shown by the dashed lines in Figures 7.1–7.3.

### 7.3.2 Nonlinear Soil Properties

#### (a) *Target Material Curves*

For La Cienega, 13 material curves are selected to model the nonlinear soil behavior for different depth ranges. These curves are based on material-specific testing as indicated in Table 7.1. For KGWH02, the 15 material curves selected are based on models by Darendeli (2001) (for soil) and Silva et al. (1996) (for rock), as indicated in Table 7.2. Figure 7.5 shows the depth-dependent rock curves developed by Silva et al. (1996). For Lotung, three material curves are selected based on inference of in-situ modulus reduction and damping from vertical array data by Zeghal et al. (1995). These curves are summarized in Table 7.3 and compared to a set of expert-interpreted curves from the EPRI (1993) study. The target curve from EPRI is generally more linear (associated with less reduction and damping) than Zeghal's curves.

All the curves listed in Tables 7.1–7.3 represent the target curves for the baseline geotechnical model. The variability in target material curves for La Cienega and KGWH02 is considered by adding and subtracting to the baseline curves  $\sqrt{3}$  times the strain-dependent standard deviation, taken from Darendeli (2001). The variability in target material curves is considered by adding and subtracting to the baseline curves  $\sqrt{3}$  times the strain-dependent standard deviation, taken from Darendeli (2001). For rock layers, only the variability in the damping curves is considered. The variability in the modulus reduction curves was neglected due to the small strains in rock, resulting in minimal modulus reduction. For Lotung, the upper and lower bounds of the statistical fitting for the back-calculation were estimated by Andrade and Borja (2006) (each bound represents one sigma away from the best fitted curves). The standard deviation in modulus reduction and damping is estimated as half of the distance between the upper- and lower-bound values at a specific strain level. The variability in target material curves is considered by adding and subtracting to the baseline curves  $\sqrt{3}$  times these strain-dependent

standard deviations. Figures 7.6–7.11 plot the target curves along with the variability for La Cienega, KGWH02, and Lotung.

**(b) Fitted Material Curves**

For DEEPSOIL, D-MOD\_2, and OpenSees, the actual curves used in analyses are obtained by a fitting procedure (“MRD fitting”) that can simultaneously minimize the misfit (compared to the target) in modulus reduction and damping curves across a selected strain range (details can be found in Section 4.2). That strain range was taken as “small” ( $\sim 10^{-4}\%$ ) to 1%. For TESS and SUMDES, only the fit of the modulus reduction curve is optimized (‘MR fitting’). For TESS, this is due to developer preference for this approach. For SUMDES, this is due to the manner in which the modulus reduction curve is mathematically described (MRD fits are not practical). The reference strain value is approximated by the pseudo-reference strain as described in Section 4.2. Figures 7.12–7.14 compare the pseudo-reference strains used in different nonlinear codes for La Cienega, KGWH02, and Lotung, respectively. Tables 7.4–7.6 summarize the engineering model used for La Cienega, KGWH02, and Lotung, respectively.

## **7.4 RECORDED MOTIONS**

For La Cienega, the recordings from a  $M_w=4.2$  event that occurred 2.7 km from the site on 09/09/2001 are used, while for KGWH02, the recordings from a  $M_w=6.4$  event that occurred 93 km from the site on 03/24/2001 are used. For Lotung, the recordings from a  $M_w=6.5$  event that occurred 66 km from the site on 05/20/1986 (LSST 7) are used. Figures 7.15 and 7.17 show the acceleration histories recorded at the La Cienega vertical array (0, 18.3, 100.6, and 252.1 m), KGWH02 vertical array (0 and 200 m), and Lotung vertical array (0, 6, 11, 17, 47 m), respectively.

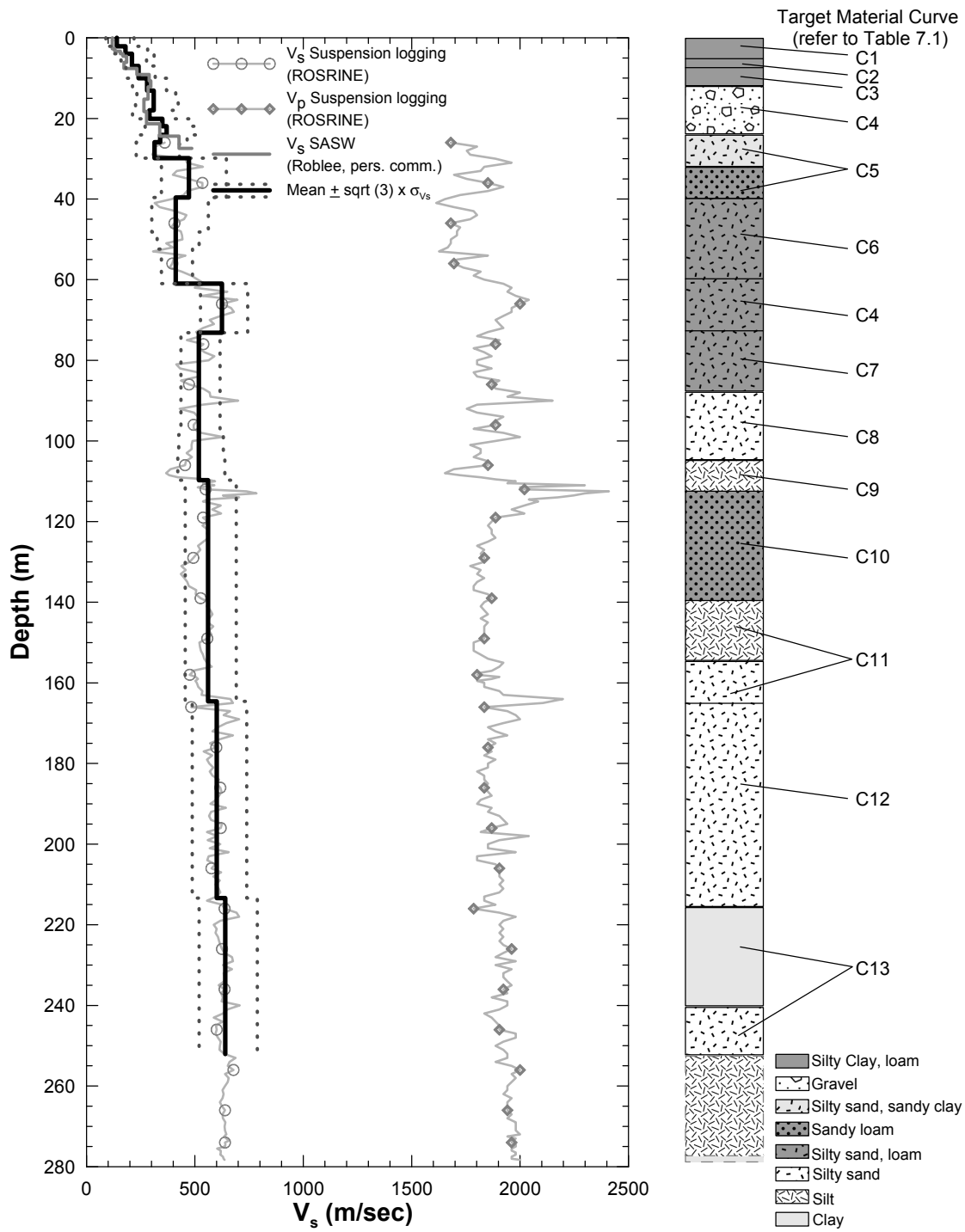


Fig. 7.1 Velocity data and model used for analysis of La Cienega site.

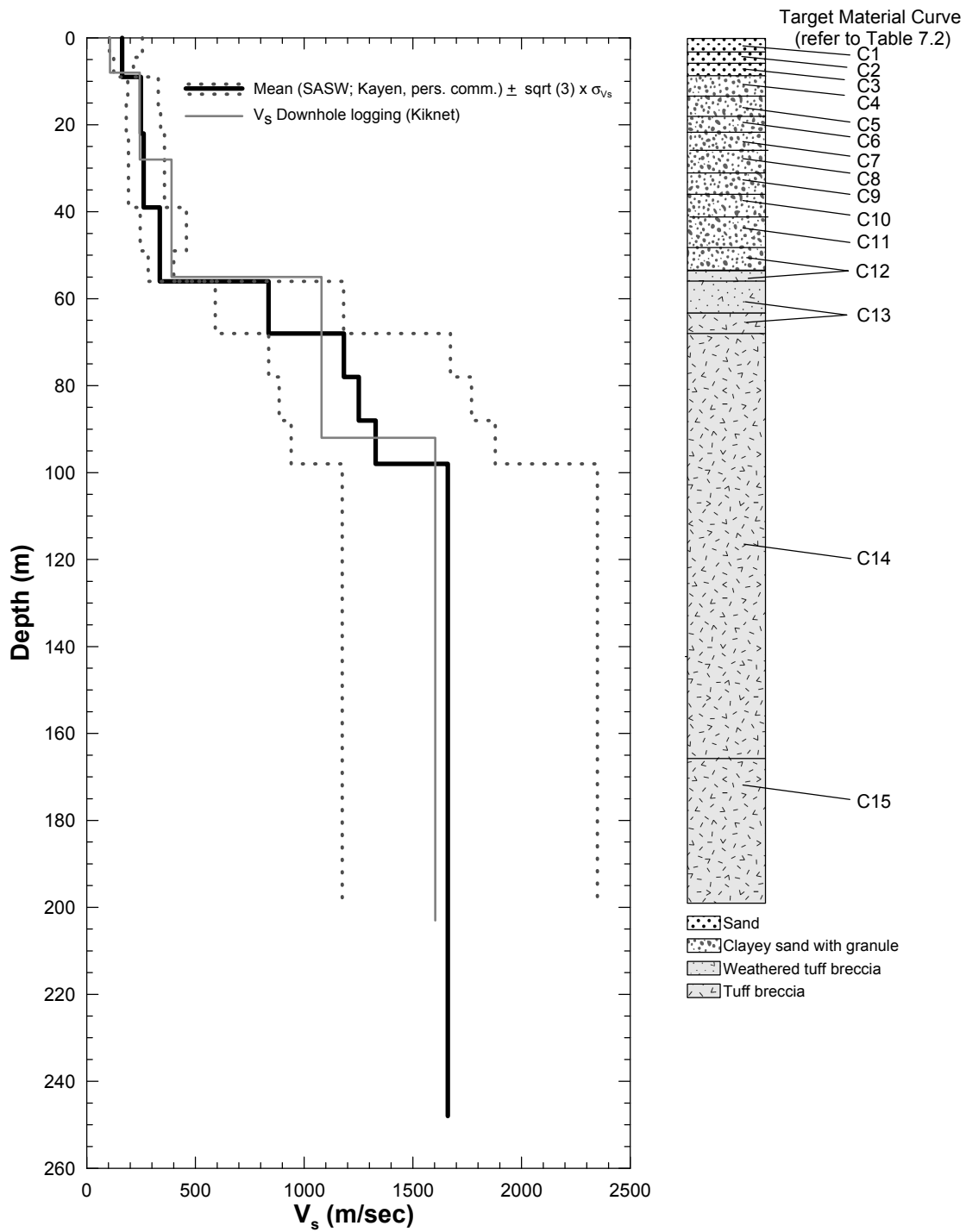
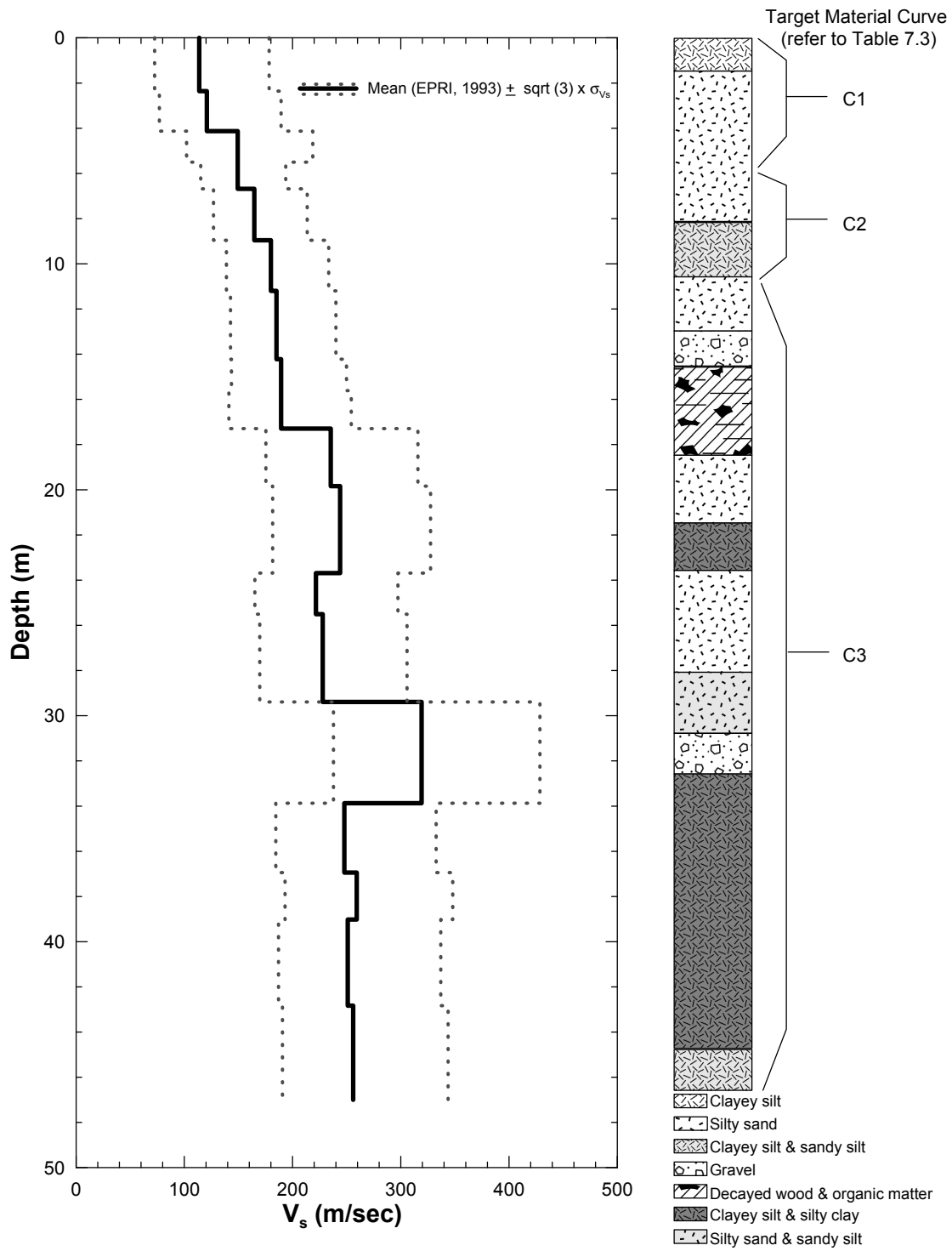
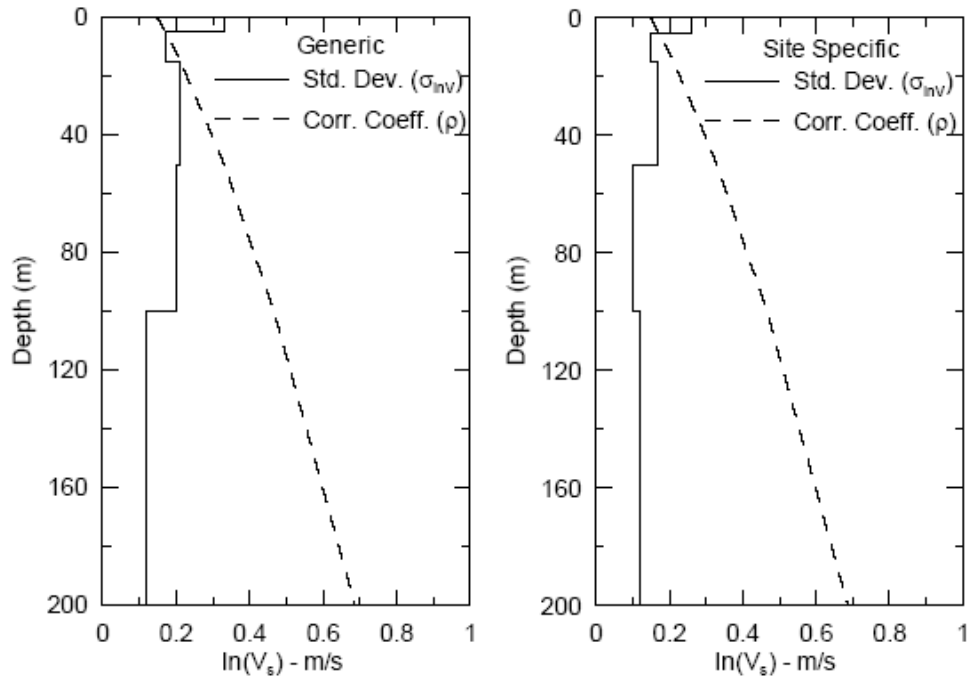


Fig. 7.2 Velocity data and model used for analysis of KWHH02 site.



**Fig. 7.3 Velocity data and model used for analysis of Lotung site.**



**Fig. 7.4 Variation of standard deviation and correlation coefficient with depth for generic and site-specific site profiles (Toro 1997).**

**Table 7.1 Target material curves for La Cienega.**

Target Material Curve #	Description	Source
C1	La Cienega: UCLA Sample L1-1, 4.9 m	ROSRINE
C2	La Cienega: UCLA Sample L2-2, 6.4 m	ROSRINE
C3	La Cienega: UCLA Sample S-5, 7.9 m	ROSRINE
C4	Upper bound sand $G/G_{max}$ curve and lower bound sand damping curve	Seed et al. (1984)
C5	La Cienega: UT Sample L, 36 m	ROSRINE
C6	La Cienega: UT Sample Q, 52.4 m	ROSRINE
C7	Sand for 76.5 - 152.4 m	EPRI (1993)
C8	La Cienega: UT Sample M, 94.5 m	ROSRINE
C9	La Cienega: UT Sample R, 106.7 m	ROSRINE
C10	La Cienega: UT Sample N, 125 m	ROSRINE
C11	La Cienega: UT Sample S, 149.7 m	ROSRINE
C12	La Cienega: UT Sample O, 185.9 m	ROSRINE
C13	La Cienega: UT Sample P, 241.1 m	ROSRINE

**Table 7.2 Target material curves for KGWH02.**

Target Material Curve #	Description	Source
C1	PI = 0, OCR = 1, freq = 2 Hz, Num. Cycle = 10, $\sigma_0' = 0.28$ atm	Darendeli (2001)
C2	PI = 0, OCR = 1, freq = 2 Hz, Num. Cycle = 10, $\sigma_0' = 0.84$ atm	Darendeli (2001)
C3	PI = 0, OCR = 1, freq = 2 Hz, Num. Cycle = 10, $\sigma_0' = 1.40$ atm	Darendeli (2001)
C4	PI = 10, OCR = 1, freq = 2 Hz, Num. Cycle = 10, $\sigma_0' = 2.06$ atm	Darendeli (2001)
C5	PI = 10, OCR = 1, freq = 2 Hz, Num. Cycle = 10, $\sigma_0' = 2.87$ atm	Darendeli (2001)
C6	PI = 10, OCR = 1, freq = 2 Hz, Num. Cycle = 10, $\sigma_0' = 3.68$ atm	Darendeli (2001)
C7	PI = 10, OCR = 1, freq = 2 Hz, Num. Cycle = 10, $\sigma_0' = 4.49$ atm	Darendeli (2001)
C8	PI = 10, OCR = 1, freq = 2 Hz, Num. Cycle = 10, $\sigma_0' = 5.40$ atm	Darendeli (2001)
C9	PI = 10, OCR = 1, freq = 2 Hz, Num. Cycle = 10, $\sigma_0' = 6.33$ atm	Darendeli (2001)
C10	PI = 10, OCR = 1, freq = 2 Hz, Num. Cycle = 10, $\sigma_0' = 7.28$ atm	Darendeli (2001)
C11	PI = 10, OCR = 1, freq = 2 Hz, Num. Cycle = 10, $\sigma_0' = 8.47$ atm	Darendeli (2001)
C12	PI = 10, OCR = 1, freq = 2 Hz, Num. Cycle = 10, $\sigma_0' = 9.77$ atm	Darendeli (2001)
C13	PI = 0, OCR = 1, freq = 2 Hz, Num. Cycle = 10, $\sigma_0' = 11.63$ atm	Darendeli (2001)
C14	Rock: 76.5 - 152.4 m	Silva et al. (1996)
C15	Rock: 152.4 - 304.8 m	Silva et al. (1996)

**Table 7.3 Target material curves for Lotung.**

Target Material Curve #	Description	Source
C1	Lotung: Back Calculation at 6 m	Zeghal et al. (1995)
C2	Lotung: Back Calculation at 11 m	Zeghal et al. (1995)
C3	Lotung: Back Calculation at 17 m	Zeghal et al. (1995)

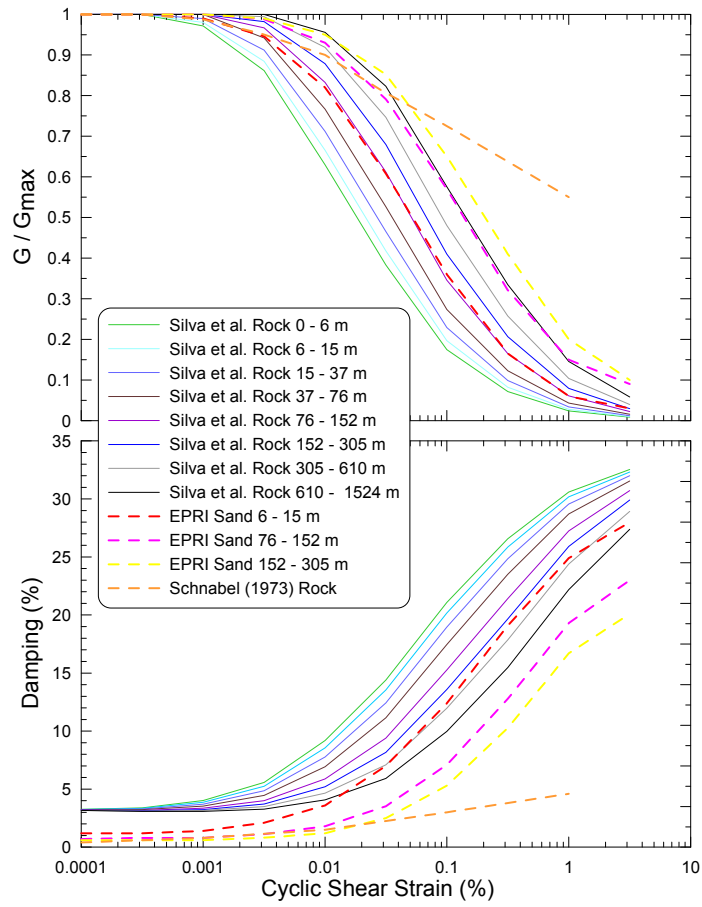


**Fig. 7.5 Material curves for rock developed by Silva et al. (1996).**

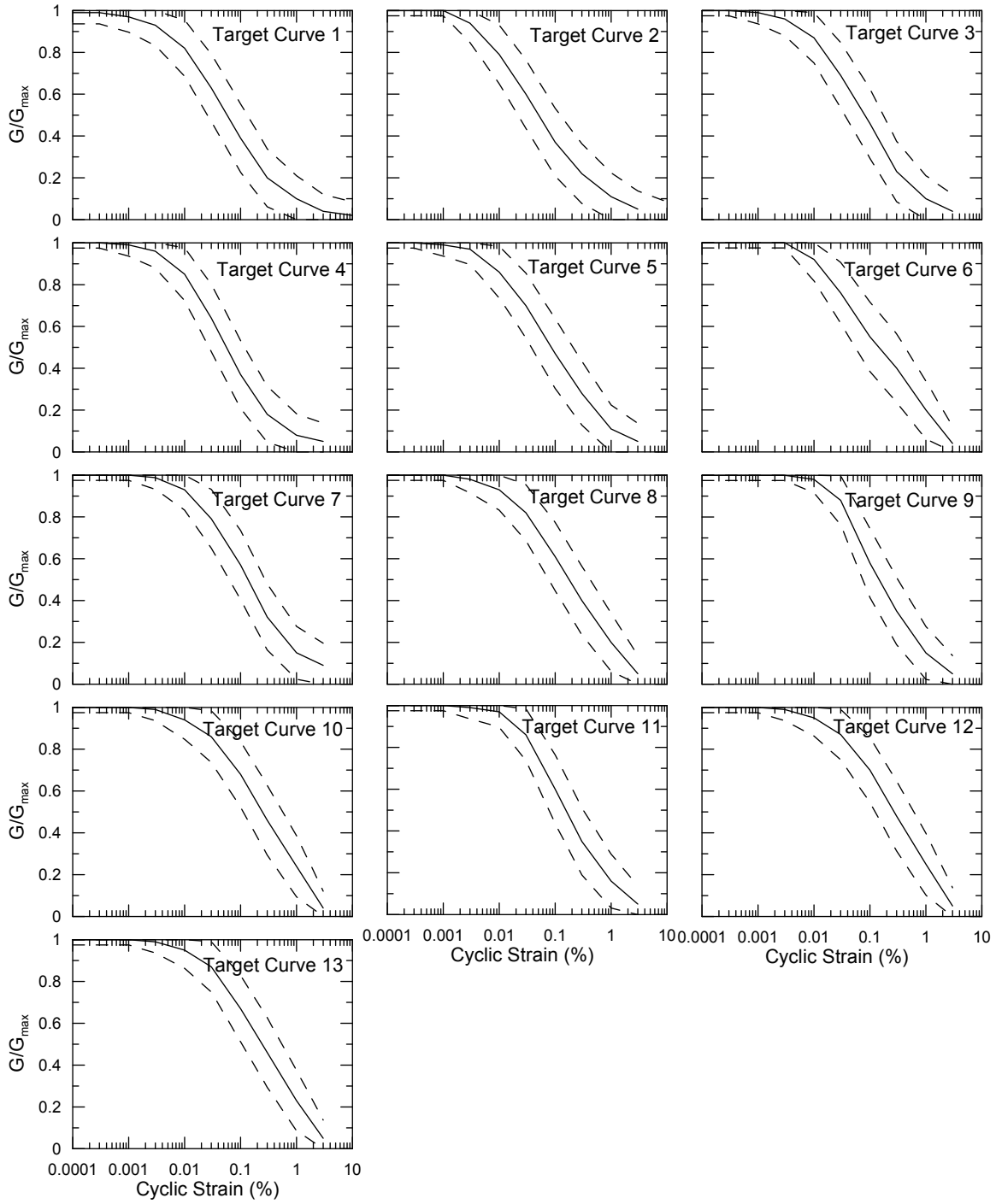


**Fig. 7.6 Target upper and lower bounds ( $\pm\sqrt{3}\sigma$ ) of modulus reduction curve for La Cienega.**

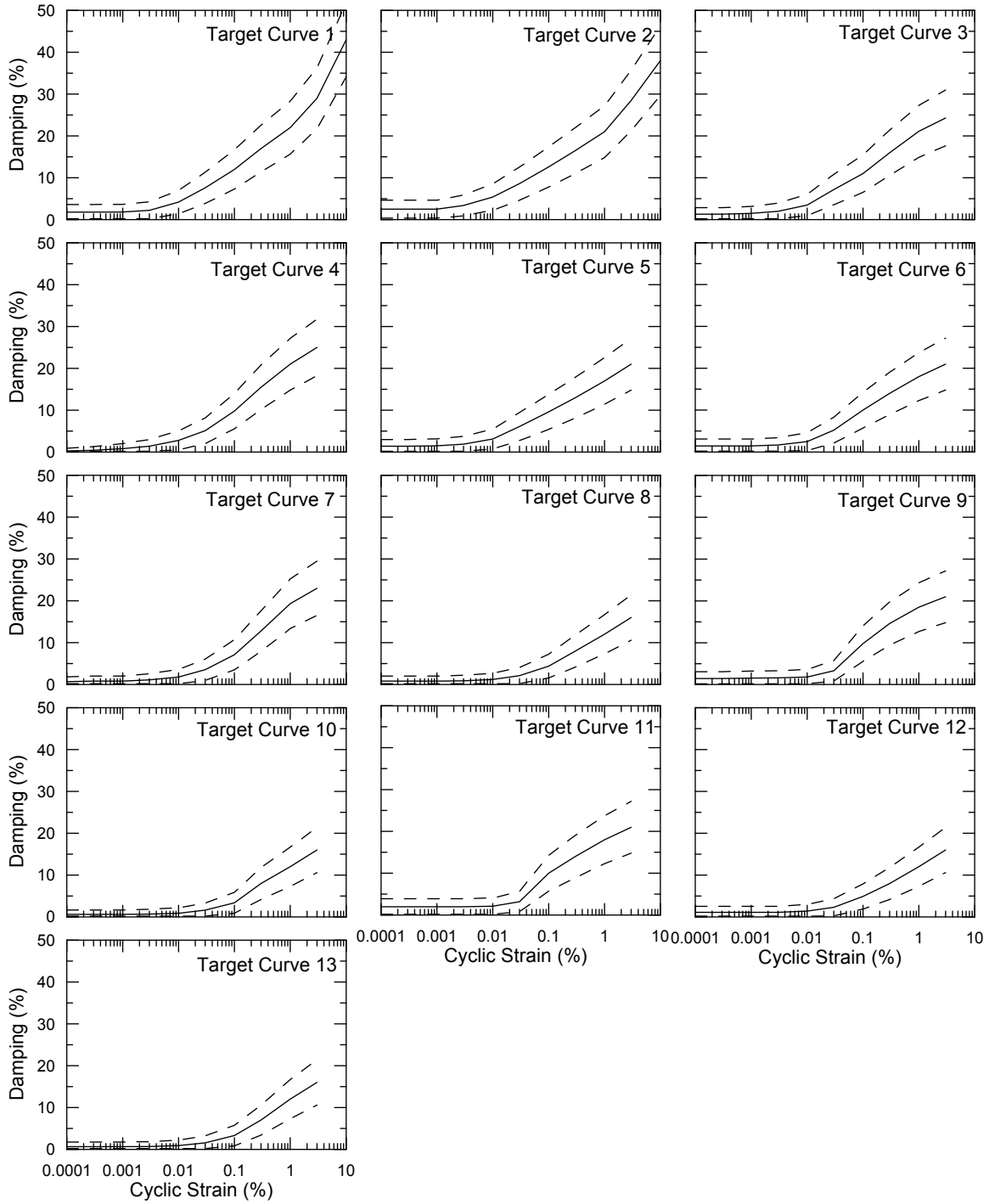


**Fig. 7.7** Target upper and lower bounds ( $\pm\sqrt{3}\sigma$ ) of damping curves for La Cienega.

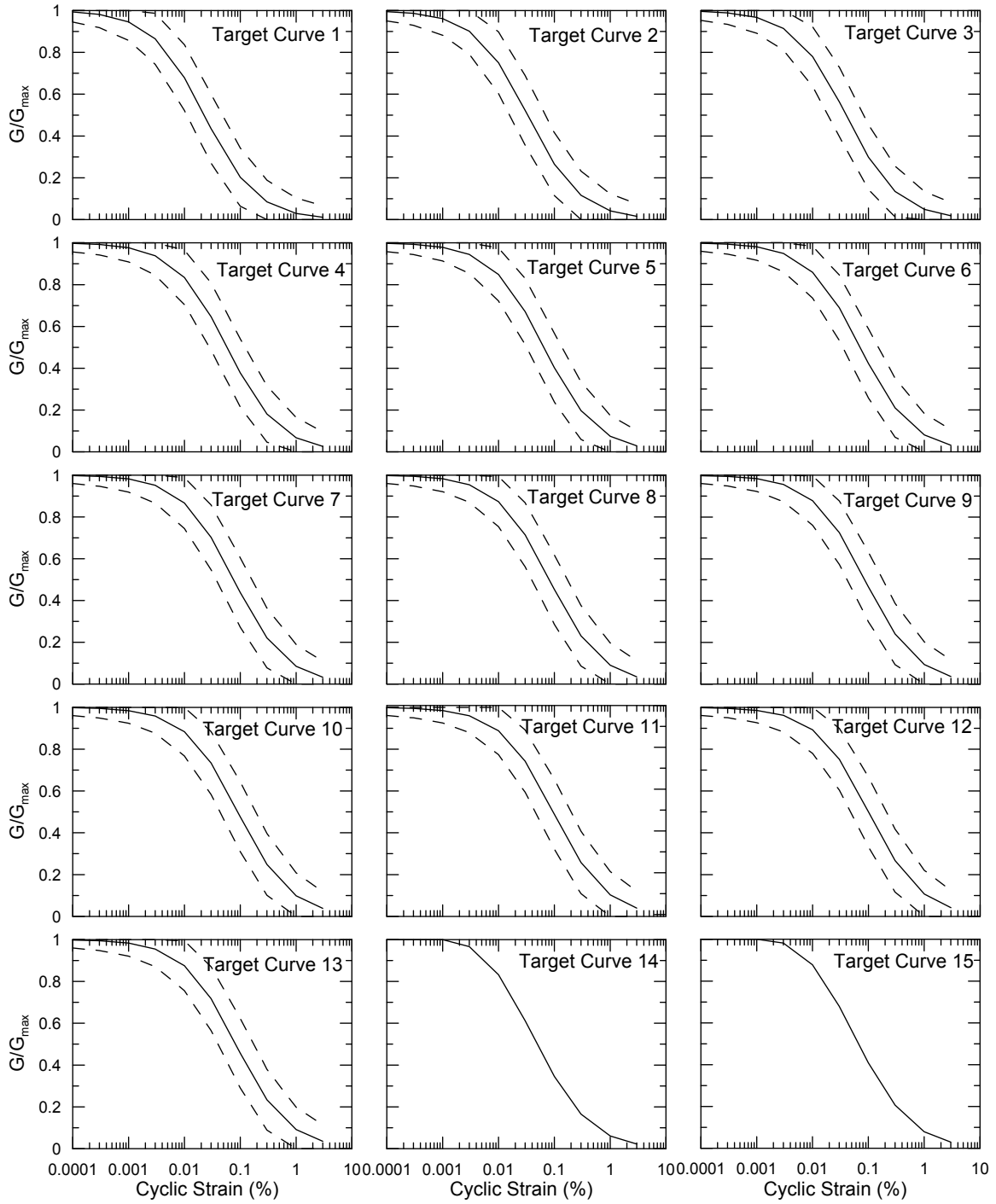


**Fig. 7.8 Target upper and lower bounds ( $\pm\sqrt{3}\sigma$ ) of modulus reduction curve for KGWH02.**

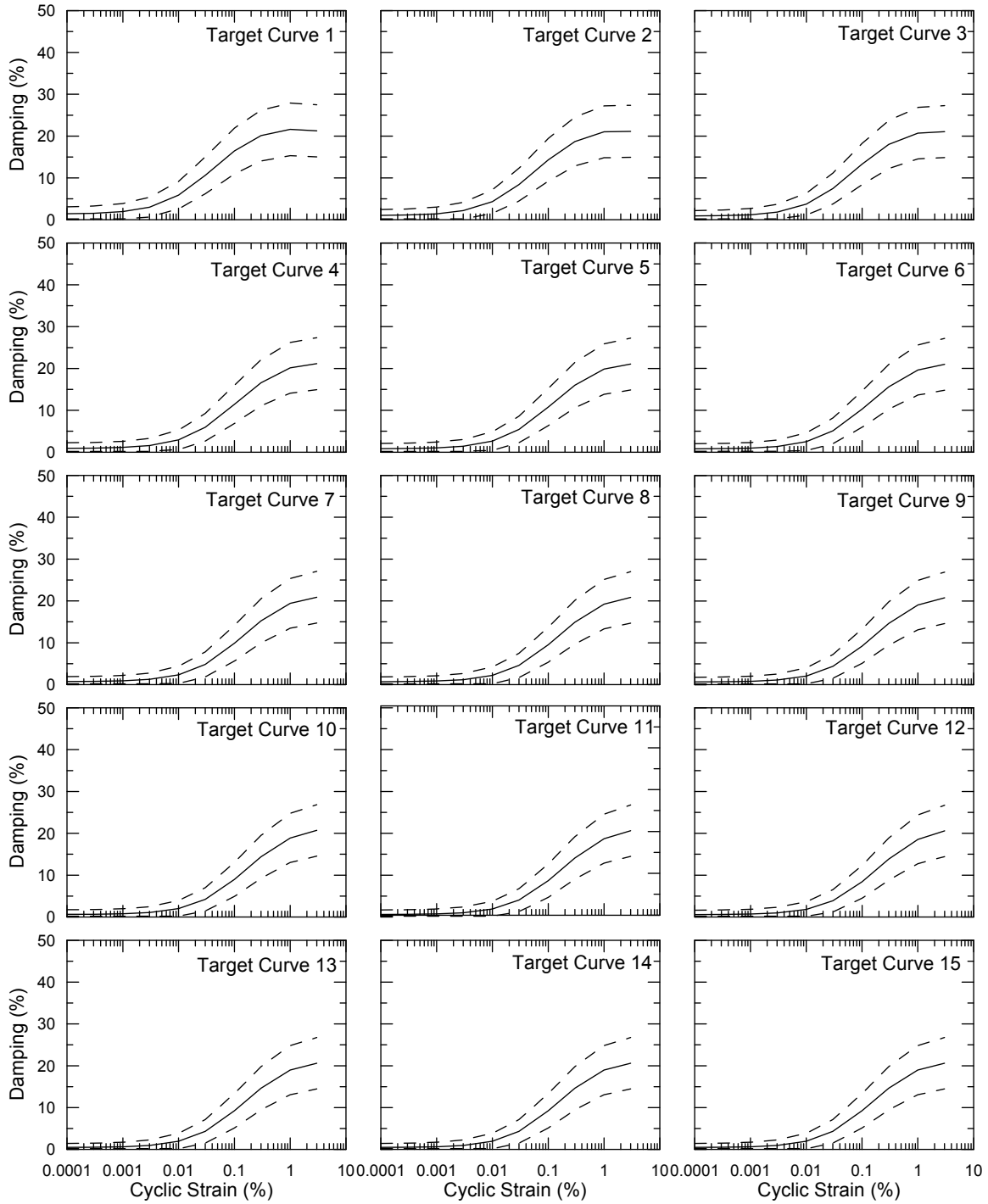


**Fig. 7.9 Target upper and lower bounds ( $\pm\sqrt{3}\sigma$ ) of damping curves for KGWH02.**

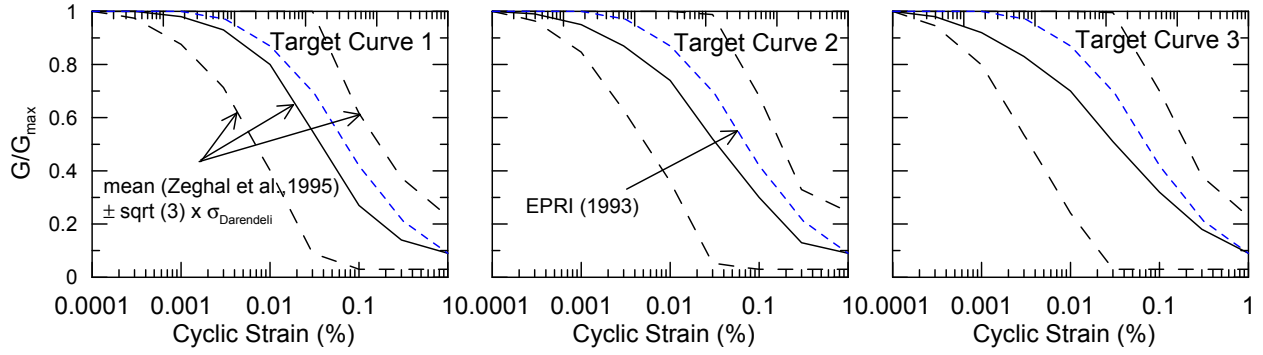


**Fig. 7.10 Target upper and lower bounds ( $\pm\sqrt{3}\sigma$ ) of modulus reduction curve for Lotung.**

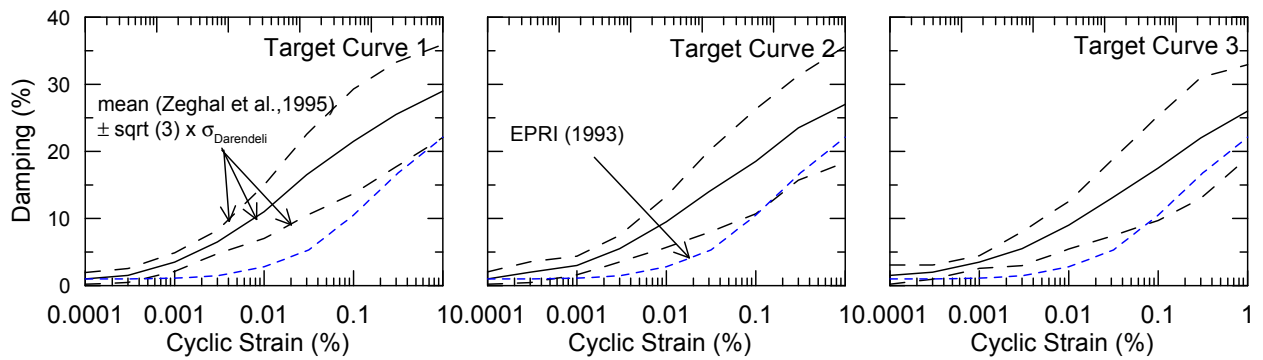


**Fig. 7.11 Target upper and lower bounds ( $\pm\sqrt{3}\sigma$ ) of damping curves for Lotung.**

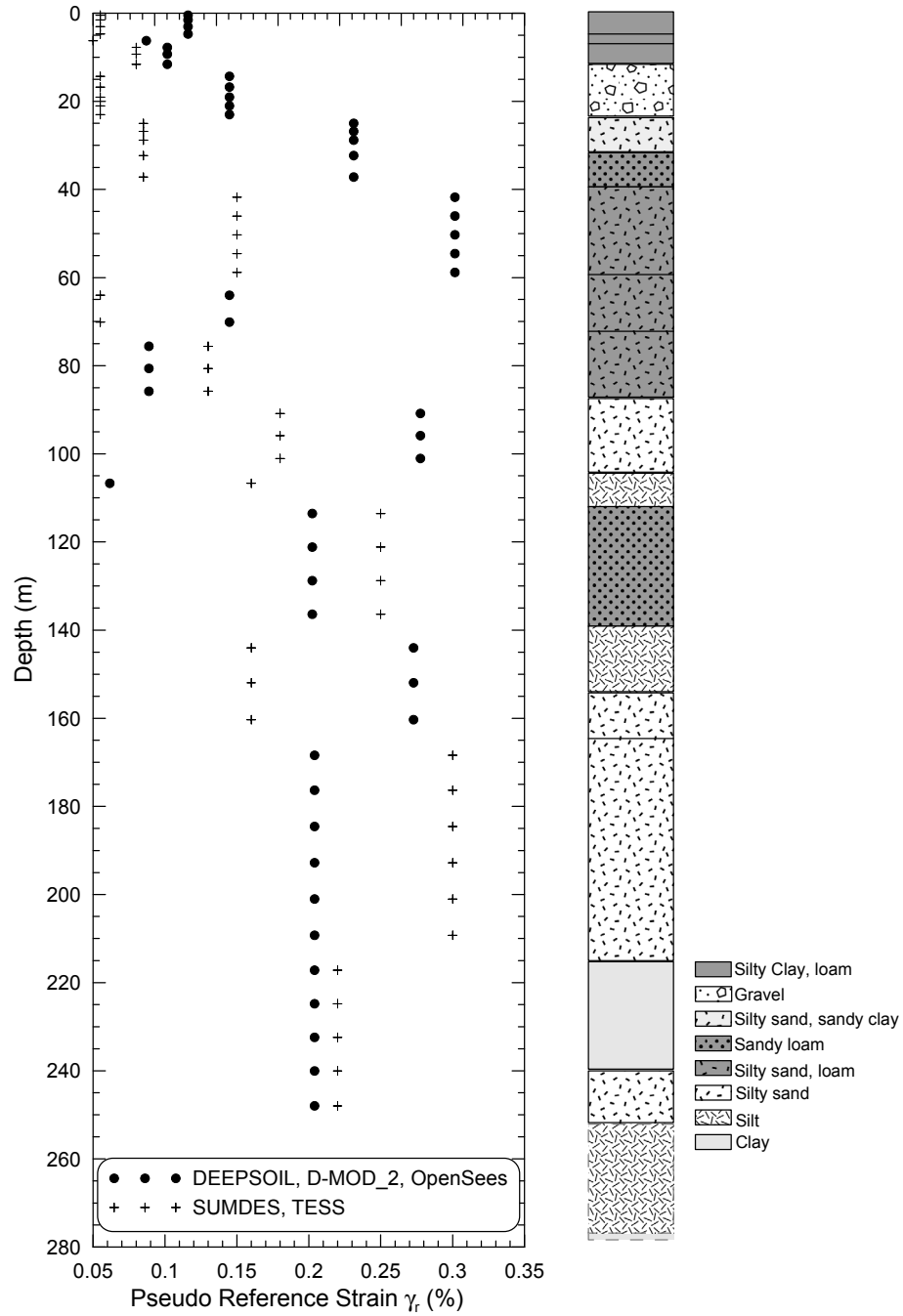


**Fig. 7.12 Reference strains used in different nonlinear codes for La Cienega.**

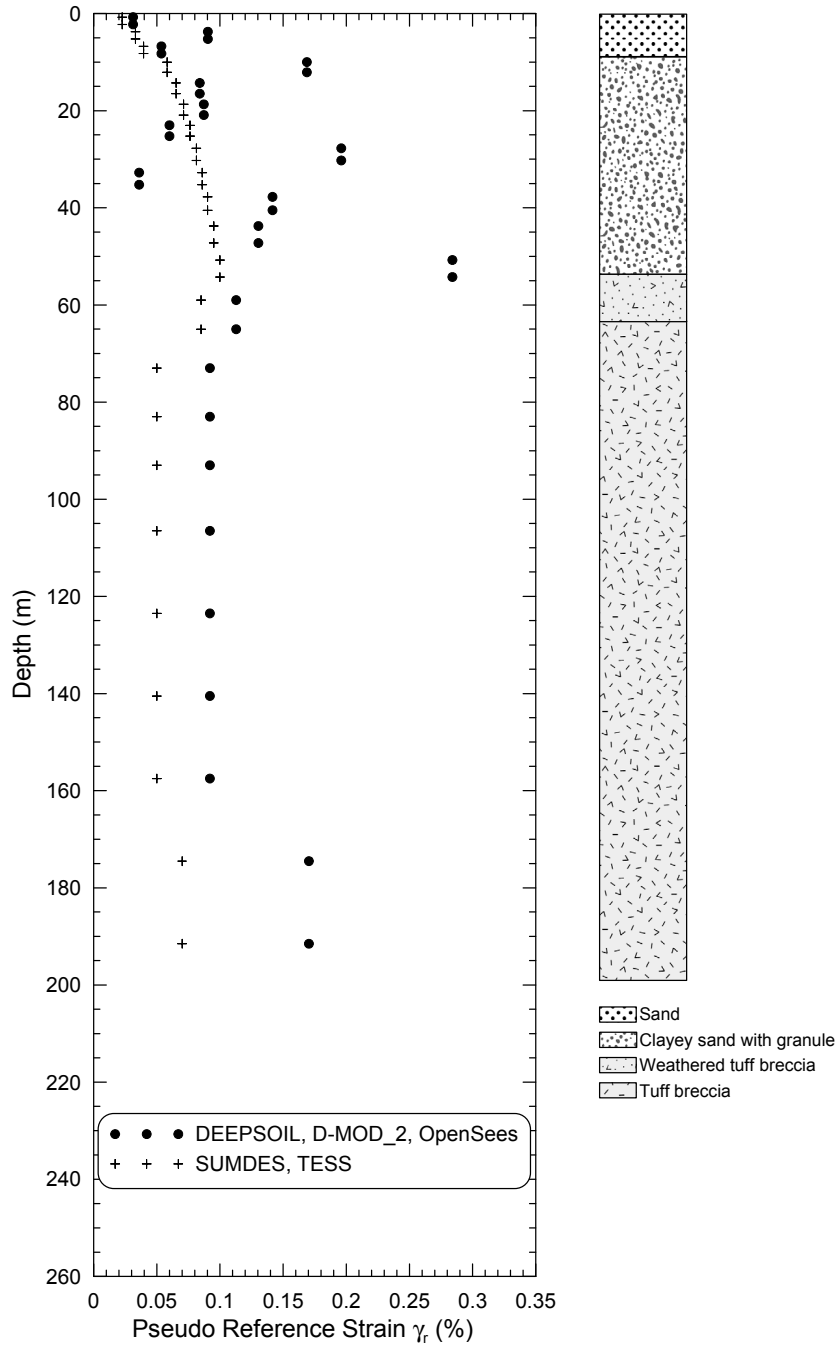


**Fig. 7.13 Reference strains used in different nonlinear codes for KGWH02.**

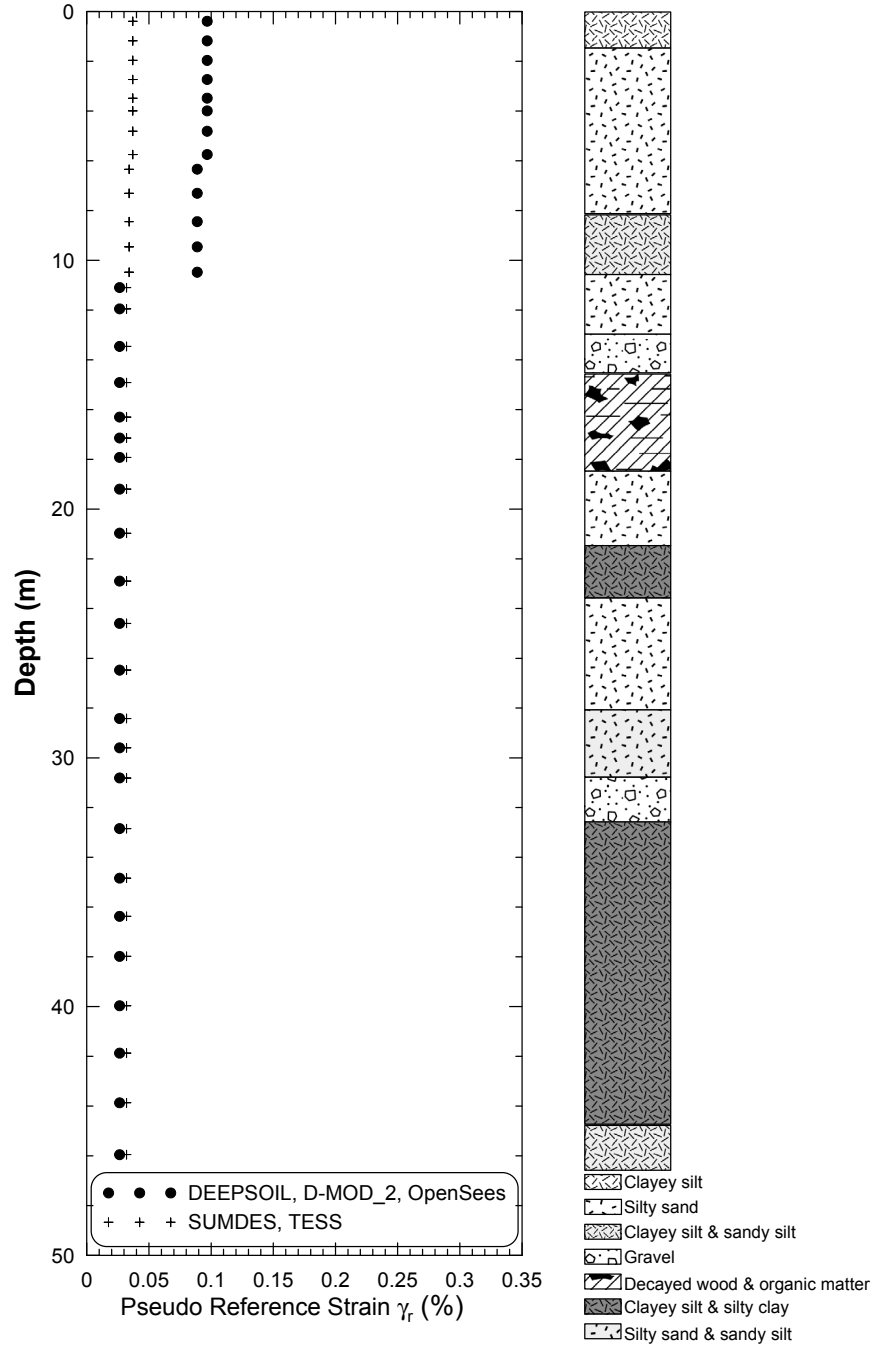


**Fig. 7.14 Reference strains used in different nonlinear codes for Lotung.**

**Table 7.4 Summary of engineering model for La Cienega.**

Layer #	Thickness (m)	Vs (m/s)	$\sigma_v$ (ln(m/s))	Unit Weight (kN/m <sup>3</sup> )	Target Material Curve	Fitted Curves for D-MOD 2, DEEPSOIL and OpenSees				Fitted Curves for TESS		
						$\gamma$ (%)	$\beta$	s	Viscous Damping (%)	$\gamma$ (%)*	VT (%)	$\alpha$
1	0.9	140	0.26	20.1	1	0.116	1.50	0.70	1.80	0.055	1.80	0.85
2	1.2	140	0.26	20.1	1	0.116	1.50	0.70	1.80	0.055	1.80	0.85
3	1.8	180	0.26	20.1	1	0.116	1.50	0.70	1.80	0.055	1.80	0.85
4	1.5	210	0.23	20.1	1	0.116	1.50	0.70	1.80	0.055	1.80	0.85
5	1.5	210	0.16	20.1	2	0.087	1.26	0.66	2.50	0.080	2.50	0.85
6	1.5	240	0.16	20.1	3	0.102	1.10	0.74	1.30	0.080	1.30	0.85
7	1.5	240	0.16	20.1	3	0.102	1.10	0.74	1.30	0.080	1.30	0.85
8	3.0	280	0.16	20.1	3	0.102	1.10	0.74	1.30	0.080	1.30	0.85
9	2.4	310	0.16	20.1	4	0.145	1.74	0.70	0.24	0.055	0.24	0.85
10	2.4	310	0.18	20.1	4	0.145	1.74	0.70	0.24	0.055	0.24	0.85
11	2.1	290	0.18	20.1	4	0.145	1.74	0.70	0.24	0.055	0.24	0.85
12	1.8	350	0.18	20.1	4	0.145	1.74	0.70	0.24	0.055	0.24	0.85
13	2.1	370	0.18	20.1	4	0.145	1.74	0.70	0.24	0.055	0.24	0.85
14	1.8	340	0.18	20.1	5	0.231	1.70	0.66	1.40	0.085	1.40	0.85
15	1.8	314	0.18	20.1	5	0.231	1.70	0.66	1.40	0.085	1.40	0.85
16	2.1	314	0.18	20.1	5	0.231	1.70	0.66	1.40	0.085	1.40	0.85
17	4.9	472	0.18	20.1	5	0.231	1.70	0.66	1.40	0.085	1.40	0.85
18	4.9	472	0.18	20.1	5	0.231	1.70	0.66	1.40	0.085	1.40	0.85
19	4.3	411	0.18	20.1	6	0.302	1.50	0.70	1.44	0.150	1.44	0.85
20	4.3	411	0.18	20.1	6	0.302	1.50	0.70	1.44	0.150	1.44	0.85
21	4.3	411	0.13	20.1	6	0.302	1.50	0.70	1.44	0.150	1.44	0.85
22	4.3	411	0.10	20.1	6	0.302	1.50	0.70	1.44	0.150	1.44	0.85
23	4.3	411	0.10	20.1	6	0.302	1.50	0.70	1.44	0.150	1.44	0.85
24	6.1	625	0.10	20.1	4	0.145	1.74	0.70	0.24	0.055	0.24	0.85
25	6.1	625	0.10	20.1	4	0.145	1.74	0.70	0.24	0.055	0.24	0.85
26	4.9	518	0.10	20.1	7	0.089	0.66	0.74	0.70	0.130	0.70	0.85
27	5.2	518	0.10	20.1	7	0.089	0.66	0.74	0.70	0.130	0.70	0.85
28	5.2	518	0.10	20.1	7	0.089	0.66	0.74	0.70	0.130	0.70	0.85
29	4.9	518	0.10	20.1	8	0.278	1.10	0.62	0.80	0.180	0.80	0.85
30	5.2	518	0.10	20.1	8	0.278	1.10	0.62	0.80	0.180	0.80	0.85
31	5.2	518	0.11	20.1	8	0.278	1.10	0.62	0.80	0.180	0.80	0.85
32	6.1	518	0.12	20.1	9	0.062	0.42	0.78	1.45	0.160	1.45	0.80
33	7.6	561	0.12	20.1	10	0.202	0.74	0.66	0.60	0.250	0.60	0.85
34	7.6	561	0.12	20.1	10	0.202	0.74	0.66	0.60	0.250	0.60	0.85
35	7.6	561	0.12	20.1	10	0.202	0.74	0.66	0.60	0.250	0.60	0.85
36	7.6	561	0.12	20.1	10	0.202	0.74	0.66	0.60	0.250	0.60	0.85
37	7.6	561	0.12	20.1	11	0.273	1.30	0.74	2.00	0.160	2.00	0.80
38	8.2	561	0.12	20.1	11	0.273	1.30	0.74	2.00	0.160	2.00	0.80
39	8.5	561	0.12	20.1	11	0.273	1.30	0.74	2.00	0.160	2.00	0.80
40	7.6	600	0.12	20.1	12	0.204	0.70	0.66	1.10	0.300	1.10	0.85
41	8.2	600	0.12	20.1	12	0.204	0.70	0.66	1.10	0.300	1.10	0.85
42	8.2	600	0.12	20.1	12	0.204	0.70	0.66	1.10	0.300	1.10	0.85
43	8.2	600	0.12	20.1	12	0.204	0.70	0.66	1.10	0.300	1.10	0.85
44	8.2	600	0.12	20.1	12	0.204	0.70	0.66	1.10	0.300	1.10	0.85
45	8.2	600	0.12	20.1	12	0.204	0.70	0.66	1.10	0.300	1.10	0.85
46	7.6	640	0.12	20.1	13	0.204	0.74	0.66	0.65	0.220	0.65	0.85
47	7.6	640	0.12	20.1	13	0.204	0.74	0.66	0.65	0.220	0.65	0.85
48	7.6	640	0.12	20.1	13	0.204	0.74	0.66	0.65	0.220	0.65	0.85
49	7.6	640	0.12	20.1	13	0.204	0.74	0.66	0.65	0.220	0.65	0.85
50	8.2	640	0.12	20.1	13	0.204	0.74	0.66	0.65	0.220	0.65	0.85

\* All values in SI units

**Table 7.5 Summary of engineering model for Kiknet KGWH02.**

Layer #	Thickness (m)	Vs (m/s)	$\sigma_v$ (ln(m/s))	Unit Weight (kN/m <sup>3</sup> )	Target Material Curve	Fitted Curves for D-MOD 2, DEEPSOIL and OpenSees				Fitted Curves for TESS		
						$\gamma$ (%)	$\beta$	s	Viscous Damping (%)	$\gamma$ (%)*	VT (%)	$\alpha$
1	1.5	163	0.26	18.9	1	0.031	1.18	0.66	1.45	0.023	1.45	0.85
2	1.5	163	0.26	18.9	1	0.031	1.18	0.66	1.45	0.023	1.45	0.85
3	1.5	163	0.26	18.9	2	0.090	1.86	0.70	1.05	0.033	1.05	0.85
4	1.5	163	0.16	18.9	2	0.090	1.86	0.70	1.05	0.033	1.05	0.85
5	1.5	163	0.16	18.9	3	0.054	1.14	0.70	0.91	0.040	0.91	0.85
6	1.5	163	0.16	18.9	3	0.054	1.14	0.70	0.91	0.040	0.91	0.85
7	2.0	249	0.16	18.9	4	0.169	1.94	0.70	0.93	0.058	0.93	0.85
8	2.2	249	0.16	18.9	4	0.169	1.94	0.70	0.93	0.058	0.93	0.85
9	2.2	249	0.16	18.9	5	0.084	1.10	0.70	0.85	0.065	0.85	0.85
10	2.2	249	0.18	18.9	5	0.084	1.10	0.70	0.85	0.065	0.85	0.85
11	2.2	249	0.18	18.9	6	0.087	1.06	0.70	0.79	0.071	0.79	0.85
12	2.2	249	0.18	18.9	6	0.087	1.06	0.70	0.79	0.071	0.79	0.85
13	2.0	262	0.18	18.9	7	0.060	0.78	0.70	0.74	0.076	0.74	0.85
14	2.5	262	0.18	18.9	7	0.060	0.78	0.70	0.74	0.076	0.74	0.85
15	2.5	262	0.18	18.9	8	0.196	1.70	0.70	0.70	0.081	0.70	0.85
16	2.5	262	0.18	18.9	8	0.196	1.70	0.70	0.70	0.081	0.70	0.85
17	2.5	262	0.18	18.9	9	0.036	0.50	0.70	0.67	0.086	0.67	0.85
18	2.5	262	0.18	18.9	9	0.036	0.50	0.70	0.67	0.086	0.67	0.85
19	2.5	262	0.18	18.9	10	0.142	1.26	0.70	0.64	0.090	0.64	0.85
20	3.0	336	0.18	18.9	10	0.142	1.26	0.70	0.64	0.090	0.64	0.85
21	3.5	336	0.18	18.9	11	0.130	1.14	0.70	0.62	0.095	0.62	0.85
22	3.5	336	0.18	18.9	11	0.130	1.14	0.70	0.62	0.095	0.62	0.85
23	3.5	336	0.10	18.9	12	0.284	1.90	0.70	0.59	0.100	0.59	0.85
24	3.5	336	0.10	18.9	12	0.284	1.90	0.70	0.59	0.100	0.59	0.85
25	6.0	836	0.20	20.4	13	0.113	1.14	0.70	0.49	0.085	0.49	0.85
26	6.0	836	0.20	20.4	13	0.113	1.14	0.70	0.49	0.085	0.49	0.85
27	10.0	1183	0.20	21.2	14	0.092	1.42	0.78	3.17	0.050	3.17	0.85
28	10.0	1252	0.20	21.2	14	0.092	1.42	0.78	3.17	0.050	3.17	0.85
29	10.0	1329	0.20	21.2	14	0.092	1.42	0.78	3.17	0.050	3.17	0.85
30	17.0	1661	0.20	21.2	14	0.092	1.42	0.78	3.17	0.050	3.17	0.85
31	17.0	1661	0.20	21.2	14	0.092	1.42	0.78	3.17	0.050	3.17	0.85
32	17.0	1661	0.20	21.2	14	0.092	1.42	0.78	3.17	0.050	3.17	0.85
33	17.0	1661	0.20	21.2	14	0.092	1.42	0.78	3.17	0.050	3.17	0.85
34	17.0	1661	0.20	21.2	15	0.170	1.82	0.78	3.13	0.070	3.13	0.85
35	17.0	1661	0.20	21.2	15	0.170	1.82	0.78	3.13	0.070	3.13	0.85

\* Also used in STAMP

**Table 7.6 Summary of engineering model for Lotung.**

Layer #	Thickness (m)	Vs (m/s)	$\sigma_v$ (ln(m/s))	Unit Weight (kN/m <sup>3</sup> )	Target Material Curve	Fitted Curves for D-MOD 2, DEEPSOIL and OpenSees				Fitted Curves for TESS		
						$\gamma$ (%)	$\beta$	s	Viscous Damping (%)	$\gamma$ (%)*	VT (%)	$\alpha$
1	0.8	114	0.26	17.6	1	0.097	2.06	0.78	1.00	0.037	1.00	0.85
2	0.8	114	0.26	17.6	1	0.097	2.06	0.78	1.00	0.037	1.00	0.85
3	0.8	114	0.26	17.6	1	0.097	2.06	0.78	1.00	0.037	1.00	0.85
4	0.7	121	0.26	17.6	1	0.097	2.06	0.78	1.00	0.037	1.00	0.85
5	0.7	121	0.26	17.6	1	0.097	2.06	0.78	1.00	0.037	1.00	0.85
6	0.3	121	0.26	17.6	1	0.097	2.06	0.78	1.00	0.037	1.00	0.85
7	1.4	149	0.22	17.6	1	0.097	2.06	0.78	1.00	0.037	1.00	0.85
8	0.5	149	0.15	17.6	1	0.097	2.06	0.78	1.00	0.037	1.00	0.85
9	0.7	149	0.15	17.6	2	0.089	2.02	0.74	1.00	0.034	1.00	0.85
10	1.3	165	0.15	18.1	2	0.089	2.02	0.74	1.00	0.034	1.00	0.85
11	1.0	165	0.15	18.1	2	0.089	2.02	0.74	1.00	0.034	1.00	0.85
12	1.0	180	0.15	18.1	2	0.089	2.02	0.74	1.00	0.034	1.00	0.85
13	1.0	180	0.15	18.1	2	0.089	2.02	0.74	1.00	0.034	1.00	0.85
14	0.2	180	0.15	17.6	3	0.026	0.86	0.66	1.50	0.032	1.50	0.85
15	1.5	185	0.15	17.6	3	0.026	0.86	0.66	1.50	0.032	1.50	0.85
16	1.5	185	0.15	17.6	3	0.026	0.86	0.66	1.50	0.032	1.50	0.85
17	1.4	189	0.16	17.6	3	0.026	0.86	0.66	1.50	0.032	1.50	0.85
18	1.4	189	0.17	17.6	3	0.026	0.86	0.66	1.50	0.032	1.50	0.85
19	0.3	189	0.17	19.7	3	0.026	0.86	0.66	1.50	0.032	1.50	0.85
20	1.3	235	0.17	19.7	3	0.026	0.86	0.66	1.50	0.032	1.50	0.85
21	1.3	235	0.17	19.7	3	0.026	0.86	0.66	1.50	0.032	1.50	0.85
22	2.3	244	0.17	19.7	3	0.026	0.86	0.66	1.50	0.032	1.50	0.85
23	1.6	244	0.17	18.7	3	0.026	0.86	0.66	1.50	0.032	1.50	0.85
24	1.8	222	0.17	18.7	3	0.026	0.86	0.66	1.50	0.032	1.50	0.85
25	1.9	228	0.17	18.7	3	0.026	0.86	0.66	1.50	0.032	1.50	0.85
26	1.9	228	0.17	18.7	3	0.026	0.86	0.66	1.50	0.032	1.50	0.85
27	0.4	319	0.17	18.7	3	0.026	0.86	0.66	1.50	0.032	1.50	0.85
28	2.0	319	0.17	18.7	3	0.026	0.86	0.66	1.50	0.032	1.50	0.85
29	2.1	319	0.17	18.7	3	0.026	0.86	0.66	1.50	0.032	1.50	0.85
30	1.9	248	0.17	18.7	3	0.026	0.86	0.66	1.50	0.032	1.50	0.85
31	1.1	248	0.17	18.7	3	0.026	0.86	0.66	1.50	0.032	1.50	0.85
32	2.1	259	0.17	17.6	3	0.026	0.86	0.66	1.50	0.032	1.50	0.85
33	1.9	251	0.17	17.6	3	0.026	0.86	0.66	1.50	0.032	1.50	0.85
34	1.9	251	0.17	17.6	3	0.026	0.86	0.66	1.50	0.032	1.50	0.85
35	2.1	256	0.17	19.7	3	0.026	0.86	0.66	1.50	0.032	1.50	0.85
36	2.1	256	0.17	19.7	3	0.026	0.86	0.66	1.50	0.032	1.50	0.85

\* Also used in STAMP

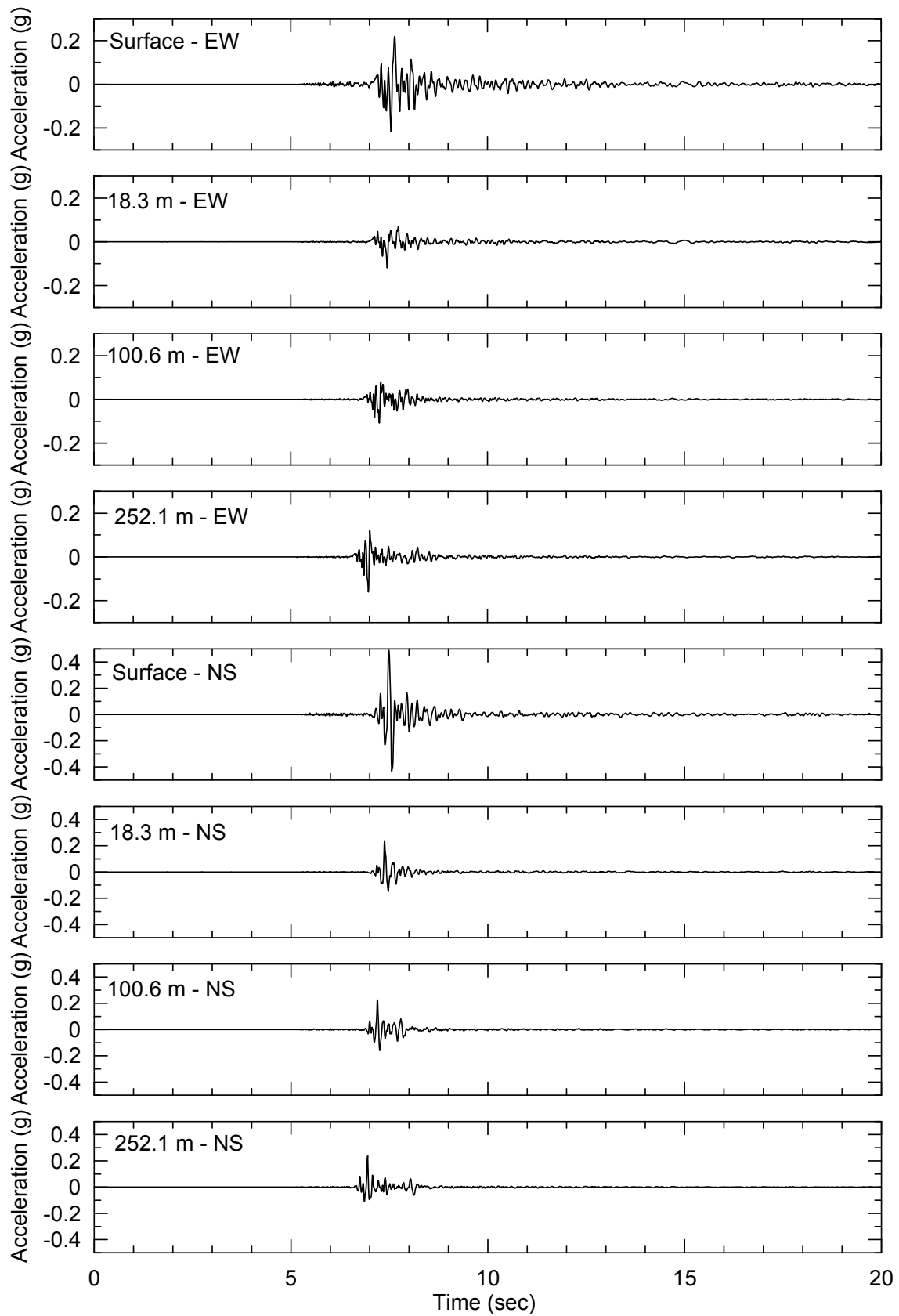


**Fig. 7.15** Acceleration histories recorded at La Cienega array.

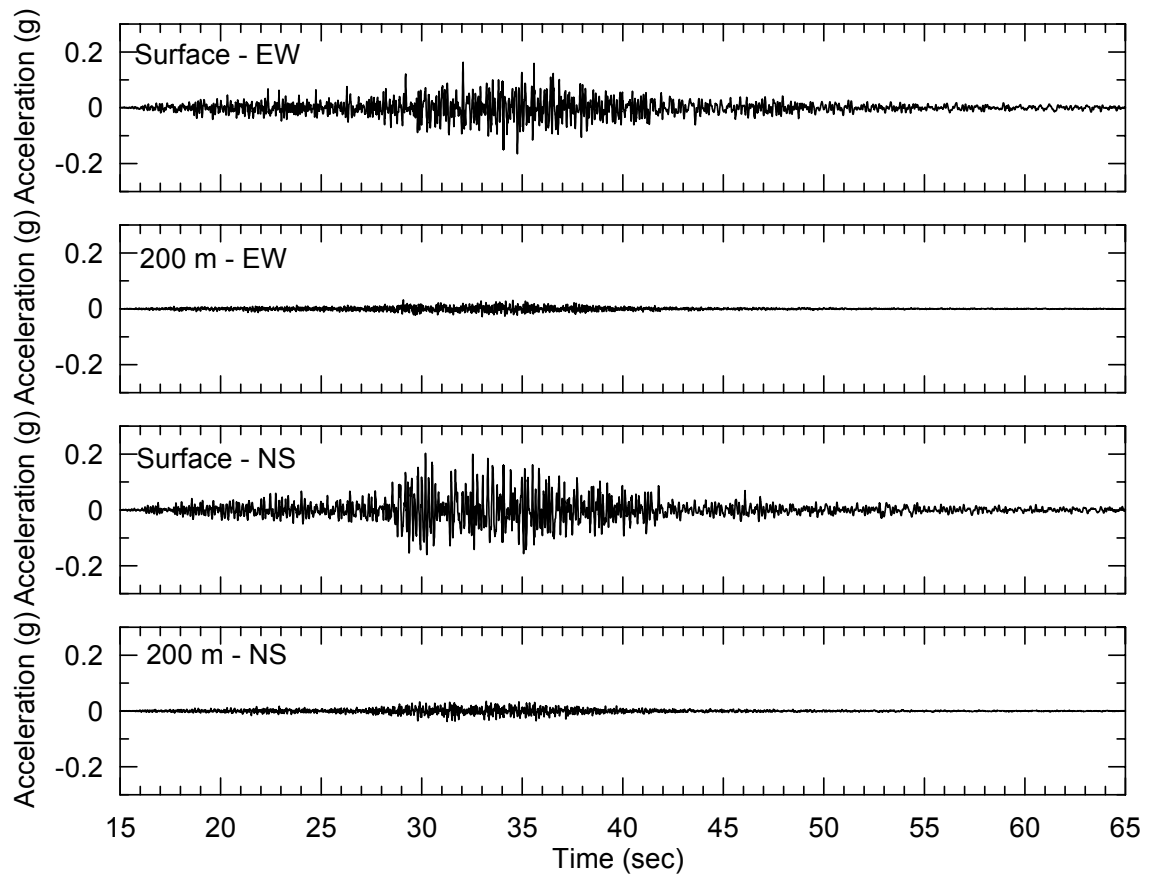


**Fig. 7.16** Acceleration histories recorded at Kiknet KGWH02 array.

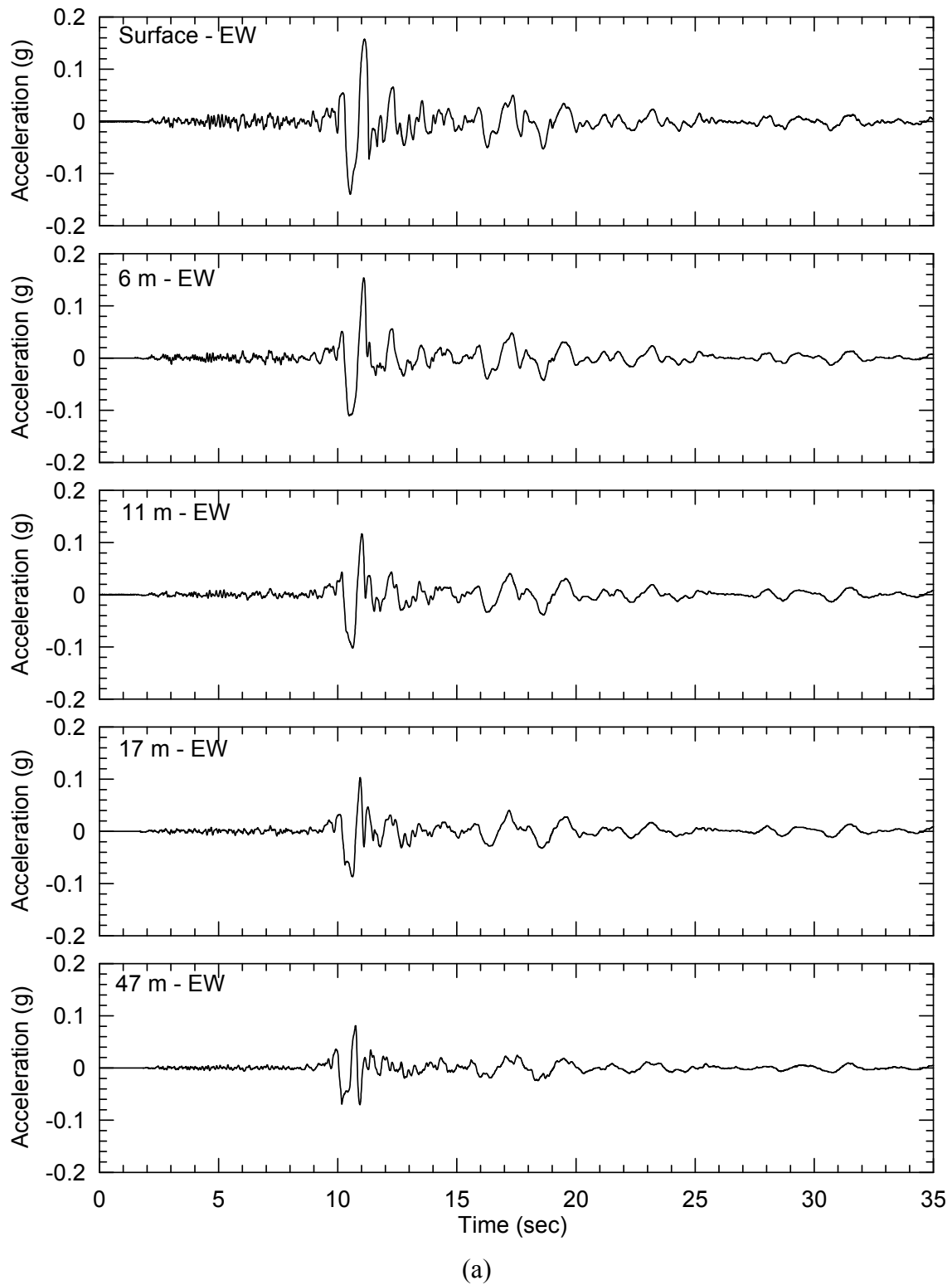


**Fig. 7.17 Acceleration histories for (a) EW direction recorded at Lotung array and (b) NS direction recorded at Lotung array.**

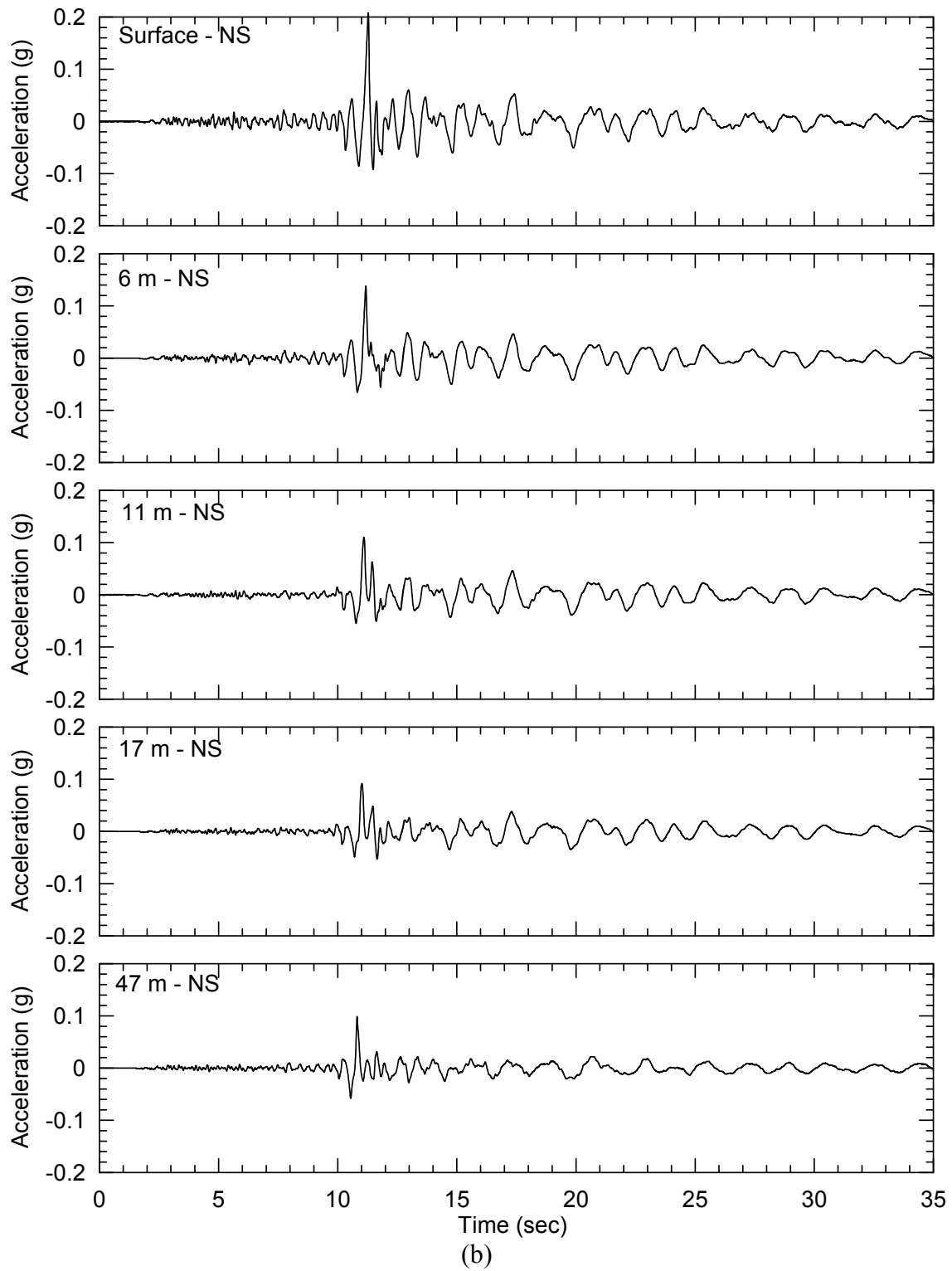


**Fig. 7.17—Continued.**

## 7.5 RESULTS

Ground response analyses are performed based on the code usage protocols given in Chapters 4 and 5, and the geotechnical models presented in Section 7.3. The results in which the predictions (using downhole motions presented in Section 7.4 as input motions) are compared to data are presented in Section 7.5.1, while the results with original downhole motions scaled to different levels are presented in Section 7.5.2.

### 7.5.1 Prediction Results with Unscaled Input Motions

#### (a) *La Cienega*

Figures 7.18–7.20 show 5% damped acceleration response spectra of the recorded motion and prediction results obtained using the baseline geotechnical model, while Figure 7.21 compares the predicted acceleration histories with the recordings from Figure 7.15 (results are shown for predictions from DEEPSOIL only). The results are shown for the ground surface and depths of 18.3 m and 100.6 m. Also shown in the figures are residuals calculated as:

$$R(T) = \ln(S_a(T))_{data} - \ln(S_a(T))_{pre} \quad (7.1)$$

The general comparison of the acceleration histories to data is quite favorable, although there is some bias towards overprediction of the largest pulses in the record in the EW direction and underprediction in the NS direction. The predicted acceleration histories seem to be insensitive to the type of viscous damping formulation, as extended Rayleigh damping (ERD) and full Rayleigh damping (FR) predict very similar histories as shown in Figure 7.22.

These errors in the acceleration histories translate into errors in spectra as well. For the EW component at the ground surface, the predictions from codes DEEPSOIL and D-MOD\_2 are similar to each other and are generally close to the data, although they underpredict at periods between 0.07–0.12 sec. The predictions from codes OpenSees and TESS have similar trends and are also close to the data except for overprediction near the period of 0.15 sec. SUMDES underpredicts at periods below 0.5 sec, which is probably due to the use of a simplified Rayleigh damping formulation. Close examination of the spectra and residuals reveals that predictions from all codes have bumps near  $T=2$  sec, which corresponds to the elastic period of the site from the base recording to the ground surface. For the NS component at the ground surface, all

nonlinear codes underpredict at periods below 0.5 sec. The misfits of predictions relative to data at depths of 18.3 m and 100.6 m follow similar trends to those at the ground surface.

The importance of fitting strategy is studied by using model curves obtained from the “MR” and “MRD” fitting approaches described in Section 4.2. Only DEEPSOIL is used for this study. The prediction results for ground surface motions calculated using both fitting approaches are compared in Figure 7.22. It can be observed that results from both approaches are very similar, which is probably due to the fact that the input motions used here are relatively modest and do not introduce large soil nonlinearity. That is, the strain experienced by the soil is small, and the model damping curves from both “MRD” and “MR” fitting approaches are similar for small-strain conditions.

OpenSees and SUMDES are formulated using a 3D finite element framework and are capable of simulating ground response with input motions from both horizontal and vertical components specified simultaneously. To study the 2D effect in ground response, input motions from both horizontal directions are specified simultaneously. Only OpenSees is used in this study. The prediction results for ground surface obtained from 1D and 2D simulations are compared in Figure 7.24. It is observed that the response for the NS direction is reduced when the 2D effect is considered. This is because the NS direction of the input motion is the stronger component, and the wave energy would be diverted to the EW direction when shaking in both directions is allowed to happen simultaneously.

Model-to-model variability is evaluated for the ground surface results in Figure 7.18. For period  $T$ , the median estimate  $\ln(\bar{S}_a(T))$  is first evaluated from the five nonlinear model predictions. Model variability,  $\sigma_m$ , is then calculated from the variance as follows:

$$\sigma_m^2(T) = Var(S_a(T))_{pre} = \frac{\sum_i \left[ \ln(S_a(T))_{pre,i} - \ln(\bar{S}_a(T)) \right]^2}{N-1} \quad (7.2)$$

where  $N$  = number of predictions (five). Figure 7.25 shows the variation of  $\sigma_m$  with period.

The variability in prediction results from uncertain shear wave velocity and uncertain modulus reduction and damping curves is considered. The variability in the velocity profile that was used in the analysis is shown in Figure 7.1, while the variability in material curves is shown in Figures 7.6–7.7. The response variability due to material uncertainty is assessed using DEEPSOIL predictions only. To calculate the standard deviation due to velocity, ground motions

are predicted based on two non-baseline velocity profiles (mean +  $\sqrt{3}$  standard deviation velocities and mean -  $\sqrt{3}$  standard deviation velocities). The standard deviation of the ground motions due to the variability in velocity (denoted  $\sigma_v$ ) is estimated according to the FOSM method (Baker and Cornell 2003; Melchers 1999), as follows:

$$\sigma_v = \sum_{i=1}^3 w_i (\ln(Sa(T)_i) - \overline{\ln(Sa(T))})^2 \quad (7.3)$$

where

$$\begin{aligned} Sa(T)_1 &= S_a(T)_{V_s:\mu} \\ Sa(T)_2 &= S_a(T)_{V_s:\mu+\sqrt{3}\sigma_{V_s}} \\ Sa(T)_3 &= S_a(T)_{V_s:\mu-\sqrt{3}\sigma_{V_s}} \\ \overline{\ln(S_a(T))} &= \sum_{i=1}^3 w_i \ln(S_a(T)_i) \\ w_1 &= 2/3; w_2 = w_3 = 1/6 \end{aligned} \quad (7.4)$$

The standard deviation due to the variability in material curves (denoted  $\sigma_G$ ) is estimated similarly to  $\sigma_v$ . Figure 7.25 shows the estimated standard deviation in prediction due to different sources of variability. At periods below 0.4 sec, the model and material curve variability dominate, while the velocity variability is strongest at periods above 0.4 sec.

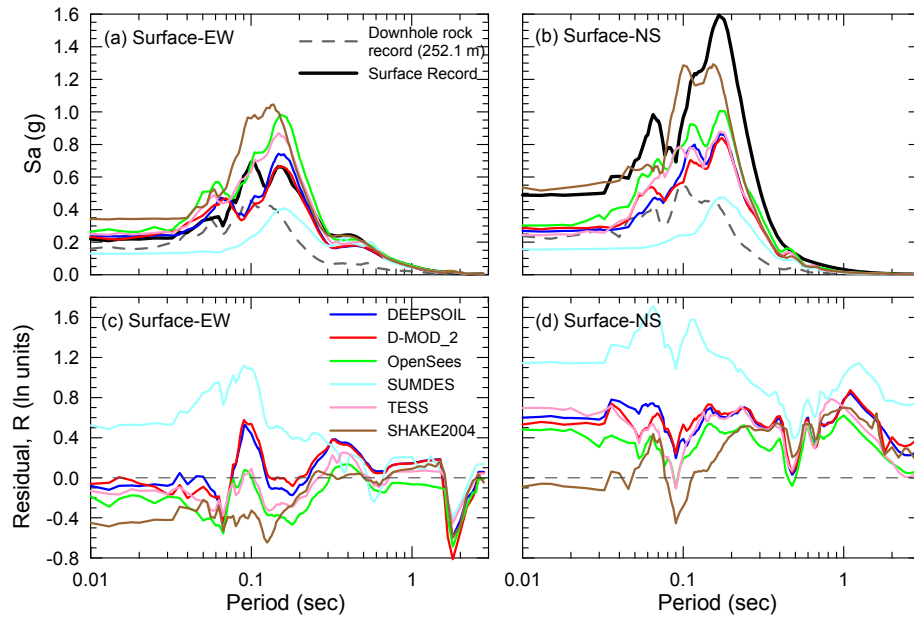


**Fig. 7.18 Acceleration response spectra for data and simulation results compared through direct spectral ordinates and prediction residuals for ground surface. Results shown for two horizontal directions.**

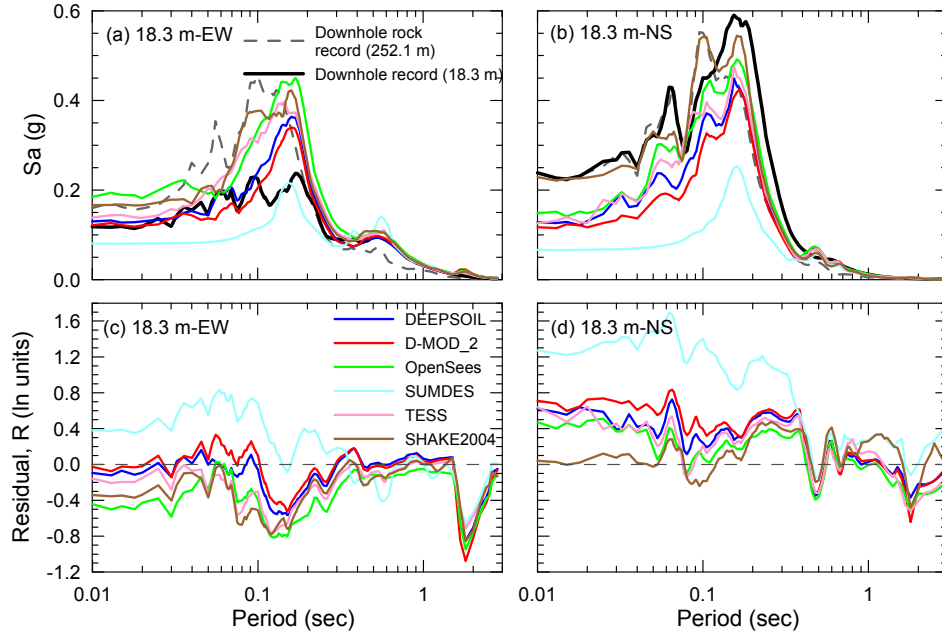


**Fig. 7.19** Acceleration response spectra for data and simulation results compared through direct spectral ordinates and prediction residuals for 18.3 m.

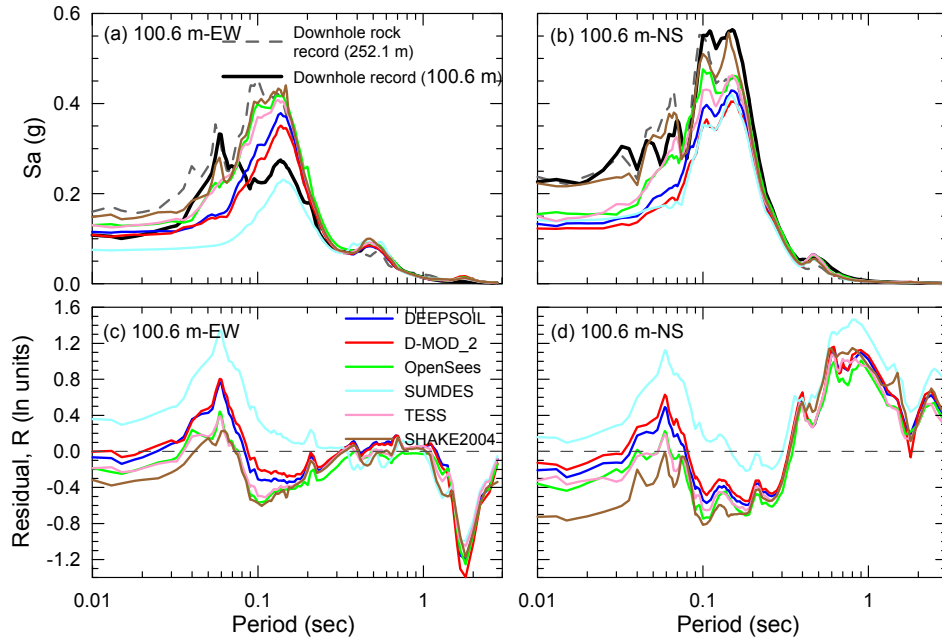


**Fig. 7.20** Acceleration response spectra for data and simulation results compared through direct spectral ordinates and prediction residuals for 100.6 m.

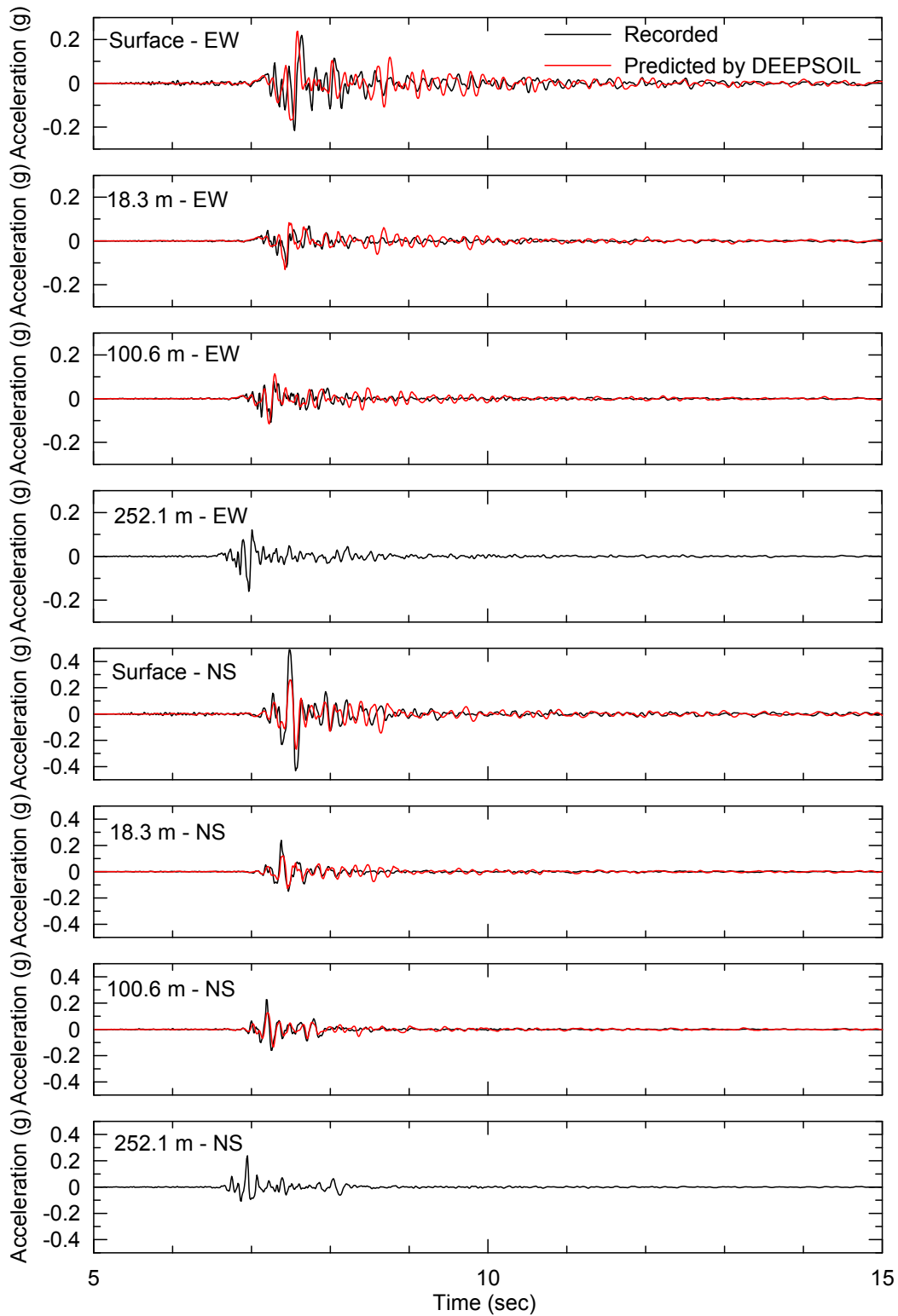


**Fig. 7.21 Acceleration histories for data and simulation results from DEEPSOIL for ground surface.**

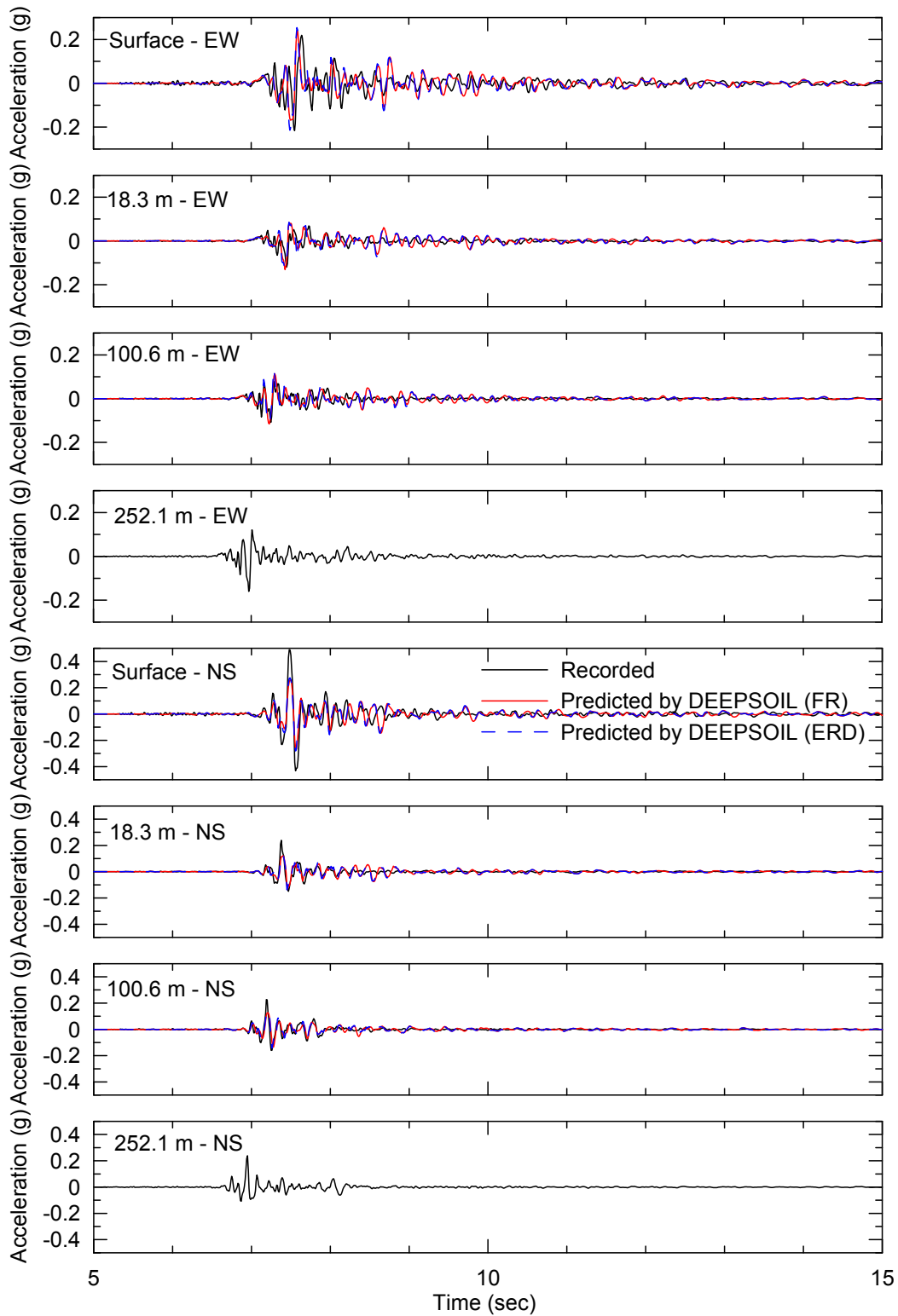


**Fig. 7.22 Acceleration histories for data and simulation results with different viscous damping formulations from DEEPSOIL for ground surface.**

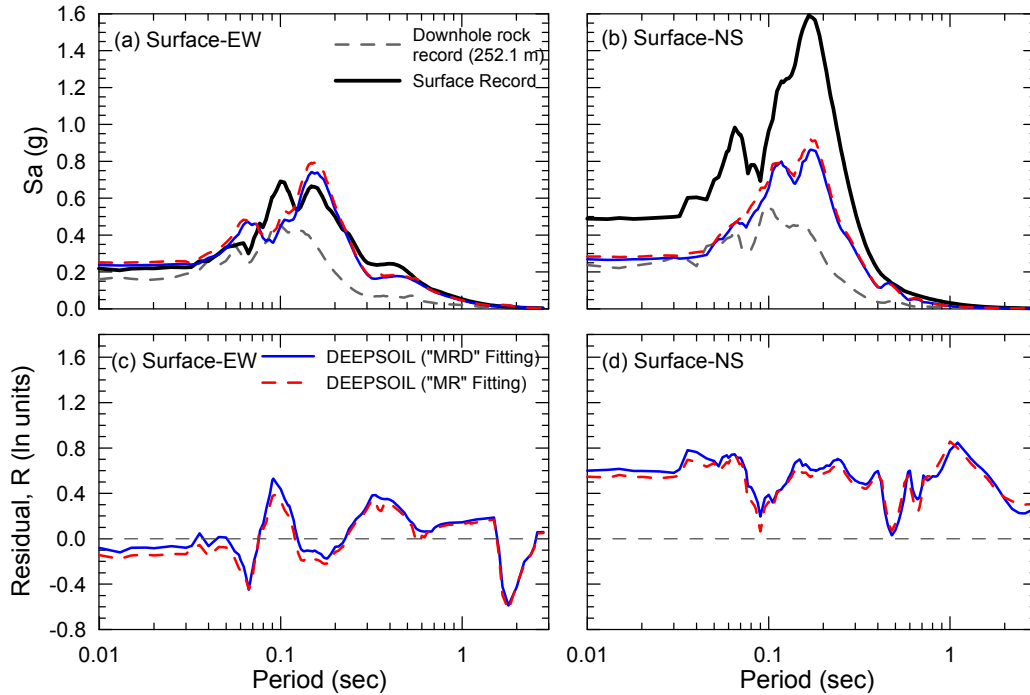


**Fig. 7.23** Acceleration response spectra for data and simulation results (with model curves obtained from both “MRD” and “MR” fitting approaches) compared through direct spectral ordinates and prediction residuals for ground surface.

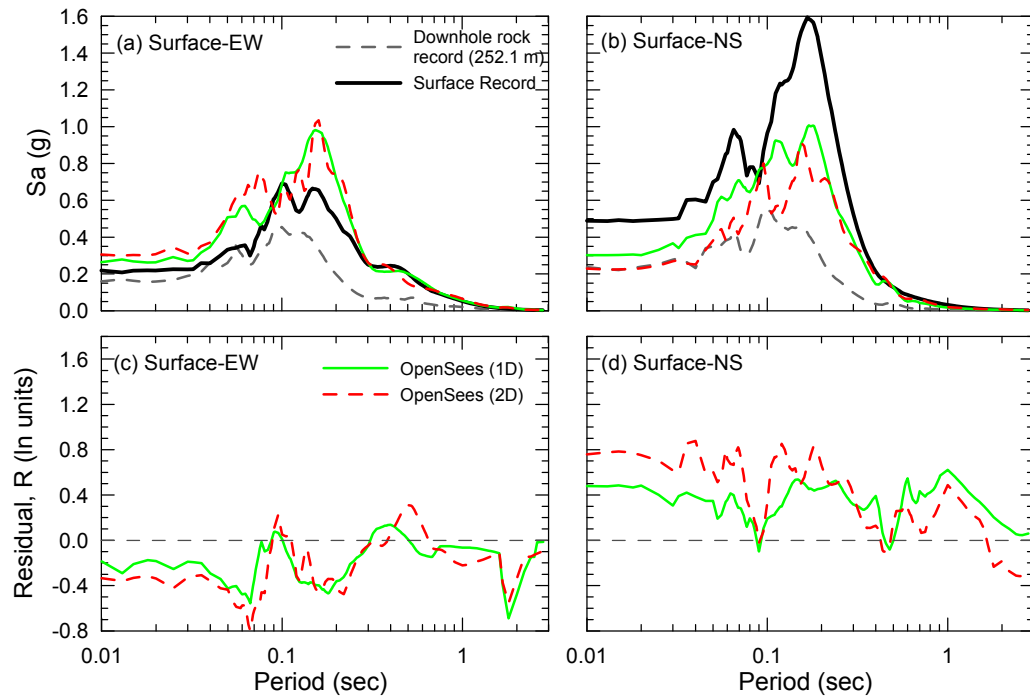


**Fig. 7.24** Acceleration response spectra for data and simulation results (using 1D and 2D simulation options in OpenSees ) compared through direct spectral ordinates and prediction residuals for ground surface.

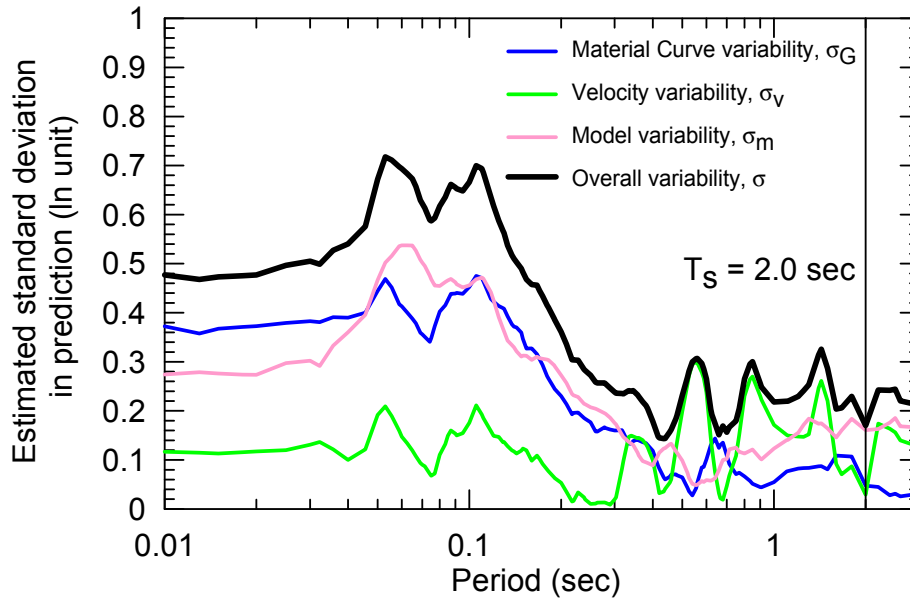


**Fig. 7.25 Standard deviation terms associated with geometric mean acceleration response spectral ordinates for ground surface.  $T_s$  denotes elastic site period.**

**(b) KGWH02**

Figure 7.26 shows 5% damped acceleration response spectra of the recorded motion and prediction results for the ground surface obtained using the baseline geotechnical model, while Figure 7.27 compares the predicted acceleration histories with the recordings from Figure 7.16 (results are shown for predictions from DEEPSOIL only). The residuals shown in the figure are calculated using Equation 7.1.

The general comparison of the acceleration histories to data is poor. The data contain a large amount of high-frequency content that is not well simulated in the predictions. Examining the response spectra, for  $T < 0.3$  sec, all codes generally underpredict the observed motions in both the EW and NS directions except for  $T = 0.04 - 0.09$  sec, where residuals are nearly zero for all codes except SUMDES. For  $T > 0.3$  sec, predictions from all codes are similar to the data except the bumps near  $T = 0.9$  sec, which correspond to the elastic period of the site for the soil layers only (from the depth of 68 m to the ground surface).

The relative merits of “MR” and “MRD” fitting approaches are also studied using KGWH02. The prediction results for ground surface motions calculated using both fitting approaches are compared in Figure 7.28. Similar to the observation from analyses for the La

Cienega site, the results from both approaches are very similar due to the modest input ground motion amplitude.

Two-dimensional effects are studied using OpenSees. The prediction results for ground surface obtained from 1D and 2D simulations are compared in Figure 7.29. The predictions from both types of simulations are similar because there is no dominant component in the input motion.

Model-to-model variability is evaluated for the ground surface results using Equation 7.2. Figure 7.30 shows the variation of  $\sigma_m$  with period.

The variability in prediction resulting from uncertain shear wave velocity and uncertain nonlinear modulus reduction and damping curves is considered. The variability in velocity profile that was used in the analysis is shown in Figure 7.2, while the variability in material curves is shown in Figures 7.8 and 7.9. The response variability due to material uncertainty is assessed using DEEPSOIL predictions only. The standard deviation due to velocity and material curves are calculated in the same way as for La Cienega. It should be mentioned that the variability of material curve for rock and soil is considered to be independent of each other. It is found that variability in rock material curves has only a slight effect on the predictions at  $T < 0.1$  sec and no discernable effect for other period ranges. Accordingly, the estimated total standard deviation excludes the uncertainty in predictions due to rock material curves. Figure 7.30 shows the estimated standard deviation in prediction due to different sources of variability.

For  $T < 0.15$  sec, the (soil) material curve variability dominates, while velocity (whole profile) variability dominates for  $T > 0.15$  sec. Standard deviation due to model variability is generally small compared to other sources of variability except in the period range  $T = 0.05 - 0.1$  sec (where the standard deviation is large due to SUMDES being significantly different from the other codes). Analyses are also performed for which only the velocity of upper 9 m of soil is varied to mean  $\pm \sqrt{3}$  standard deviation velocities. Focusing velocity variability in the upper portion of the profile increases  $\sigma_v$  for  $T < 0.5$  sec and decreases  $\sigma_v$  for longer periods. Figure 7.31 compares the 5% damped acceleration response spectra and the residuals calculated for different velocity profiles.

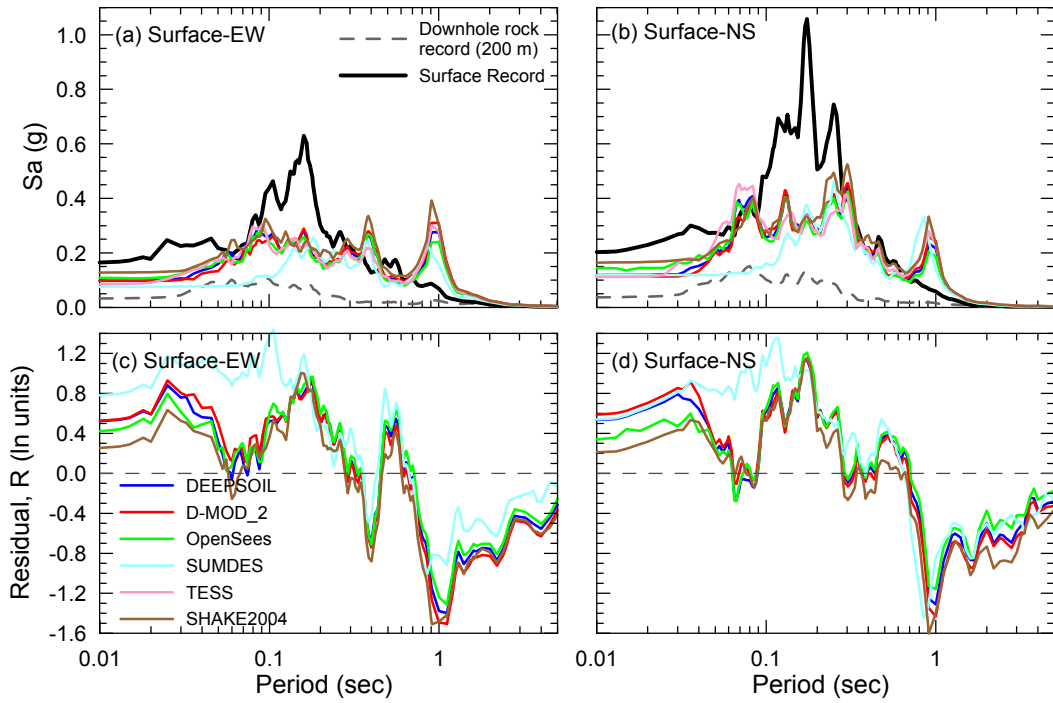


**Fig. 7.26** Acceleration response spectra for data and simulation results compared through direct spectral ordinates and prediction residuals for ground surface.

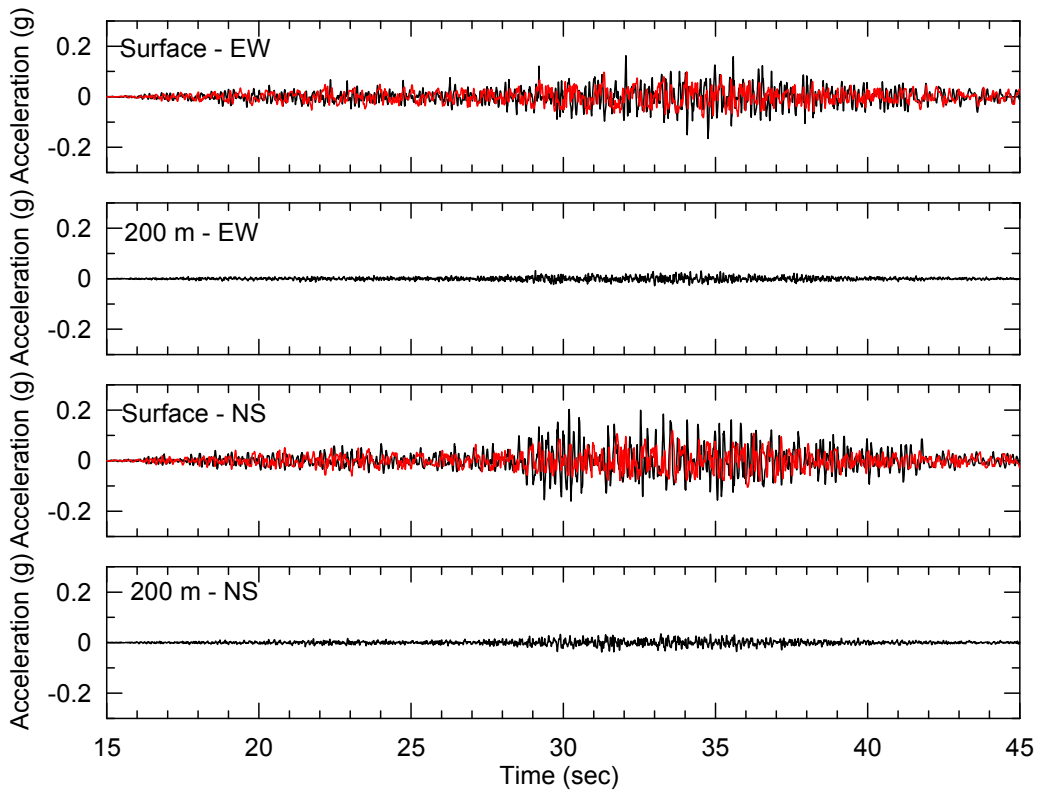


**Fig. 7.27** Acceleration histories for data and simulation results from DEEPSOIL for ground surface.

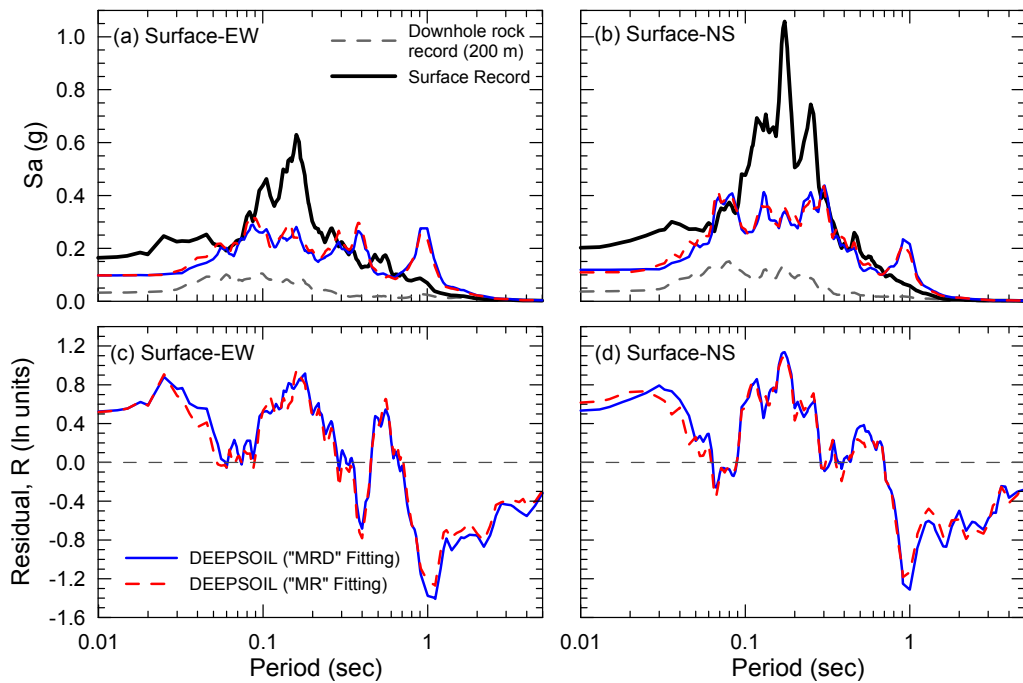


**Fig. 7.28** Acceleration response spectra for data and simulation results (with model curves obtained from both “MRD” and “MR” fitting approaches) compared through direct spectral ordinates and prediction residuals for ground surface.

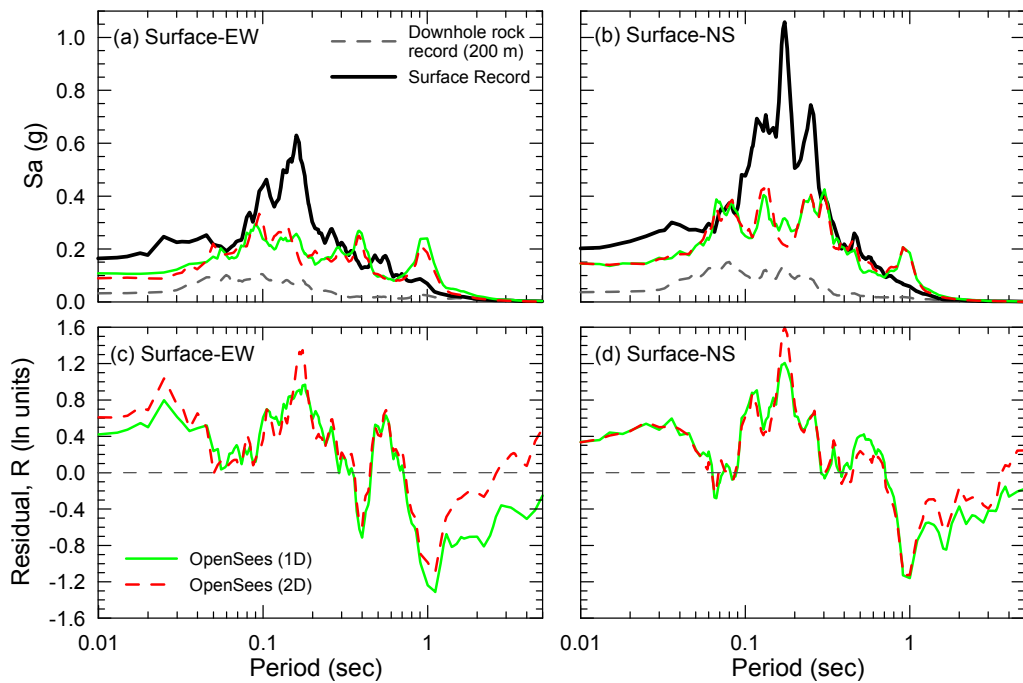


**Fig. 7.29** Acceleration response spectra for data and simulation results (using 1D and 2D simulation options in OpenSees ) compared through direct spectral ordinates and prediction residuals for ground surface.

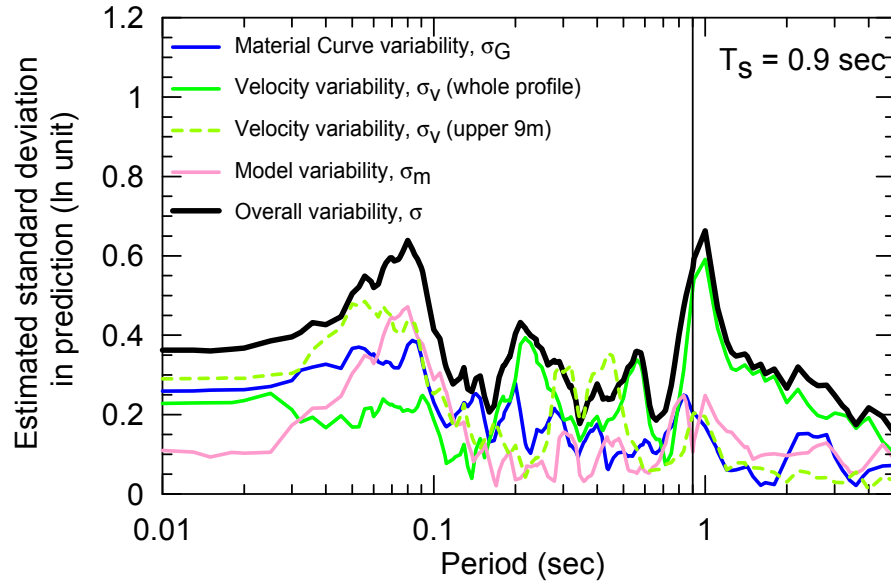


**Fig. 7.30** Standard deviation terms associated with geometric mean acceleration response spectral ordinates for ground surface.  $T_s$  denotes elastic site period (calculated excluding rock layers below 68 m)..

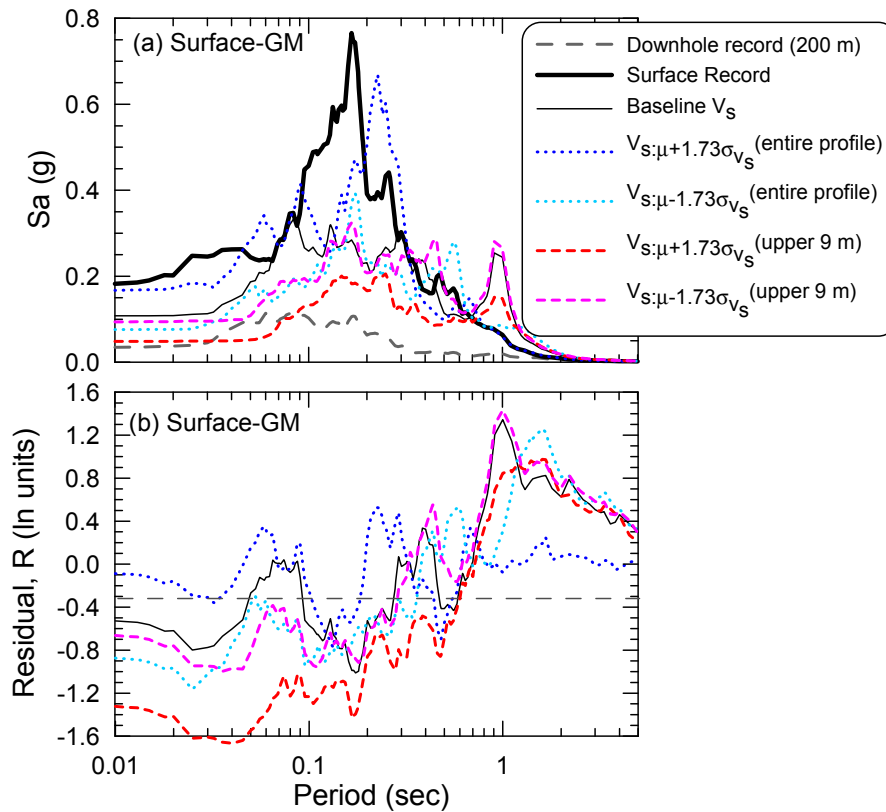


**Fig. 7.31** Acceleration response spectra for data and simulation results (using DEEPSOIL with different velocity profiles) compared through direct spectral ordinates and prediction residuals for ground surface.

(c) *Lotung*

Figures 7.32–7.35 show 5% damped acceleration response spectra of the recorded motion and predictions obtained using the baseline geotechnical model, while Figure 7.36 compares the predicted acceleration histories with the recordings from Figure 7.17 (results are shown for predictions from DEEPSOIL only). The results are shown for the ground surface and depths of 6, 11, and 17 m. The residuals shown in the figure are calculated using Equation 7.1.

The general comparison of the acceleration histories to data is quite favorable, although there is some bias towards underprediction of the largest pulses. These errors in the acceleration histories translate into errors in spectra as well. For both EW and NS components at the ground surface, the predictions from all of the codes are generally similar to each other and underpredict at periods below 0.7 sec. The misfits of predictions relative to data at depths of 6 m, 11 m, and 17 m follow similar trends to those at the ground surface. One unusual feature is that large spectral accelerations at high frequency are predicted at depth by OpenSees which are incompatible with the data.

Model-to-model variability is evaluated for the ground surface results using Equation 7.2. Figure 7.37 shows the variation of  $\sigma_m$  with period.

The variability in prediction resulting from uncertain shear wave velocity and uncertain nonlinear modulus reduction and damping curves is considered. The variability in velocity profile that was used in the analysis is shown in Figure 7.3, while the variability in material curves is shown in Figures 7.10 and 7.11. The response variability due to material uncertainty is assessed using DEEPSOIL predictions only. The standard deviation due to velocity and material curves are calculated in the same way as for La Cienega. Figure 7.37 shows the estimated standard deviation in prediction due to different sources of variability. Material curve variability dominates for periods below 1.5 sec. Figure 7.38 compares the 5% damped acceleration response spectra and the residuals calculated for different target curves (Zeghal et al. 1995 versus EPRI 1993). As expected, the use of the more linear EPRI curves leads to higher response, however the misfits at low periods are not removed.

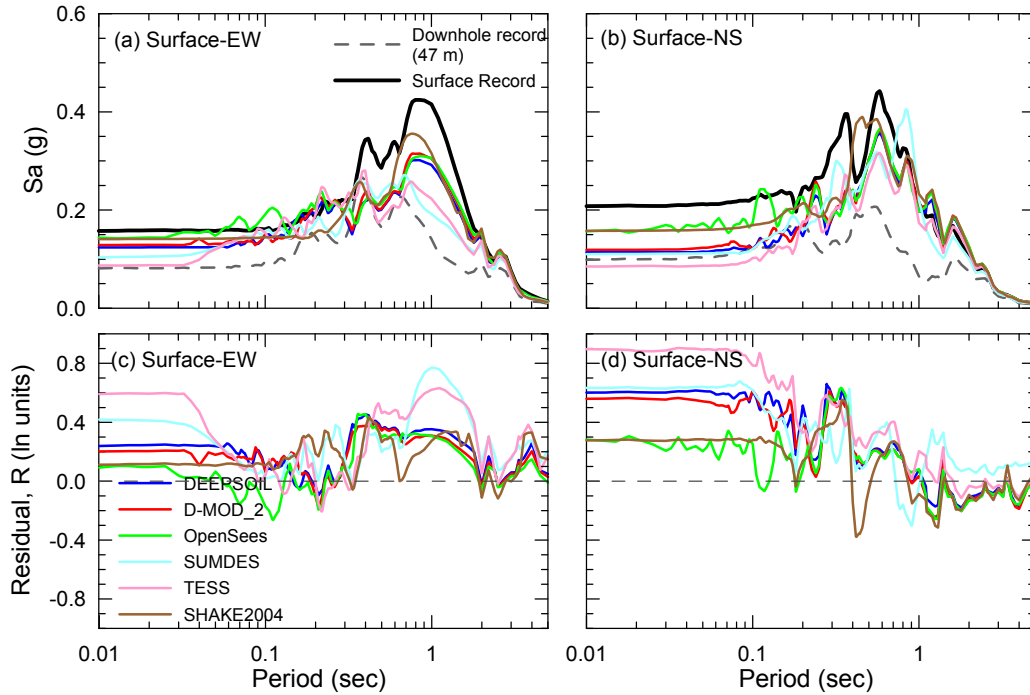


**Fig. 7.32 Acceleration response spectra for data and simulation results compared through direct spectral ordinates and prediction residuals for ground surface. Results shown for two horizontal directions.**

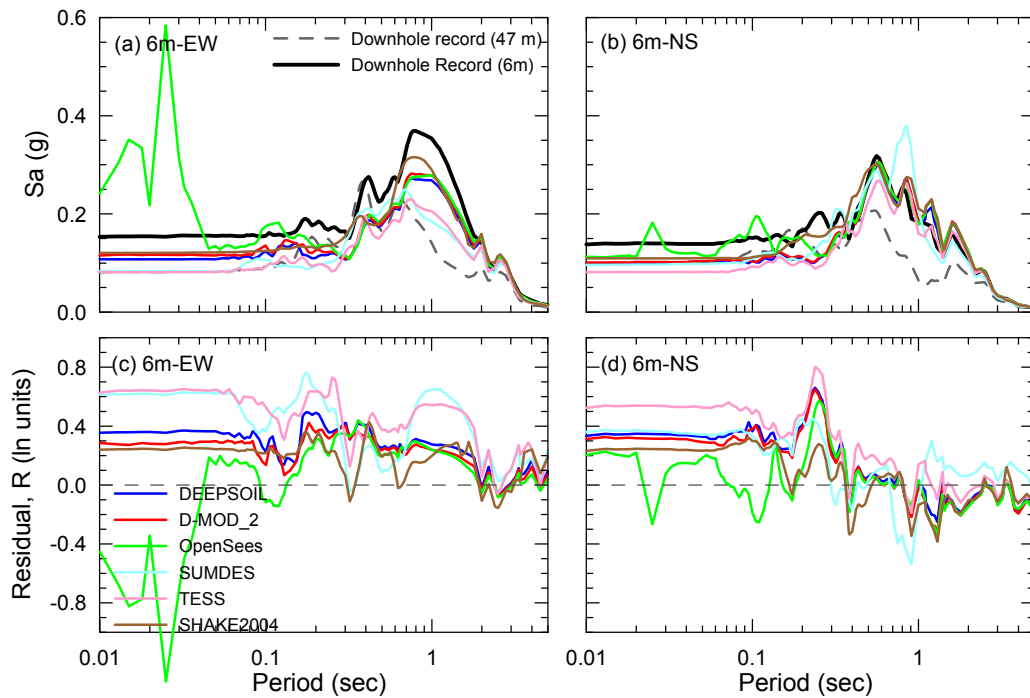


**Fig. 7.33 Acceleration response spectra for data and simulation results compared through direct spectral ordinates and prediction residuals for 6 m.**

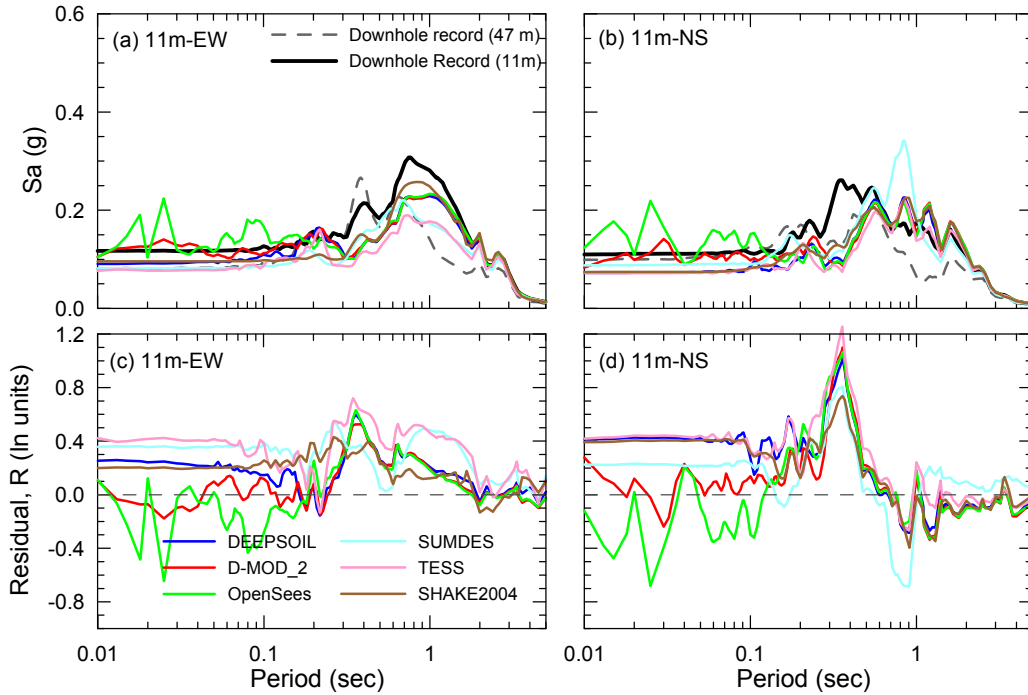


**Fig. 7.34** Acceleration response spectra for data and simulation results compared through direct spectral ordinates and prediction residuals for 11 m.

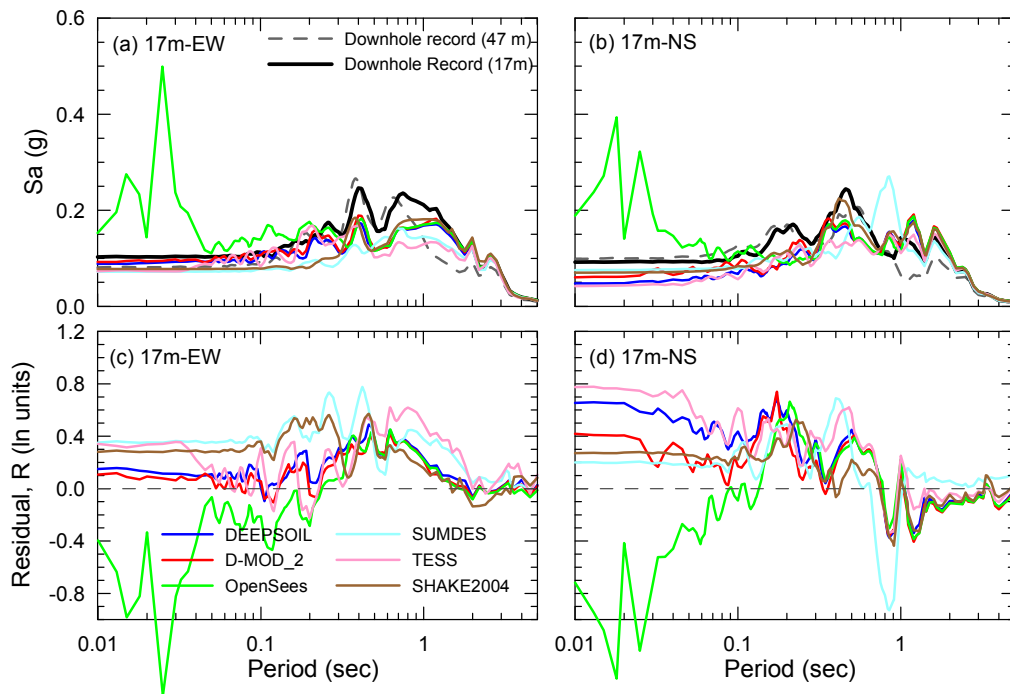


**Fig. 7.35** Acceleration response spectra for data and simulation results compared through direct spectral ordinates and prediction residuals for 17 m.

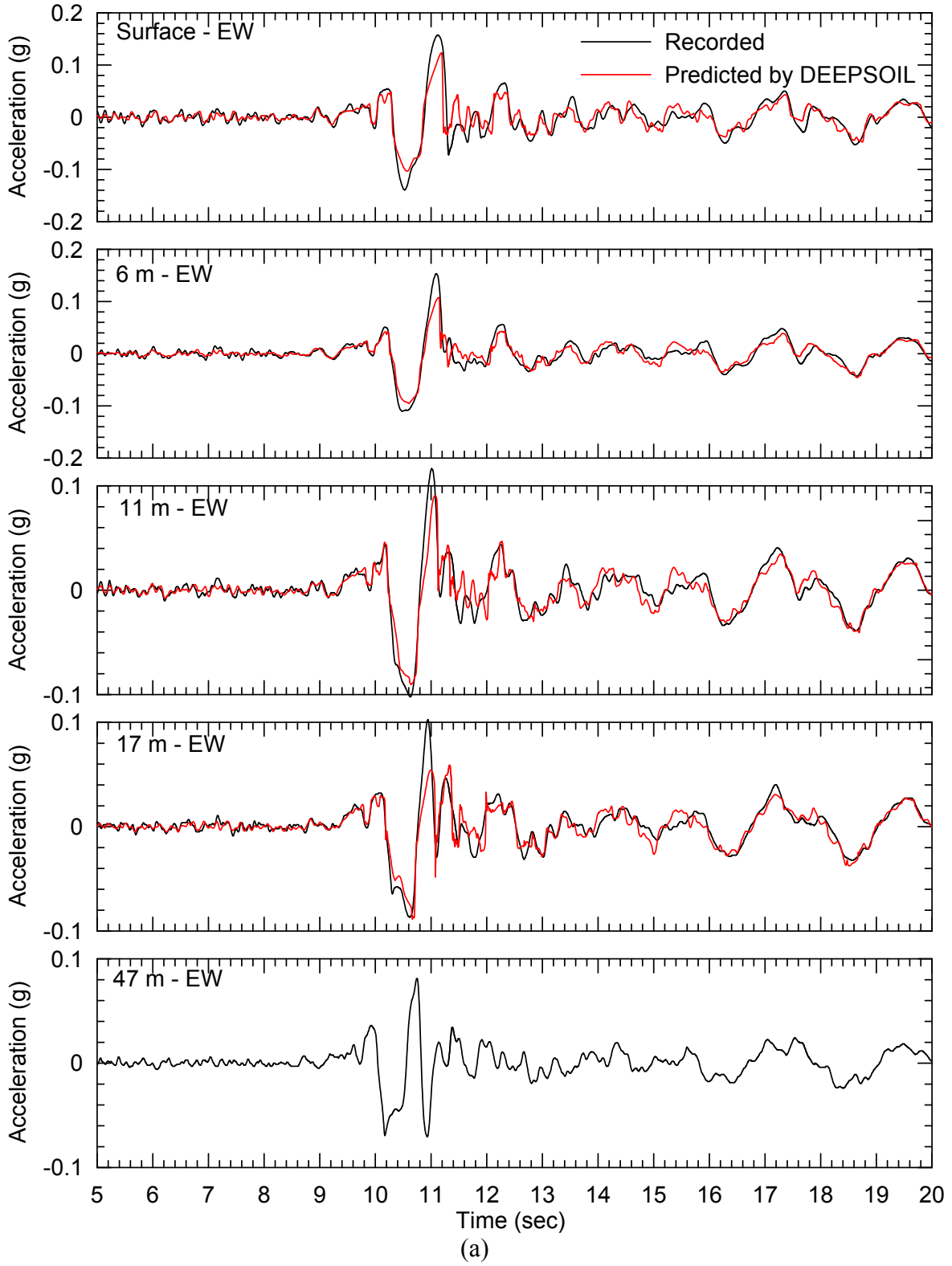


**Fig. 7.36 Acceleration histories for data and simulation results from DEEPSOIL for (a) EW direction and (b) NS direction.**

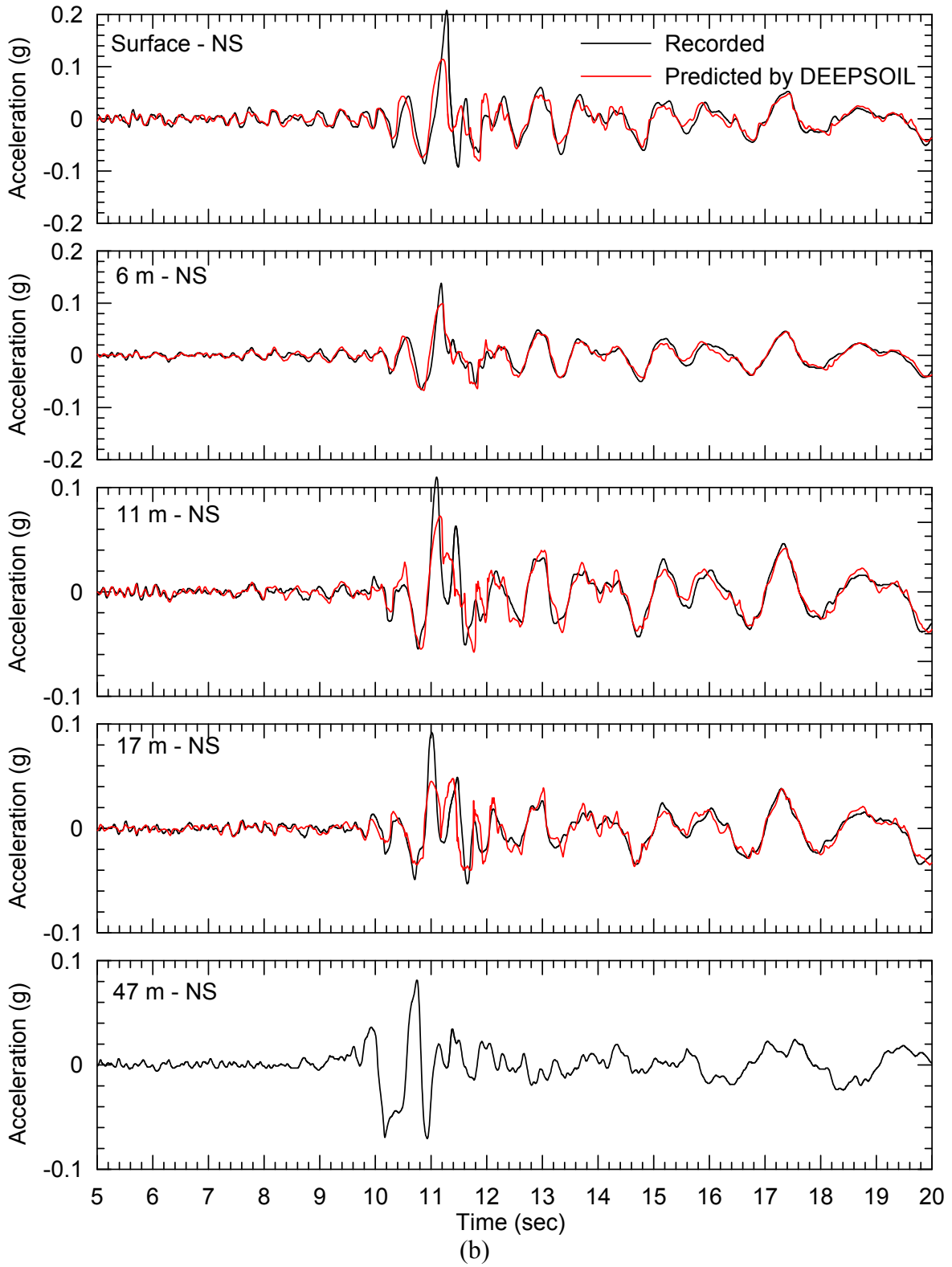


**Fig. 7.36—Continued.**

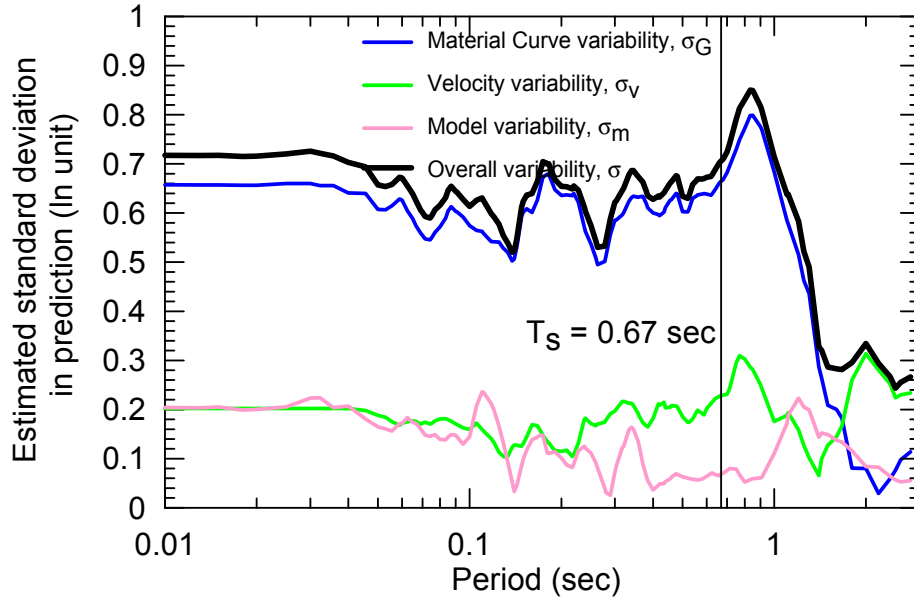


**Fig. 7.37** Standard deviation terms associated with geometric mean acceleration response spectral ordinates for ground surface.  $T_s$  denotes elastic site period.

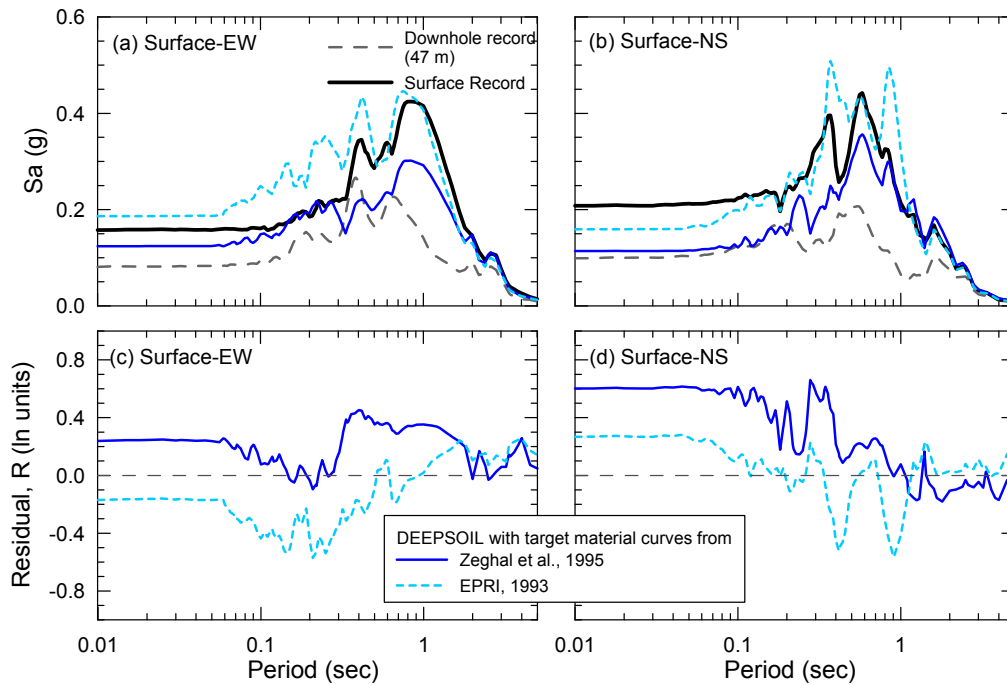


**Fig. 7.38** Acceleration response spectra for data and simulation results (using DEEPSOIL with different target material curves) compared through direct spectral ordinates and prediction residuals for ground surface.

### 7.5.2 Prediction Results with Input Motions Scaled to Different Levels for La Cienega

To study site response at different levels of input motion, site amplification factors are compiled from ground motions recorded at La Cienega from 1999–2005. Predicted amplification factors of geometric mean response spectral accelerations are derived at specified periods using the baseline geotechnical model for all codes. To estimate amplification factors for different amplitudes of input motions, the recording shown in Figure 7.15 is scaled down to various degrees. Figure 7.39 shows that the predicted amplification factors demonstrate a similar trend with respect to base motion peak acceleration ( $PGA^r$ ) as those observed from data. This suggests that nonlinearity is modeled well by nonlinear codes over this range of input motions. The level of predicted amplification is biased at multiple periods. For example, at the elastic site period (2 sec), the theoretical amplification is much larger than the empirical data.

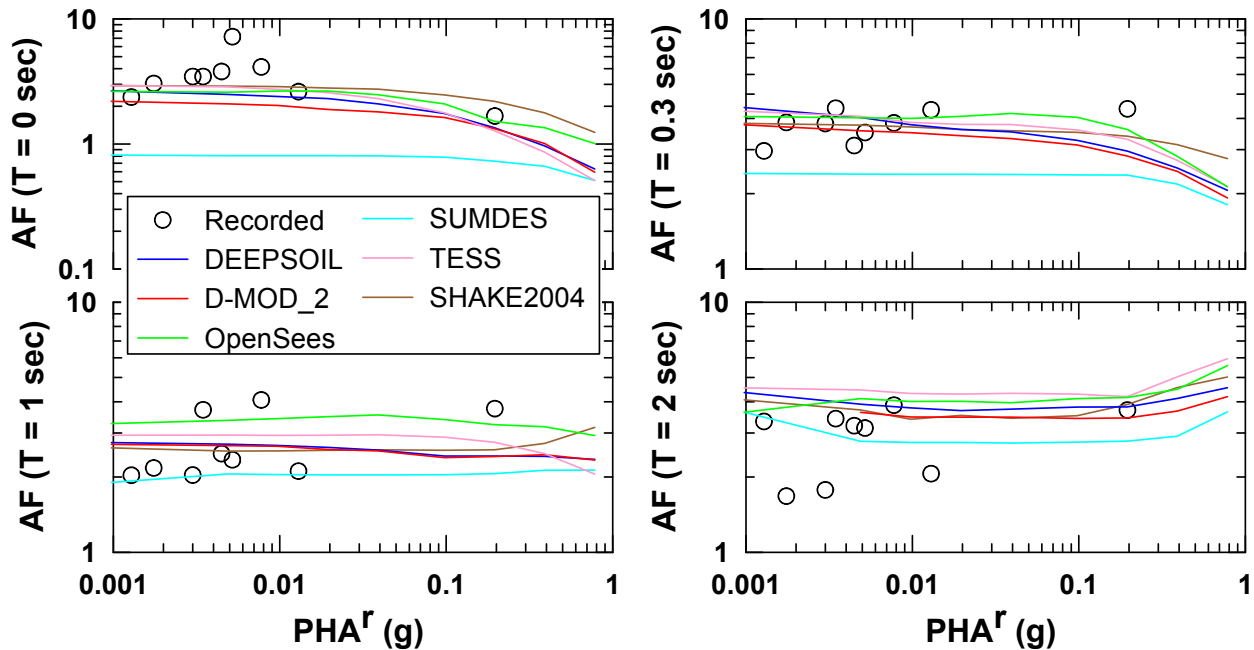


Fig. 7.39 Theoretical and observed amplification factors at La Cienega site.

### 7.6 TRENDS IN PREDICTION RESULTS ACROSS VARIOUS VERTICAL ARRAY SITES

In this section, the prediction results from the four vertical array sites (Turkey Flat, La Cienega, KGWH02, and Lotung) are compared to identify possible trends. Such trends can be useful to identify bias in the predictions of ground motions made using the selected nonlinear codes with the parameter selection protocols developed in this research.

The first set of trends discussed here concerns the period-dependence of the standard deviation terms. In Figure 7.40, the uncertainties in predictions due to different sources of variability for all four vertical array sites are plotted as a function of period (left frame) and period ratio (right frame) period ratio =  $T/T_s$  where  $T_s$  = elastic site period). The variability of predictions due to material curve uncertainty seems to be most pronounced at periods less than 0.5 sec and has no clear association with the site period. Moreover, material curve uncertainty only produces significant response variability for relatively thick site profiles — it is not a significant issue for the Turkey Flat, which is a shallow soil site.

The effect of velocity variability can have a strong influence on the predictions near the elastic site period. However, this strong influence is only observed for sites with large impedance contrast (Turkey Flat and KGWH02), which dominates the site response in these cases. This is shown in Figure 7.40 by a peak in the  $\sigma_v$  term near  $T/T_s = 1.0$ . Such a peak does not occur for the La Cienega or Lotung sites, which have a gradual variation of velocity with depth (see Figs. 7.1 and 7.3) and no pronounced impedance contrast.

Model-to-model variability is most pronounced at low periods, where the differences result principally from different damping formulations. Given the modest ground motions at the investigated sites, it is expected that variations in the viscous damping formulations are principally driving this variability. As noted previously, the predictions from SUMDES, which had only the simplified Rayleigh damping formulation at the time these predictions were made, are much lower than the predictions from codes with full Rayleigh damping formulation. This is a major contributor to the model-to-model variability at low periods.

The second set of trends discussed here concerns misfit of the models to the data. In Figures 7.41–7.44, the empirical amplification factors (spectral acceleration at ground surface normalized by downhole spectral acceleration) are compared with the theoretical factors derived by different ground response analysis codes for Turkey Flat, La Cienega, KGWH02, and Lotung, respectively. Residuals in amplification factors, taken as the difference between empirical factors and theoretical factors in natural log units are also plotted. For all sites except Turkey Flat, the residuals for very low periods (reflecting PGA) are positive, indicating that the models underpredict the high-frequency components of the ground motion. Near the elastic site period ( $T_s$ ), the models produce a local “bump” in the spectrum that results in overprediction. At periods significantly greater than  $T_s$ , the residuals disappear due to the lack of a significant site effect.

The above misfits can have many sources. In general, there are two possible sources of misfit — error in the input data (velocity profiles or nonlinear curves) or error in the models and their parameter selection protocols. The errors in the velocity profile were checked by comparing the observed (small amplitude) shear wave travel time to the time implied by the model. With the exception of the Kiknet site, these checks confirm the velocity profile used in the analysis. For KGWH02, the observed travel times are less than the model travel time, which may be due to the highly 3D nature of the site. Dr. R. Kayen (pers. comm. 2007), who performed the SASW testing for KGWH02, observed that the site is about 150 m from an outcropping hill and that the bedrock surface is steep (~30% grade). He suspected that the motions may not be vertically incident in the rock and may arrive at the site from sloping surface to the west.

Apart from velocity, other possible sources of error include incorrect modeling of material curves (modulus reduction and damping) or the presence of site response physics that cannot be captured by a 1D model. Because modulus reduction effects are likely relatively modest given the low strain levels excited by the subject earthquakes, error in the modeling in modulus reduction is not likely the source of the misfit. Given that site amplification is underpredicted for all three sites considered across a broad frequency range, a likely source of bias is overdamping in the models. This overdamping could reflect bias in the material damping curves or excessive Rayleigh damping. Further research is needed to resolve these possible sources of bias.

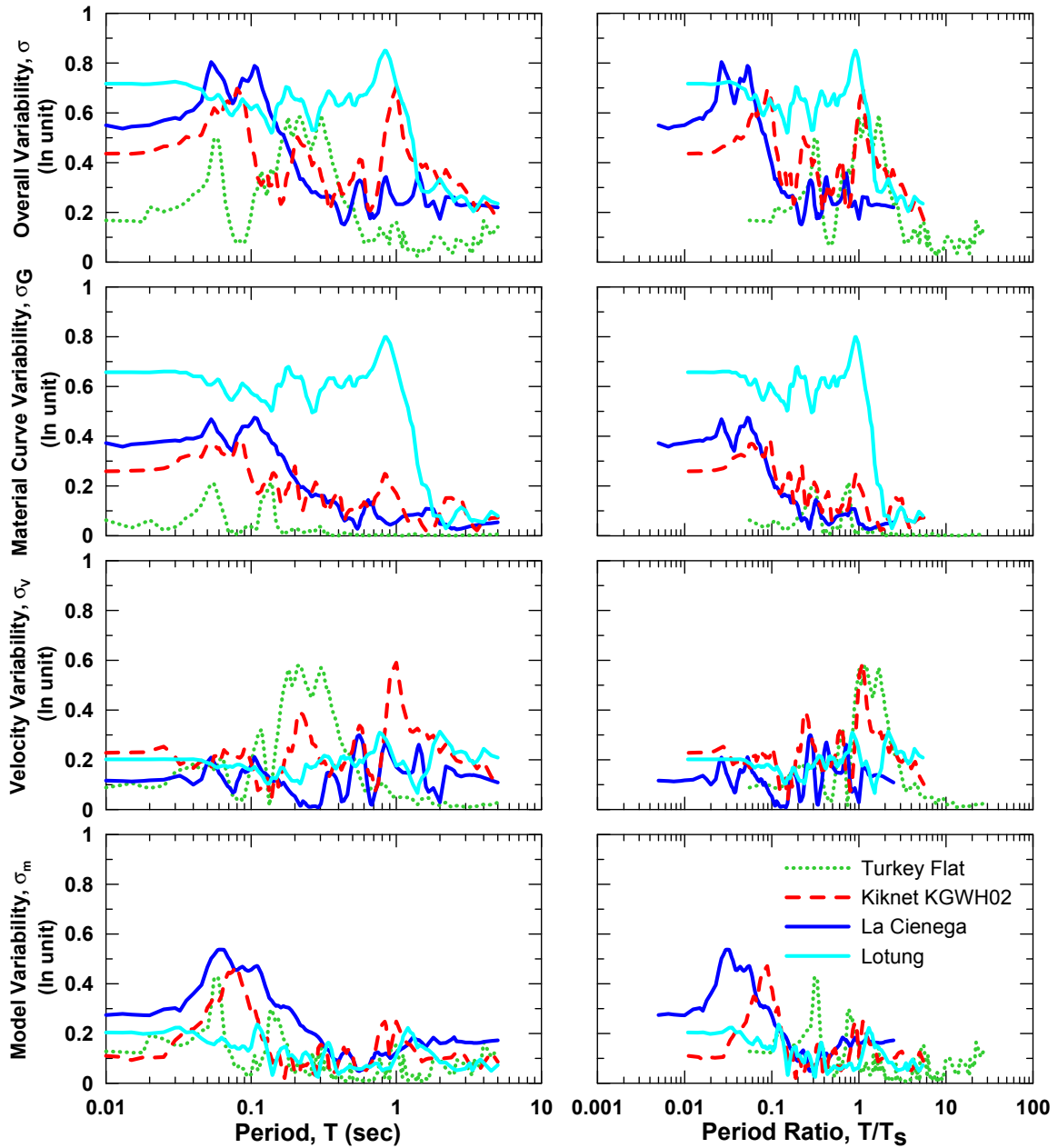
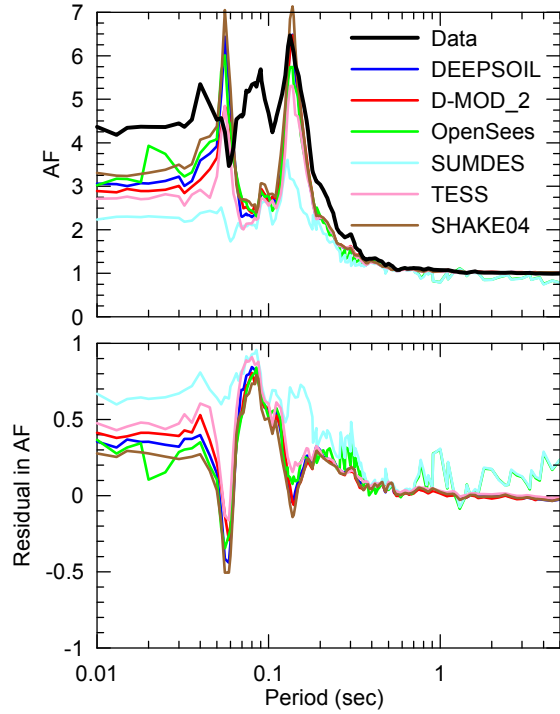
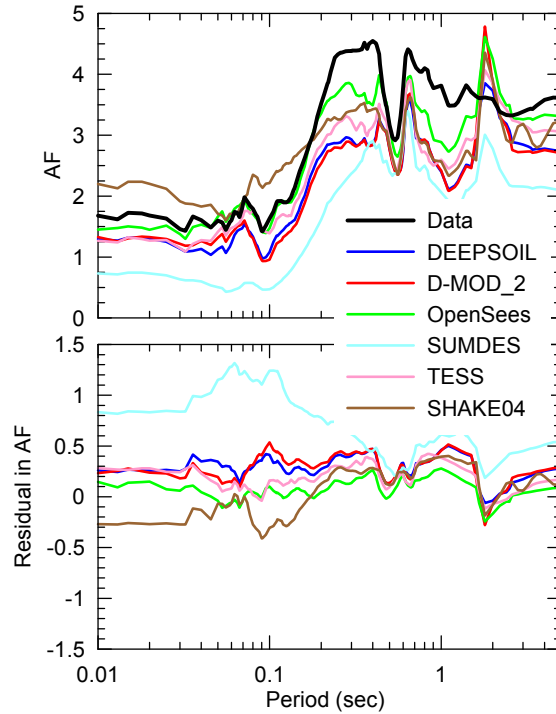


Fig. 7.40 Comparison of variabilities across three vertical array sites.



**Fig. 7.41 Comparison of empirical and theoretical amplification factors across periods for Turkey Flat site using Parkfield event.**



**Fig. 7.42 Comparison of empirical and theoretical amplification factors across periods for La Cienega site using 09/09/2001 event.**

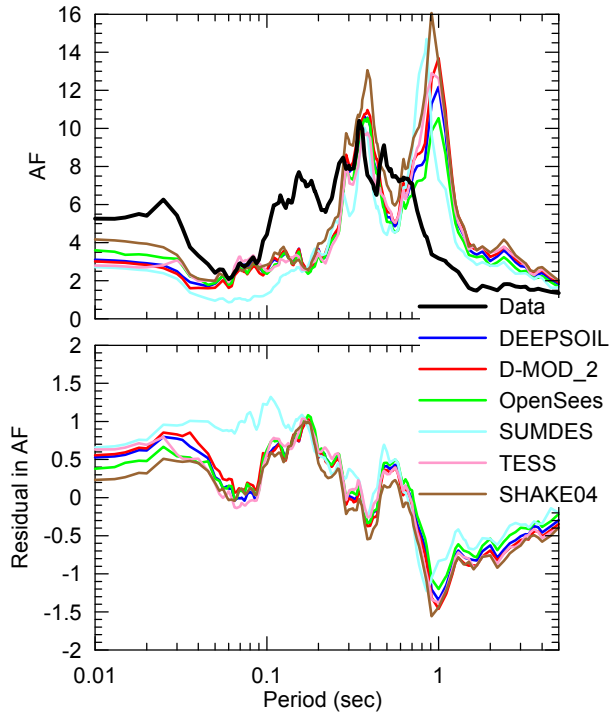


**Fig. 7.43 Comparison of empirical and theoretical amplification factors across periods for KGWH02 site using 03/24/2001 event.**

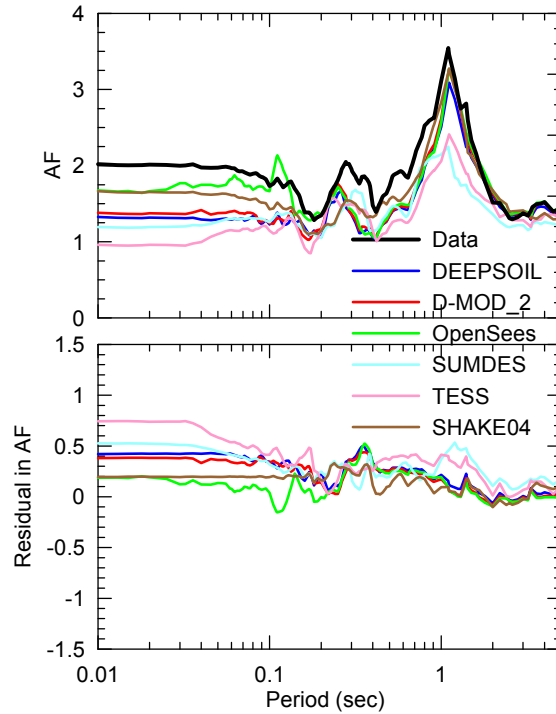


**Fig. 7.44 Comparison of empirical and theoretical amplification factors across periods for Lotung site using 5/20/1986 event ("Event 7").**

## 7.7 COMPARISON OF RESULTS FROM EQUIVALENT-LINEAR AND NONLINEAR ANALYSES

The predictions of ground motions at vertical array sites described in the previous section were made using both equivalent-linear and nonlinear codes. The aforementioned comparisons of model predictions to data showed similar trends for both methods of analysis, although the positive residuals at short periods were generally smaller for equivalent-linear.

More meaningful insight into the differences between equivalent-linear and nonlinear ground motion predictions can be made when the codes are exercised at relatively strong shaking levels that induce large strains. Representative results are shown in Figure 4.45, which shows for the La Cienega site geometric mean horizontal component predicted spectra, amplification factors (=surface/input outcropping spectral accelerations), and spectral shapes ( $S_a/PGA$ ) for a low-strain condition (left side, corresponding to observed motions during the 2001 event) and a large-strain condition produced through the use of a large amplitude synthetic input motion (right side). The results shown in Figure 4.45 apply to the baseline geotechnical model described previously. Also shown for reference purposes are predictions of empirical models for amplification (middle frames; Choi and Stewart 2005) and spectral shape (bottom frames; Campbell and Bozorgnia 2007). The empirical amplification model is exercised for a site's  $V_{s30}$  (260 m/s) and corresponding input  $PGA$ . The empirical spectrum from which the spectral shape is evaluated is calculated using  $M_w=7.5$ , site-source distance=10 km, and strike-slip focal mechanism (for synthetic). As shown in the bottom frames of Figure 4.45, the spectral shapes from equivalent-linear and nonlinear models are similar to each other for the 2001 input motion that induces relatively low strain but are significantly different for the large amplitude synthetic motion. For the large-strain simulation, the spectral shapes at low periods ( $< \sim 0.2$  sec) from equivalent-linear analyses are flatter and have less period-to-period fluctuations than those from nonlinear analyses or empirical models. This aspect of equivalent-linear results is believed to be non-physical and can be overcome with nonlinear analysis. As shown in the middle frames, the flatness of the equivalent-linear spectrum is associated with a dip in the amplification factors between periods of approximately 0.03–0.3 sec. That dip is less pronounced in the nonlinear codes, which produce amplification factor shapes more compatible with the empirical model.

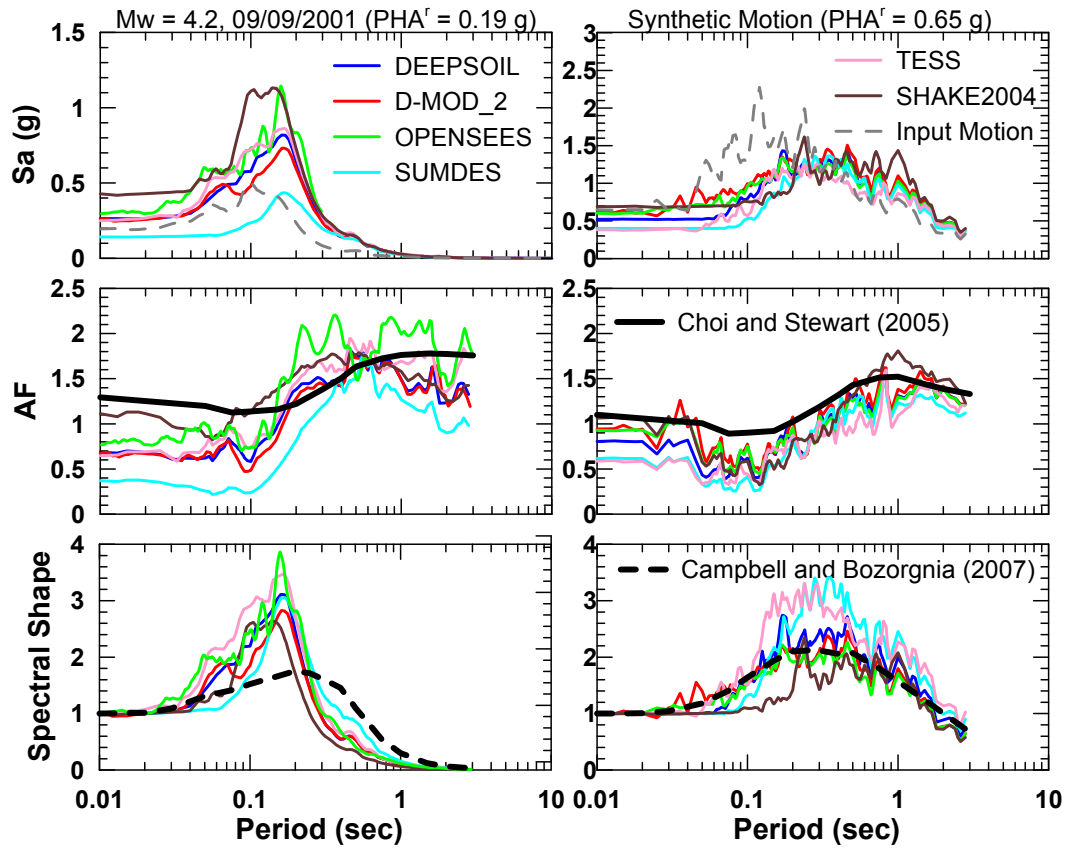


Fig. 7.45 Comparison of spectral shapes of predictions at different shaking levels for La Cienega site.

## 8 Summary and Conclusions

### 8.1 SCOPE OF RESEARCH

Ground motion prediction equations are used in seismic hazard analyses to provide a probabilistic distribution of a particular ground motion intensity measure ( $IM$ ) conditional on source, path, and site parameters. The estimates from such relationships only represent averaged values across the range of possible site conditions within the rock or soil categories, while the actual site conditions can be influenced by sediment response to upwardly propagating body waves (ground response effects), basin effects, and surface topography. Ground response effects can be quantified by site amplification factor models (derived empirically or theoretically) or site-specific theoretical ground response analyses for which soil material models can be either equivalent-linear or nonlinear.

Nonlinear ground response analyses are seldom used in engineering practice because they require the specification of input parameters that lack an obvious association with fundamental soil properties and because the sensitivity of the site response results to these parameters is not well understood. Moreover, parameter selection criteria and code usage protocols do not exist or are poorly documented for many codes, which effectively erect a barrier to code usage for non-expert users. Key hurdles to practical application of nonlinear ground response analyses were identified as the selection of parameters describing the backbone curves (which affects both soil nonlinearity and hysteretic damping), the specification of input motions (“outcropping” versus “within”), and the specification of viscous damping (i.e., the target value of the viscous damping ratio and frequencies for which the viscous damping produced by the model matches the target). Exact (linear frequency-domain) solutions for body-wave propagation through an elastic medium were used to establish guidelines for the specification of input motions and viscous damping. Strategies for specifying backbone-curve parameters armed only with basic information on soil conditions (small-strain shear modulus and target modulus reduction and damping curves as

established from information on soil type, overburden stress, PI, etc.) were developed. Because these curves are only valid for shear strains less than about 0.1–0.3%, additional guidelines were developed for intelligently extending the curves to approach the shear strength at large strains. Options are developed for optimally fitting the modulus reduction curve (MR fitting) and for establishing a simultaneously optimal fit for modulus reduction and material damping (MRD fitting).

The parameter selection protocols developed for nonlinear ground response analyses are tested by comparing predictions to data from vertical arrays and looking for trends in the results. Key issues that would ideally be examined through this validation exercise include assessing the adequacy of the viscous damping protocols and comparing alternative strategies for specifying backbone-curve parameters. In addition, the sensitivity of predictions due to different sources of variability (material properties and modeling schemes) was studied. Finally, targeted analyses were performed to facilitate comparisons of the performance of equivalent-linear and nonlinear analyses for different levels of shaking (different strain conditions).

## **8.2 RESEARCH FINDINGS AND RECOMMENDATIONS**

The results of this research can be broadly categorized as follows: (a) parameter selection protocols for nonlinear ground response analyses and (b) assessment of performance of nonlinear ground response analyses. The major conclusions from the study are grouped according to these categories in the subsections that follow.

### ***(a) Parameter Selection Protocols for Nonlinear Ground Response Analyses***

Protocols were developed regarding control motion specification, specification of viscous damping model and parameters, and specification of parameters describing the nonlinear backbone curve.

**Control Motion Specification:** Outcropping control motions should be used as-recorded with an elastic base. Motions recorded at depth should also be used as-recorded but with a rigid base. In both cases, the motions are specified at the base of the site profile. For within motions, the depth at which the recording was made should match the depth of the profile base.

**Specification of Viscous Damping Model and Parameters:** When the option of using more than one target frequency is available (such as the full Rayleigh damping formulation), it should be applied in lieu of simplified Rayleigh damping because significant bias at high frequencies can occur with the latter. Target damping ratios should be set to the small-strain material damping.

The target frequencies should be selected using an iterative process in which the frequencies are adjusted to optimally match linear frequency-domain and time-domain analyses. If such iterative analyses are not possible, or as a first guess of frequencies to get such iterative analyses started, the two target frequencies in a full Rayleigh damping formulation should be set to the site frequency and five times the site frequency.

The code SUMDES, for which only the simplified Rayleigh damping formulation is available, should be used with a damping ratio of 1% at 1 Hz (the code assumes that the target damping ratio is given at 1 Hz). The code TESS does not use viscous damping but does introduce a parameter VT that affects unload-reload behavior. This parameter can be set equal to the small-strain damping (in decimal units).

**Specification of Backbone Curve Parameters:** The selection of backbone curve parameters begins with the development of an appropriate shear wave velocity ( $V_s$ ) profile for the site and the identification of appropriate target nonlinear modulus reduction and damping curves for each soil layer at the site. The target nonlinear curves can be established from material-specific testing or, up to strain levels of approximately 0.1–0.3%, from correlation relationships (Darendeli 2001; Zhang et al. 2005). When large strains are expected in portions of a site (i.e., above a significant impedance contrast for sites subject to strong input motions), the site characterization should also include the evaluation of dynamic shear strengths in the potentially affected layers. The procedures to estimate undrained shear strength through stress normalization are well established (Ladd 1991), but require modification for rate effects (e.g., Sheahan et al. 1996).

In typical ground response analyses, most soil layers are not expected to approach soil failure. This will generally be the case in profiles with gradual changes in  $V_s$  with depth. For sites with a large impedance contrast, soil failure would likely be confined only to depth intervals immediately above (i.e., on the softer side of) the impedance contrast. For all layers not approaching soil failure, target backbone curves can be defined using modulus reduction relationships without consideration of shear strength. For problems involving moderate to large-

strain response, a hybrid representation that accounts for the shape of the modulus reduction curve at small strains and shear strength at large strain is recommended.

Ultimately it is hoped that procedures for simultaneously matching target modulus reduction and material damping curves will be implemented in nonlinear codes, but this is not currently available. At present, users can choose to match the modulus reduction curve only (MR fitting) or modulus reduction and damping curves simultaneously (MRD fitting). We recommend the use of both approaches for large-strain problems to bound the solution.

**(b) *Assessment of Performance of Nonlinear Ground Response Analyses***

The limited available validations against vertical array data suggest that the models produce reasonable results, although there is some indication of overdamping at high frequencies and overestimation of site amplification at the resonant frequency of the site model. Possible sources of the high-frequency misfit include potential bias in the velocity profile, material damping curves, or a viscous damping level that is too high.

The variability of predictions due to material curve uncertainty seems to be most pronounced at periods less than 0.5 sec and produces significant response variability only for relatively thick site profiles — it is not a significant issue for shallow sites. The effect of velocity variability can have a strong influence on the predictions near the elastic site period, but the effect is observed only for sites with a large impedance contrast that dominates the site response in these cases. Model-to-model variability is most pronounced at low periods, where the differences result principally from different damping formulations.

Nonlinearity is modeled well by nonlinear codes (for input motions with  $PHA'$  up to 0.2 g; performance of codes above this level is uncertain because no data are available) although the level of amplification from theoretical analyses and data demonstrate bias at multiple periods as explained above.

The results of equivalent-linear (EL) and nonlinear (NL) analyses can be compared by examining predicted trends in amplification factors versus input motion amplitude at various periods and by examining trends in spectral shape. With respect to the former issue, EL amplification factors tend to depart from NL factors at input  $PGA'$  (peak acceleration on rock) values above 0.1–0.2 g. In general, the EL factors were larger than the NL factors for large input motion levels. The EL and NL spectral shapes start to deviate from each other above  $PHA'$  of 0.2

g. At low periods ( $T < 0.1$  sec), the EL spectral shapes for strong shaking are flatter and have less period-to-period fluctuations than the NL spectral shapes. The NL codes DMOD\_2, DEEPSOIL, and OpenSees produce generally similar amplification factors and spectral shapes. The results from these codes can differ from TESS results at high frequencies, mostly as a result of the different damping formulation in TESS. The SUMDES results tend to be significantly different from those of other codes for deep sites, which is attributed to the use of the simplified Rayleigh damping formulation in SUMDES.

### 8.3 RECOMMENDATIONS FOR FUTURE RESEARCH

This research has identified several issues that should be considered in future work:

1. So far only three vertical array sites have been used to test the effectiveness of the parameter selection protocols. More validation sites should be tested to see if the prediction trends and biases identified in this research are also present in other sites. If they are consistent across sites, future study is needed to investigate how to reduce these biases. Possible ways may be to consider revising the current protocols for the specification of damping (both viscous and hysteretic).
2. Empirical amplification factors for the validation sites show significant event-to-event variability, particularly at high frequencies. Ground response analyses utilizing the recorded motions for events with high and low residuals should be performed to see if any of the event-to-event variability can be explained by features of the input motions (the analyses for amplification factors in this research used a common waveform). Other factors that should be considered would involve the location of the site relative to the respective sources, and consideration of possible 2D and 3D site response effects that may differ from one event to the next.
3. The nonlinear and equivalent-linear codes considered in this work have not been well validated at large strain levels. The use of centrifuge test data to enable such validations was considered, but was dissuaded because the experimental configurations do not correspond to 1D conditions (Elgamal et al. 2005). If this issue can be resolved, either through improved experiment design or by implementation of the nonlinear soil models in 2D and 3D codes, it would be very useful to generate validation data sets at large strains in the centrifuge. These data would be useful to (1) evaluate the relative ability of

EL and NL analysis to capture trends in site amplification and spectral shape as shaking levels increase; (2) demonstrate the importance of matching the true reference strain (which is based on shear strength) when specifying backbone curves in lieu of MR or MRD fitting procedures; and (3) evaluate energy dissipation in site response and the degree to which it is accurately simulated using the combined viscous and hysteretic damping formulations currently utilized in NL codes.

4. This research is based on the total stress analysis options in the respective nonlinear codes. A benchmarking exercise related to the pore pressure generation and dissipation features of nonlinear codes is needed to guide parameter selection for effective stress analyses. Validation for such cases will be challenging due to the limited number of vertical array recordings at liquefiable soil sites. As mentioned in (3) above, centrifuge studies have the potential to provide useful information in this regard. One issue that would be particularly useful to consider in the validations is the extent to which model accuracy improves for codes that consider within-cycle contractive and dilative behavior (i.e., OpenSees) relative to codes that simply degrade the strength and stiffness of the backbone curve (e.g., DMOD\_2 and TESS).

## REFERENCES

- Anderson, D.G., and Y.K. Tang (1989). "Summary of soil characterization program for the Lotung large-scale seismic experiment," *Proc. EPRI/NRC/TPC Workshop on Seismic Soil-Structure Interaction Analysis Techniques Using Data from Lotung, Taiwan, EPRI NP-6154*, Electric Power Research Institute, Palo Alto, Calif., Vol. 1, 4.1–4.20
- Andrade, J.E., and R.I. Borja (2006). "Quantifying sensitivity of local site response models to statistical variations in soil properties," *Acta Geotechnica*, 1, 3–14
- Assimaki, D. and E. Kausel (2002). "An equivalent linear algorithm with frequency- and pressure-dependent moduli and damping for the seismic analysis of deep sites," *Soil Dynamics and Earthquake Engrg.*, 22(3), 959–965
- Baker, J.W. and C.A. Cornell (2003). "Uncertainty specification and propagation for loss estimation using FOSM methods," *Proceedings, 9<sup>th</sup> Int. Conf. on Applications of Statistics and Probability in Civil Engineering (ICASP9)*, San Francisco, California: Millpress., Rotterdam, Netherlands, 8p.
- Beresnev, I. A., Wen, K. L. and Yeh Y. T. (1995) "Seismological evidence for nonlinear elastic ground behavior during large earthquakes," *Soil Dynamics and Earthquake Eng.*, 14 (2), 103–114.
- Borja, R. I., H.Y. Chao, F.J. Montans and C.H. Lin (1999). "Nonlinear ground response at Lotung LSST site," *J. Geotech. & Geoenv. Eng.*, ASCE, 125 (3), 187–197.
- Borja, R.I. and W.H. Wu (1994). "Vibration of foundations on incompressible soils with no elastic region," *J. Geotech. Engrg.*, ASCE, 120(9), 1570–1592.
- Campbell, K.W. and Y. Bozorgnia (2007). "Campbell-Bozorgnia NGA ground motion relations for the geometric mean horizontal component of peak and spectral ground motion parameters," *PEER Rpt 2007/02*, Pacific Earthquake Engineering Research Center, Richmond, California
- Chang, S.W. (1996). "Seismic response of deep stiff soil deposits," *Ph.D. Thesis*, Univ. of California, Berkeley.
- Chang, C.-Y., C.M. Mok, M.S. Power, Y.K. Tang, H.T. Tang, and J.C. Stepp (1990). "Equivalent linear versus nonlinear ground response analyses at Lotung seismic experiment site," *Proc. 4<sup>th</sup> U.S. National Conf. Eqk. Engrg.*, Vol. 1.

- Chang, S. W., J.D. Bray and R.B. Seed (1996). "Engineering implications of ground motions from the Northridge earthquake," *Bull. Seism. Soc. Am.*, 86, S270–S288.
- Ching, J., K.A. Porter, and J.L. Beck (2004). "Uncertainty propagation and feature selection for loss estimation in performance-based earthquake engineering," *EERL Report 2004-02*, Earthquake Engineering Research Laboratory, California Institute of Technology, Pasadena, California.
- Chiu, P., D.E. Pradel, A.O.L. Kwok and J.P. Stewart (2008). "Seismic response analyses for the Silicon Valley Rapid Transit Project," *Proc. 4<sup>th</sup> Decennial Geotechnical Earthquake Engineering and Soil Dynamics Conference*, ASCE, Sacramento, CA
- Choi, Y. and J.P. Stewart (2005). "Nonlinear site amplification as function of 30 m shear wave velocity," *Earthquake Spectra*, 21, 1–30.
- Chopra, A.K. (2000). *Dynamics of Structures*, 2<sup>nd</sup> Ed., Prentice Hall, Englewood Cliffs, New Jersey
- Clough, G.W., and J. Penzien (1993). *Dynamics of Structures*, 2<sup>nd</sup> Ed., McGraw-Hill, New York.
- Cramer, C.H. (1995). "Weak-motion observations and modeling for the Turkey Flat, U.S., site-effects test area near Parkfield, California," *Bull. Seism. Soc. Am.*, 85 (2), 440–451
- Cramer, C.H. and C.R. Real (1992). "A statistical analysis of submitted site-effects predictions for the weak-motion blind prediction test conducted at the Turkey Flat, USA, site effects test area near Parkfield, California," *Proceedings, Int. Sym. on the Effects of Surface Geology on Seismic Motion*, v. 2, March 25–27, Odawara, Japan
- Dafalias, Y.F. and E.P. Popov (1979). "A model for nonlinearly hardening materials for complex loading," *Acta Mechanica*, 21(3), 173–192
- Darendeli, M. (2001). "Development of a new family of normalized modulus reduction and material damping curves." *Ph.D. Thesis*, Dept. of Civil Eng., Univ. of Texas, Austin.
- Darragh, R.B. and I.M. Idriss (1997). "A tale of two sites: Gilroy #2 and Treasure Island – Site response using an equivalent linear technique," NEHRP Professional Fellowship Report, EERI, Oakland, CA.
- Day, S. M., J. Bielak, D. Dreger, R. Graves, S. Larsen, K.B. Olsen, A. Pitarka, and L. Ramirez-Guzman (2006). "Numerical simulation of basin effects on long-period ground motion," paper 1857, presented at the *8th U.S. National Conference on Earthquake Engineering*, 18–22 April, San Francisco, California

- Dickenson, S.E. (1994). "The dynamic response of soft and deep cohesive soils during the Loma Prieta earthquake of October 17, 1989," *Ph.D. Thesis*, Univ. of California, Berkeley.
- Dobry, R., R.S. Ladd, F.Y. Yokel, R.M. Chung and D. Powell (1982). "Prediction of pore water pressure buildup and liquefaction of sands during earthquakes by the cyclic strain method," National Bureau of Standards Building Science Series 138, National Bureau of Standards and Technology, Gaithersburg, Md., 150
- Dobry, R., W.G. Pierce, R. Dyvik, G.E. Thomas, and R.S. Ladd. (1985). "Pore pressure model for cyclic straining of sand," Research Report, Civil Eng. Dept., Rensselaer Polytechnic Institute, Troy, New York
- Electrical Power Research Institute, EPRI (1993). "Guidelines for determining design basis ground motions," *Rpt. No. EPRI TR-102293*, Electrical Power Research Institute, Palo Alto, CA.
- Elgamal, A.W., M. Zeghal, and E. Parra (1996). "Liquefaction of reclaimed island in Kobe, Japan," *J. Geotech. Eng.*, 122 (1), 39–49.
- Elgamal, A.W., Z. Yang, T. Lai, B.L. Kutter, D.W. Wilson (2005). "Dynamics response of saturated dense sand in laminated centrifuge container," *J. Geotech. and Geoenviron. Eng.*, ASCE, 131(5), 598–609
- Field, E.H. and K.H. Jacob (1993). "Monte-Carlo simulation of the theoretical site response variability at Turkey Flat, California, given the uncertainty in the geotechnically derived input parameters," *Earthquake Spectra*, 9 (4), 669–701
- Finn, W. D. L., K.W. Lee, and G.R. Martin (1977). "An effective stress model for liquefaction," *J. Geotech. Eng. Div.*, ASCE, 103 (6), 517–553.
- Graves, R. W. (1996). "Simulating seismic wave propagation in 3D elastic media using staggered-grid finite-differences," *Bull. Seism. Soc. Am.*, 86, 1091–1106.
- Hardin, B.O. and V.P. Drnevich (1972). "Shear modulus and damping in soils: design equations and curves," *J. of the Soil Mechanics and Foundations Div.*, ASCE, 98 (SM7), 667–692
- Hashash, Y.M.A. and D. Park (2001). "Non-linear one-dimensional seismic ground motion propagation in the Mississippi embayment," *Eng. Geology*, Amsterdam, 62(1–3), 185–206.
- Hashash, Y.M.A. and D. Park (2002). "Viscous damping formulation and high frequency motion propagation in nonlinear site response analysis," *Soil Dynamics and Earthquake Engrg.*, 22(7), 611–624.

- Hudson, M., I.M. Idriss, and M. Beikae (1994). "QUAD4M – A computer program to evaluate the seismic response of soil structures using finite element procedures and incorporating a compliant base." Center for Geotechnical Modeling, Dept. Civil and Envir. Eng., Univ. of Calif., Davis, CA
- Idriss, I.M. (1990). "Response of soft soil sites during earthquakes," *Proc. H. Bolton Seed Memorial Symposium*, J.M. Duncan (ed.), Vol. 2, 273–290.
- Idriss, I.M. and J.I. Sun (1992). *SHAKE91: A computer program for conducting equivalent linear seismic response analyses of horizontally layered soil deposits*, Center for Geotech. Modeling, Univ. of Calif., Davis.
- Idriss, I.M. (1993). "Assessment of site response analysis procedures," *Report to National Institute of Standards and Technology*, Gaithersburg, Maryland, Dept. of Civil & Environmental Eng., Univ. of California, Davis.
- Idriss, I.M., R. Dobry and R.D. Singh (1978). "Nonlinear behavior of soft clays during cyclic loading," *J. Geotech. Eng. Div.*, ASCE, 104 (GT12), 1427–1447
- Isenhower, W. M. , and K. H., II Stokoe (1981). "Strain-rate dependent shear modulus of San Francisco Bay mud," *International Conference on Recent Advances in Geotechnical Earthquake Eng. and Soil Dynamics*; St. Louis, Mo., pp. 597–602.
- Ishihara, K. (1986). "Evaluation of soil properties for use in earthquake response analysis," *Geomechanical Modeling in Eng. Practice*, R. Dungar and J.A. Studer, Eds., A.A.Balkema, Rotterdam, the Netherlands, 241–275
- Iwan, W.D. (1967). "On a class of models for the yielding behavior of continuous and composite systems," *J. of Applied Mechanics*, 34 (E3), 612–617
- Jacobsen, L.S. (1930). "Steady forced vibrations as influenced by damping." *Transactions*, ASME, Vol. 52, No. 15, 169 - 181.
- Joyner, W. B. and A.T.F. Chen (1975). "Calculation of nonlinear ground response in earthquakes," *Bull. Seism. Soc. Am.*, 65(5), 1315–1336
- Kausel, E. and D. Assimaki (2002). "Seismic simulation inelastic soils via frequency-dependent moduli and damping." *J. of Engrg. Mech.*, ASCE, 128(1), 34–47.
- Kondner, R. L., and J.S. Zelasko (1963). "A hyperbolic stress-strain formulation of sands," *Proc. of 2<sup>nd</sup> Pan American Conference on Soil Mechanics and Foundation Engineering*, Sao Paulo, Brasil, 289–324

- Kramer, S.L. (1996). *Geotechnical Earthquake Engineering*, Prentice Hall, Englewood Cliffs, New Jersey
- Kramer, S.L. and A.W. Elgamal (2001). “Modeling soil liquefaction hazards for performance-based earthquake engineering,” *PEER Rept 2001/13*, Pacific Earthquake Engineering Research Center, Richmond, California
- Kramer, S.L. and S.B. Paulsen (2004). “Practical use of geotechnical site response models,” *Proc. Int. Workshop on Uncertainties in Nonlinear Soil Properties and their Impact on Modeling Dynamic Soil Response*, PEER Center Headquarters, Richmond, CA
- Kwok, O.L.A. (2007). “Application of one-dimensional geotechnical modeling for site response predictions,” *PhD. Thesis*, Department of Civil and Environmental Engineering, University of California, Los Angeles
- Kwok, O.L.A., and J.P. Stewart (2006). “Application of theoretical 1D amplification factors for evaluation of seismic site effects,” *Bull. Seismol. Soc. Am.*, 96, no. 4a, 1422–1436
- Kwok, O.L.A., J.P. Stewart, Y.M.A. Hashash, N. Matasovic, R.M. Pyke, Z.L. Wang, and Z. Yang. (2006). “Utilizing nonlinear seismic ground response analysis for Turkey Flat blind predictions,” *Proceedings, 3rd Int. Sym. on the Effects of Surface Geology on Seismic Motion*, August 29 – September 1, Grenoble, France, Paper 50.
- Kwok, O.L.A., J.P. Stewart, Y.M.A. Hashash, N. Matasovic, R.M. Pyke, Z.L. Wang, and Z. Yang (2007). “Use of exact solutions of wave propagation problems to guide implementation of nonlinear seismic ground response analysis procedures,” *J. of Geotech. & Geoenviron. Eng.*, ASCE, 133, no. 11, 1385–1398
- Lacy, S. (1986). “Numerical procedures for nonlinear transient analysis of two-phase soil system,” *PhD Thesis*, Princeton Univ. Princeton, N.J.
- Ladd, C.C. (1991). “Stability evaluation during staged construction: 22<sup>nd</sup> Terzaghi Lecture,” *J. Geotech. Engr.*, ASCE, 117 (4), 537–615
- Laird, J.P and K.H. Stokoe (1993). “Dynamic properties of remolded and undisturbed soil sample tests at high confining pressure,” *GR93-6*, Electric Power Research Institute
- Lanzo, G. and M. Vucetic (1999). “Effect of soil plasticity on damping ratio at small cyclic strains,” *Soils and Foundations*, 39(4), 131–141.

- Lee, M. K. W., and W.D.L. Finn (1975). "DESRA-1, Program for the dynamic effective stress response analysis of soil deposits including liquefaction evaluation," *Soil Mechanics Series No.36*, Department of Civil Eng., University of British Columbia, Vancouver, Canada
- Lee, M.K.W. and W.D.L. Finn. (1978). "DESRA-2: Dynamic effective stress response analysis of soil deposits with energy transmitting boundary including assessment of liquefaction potential," *Soil Mechanics Series 36*, Dept. of Civil Eng., Univ. of British Columbia, Vancouver, Canada, 60 p
- Li, X.S., Z.L. Wang and C.K. Shen (1992). *SUMDES: A nonlinear procedure for response analysis of horizontally-layered sites subjected to multi-directional earthquake loading*, Dept. of Civil Eng., Univ. of Calif., Davis.
- Li, X. S., C.K. Shen, and Z.L. Wang (1998). "Fully coupled inelastic site response analysis for 1986 Lotung earthquake," *J. Geotech. & Geoenv. Eng.*, ASCE, 124 (7), 560–573.
- Liu, A.H., J.P. Stewart, N.A. Abrahamson, Y. Moriwaki, Y. (2001). "Equivalent number of uniform stress cycles for soil liquefaction analysis," *J. Geotech. & Geoenv. Eng.*, ASCE, 127 (12), 1017–1026.
- Lo Presti, D.C.F., Lai, C.G. and I. Puci (2006). "ONDA: Computer code for nonlinear seismic response analyses of soil deposits." *J. of Geotech. and Geoenvir. Eng.*, ASCE, 132(2), 223–236
- Lysmer, J., H.B. Seed and P.B. Schnabel (1971). "Influence of base-rock characteristics on ground response." *Bull. Seism. Soc. Am.*, 61(5), 1213–1232
- Martin, G.R., W.D.L. Finn, and H.B. Seed (1975). "Fundamentals of liquefaction under cyclic loading," *J. of the Geotech. Eng. Div.*, ASCE, 101 (5), 423–438
- Martin, P. P. (1975). "Non-linear methods for dynamic analysis of ground response," *Ph. D. Thesis*, Univ. of California, Berkeley.
- Martin, P.P and H.B. Seed (1978). " APOLLO, a computer program for the non-linear analysis of pore pressure generation and dissipation in horizontal sand layers during cyclic earthquake loading, " *Report No. EERC 78-21*, Earthquake Eng. Research Center, Univ. of Calif., Berkeley , California
- Masing, G. (1926). "Eigenspannungen and verfertigung beim messing." *Proc. 2<sup>nd</sup> Int. Congress on Applied Mech.*, Zurich, Switzerland

- Matasovic, N. (2006). "D-MOD\_2 – A Computer Program for Seismic Response Analysis of Horizontally Layered Soil Deposits, Earthfill Dams, and Solid Waste Landfills." *User's Manual*, GeoMotions, LLC, Lacey, Washington, 20 p. (plus Appendices).
- Matasovic, N., Kavazanjian, E., Jr. and Abourjeily, F. (1995), "Dynamic Properties of Solid Waste from Field Observations," *Proc. 1st International Conference on Earthquake Geotechnical Engineering*, Tokyo, Japan, Vol. 1, pp. 549-554.
- Matasovic, N. and M. Vucetic (1993a). "Cyclic Characterization of Liquefiable Sands," *J. of Geotech. Eng.*, ASCE, 119(11), 1805-1822
- Matasovic, N. and M. Vucetic (1993b). "Seismic response of horizontally layered soil deposits," *Report No. ENG 93-182*, School of Engineering and Applied Science, University of California, Los Angeles.
- Matasovic, N. and M. Vucetic (1995). "Generalized cyclic degradation-pore pressure generation model for clays," *J. Geotech. Eng.*, ASCE, 121 (1), 33-42.
- Matasovic, J. and M. Vucetic (1996). "Analysis of seismic records from the Wildlife Liquefaction site," *Proc. 11<sup>th</sup> World Conf. Earthquake Eng.*, Disc 1, Paper 209.
- McKenna, F. and G.L. Fenves (2001). "The OpenSees command language manual, version 1.2." Pacific Earthquake Engrg. Research Center, Univ. of Calif., Berkeley. (<http://opensees.berkeley.edu>).
- Melchers, R.E. (1999). *Structural Reliability Analysis and Prediction*. John Wiley and Sons, Chichester.
- Mroz, Z. (1967). "On the description of anisotropic work hardening," *J. Mech. And Physics of Solids*, 15, 163-175
- Newmark, N.M. (1959). "A method of computation for structural dynamics," *J. Eng Mech. Div.*, ASCE, 67-94
- Nigbor, R. and T. Imai (1994). "The Suspension P-S Velocity Logging Method," in *Geophysical Characterization of Sites*, ISSMFE Special Publication TC 10.
- Olsen, K.B. (2000). "Site amplification in the Los Angeles basin from three-dimensional modeling of ground motion," *Bull. Seism. Soc. Am.*, 90, S77-S94.
- Park, D. and Y.M.A. Hashash (2004). "Soil damping formulation in nonlinear time domain site response analysis," *J. of Earthquake Eng.*, 8(2), 249-274.

- Parra, E. (1996). "Numerical modeling of liquefaction and lateral ground deformation including cyclic mobility and dilation response in soil systems" *PhD Thesis*, Dept. of Civil Engrg., Rensselaer Polytechnic Institute, Troy, NY.
- Pestana, J.M. and F. Nadim (2000). "Nonlinear site response analysis of submerged slopes," *Report No. UCB/GT/2000-04*, Dept. of Civil & Envir. Eng., U.C. Berkeley.
- Potts, D.M. and L. Zdravković (1999). *Finite element analysis in geotechnical engineering: theory*, Thomas Telford Ltd., London
- Prevost, J.H. (1977). "Mathematical modeling of monotonic and cyclic undrained clay behavior," *Int. J. Numerical and Analytical Methods in Geomechanics*, 1 (2), 195-216
- Prevost, J.H. (1985). "A simple plasticity theory for frictional cohesionless soils," *Soil Dyn. Earthquake Eng.*, 4(1), 9-17
- Prevost, J.H. (1989). "DYNA1D - A computer program for nonlinear seismic site response analysis: Technical documentation," *Rpt. No. NCEER-89-0025*, National Center for Earthquake Engineering Research, Buffalo, N.Y.
- Pyke, R.M. (1979). "Nonlinear soil models for irregular cyclic loadings," *J. Geotech. Eng.*, ASCE, 105(GT6), 715-726.
- Pyke, R.M. (2000). *TESS: A computer program for nonlinear ground response analyses*. TAGA Engineering Systems & Software, Lafayette, Calif.
- Qiu, P. (1997). "Earthquake induced nonlinear ground deformation analyses," *Ph.D. Thesis*, Univ. of Southern California.
- Ragheb, A. M. (1994). "Numerical analysis of seismically induced deformations in saturated granular soil strata," *PhD Thesis*, Dept. of Civil Eng., Rensselaer Polytechnic Institute, Troy, NY.
- Ramberg, W. and W.R. Osgood (1943) "Description of stress-strain curves by three parameters," *Technical Note 902*, National Advisory Committee for Aeronautics, Washington, D.C.
- Rayleigh, J.W.S and R.B. Lindsay (1945). *The theory of sound*, Dover Publications, New York
- Real, C.R. (1988). "Turkey Flat, USA site effects test area – report 2, site characterization," *TR 88-2*, Calif. Div. of Mines and Geology
- Real, C.R. and C.H. Cramer. (1989) "Turkey Flat, USA Site Effects Test Area – report 3: weak-motion test: prediction criteria and input rock motions," *TR 89-1*, Calif. Div. of Mines and Geology

- Real, C.R. and A.F. Shakal. (2005). "Turkey Flat, USA site effects test area - report 7, strong motion test: prediction criteria and data formats," *CSMIP Rept. OSMS 05-01*, Calif. Geological Survey, Dept. of Conservation.
- Real, C.R., A.F. Shakal, B.E. Tucker (2006). "Turkey Flat, U.S.A. site effects test area: anatomy of a blind ground-motion prediction test," *Proceedings, 3rd Int. Sym. on the Effects of Surface Geology on Seismic Motion*, August 29 e.g., September 1, Grenoble, France, Paper KN 3.
- Roblee, C.J., W.J. Silva, G.R. Toro and N.A. Abrahamson (1996). "Variability in site-specific seismic ground motion design predictions," *ASCE Geotech. Special Publication No. 58*, Uncertainty in the Geologic Environment: From Theory to Practice, C.D. Shakelford, P.P. Nelson (eds.), Vol. 2, 1113-1133
- Roesset, J.M. and R.V. Whitman (1969). "Theoretical background for amplification studies." *Research report R69-15, Soils publications no. 231*, Massachusetts Institute of Technology, Cambridge, Massachusetts
- Roscoe, K.H. and J.B. Burland (1968). "On the generalized stress-strain behavior of 'wet' clay," J. Heyman and F.A. Leckie, eds., *Eng. Plasticity*, University Press, Cambridge, 535-609
- Roscoe, K.H. and A.N. Schofield (1963). "Mechanical behavior of an idealized 'wet' clay," *Proc. of 2<sup>nd</sup> European Conference on Soil Mechanics*, Wiesbaden, Germany, Vol. 1, 47-54
- Rosenblueth, E., 1975, "Point estimates for probability moments," *Proc. Nat. Acad. of Sci.*, **72**(10), 3812-3814
- ROSRINE, Resolution of Site Response Issues from the Northridge Earthquake, <http://gees.usc.edu/ROSRINE>
- Rymer, M.J., J.C. Tinsley III, J.A. Treiman, J.R. Arrowsmith, K.B. Clahan, A.M. Rosinski, W.A. Bryant, H.A. Snyder, G.S. Fuis, N.A. Toke and G.W. Bawden (2006). "Surface fault slip associated with the 2004 Parkfield, California, earthquake," *Bull. Seism. Soc. Am.*, 96 (4B), S11-S27
- Schnabel, P.B, J. Lysmer and H.B. Seed (1972). "SHAKE: A computer program for earthquake response analysis of horizontally layered site,." *Report no. UCB/EERC-72/12*, Earthquake Engrg. Research Center, Univ. of Calif., Berkeley, California, 102p
- Seed, H.B. (1979). "Soil liquefaction and cyclic mobility evaluation for level ground during earthquake," *J. Geotech. Engr. Div.*, ASCE, 105, GT2, 201-225

- Seed, H.B. and I.M. Idriss (1970). "Soil moduli and damping factors for dynamic response analyses," *Report EERC 70-10*, Earthquake Engineering Research Center, University of California, Berkeley.
- Seed, H.B., I.M. Idriss, F. Makdisi, and N. Banerjee (1975) "Representation of irregular stress time histories by equivalent uniform stress series in liquefaction analyses," *Rpt EERC 75-29*, Earthquake Engineering Research Center, Univ. of California, Berkeley.
- Seed, H.B., P.P. Martin and J. Lysmer (1976) "Pore-water pressure changes during soil liquefaction," *J. Geotech. Eng. Div.*, ASCE, 102 (GT4), 323-346
- Seed, H.B., M.P. Romo, J.I. Sun, A. Jaime and J. Lysmer (1987). "Relationships between soil conditions and earthquake ground motions in Mexico City in the earthquake of September 19, 1985," *Rpt. No. UCB/EERC-87/15*, Earthquake Eng. Research Center, Univ. of Calif., Berkeley.
- Seed, H.B., R.T. Wong, I.M. Idriss and K. Tokimatsu (1984). "Moduli and damping factors for dynamic analyses of cohesionless soils," *Rpt UCB/EERC-84/14*, Earthquake Engineering Research Center, Univ. of California, Berkeley, Calif.
- Sheahan, T.C., C.C. Ladd, and J.T. Germaine (1996) "Rate-dependent undrained shear behavior of saturated clay," *J. Geotech. Engr.*, ASCE, 122 (2), 99-108
- Silva, W.J., N. Abrahamson, G. Toro, C. Costantino (1996) "Description and validation of the stochastic ground motion model," Research report prepared for the Engineering Research and Applications Division, Department of Nuclear Energy, Brookhaven National Laboratory, Associated Universities, New York
- Silva, W.J. and K. Lee (1987). "WES RASCAL code for synthesizing earthquake ground motions," State of the Art for Assessing Earthquake Hazards in the United States, *Report 24*, U.S. Army Engineers Waterway Experiment Station, *Misc. Paper S-73-1*.
- Silva, W.J., R.B. Darragh, N. Gregor, G. Martin, N.A. Abrahamson, and C. Kircher (2000). "Reassessment of site coefficients and near-fault factors for building code provisions," Report to U.S. Geological Survey, National Earthquake Hazards Reduction Program.
- Stewart, J.P., O.L.A. Kwok, Y.M.A. Hashash, N. Matasovic, R. Pyke, Z.L. Wang, and Z. Yang (2006). "Overcoming hurdles that limit the application of nonlinear seismic ground response analysis in engineering practice," *5<sup>th</sup> National Seismic Conference on Bridges and Highways*, San Francisco, CA

- Stewart, J.P. and O.L.A. Kwok (2008). "Nonlinear seismic ground response analysis: code usage protocols and verification against vertical array data," *Proc. 4<sup>th</sup> Decennial Geotechnical Earthquake Engineering and Soil Dynamics Conference*, ASCE, Sacramento, CA
- Sun, J.I., R. Golesorkhi, and H.B. Seed (1988). "Dynamic moduli and damping ratios for cohesive soils," *Rpt UCB/EERC-88/15*, Earthquake Engineering Research Center, Univ. of California, Berkeley, Calif.
- Tan, K. and M. Vucetic (1989). "Behavior of medium and low plasticity clays under cyclic simple shear conditions," *Proc. 4<sup>th</sup> International Conference on Soil Dynamics and Earthquake Engineering*, Soil Dynamics and Liquefaction Volume, Mexico City, 131-142
- Terzaghi, K. (1925). *Erdbaumechanik auf Bodenphysikalischer Grundlage*, Franz Deuticke, Leipzig und Wien
- Toro, G. R. (1997). "Probabilistic models of shear-wave velocity profiles at the Savannah River site, South Carolina." *Rep. to Pacific Engineering and Analysis*, El Cerrito, Calif.
- Tucker, B.E. and C.R. Real (1986). "Turkey Flat, USA site effects test area – report 1: needs, goals, and objectives," *TR 86-1*, Calif. Div. of Mines and Geology
- Vucetic, M. (1990). "Normalized behavior of clay under irregular cyclic loading." *Canadian Geotech. J.*, 27, 29-46.
- Vucetic, M. (1994). "Cyclic characterization for seismic regions based on PI," *Proc. XIII International (World) Conference on Soil Mechanics and Foundation Engineering*, New Delhi, India, Vol 1, 329-332
- Vucetic, M. and R. Dobry (1986). "Pore pressure buildup and liquefaction at level sandy sites during earthquakes," *Research report CE-86-3*, Dept. Civil Eng., Rensselaer Polytechnic Institute, New York
- Vucetic, M. and R. Dobry (1988). "Degradation of marine clays under cyclic loading," *J. of the Geotech. Eng.*, ASCE, 114 (2), 133-149
- Vucetic, M. and R. Dobry (1991). "Effect of soil plasticity on cyclic response," *J. Geotech. Eng.*, 117, 89-107.
- Vucetic, M., G. Lanzo, and M. Doroudian (1998). "Damping at small strains in cyclic simple shear test." *J. Geotech. and Geoenviron. Eng.*, ASCE, 124(7), 585-594.

- Wang, Z.L. (1990). "Bounding surface hypoplasticity model for granular soils and its applications." *PhD. Thesis*, Univ. of Calif., Davis
- Wang, Z.L., Y.F. Dafalias, C.K. Shen (1990). "Bounding surface hypoplasticity model for sand," *J. Eng. Mech.*, ASCE, 116 (5)
- Wang, Z.L., Q.Y. Han, and G.S. Zhou (1980). "Wave propagation method of site seismic response by visco-elastoplastic model," *Proc. of Seventh World Conf. on Earthquake Eng.*, V2, 379-386
- Wang, Z.L., C.-Y. Chang, and C.M. Mok (2001). "Evaluation of site response using downhole array data from a liquefied site," *Proc. 4<sup>th</sup> Int. Conf. Recent Advances in Geotech. Eqk. Eng. Soil Dyn.*, Paper 4.30.
- Weiler, W.A. (1988). "Small strain shear modulus of clay," *Proc. of ASCE Conference on Earthquake Engineering and Soil Dynamics II: Recent Advances in Ground Motion Evaluation*, Geotechnical Special Publication 20, ASCE, New York, 331-345.
- Wilson, E.L. (1968). "A computer program for the dynamic stress analysis of underground structures," EERC Rpt 76-29, Earthquake Eng. Research Center, Univ. of California, Berkeley
- Yang, Z. (2000). "Numerical modeling of earthquake site response including dilation and liquefaction," *PhD Thesis*, Dept. of Civil Eng. and Eng. Mech., Columbia University, NY, New York
- Yang, Z., A. Elgamal and E. Parra (2003). "Computational model for cyclic mobility and associated shear deformation," *J. Geotech. and Geoenviron. Eng.*, ASCE, 129(12), 1119-1127.
- Youngs, R.R. (2004). *Software validation report for SHAKE04*, Geomatrix Consultants
- Zhang, J., R.D. Andrus and C.H. Juang (2005) "Normalized shear modulus and material damping ratio relationships," *J. Geotech. and Geoenviron. Eng.*, ASCE, 131(4), 453-464.
- Zeghal M., A.W. Elgamal, H.T. Tang, and J.C. Stepp (1995). "Lotung downhole array II: evaluation of soil nonlinear properties," *J. Geotech. Engr.*, 121(4), 363-378

## PEER REPORTS

PEER reports are available from the National Information Service for Earthquake Engineering (NISEE). To order PEER reports, please contact the Pacific Earthquake Engineering Research Center, 1301 South 46<sup>th</sup> Street, Richmond, California 94804-4698. Tel.: (510) 665-3405; Fax: (510) 665-3420.

- PEER 2008/05** *Performance-Based Earthquake Engineering Design Evaluation Procedure for Bridge Foundations Undergoing Liquefaction-Induced Lateral Ground Displacement.* Christian A. Ledezma and Jonathan D. Bray. August 2008.
- PEER 2008/04** *Benchmarking of Nonlinear Geotechnical Ground Response Analysis Procedures.* Jonathan P. Stewart, Annie On-Lei Kwok, Youssef M. A. Hashash, Neven Matasovic, Robert Pyke, Zhiliang Wang, and Zhaohui Yang. August 2008.
- PEER 2008/03** *Guidelines for Nonlinear Analysis of Bridge Structures in California.* Ady Aviram, Kevin R. Mackie, and Božidar Stojadinović. August 2008.
- PEER 2008/02** *Treatment of Uncertainties in Seismic-Risk Analysis of Transportation Systems.* Evangelos Stergiou and Anne S. Kiremidjian. July 2008.
- PEER 2008/01** *Seismic Performance Objectives for Tall Buildings.* William T. Holmes, Charles Kircher, William Petak, and Nabih Youssef. August 2008.
- PEER 2007/12** *An Assessment to Benchmark the Seismic Performance of a Code-Conforming Reinforced Concrete Moment-Frame Building.* Curt Haselton, Christine A. Goulet, Judith Mitrani-Reiser, James L. Beck, Gregory G. Deierlein, Keith A. Porter, Jonathan P. Stewart, and Ertugrul Taciroglu. August 2008.
- PEER 2007/11** *Bar Buckling in Reinforced Concrete Bridge Columns.* Wayne A. Brown, Dawn E. Lehman, and John F. Stanton. February 2008.
- PEER 2007/10** *Computational Modeling of Progressive Collapse in Reinforced Concrete Frame Structures.* Mohamed M. Talaat and Khalid M. Mosalam. May 2008.
- PEER 2007/09** *Integrated Probabilistic Performance-Based Evaluation of Benchmark Reinforced Concrete Bridges.* Kevin R. Mackie, John-Michael Wong, and Božidar Stojadinović. January 2008.
- PEER 2007/08** *Assessing Seismic Collapse Safety of Modern Reinforced Concrete Moment-Frame Buildings.* Curt B. Haselton and Gregory G. Deierlein. February 2008.
- PEER 2007/07** *Performance Modeling Strategies for Modern Reinforced Concrete Bridge Columns.* Michael P. Berry and Marc O. Eberhard. April 2008.
- PEER 2007/06** *Development of Improved Procedures for Seismic Design of Buried and Partially Buried Structures.* Linda Al Atik and Nicholas Sitar. June 2007.
- PEER 2007/05** *Uncertainty and Correlation in Seismic Risk Assessment of Transportation Systems.* Renee G. Lee and Anne S. Kiremidjian. July 2007.
- PEER 2007/04** *Numerical Models for Analysis and Performance-Based Design of Shallow Foundations Subjected to Seismic Loading.* Sivapalan Gajan, Tara C. Hutchinson, Bruce L. Kutter, Prishati Raychowdhury, José A. Ugalde, and Jonathan P. Stewart. May 2008.
- PEER 2007/03** *Beam-Column Element Model Calibrated for Predicting Flexural Response Leading to Global Collapse of RC Frame Buildings.* Curt B. Haselton, Abbie B. Liel, Sarah Taylor Lange, and Gregory G. Deierlein. May 2008.
- PEER 2007/02** *Campbell-Bozorgnia NGA Ground Motion Relations for the Geometric Mean Horizontal Component of Peak and Spectral Ground Motion Parameters.* Kenneth W. Campbell and Yousef Bozorgnia. May 2007.
- PEER 2007/01** *Boore-Atkinson NGA Ground Motion Relations for the Geometric Mean Horizontal Component of Peak and Spectral Ground Motion Parameters.* David M. Boore and Gail M. Atkinson. May 2007.
- PEER 2006/12** *Societal Implications of Performance-Based Earthquake Engineering.* Peter J. May. May 2007.
- PEER 2006/11** *Probabilistic Seismic Demand Analysis Using Advanced Ground Motion Intensity Measures, Attenuation Relationships, and Near-Fault Effects.* Polsak Tothong and C. Allin Cornell. March 2007.
- PEER 2006/10** *Application of the PEER PBEE Methodology to the I-880 Viaduct.* Sashi Kunnath. February 2007.
- PEER 2006/09** *Quantifying Economic Losses from Travel Forgone Following a Large Metropolitan Earthquake.* James Moore, Sungbin Cho, Yue Yue Fan, and Stuart Werner. November 2006.
- PEER 2006/08** *Vector-Valued Ground Motion Intensity Measures for Probabilistic Seismic Demand Analysis.* Jack W. Baker and C. Allin Cornell. October 2006.

- PEER 2006/07** *Analytical Modeling of Reinforced Concrete Walls for Predicting Flexural and Coupled–Shear–Flexural Responses.* Kutay Orakcal, Loenardo M. Massone, and John W. Wallace. October 2006.
- PEER 2006/06** *Nonlinear Analysis of a Soil-Drilled Pier System under Static and Dynamic Axial Loading.* Gang Wang and Nicholas Sitar. November 2006.
- PEER 2006/05** *Advanced Seismic Assessment Guidelines.* Paolo Bazzurro, C. Allin Cornell, Charles Menun, Maziar Motahari, and Nicolas Luco. September 2006.
- PEER 2006/04** *Probabilistic Seismic Evaluation of Reinforced Concrete Structural Components and Systems.* Tae Hyung Lee and Khalid M. Mosalam. August 2006.
- PEER 2006/03** *Performance of Lifelines Subjected to Lateral Spreading.* Scott A. Ashford and Teerawut Juirnarongrit. July 2006.
- PEER 2006/02** *Pacific Earthquake Engineering Research Center Highway Demonstration Project.* Anne Kiremidjian, James Moore, Yue Yue Fan, Nesrin Basoz, Ozgur Yazali, and Meredith Williams. April 2006.
- PEER 2006/01** *Bracing Berkeley. A Guide to Seismic Safety on the UC Berkeley Campus.* Mary C. Comerio, Stephen Tوبرiner, and Ariane Fehrenkamp. January 2006.
- PEER 2005/16** *Seismic Response and Reliability of Electrical Substation Equipment and Systems.* Junho Song, Armen Der Kiureghian, and Jerome L. Sackman. April 2006.
- PEER 2005/15** *CPT-Based Probabilistic Assessment of Seismic Soil Liquefaction Initiation.* R. E. S. Moss, R. B. Seed, R. E. Kayen, J. P. Stewart, and A. Der Kiureghian. April 2006.
- PEER 2005/14** *Workshop on Modeling of Nonlinear Cyclic Load-Deformation Behavior of Shallow Foundations.* Bruce L. Kutter, Geoffrey Martin, Tara Hutchinson, Chad Harden, Sivapalan Gajan, and Justin Phalen. March 2006.
- PEER 2005/13** *Stochastic Characterization and Decision Bases under Time-Dependent Aftershock Risk in Performance-Based Earthquake Engineering.* Gee Liek Yeo and C. Allin Cornell. July 2005.
- PEER 2005/12** *PEER Testbed Study on a Laboratory Building: Exercising Seismic Performance Assessment.* Mary C. Comerio, editor. November 2005.
- PEER 2005/11** *Van Nuys Hotel Building Testbed Report: Exercising Seismic Performance Assessment.* Helmut Krawinkler, editor. October 2005.
- PEER 2005/10** *First NEES/E-Defense Workshop on Collapse Simulation of Reinforced Concrete Building Structures.* September 2005.
- PEER 2005/09** *Test Applications of Advanced Seismic Assessment Guidelines.* Joe Maffei, Karl Telleen, Danya Mohr, William Holmes, and Yuki Nakayama. August 2006.
- PEER 2005/08** *Damage Accumulation in Lightly Confined Reinforced Concrete Bridge Columns.* R. Tyler Ranf, Jared M. Nelson, Zach Price, Marc O. Eberhard, and John F. Stanton. April 2006.
- PEER 2005/07** *Experimental and Analytical Studies on the Seismic Response of Freestanding and Anchored Laboratory Equipment.* Dimitrios Konstantinidis and Nicos Makris. January 2005.
- PEER 2005/06** *Global Collapse of Frame Structures under Seismic Excitations.* Luis F. Ibarra and Helmut Krawinkler. September 2005.
- PEER 2005/05** *Performance Characterization of Bench- and Shelf-Mounted Equipment.* Samit Ray Chaudhuri and Tara C. Hutchinson. May 2006.
- PEER 2005/04** *Numerical Modeling of the Nonlinear Cyclic Response of Shallow Foundations.* Chad Harden, Tara Hutchinson, Geoffrey R. Martin, and Bruce L. Kutter. August 2005.
- PEER 2005/03** *A Taxonomy of Building Components for Performance-Based Earthquake Engineering.* Keith A. Porter. September 2005.
- PEER 2005/02** *Fragility Basis for California Highway Overpass Bridge Seismic Decision Making.* Kevin R. Mackie and Božidar Stojadinović. June 2005.
- PEER 2005/01** *Empirical Characterization of Site Conditions on Strong Ground Motion.* Jonathan P. Stewart, Yoojoong Choi, and Robert W. Graves. June 2005.
- PEER 2004/09** *Electrical Substation Equipment Interaction: Experimental Rigid Conductor Studies.* Christopher Stearns and André Filiatrault. February 2005.
- PEER 2004/08** *Seismic Qualification and Fragility Testing of Line Break 550-kV Disconnect Switches.* Shakhzod M. Takhirov, Gregory L. Fenves, and Eric Fujisaki. January 2005.
- PEER 2004/07** *Ground Motions for Earthquake Simulator Qualification of Electrical Substation Equipment.* Shakhzod M. Takhirov, Gregory L. Fenves, Eric Fujisaki, and Don Clyde. January 2005.

- PEER 2004/06** *Performance-Based Regulation and Regulatory Regimes.* Peter J. May and Chris Koski. September 2004.
- PEER 2004/05** *Performance-Based Seismic Design Concepts and Implementation: Proceedings of an International Workshop.* Peter Fajfar and Helmut Krawinkler, editors. September 2004.
- PEER 2004/04** *Seismic Performance of an Instrumented Tilt-up Wall Building.* James C. Anderson and Vitelmo V. Bertero. July 2004.
- PEER 2004/03** *Evaluation and Application of Concrete Tilt-up Assessment Methodologies.* Timothy Graf and James O. Malley. October 2004.
- PEER 2004/02** *Analytical Investigations of New Methods for Reducing Residual Displacements of Reinforced Concrete Bridge Columns.* Junichi Sakai and Stephen A. Mahin. August 2004.
- PEER 2004/01** *Seismic Performance of Masonry Buildings and Design Implications.* Kerri Anne Taeko Tokoro, James C. Anderson, and Vitelmo V. Bertero. February 2004.
- PEER 2003/18** *Performance Models for Flexural Damage in Reinforced Concrete Columns.* Michael Berry and Marc Eberhard. August 2003.
- PEER 2003/17** *Predicting Earthquake Damage in Older Reinforced Concrete Beam-Column Joints.* Catherine Pagni and Laura Lowes. October 2004.
- PEER 2003/16** *Seismic Demands for Performance-Based Design of Bridges.* Kevin Mackie and Božidar Stojadinović. August 2003.
- PEER 2003/15** *Seismic Demands for Nondeteriorating Frame Structures and Their Dependence on Ground Motions.* Ricardo Antonio Medina and Helmut Krawinkler. May 2004.
- PEER 2003/14** *Finite Element Reliability and Sensitivity Methods for Performance-Based Earthquake Engineering.* Terje Haukaas and Armen Der Kiureghian. April 2004.
- PEER 2003/13** *Effects of Connection Hysteretic Degradation on the Seismic Behavior of Steel Moment-Resisting Frames.* Janise E. Rodgers and Stephen A. Mahin. March 2004.
- PEER 2003/12** *Implementation Manual for the Seismic Protection of Laboratory Contents: Format and Case Studies.* William T. Holmes and Mary C. Comerio. October 2003.
- PEER 2003/11** *Fifth U.S.-Japan Workshop on Performance-Based Earthquake Engineering Methodology for Reinforced Concrete Building Structures.* February 2004.
- PEER 2003/10** *A Beam-Column Joint Model for Simulating the Earthquake Response of Reinforced Concrete Frames.* Laura N. Lowes, Nilanjan Mitra, and Arash Altoontash. February 2004.
- PEER 2003/09** *Sequencing Repairs after an Earthquake: An Economic Approach.* Marco Casari and Simon J. Wilkie. April 2004.
- PEER 2003/08** *A Technical Framework for Probability-Based Demand and Capacity Factor Design (DCFD) Seismic Formats.* Fatemeh Jalayer and C. Allin Cornell. November 2003.
- PEER 2003/07** *Uncertainty Specification and Propagation for Loss Estimation Using FOSM Methods.* Jack W. Baker and C. Allin Cornell. September 2003.
- PEER 2003/06** *Performance of Circular Reinforced Concrete Bridge Columns under Bidirectional Earthquake Loading.* Mahmoud M. Hachem, Stephen A. Mahin, and Jack P. Moehle. February 2003.
- PEER 2003/05** *Response Assessment for Building-Specific Loss Estimation.* Eduardo Miranda and Shahram Taghavi. September 2003.
- PEER 2003/04** *Experimental Assessment of Columns with Short Lap Splices Subjected to Cyclic Loads.* Murat Melek, John W. Wallace, and Joel Conte. April 2003.
- PEER 2003/03** *Probabilistic Response Assessment for Building-Specific Loss Estimation.* Eduardo Miranda and Hesameddin Aslani. September 2003.
- PEER 2003/02** *Software Framework for Collaborative Development of Nonlinear Dynamic Analysis Program.* Jun Peng and Kincho H. Law. September 2003.
- PEER 2003/01** *Shake Table Tests and Analytical Studies on the Gravity Load Collapse of Reinforced Concrete Frames.* Kenneth John Elwood and Jack P. Moehle. November 2003.
- PEER 2002/24** *Performance of Beam to Column Bridge Joints Subjected to a Large Velocity Pulse.* Natalie Gibson, André Filiatrault, and Scott A. Ashford. April 2002.
- PEER 2002/23** *Effects of Large Velocity Pulses on Reinforced Concrete Bridge Columns.* Greg L. Orozco and Scott A. Ashford. April 2002.

- PEER 2002/22** *Characterization of Large Velocity Pulses for Laboratory Testing.* Kenneth E. Cox and Scott A. Ashford. April 2002.
- PEER 2002/21** *Fourth U.S.-Japan Workshop on Performance-Based Earthquake Engineering Methodology for Reinforced Concrete Building Structures.* December 2002.
- PEER 2002/20** *Barriers to Adoption and Implementation of PBEE Innovations.* Peter J. May. August 2002.
- PEER 2002/19** *Economic-Engineered Integrated Models for Earthquakes: Socioeconomic Impacts.* Peter Gordon, James E. Moore II, and Harry W. Richardson. July 2002.
- PEER 2002/18** *Assessment of Reinforced Concrete Building Exterior Joints with Substandard Details.* Chris P. Pantelides, Jon Hansen, Justin Nadauld, and Lawrence D. Reaveley. May 2002.
- PEER 2002/17** *Structural Characterization and Seismic Response Analysis of a Highway Overcrossing Equipped with Elastomeric Bearings and Fluid Dampers: A Case Study.* Nicos Makris and Jian Zhang. November 2002.
- PEER 2002/16** *Estimation of Uncertainty in Geotechnical Properties for Performance-Based Earthquake Engineering.* Allen L. Jones, Steven L. Kramer, and Pedro Arduino. December 2002.
- PEER 2002/15** *Seismic Behavior of Bridge Columns Subjected to Various Loading Patterns.* Asadollah Esmaeily-Gh. and Yan Xiao. December 2002.
- PEER 2002/14** *Inelastic Seismic Response of Extended Pile Shaft Supported Bridge Structures.* T.C. Hutchinson, R.W. Boulanger, Y.H. Chai, and I.M. Idriss. December 2002.
- PEER 2002/13** *Probabilistic Models and Fragility Estimates for Bridge Components and Systems.* Paolo Gardoni, Armen Der Kiureghian, and Khalid M. Mosalam. June 2002.
- PEER 2002/12** *Effects of Fault Dip and Slip Rake on Near-Source Ground Motions: Why Chi-Chi Was a Relatively Mild M7.6 Earthquake.* Brad T. Agaard, John F. Hall, and Thomas H. Heaton. December 2002.
- PEER 2002/11** *Analytical and Experimental Study of Fiber-Reinforced Strip Isolators.* James M. Kelly and Shakhzod M. Takhirov. September 2002.
- PEER 2002/10** *Centrifuge Modeling of Settlement and Lateral Spreading with Comparisons to Numerical Analyses.* Sivapalan Gajan and Bruce L. Kutter. January 2003.
- PEER 2002/09** *Documentation and Analysis of Field Case Histories of Seismic Compression during the 1994 Northridge, California, Earthquake.* Jonathan P. Stewart, Patrick M. Smith, Daniel H. Whang, and Jonathan D. Bray. October 2002.
- PEER 2002/08** *Component Testing, Stability Analysis and Characterization of Buckling-Restrained Unbonded Braces™.* Cameron Black, Nicos Makris, and Ian Aiken. September 2002.
- PEER 2002/07** *Seismic Performance of Pile-Wharf Connections.* Charles W. Roeder, Robert Graff, Jennifer Soderstrom, and Jun Han Yoo. December 2001.
- PEER 2002/06** *The Use of Benefit-Cost Analysis for Evaluation of Performance-Based Earthquake Engineering Decisions.* Richard O. Zerbe and Anthony Falit-Baiamonte. September 2001.
- PEER 2002/05** *Guidelines, Specifications, and Seismic Performance Characterization of Nonstructural Building Components and Equipment.* André Filiatrault, Constantin Christopoulos, and Christopher Stearns. September 2001.
- PEER 2002/04** *Consortium of Organizations for Strong-Motion Observation Systems and the Pacific Earthquake Engineering Research Center Lifelines Program: Invited Workshop on Archiving and Web Dissemination of Geotechnical Data, 4–5 October 2001.* September 2002.
- PEER 2002/03** *Investigation of Sensitivity of Building Loss Estimates to Major Uncertain Variables for the Van Nuys Testbed.* Keith A. Porter, James L. Beck, and Rustem V. Shaikhutdinov. August 2002.
- PEER 2002/02** *The Third U.S.-Japan Workshop on Performance-Based Earthquake Engineering Methodology for Reinforced Concrete Building Structures.* July 2002.
- PEER 2002/01** *Nonstructural Loss Estimation: The UC Berkeley Case Study.* Mary C. Comerio and John C. Stallmeyer. December 2001.
- PEER 2001/16** *Statistics of SDF-System Estimate of Roof Displacement for Pushover Analysis of Buildings.* Anil K. Chopra, Rakesh K. Goel, and Chatpan Chintanapakdee. December 2001.
- PEER 2001/15** *Damage to Bridges during the 2001 Nisqually Earthquake.* R. Tyler Ranf, Marc O. Eberhard, and Michael P. Berry. November 2001.
- PEER 2001/14** *Rocking Response of Equipment Anchored to a Base Foundation.* Nicos Makris and Cameron J. Black. September 2001.

- PEER 2001/13** *Modeling Soil Liquefaction Hazards for Performance-Based Earthquake Engineering.* Steven L. Kramer and Ahmed-W. Elgamal. February 2001.
- PEER 2001/12** *Development of Geotechnical Capabilities in OpenSees.* Boris Jeremi . September 2001.
- PEER 2001/11** *Analytical and Experimental Study of Fiber-Reinforced Elastomeric Isolators.* James M. Kelly and Shakhzod M. Takhirov. September 2001.
- PEER 2001/10** *Amplification Factors for Spectral Acceleration in Active Regions.* Jonathan P. Stewart, Andrew H. Liu, Yoojoong Choi, and Mehmet B. Baturay. December 2001.
- PEER 2001/09** *Ground Motion Evaluation Procedures for Performance-Based Design.* Jonathan P. Stewart, Shyh-Jeng Chiou, Jonathan D. Bray, Robert W. Graves, Paul G. Somerville, and Norman A. Abrahamson. September 2001.
- PEER 2001/08** *Experimental and Computational Evaluation of Reinforced Concrete Bridge Beam-Column Connections for Seismic Performance.* Clay J. Naito, Jack P. Moehle, and Khalid M. Mosalam. November 2001.
- PEER 2001/07** *The Rocking Spectrum and the Shortcomings of Design Guidelines.* Nicos Makris and Dimitrios Konstantinidis. August 2001.
- PEER 2001/06** *Development of an Electrical Substation Equipment Performance Database for Evaluation of Equipment Fragilities.* Thalia Agnanos. April 1999.
- PEER 2001/05** *Stiffness Analysis of Fiber-Reinforced Elastomeric Isolators.* Hsiang-Chuan Tsai and James M. Kelly. May 2001.
- PEER 2001/04** *Organizational and Societal Considerations for Performance-Based Earthquake Engineering.* Peter J. May. April 2001.
- PEER 2001/03** *A Modal Pushover Analysis Procedure to Estimate Seismic Demands for Buildings: Theory and Preliminary Evaluation.* Anil K. Chopra and Rakesh K. Goel. January 2001.
- PEER 2001/02** *Seismic Response Analysis of Highway Overcrossings Including Soil-Structure Interaction.* Jian Zhang and Nicos Makris. March 2001.
- PEER 2001/01** *Experimental Study of Large Seismic Steel Beam-to-Column Connections.* Egor P. Popov and Shakhzod M. Takhirov. November 2000.
- PEER 2000/10** *The Second U.S.-Japan Workshop on Performance-Based Earthquake Engineering Methodology for Reinforced Concrete Building Structures.* March 2000.
- PEER 2000/09** *Structural Engineering Reconnaissance of the August 17, 1999 Earthquake: Kocaeli (Izmit), Turkey.* Halil Sezen, Kenneth J. Elwood, Andrew S. Whittaker, Khalid Mosalam, John J. Wallace, and John F. Stanton. December 2000.
- PEER 2000/08** *Behavior of Reinforced Concrete Bridge Columns Having Varying Aspect Ratios and Varying Lengths of Confinement.* Anthony J. Calderone, Dawn E. Lehman, and Jack P. Moehle. January 2001.
- PEER 2000/07** *Cover-Plate and Flange-Plate Reinforced Steel Moment-Resisting Connections.* Taejin Kim, Andrew S. Whittaker, Amir S. Gilani, Vitelmo V. Bertero, and Shakhzod M. Takhirov. September 2000.
- PEER 2000/06** *Seismic Evaluation and Analysis of 230-kV Disconnect Switches.* Amir S. J. Gilani, Andrew S. Whittaker, Gregory L. Fenves, Chun-Hao Chen, Henry Ho, and Eric Fujisaki. July 2000.
- PEER 2000/05** *Performance-Based Evaluation of Exterior Reinforced Concrete Building Joints for Seismic Excitation.* Chandra Clyde, Chris P. Pantelides, and Lawrence D. Reaveley. July 2000.
- PEER 2000/04** *An Evaluation of Seismic Energy Demand: An Attenuation Approach.* Chung-Che Chou and Chia-Ming Uang. July 1999.
- PEER 2000/03** *Framing Earthquake Retrofitting Decisions: The Case of Hillside Homes in Los Angeles.* Detlof von Winterfeldt, Nels Roselund, and Alicia Kitsuse. March 2000.
- PEER 2000/02** *U.S.-Japan Workshop on the Effects of Near-Field Earthquake Shaking.* Andrew Whittaker, ed. July 2000.
- PEER 2000/01** *Further Studies on Seismic Interaction in Interconnected Electrical Substation Equipment.* Armen Der Kiureghian, Kee-Jeung Hong, and Jerome L. Sackman. November 1999.
- PEER 1999/14** *Seismic Evaluation and Retrofit of 230-kV Porcelain Transformer Bushings.* Amir S. Gilani, Andrew S. Whittaker, Gregory L. Fenves, and Eric Fujisaki. December 1999.
- PEER 1999/13** *Building Vulnerability Studies: Modeling and Evaluation of Tilt-up and Steel Reinforced Concrete Buildings.* John W. Wallace, Jonathan P. Stewart, and Andrew S. Whittaker, editors. December 1999.
- PEER 1999/12** *Rehabilitation of Nonductile RC Frame Building Using Encasement Plates and Energy-Dissipating Devices.* Mehrdad Sasani, Vitelmo V. Bertero, James C. Anderson. December 1999.

- PEER 1999/11** *Performance Evaluation Database for Concrete Bridge Components and Systems under Simulated Seismic Loads.* Yael D. Hose and Frieder Seible. November 1999.
- PEER 1999/10** *U.S.-Japan Workshop on Performance-Based Earthquake Engineering Methodology for Reinforced Concrete Building Structures.* December 1999.
- PEER 1999/09** *Performance Improvement of Long Period Building Structures Subjected to Severe Pulse-Type Ground Motions.* James C. Anderson, Vitelmo V. Bertero, and Raul Bertero. October 1999.
- PEER 1999/08** *Envelopes for Seismic Response Vectors.* Charles Menun and Armen Der Kiureghian. July 1999.
- PEER 1999/07** *Documentation of Strengths and Weaknesses of Current Computer Analysis Methods for Seismic Performance of Reinforced Concrete Members.* William F. Cofer. November 1999.
- PEER 1999/06** *Rocking Response and Overturning of Anchored Equipment under Seismic Excitations.* Nicos Makris and Jian Zhang. November 1999.
- PEER 1999/05** *Seismic Evaluation of 550 kV Porcelain Transformer Bushings.* Amir S. Gilani, Andrew S. Whittaker, Gregory L. Fennes, and Eric Fujisaki. October 1999.
- PEER 1999/04** *Adoption and Enforcement of Earthquake Risk-Reduction Measures.* Peter J. May, Raymond J. Burby, T. Jens Feeley, and Robert Wood.
- PEER 1999/03** *Task 3 Characterization of Site Response General Site Categories.* Adrian Rodriguez-Marek, Jonathan D. Bray, and Norman Abrahamson. February 1999.
- PEER 1999/02** *Capacity-Demand-Diagram Methods for Estimating Seismic Deformation of Inelastic Structures: SDF Systems.* Anil K. Chopra and Rakesh Goel. April 1999.
- PEER 1999/01** *Interaction in Interconnected Electrical Substation Equipment Subjected to Earthquake Ground Motions.* Armen Der Kiureghian, Jerome L. Sackman, and Kee-Jeung Hong. February 1999.
- PEER 1998/08** *Behavior and Failure Analysis of a Multiple-Frame Highway Bridge in the 1994 Northridge Earthquake.* Gregory L. Fennes and Michael Ellery. December 1998.
- PEER 1998/07** *Empirical Evaluation of Inertial Soil-Structure Interaction Effects.* Jonathan P. Stewart, Raymond B. Seed, and Gregory L. Fennes. November 1998.
- PEER 1998/06** *Effect of Damping Mechanisms on the Response of Seismic Isolated Structures.* Nicos Makris and Shih-Po Chang. November 1998.
- PEER 1998/05** *Rocking Response and Overturning of Equipment under Horizontal Pulse-Type Motions.* Nicos Makris and Yiannis Roussos. October 1998.
- PEER 1998/04** *Pacific Earthquake Engineering Research Invitational Workshop Proceedings, May 14-15, 1998: Defining the Links between Planning, Policy Analysis, Economics and Earthquake Engineering.* Mary Comerio and Peter Gordon. September 1998.
- PEER 1998/03** *Repair/Upgrade Procedures for Welded Beam to Column Connections.* James C. Anderson and Xiaojing Duan. May 1998.
- PEER 1998/02** *Seismic Evaluation of 196 kV Porcelain Transformer Bushings.* Amir S. Gilani, Juan W. Chavez, Gregory L. Fennes, and Andrew S. Whittaker. May 1998.
- PEER 1998/01** *Seismic Performance of Well-Confined Concrete Bridge Columns.* Dawn E. Lehman and Jack P. Moehle. December 2000.

## ONLINE REPORTS

The following PEER reports are available by Internet only at [http://peer.berkeley.edu/publications/peer\\_reports.html](http://peer.berkeley.edu/publications/peer_reports.html)

- PEER 2008/101** *Seismic Performance Objectives for Tall Buildings*. William T. Holmes, Charles Kircher, William Petak, and Nabih Youssef. August 2008.
- PEER 2007/101** *Generalized Hybrid Simulation Framework for Structural Systems Subjected to Seismic Loading*. Tarek Elkhoraibi and Khalid M. Mosalam. July 2007.
- PEER 2007/100** *Seismic Evaluation of Reinforced Concrete Buildings Including Effects of Masonry Infill Walls*. Alidad Hashemi and Khalid M. Mosalam. July 2007.